中国科学技术大学

博士学位论文

MRPC 在高能重离子实验上的应用研究

作者姓名： 胡东栋

学科专业： 粒子物理与原子核物理

导师姓名： 邵明 教授　孙勇杰 副教授 Norbert Herrmann 教授

完成时间： 二〇一九年六月四日

University of Science and Technology of China

A dissertation for doctor's degree

The study on MRPC application in Heavy-ion experiment and the quality control of mass production for STAR/CBM-eTOF upgrade

Author: Dongdong Hu

Speciality: Particle and Nuclear Physics

Supervisors: Prof. Ming Shao, Associate Prof. Yongjie Sun,
Prof. Norbert Herrmann

Finished time: June 4, 2019

摘　要

根据 QCD（Quantum Chromodynamics，量子色动力学）的预测，如果温度足够高或者能量密度足够大，强子物质会转变为 QGP（Quark Gluon Plasma，夸克胶子等离子）态。这种极端的高温高密物质形态，在实验室中，可以通过相对论重离子碰撞实现。寻找转变的相边界和临界点，是当前高能重离子物理领域亟待解决的关键问题。

德国正在建造的 FAIR（Facility for Antiproton and Ion Research）加速器上的 CBM（Compressed Baryonic Matter）实验，是有望实现这一目标的主要实验之一。CBM 实验预期于 2025 年首次物理运行取数，工作在 FAIR 的 SIS100 加速器下，对应的能量范围在 2–11 AGeV 之间。为了获得更高的重子数密度，CBM 设计工作在固定靶模式下。在 CBM 实验中，TOF（Time-of-Flight，飞行时间探测器）是实现粒子鉴别的关键子探测器系统。CBM TOF 系统设计面积约 120 平方米。在这样大的面积下，MRPC（Multi-gap Resistive Plate Chamber，多气隙电阻板室）技术几乎是唯一的选择。作为一个高亮度的重离子打靶实验，在前向将产生极高的末态粒子通量，在 TOF 对应的平面上，末态粒子计数率在 0.1 - 100 kHz/cm^2 范围内。在占总面积超过 50% 的 CBM-TOF 的外围区域，计数率 ∼1 kHz/cm^2，采用超薄浮法玻璃电极的 MRPC 是实现所需性能的最可行选择。

美国布鲁克海文国家实验室的 RHIC(Relativistic Heavy Ion Collider，相对论重离子对撞机) 加速器上的 STAR(Solenoidal Tracker At RHIC) 实验，是目前正在运行的一个重要的相对论重离子实验装置。通过已经完成的 BES-I（Beam Energy Scan-I，一期束流能量扫描），STAR 已经发现了 QGP 存在的关键证据。为了对 QCD 相图进行更精细的研究，STAR 计划在 2019-2021 年开展二期束流能量扫描（BES-II），并在固定靶条件下运行取数。这要求在前向区域具有更好的径迹、粒子分辨能力。因此，端盖 TOF（eTOF）成为 STAR 升级的关键探测器之一。根据 CBM 和 STAR 合作组达成的协议，部分 CBM TOF MRPC 安装到 STAR 实验，组成东端盖 TOF，提高 STAR 前向的粒子鉴别能力。STAR eTOF 由 36 个模块组成，包含 108 个 MRPC，6912 个读出电子学通道。通过 eTOF 结合内时间投影室的升级，可以把前向 π/ K 粒子鉴别的能力从 0.75 提高到 1.60 GeV/c，π/K/p 鉴别能力从 1.1 提高到 3.0 GeV/c。这对寻找 QCD 一级相变及其临界点至关重要。

在国内兰州重离子研究装置冷却储存环（Heavy Ion Research Facility in Lanzhou-Cooling Storage Ring）上的低温高密度核物质测量谱仪（CSR-External-Target-Facility Experiment，CEE）实验，是中国第一个大规模重离子物理实验装置。CEE 期望通过测量 π^-/π^+ 比率（和其他相关的可观测量），研究各种重离子碰撞系统

的核对称能的密度依赖性; 在低温和高净重子密度区域，超饱和密度核状态方程（EOS）; 以及高重子数密度下，量子色动力学（QCD）的相图。在 CEE 的靶点附近，设计了一个新型的起点触发（T0）探测器，为整个系统提供触发、用来测量带电粒子的多重数、角度分布和时间信息。这个 T0 探测器，将采用 MRPC 技术建造，它可以提供精确的对撞时间和对撞几何信息。

经过二十余年的发展，MRPC 已经成为大面积高分辨飞行时间探测领域探测器的不二之选。MRPC 具有低价、易于建造、易于组装、并且有极好的时间分辨等优势，其本征时间分辨可达 50 ps，在很宽的电压坪下其效率高于 95%。所有的优势都适合于重离子物理实验，已经或正在被大多数的重离子实验所采用。

本论文主要从下面三个方面，研究 MRPC 在高能量重离子实验领域的应用。

1) CBM TOF MRPC3b 型探测器的设计。CBM-TOF 对 MRPC 的最大挑战是计数率。尽管 MRPC3b 所在的外围区域计数率 ～ 1 kHz/cm^2，普通浮法玻璃电极的 MRPC 仍无法满足此需求。通过降低玻璃电阻板的厚度，可以有效提高 MRPC 的计数率，但同时也对 MRPC 的设计和制作提出了更高的要求。CBM 实验面临的另一挑战是高通量下的无触发数据获取模式（free streaming），要求所有的探测器，尽可能降低假信号。对于 MRPC 来说，需要通过阻抗匹配设计，消除信号的反射本论文的研究工作重点针对这两项关键需求，研究了提高计数率的方法和 MRPC 的阻抗性质，最终完成了 MRPC3b 原型探测器设计，宇宙线测试和束流测试结果显示，各项性能满足 CBM-TOF 的设计要求。

2) CBM/STAR eTOF 批量制作中的生产工艺和质量控制方法。为了完成用于 STAR eTOF 的 80 个 MRPC3b 的批量制作和性能测试，论文期间研究并优化了 MRPC 的批量制作工艺，建立了探测器和 eTOF 模块的质量控制（QC）和质量保证（QA）方法。为确保探测器和 eTOF 模块的性能, 搭建了三套不同的测试系统，同时应用于宇宙线性能测试。在对测试结果的分析过程中，首次把径迹重建的方法引入 MRPC 测试系统，提高了测试结果的可靠性。为了便于质量跟踪，在 CERN ROOT 基础上建立了批量制作的专用数据库。目前，STAR eTOF 已顺利安装完成，证明了生产工艺设计和质量控制方法可行、可靠，为将来 TOF 系统工程建造奠定了坚实的基础。

3) CEE T0 MRPC 探测器的设计和研制。论文期间同时完成了 CEE T0 探测器从概念性设计到技术设计和制作的整个过程，分别利用强子束流和重离子束流测试了原型样机的性能。通过模拟结果和实验结果的对比，原型探测器的时间分辨好于 50 ps。整个 T0 探测器系统，包括电子学和探测器两部分的定时性能满足 CEE 实验的要求。

关键词：多气隙电阻板室；重离子物理；CBM；STAR；CEE；时间分辨

ABSTRACT

Quantum Chromodynamics (QCD) predicts a transition from the hadronic matter to a deconfined state of matter, quark-gluon plasma (QGP), if the temperature or energy density are high enough. The creation of QGP, a fundamentally new state of matter under extreme conditions, is expected to be realized in the laboratory by colliding high energy heavy-ions. To explore the phase boundary and critical point of the transition has become a major subject in the current high-energy heavy ion physics research.

The CBM (Compressed Baryonic Matter) experiment on the FAIR (Facility for Antiproton and Ion Research) accelerator being built in Germany is one of the main experiments for this research. The CBM experiment is expected to be operational in 2025 at incident energies between 2 and 11AGeV in heavy-ion collisions at the FAIR's SIS100 accelerator. For the CBM detector system, the key element providing hadron identification is the Time-of-Flight (TOF) wall covering the polar angular range of 2.5^o–25^o and full azimuth. The TOF is located from the target with a distance of 6 to 10 m, and a corresponding area of approximately 120 m^2. In such a large area, the MRPC (Multi-gap Resistive Plate Chamber) technology is likely the only choice under the consideration of cost and performance. As a high-intensity heavy ion fix-target experiment, a very large final state particle flux is generated in the forward direction, and in the TOF plane, the final particle rate is about 0.1 - 100 kHz/cm^2. In the low rate region of the CBM-TOF with a total area of more than 50%, the rate is $\sim$1 kHz/cm^2, and the MRPC with ultra-thin float glass sheets is the most viable option to achieve the desired performance.

The STAR (Solenoidal Tracker At RHIC) experiment on the RHIC (Relativistic Heavy Ion Collider) accelerator at the Brookhaven National Laboratory is an important relativistic heavy ion experimental device currently in operation. STAR has found key evidence for the existence of QGP through the already completed BES-I (Beam Energy Scan-I) run. In order to study the QCD phase diagram in more detail, STAR plans to conduct a second-phase beam energy scan (BES-II) in 2019-2021 and run under the fix-target mode. This requires better tracking and particle identification (PID) in the forward region. Therefore, the endcap TOF (eTOF) has become one of the key detectors for STAR upgrades. Before the operation of the CBM, the CBM and STAR reached an agreement to install some CBM TOF MRPCs into the STAR experiment to form the eTOF to improve the forward PID capability at STAR. The STAR eTOF consists of

36 modules, including 108 MRPCs and 6912 readout electronics channels. Through the upgrade of eTOF combined with the internal time projection chamber (TPC), the ability to identify the forward π/K particles can be improved from 0.75 to 1.60 GeV/c, and the π/K/p discrimination ability is increased from 1.1 to 3.0 GeV/c. This is crucial for searching the QCD first-order phase transition.

The CSR-External-Target-Facility Experiment (CEE) on the Heavy Ion Research Facility in Lanzhou(HIRFL)-Cooling Storage Ring (CSR) is the first large-scale heavy-ion experimental device in China. CEE expects to study the density dependence of the nuclear symmetry energy of various heavy ion collision systems by measuring the ratio of π^-/π^+ (and other related observables) and study the nuclear equation of state (EOS) at suprasaturation density, as well as the rich QCD phase at high-density/low-temperature. Near the CEE target, a new type of T0/trigger detector was designed to provide triggering for the entire system to measure the multiplicity, angular distribution and time information of charged particles. This T0/Triggers detector, which will be built using MRPC technology, provides accurate collision time and collision geometry information for the CEE.

MRPC technology was born in the LAA project of the European Nuclear Research Center (CERN). After more than 20 years of development, MRPC has become the best choice for large-area detectors in precision time-of-flight detection. The MRPC technology has proved to be very inexpensive, easy to build, easily segmented, and have an excellent time resolution. Its intrinsic time resolution can reach 50 ps or better and its efficiency is higher than 95% at a wide voltage plateau, all of which are well suited for the heavy-ion experiment. So most of the heavy-ion experiments have adopted MRPC or will adopt MRPC to construct their TOF detector.

This thesis mainly studies the application of MRPC in high energy heavy ion experiments from the following three aspects.

1) *Design of CBM TOF MRPC3b detector.* The most challenging requirement for the CBM-TOF wall is its a rate capability. Although the MRPC3b is in the low rate region at $\sim$1 kHz/cm^2, the MRPC using normal float glass plates cannot meet this requirement. By reducing the thickness of the glass plate, the rate of the MRPC can be effectively improved, but at the same time, higher requirements are placed on the design and assembly of the MRPC. Another challenge in the CBM experiment is the high-flux, triggerless data acquisition mode, which requires all detectors to minimize false signals. So, it is necessary to eliminate the reflection of the signal by improved impedance matching design for MRPC. The thesis has focused on these two key requirements, s-

tudied the method of improving the rate ability and the impedance properties of MRPC, and finally completed the MRPC3b prototype detector design. The cosmic ray test and beam test results show that the performance meets requirements of CBM -TOF.

2) *Production process and quality control methods in CBM/STAR eTOF mass production.* In order to complete the mass production and performance testing of 80 MRPC3bs for STAR eTOF, the mass production process of MRPC was studied and optimized, and the quality control (QC) and quality assurance (QA) methods for the eTOF modules were established. To ensure the performance of the eTOF module, three different cosmic-ray test systems were built and applied to test the MRPC performance. In the analysis of the data, the method of track reconstruction was introduced into the MRPC test system for the first time, which improved the reliability of the test results. For convenience quality tracking, a dedicated database for mass production has been established based on CERN ROOT. At present, STAR eTOF has been successfully installed, which proves that the production process design and quality control methods are feasible and reliable, which lays a solid foundation for the future TOF system engineering construction.

3) *Design of the CEE T0 MRPC detector.* In the thesis, the whole process of CEE T0 detector from conceptual design to technical design and construction was completed. The performance of the prototype was tested by using the hadron beam and the heavy ion beam respectively. The time resolution of the prototype detector is better than 50 ps by comparing the simulation results with the experimental results. The timing performance of the T0 system, including electronics and detectors, meets the requirements of the CEE experiment.

Key Words: MRPC; Heavy-ion; CBM; STAR; Time resolution; CEE

Contents

List of Figures

3.40 The measured detection efficiency and time resolution vs. HV, (a) for 140 μm-gap MRPC and (b) for 230 μm-gap MRPC respectively. 69
3.41 Image (a) shows the counter damaged by the discharge close to the HV contact. (b) depicts the design of the HV strip. Figure (c) is our newly designed glass blocker with 3D printing technology and a precision of 100 μm. 70

4.1 Simulation of eTOF hits and rate distribution[4] 72
4.2 Mass production schedule of the MRPC3b. 73
4.3 (a) The appearance of MRPC3b in a real size 3D model and (b) The readout pattern. 73
4.4 (a) The signal transmission to the middle PCB and the connector to FEE. (b) The HV connection on the bottom PCB. 73
4.5 The flow diagram of QC&QA at various production stages. 75
4.6 MRPC assembly record for the mass production. 75
4.7 The definition of the position ID. 75
4.8 Unqualified PCB found in the mass production. 75
4.9 Manufacturing MRPCs in the clean room and assembling MRPC on the clean desk. 77
4.10 Qrcode for the mass production. 78
4.11 The assembly flowchart for eTOF module. 78
4.12 The parameters of both counters 79
4.13 In the course of transportation, the high voltage line breaks. 79
4.14 The photo shows two kinds of MRPC. (a) is MRPC3a. (b) is MRPC3b. . . 80
4.15 Exploded view of the eTOF module box. 80
4.16 high voltage connector. 81
4.17 eTOF module assembled by MRPC3a (a) and MRPC3b (b). 81
4.18 Actual picture of 36 modules after assembly in the clean room. 82
4.19 FairDB design framework 83
4.20 Conceptual design of the CBM/STAR eTOF database 85
4.21 main webpage of the database website. 86
4.22 The generator webpage (a) and enter data webpage (b). 86
4.23 (a) is qurey webpage and (b) is the data display page. 87
4.24 PADI layout 88
4.25 Design layout of the PADI FEE (a), and the real FEE board (b). 89

6.3 System time resolution and intrinsic time resolution of the eTOF module.· · 150

A.1 Distribution event sample in the time difference to previous event. The signal from the decay of the muon · 160

List of Tables

Chapter 1 Introduction

1.1 Background of the Heavy Ion Physics Experiment

1.1.1 High Energy Heavy Ion Physics

1. High Energy Heavy Ion Physics

In the 1970's, deep inelastic electron-proton experiments indicated that nucleons have sub-structure. Within the Standard Model, nucleons are consisting of quarks and gluons, held together by nuclear forces. The theory of strong interactions, Quantum chromodynamics (QCD), describes the interactions between these quanta. According to the QCD theory, quarks and anti-quarks, which are elementary particles in the QCD frame, interact with one another by exchanging gluons, namely strong force[6]. Particles consisting of quarks and gluons are called as 'hadrons' and in two main types, mesons and baryons[7]. A meson is built of a quark and an anti-quark and a baryon contains three quarks.[7]. The gluon corresponds to the photon in QED and its mediates the strong force by exchanging 'color' between particles. Unlike the photon, the gluon is itself charged. The strong force confines quarks and gluons in the hadrons. The hadrons have no color charge but free quark or gluon is not observed in the physical world.

One of the most important characteristics of high energy nucleus-nucleus collisions is the large amount of energy involved. When a large fraction of this energy is deposited in a small region of space in a short duration of time, the energy density can be very high[8]. In such extremely conditions, the collision "melts" the protons and neutrons and, for a brief instant, liberates their constituent quarks and gluons. QCD predicts the new state of the matter, Quark Gluon Plasma (QGP) that free quarks and free gluons exist in a large volume will be produced at such extreme temperature and/or high matter density. In 1974 Tsung-Dao Lee proposed (Fig.1.1), the creation of the QGP, a fundamentally new state of matter, is expected to be realized in the laboratory by colliding high energy heavy-ions.

（1） Quark-gluon plasma

Ultra-relativistic heavy-ion physics was thus born with the aim of applying and extending the Standard Model to complex and dynamically evolving systems of finite size, and to explore the strongly interacting QCD matter under extreme conditions of ener-

gy density. The transition from the normal matter to the QGP transition is expected to happen at a critical temperature, T_c (160MeV), of the order of the QCD energy scale parameter. In addition, it is thought that such state of matter existed in the early state of the universe and may present in the neutron star. An early discovery was that the quark-gluon plasma behaves more like a perfect fluid with small viscosity than like a gas, as many researchers had expected. More exotic phases, like color superconductivity formed by correlated quark-quark pairs, are speculated at low temperatures and very high net-baryon densities.

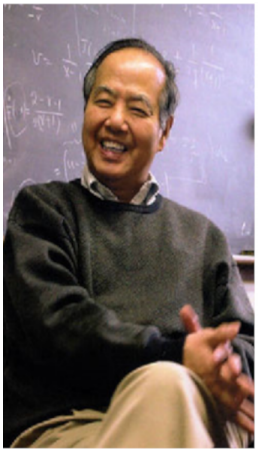

PHYSICAL REVIEW VOLUME 87, NUMBER 3 AUGUST 1, 1952

Statistical Theory of Equations of State and Phase Transitions.
II. Lattice Gas and Ising Model

T. D. LEE AND C. N. YANG
Institute for Advanced Study, Princeton, New Jersey
(Received March 31, 1952)

The problems of an Ising model in a magnetic field and a lattice gas are proved mathematically equivalent. From this equivalence an example of a two-dimensional lattice gas is given for which the phase transition regions in the $p-v$ diagram is exactly calculated.
A theorem is proved which states that under a class of general conditions the roots of the grand partition function always lie on a circle. Consequences of this theorem and its relation with practical approximation methods are discussed. All the known exact results about the two-dimensional square Ising lattice are summarized, and some new results are quoted.

INTRODUCTION

IN paper I[1] we have seen that the problem of a statistical theory of phase transitions and equations of state is closely connected with the distribution of roots of the grand partition function. It was shown there that the distribution of roots determines completely the equation of state, and in particular its behavior near the positive real axis prescribes the properties of the system in relation to phase transitions. It was also shown there that the equation of state of the condensed phases as well as the gas phase can be cor-

as a theorem in Sec. IV of the present paper and proved in the appendix. Implications of the theorem are discussed in Sec. V.
Also in this paper we shall give a proof (Sec. II) that the problem of an Ising model with a magnetic field is mathematically identical with that of a "lattice gas." From this identification we were able to trace exactly the transition region in the $p-v$ diagram of a two-dimensional lattice gas in detail. This will be presented in Sec. III and forms a clear illustration of the discussions of paper I and of Sec. V of the present paper.

Fig. 1.1 T. D. Lee and his theory on QCD phase transition.

（2） Space-time Evolution of High-Energy Nuclear Collisions

At very high temperatures or densities the hadrons matter melt into a plasma of free quarks and gluons degree, form new phases, such as QGP or other exotic states. To create such extreme conditions in the laboratory, requires a sufficiently large volume of hot matter and is therefore pursued in collisions of heavy nuclei at the sufficiently high energy, Accelerator technology was applied to create relativistic heavy-element nuclei beams and collide them.

As illustrated in Fig.1.2, fast-moving nuclei are initially compressed into a pancake shape in the beam direction due to the Lorentz contraction. Shortly after the reaction, the colliding nuclei recede from each other, an enormous amount of energy is released into a tiny volume ($\sim$10 fm in diameter) and in a short duration of time wherein a QGP medium may possibly form. Subsequently the evolution may be governed by the law of thermodynamics. The fireball (QGP) will expand and instantly cool. Once its temperaure falls below T_c, bound states of quarks and gluons will form, a process called hadronization. Hadronization takes place and after some time the interaction seize (freeze-out). All hadrons now freely speed away in all directions. The full evolution of the created

fireball is over. Finally, experimental detectors placed around the reaction point will capture the hadronized particles from QGP and reconstruct their trajectories to trace back relevant information during the course of collision.

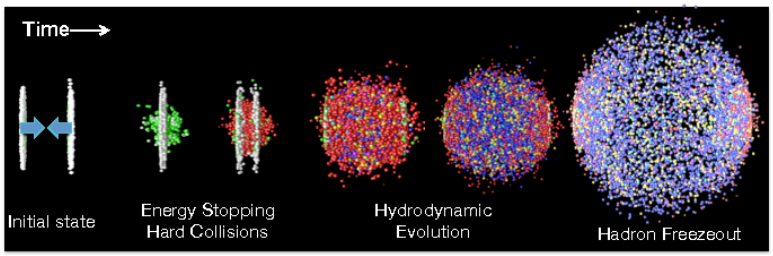

Fig. 1.2 The time evolution of a high energy heavy ion collision

2. Exploring the Phase Diagram of Nuclear Matter

One of the main goals of heavy-ion collisions is to explore the phase structure of hot and dense nuclear matters[9], which can be displayed in the phase diagram of QCD. Fig.1.3 shows the conjectured QCD phase diagram on the basis of the theoretical calculations that expressed into a two dimensional diagram, baryon chemical potential (μ_B, X-axis) and temperature (T, Y-axis). The transition from the hadron gas phase to the QGP phase is a smooth crossover at $\mu_B = 0$[10], whereas a first order phase transition is expected at high baryon chemical region[11]. The endpoint of the first order phase boundary towards the crossover region is so called the QCD critical point[12]. There are large uncertainties from theoretical calculations in determining the QCD phase structure at high baryon density region. The first-principle Lattice QCD calculations shedding light on thermodynamics of the strongly interacting matter, however, is restricted to small net-baryon densities and high temperature. So the collection of more experimental data will allow us to delve further into the subject.

1.1.2 Heavy ion Experiment

For the heavy ion experiment, the main goal is to form and characterize a microscopic (in QCD scales) state of deconfined quarks and gluons in local thermal equilibrium. Although Quark-gluon phase has been discovered at RHIC, its precise properties are still not yet established. With the phase diagram of strongly interacting matter (QCD phase diagram) also being largely unknown, these are great times for research. Beyond that, the potentially rich structure of the QCD phase diagram at high net-baryon densities as suggested by theory also calls for experimental verification[13].

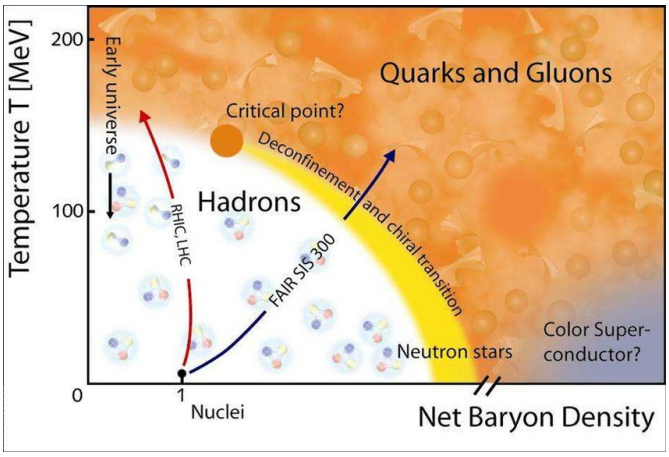

Fig. 1.3 Phase diagram of strongly interacting matter in the temperature and baryonic chemical potential (T, μ_B) plane. Picture taken from Ref[1].

To create these conditions in the laboratory, heavy ions (e.g. lead nuclei) are accelerated and made to head-on collision. The Heavy ion experiments have two different kinds of collisions, collider and fixed target mode as seen in Fig.1.4.

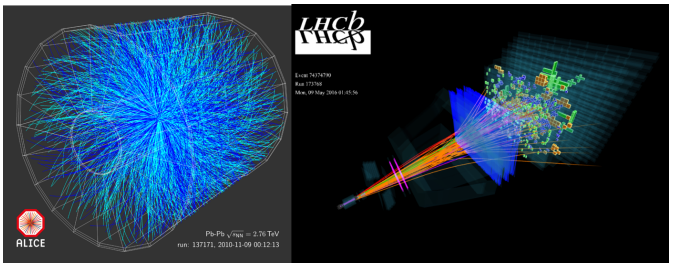

Fig. 1.4 Two collide mode, left side is collide mode and right side is fixed target.

Currently, several heavy-ion experimental programs are devoted to the exploration of the QCD phase diagram. The Fig.1.5 shows the global map of present high-energy heavy ion experiments. The Relativistic Heavy Ion Collider (RHIC) has scanned the beam energies in order to search for the QCD critical endpoint[14]. For the same reason, measurements are performed at the CERN-SPS with the upgraded NA49 detector (NA61) using beams of light and medium-heavy ions[15]. However, because of limitations in luminosity or detector design, these experiments are constrained to the investigation of abundantly produced particles. As a comparison, the Compressed Baryonic Matter (CBM) experiment in Darmstadt[16], using the high-intensity heavy-ion beams provided by the Facility for Antiproton and Ion Research (FAIR) accelerators[17], will be a high-rate fixed target experiment designed for precision measurements of multi-dimensional observables, including particles with very low production cross sections. At the Joint Institute for Nuclear Research (JINR) in Dubna, a Nuclotron-based Ion Collider (NICA) is planned with the goal to search for the coexistence phase of nuclear

matter[18]. In addition, a study on the QCD phase structure at extremely high baryon density program, CSR External-Target Experiment (CEE)[19] at China, has also entered the world-wide effort.

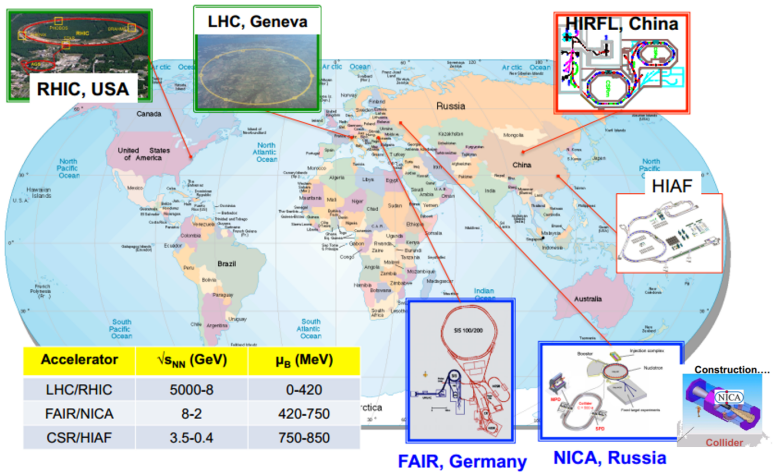

Fig. 1.5 The global map of present high-energy heavy ion experiments.

1. CBM Experiment

The CBM spectrometer is expected to be operational in the year 2024. The heavy-ion experiment CBM, considered as one of the core projects of the future accelerator facility FAIR (Fig.1.6), will investigate nucleus-nucleus collisions from 10 to 45 AGeV, thus exploring the QCD phase diagram in the region of highest baryon densities. High machine availability and interaction rates will give access to rare observables like charm near threshold. CBM spectrometer is designed as a multi-purpose device which can measure hadrons, electrons and muons in heavy-ion collisions[20]. The goal of the CBM research program is to explore the QCD phase diagram in the region of high baryon densities. This includes the study of the equation-of-state of nuclear matter at neutron star core densities, and the search for phase transitions, chiral symmetry restoration, and exotic forms of (strange) QCD matter.

（1） FAIR

Currently the international accelerator facility FAIR, one of the largest research projects worldwide, is under construction at GSI Helmholtzzentrum für Schwerionenforschung in Darmstadt, Germany. Its existing accelerator facilities will become part of FAIR and will serve as first acceleration stage, will provide unique research opportunities on the fields of nuclear, hadron, atomic and plasma physics[21]. The research program devoted to the exploration of compressed baryonic matter will start with primary beams from SIS100 (protons up to 29 GeV, Au up to 11 AGeV, nuclei with Z/A = 0.5 up to 14

AGeV) and will be continued with beams from SIS300 (protons up to 90 GeV, Au up to 35 AGeV, nuclei with Z/A = 0.5 up to 45 AGeV). The layout of FAIR is presented in Fig 1.6. The beam extracted to the CBM cave will reach intensities up to 10^9 Au ions per second.

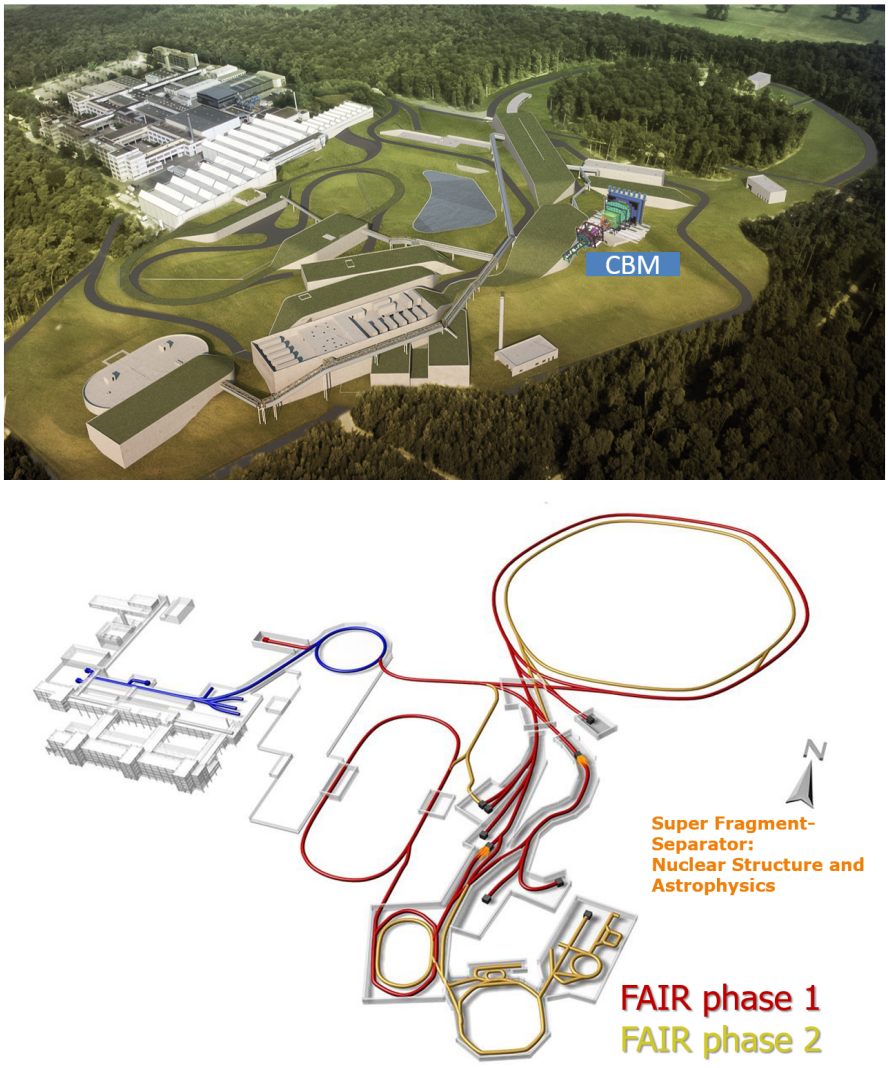

Fig. 1.6 The layout of the Facility for Antiproton and Ion Research.

（2） Conceptual design of CBM Detector

The CBM detector is designed to measure the collective behavior of hadrons, together with rare diagnostic probes such as multi-strange hyperons, charmed particles and vector mesons decaying into lepton pairs with unprecedented precision and statistics. Most of these particles will be studied for the first time in the FAIR energy range. In order to achieve the required precision, the measurements will be performed at reaction rates up to 10 MHz. This requires very fast and radiation hard detectors, a novel data read-out and analysis concept including free streaming front-end electronics, and a

high performance computing cluster for online event selection. The unique combination of an accelerator which delivers a high-intensity heavy-ion beam with a modern high-rate experiment based on innovative detector and computer technology offers optimal conditions for a research program with substantial discovery potential for fundamental properties of QCD matter.

The current CBM detector layout comprises a high-resolution silicon tracking system (STS) placed in the field of a superconducting dipole magnet. This systems should provide momentum determination better than 1 % and the reconstruction of secondary vertices with a precision of about 50 μm . Outside of the magnetic field, a RICH detector and several stations of transition radiation detectors (TRD) will identify electrons in the momentum ranges relevant for low-mass vector meson and charmonium measurements. Hadron identification will be achieved by the time-of-flight (TOF) measurement in an array of multi-gap resistive plate chambers (MRPC). The setup is completed by an electromagnetic calorimeter (ECAL) and a Muon Chamber system (MUCH) for identification of photons, electrons and muons. The position information from the TRDs is used for a global tracking through the detector. Fig.1.7 shows the layout of the planned experimental setup.

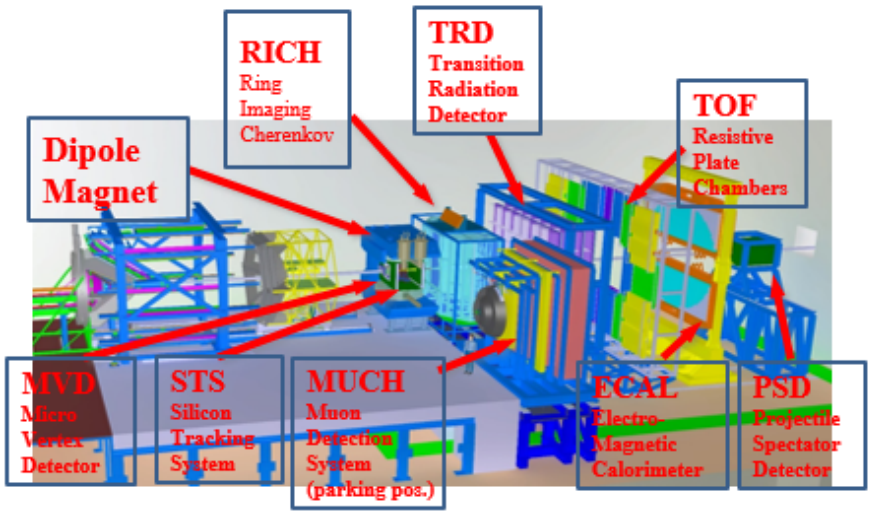

Fig. 1.7 Sketch of the conceptual design Compressed Baryonic Matter (CBM) experiment. The setup consists of a superconducting dipole magnet with a Silicon tracker System inside, a Rich Imaging Cherenkov detector (RICH), the three Transition Radiation Detectors (TRD), the Time-Of Flight (TOF) wall which is a Resistive Plate Chamber (RPC) and the electromagnetic Calorimeter (ECAL). The total length of the setup is approximately 12 m.

2. The Solenoidal Tracker At RHIC (STAR) Experiment

The primary physics task of STAR is to study the formation and characteristics of the QGP. Now STAR has completed the first phase RHIC Beam Energy Scan (BES-I) program to find the critical point and first order phase transition boundary. The results of study narrowed the area of interest to the collision energy between 7.7 and 20 GeV. However, to get a clear conclusion, better measurement accuracy and theoretical explanation are also needed. The former can be implemented in the second RHIC Beam Energy Scan (BES-II) program, with the STAR detector upgrades[22].

STAR makes use of a variety of simultaneous studies in order to draw strong conclusions about the QGP. This is due both to the complexity of the system formed in the high-energy nuclear collision and the unexplored landscape of the physics we study. STAR therefore consists of several types of detectors, each specializing in detecting certain types of particles or characterizing their motion. These detectors work together in an advanced data acquisition and subsequent physics analysis that allows final statements to be made about the collision.

（1） STAR Detector overview

STAR was designed primarily for measurements of hadron production over a large solid angle, featuring detector systems for high precision tracking, momentum analysis, and particle identification at the center of mass (c.m.) rapidity. The large acceptance of STAR makes it particularly well suited for event-by-event characterizations of heavy ion collisions and for the detection of hadron jets.

The layouts of the STAR experiment and the RHIC complex are displayed in Fig.1.8 and Fig.1.9 respectively[23-24]. A room temperature solenoidal magnet[24] with a uniform magnetic field of maximum value 0.5 T provides for charged particle momentum analysis. A large volume Time Projection Chamber (TPC)[25] for charged particle tracking and particle identification is located at a radial distance from 50 to 200 cm from the beam axis[25]. The Heavy Flavor Tracker (HFT) is installed between the beam pipe and the TPC. It consists of 3 sub-detector systems, the Silicon Pixel (PXL) detector, Intermediate Silicon Tracker (IST) and Silicon Strip Detector (SSD). Silicon tracking close to the interaction allows precision localization of the primary interaction vertex and identification of secondary vertices from weak decays of. Muon Telescope Detector (MTD) is mounted outside the STAR Solenoid magnet and covering 45% of the 2π azimuth in the pseudo-rapidity range $-0.5<\eta<0.5$. The BES-II program will rely on low-energy electron cooling and longitudinally extended bunches to improve the lumi-

nosity[26-27]. The program in normal collider mode will cover the energy range from 7.7 to 19.6 GeV and the energies from 3.0 to 7.7 GeV will be accessible through the use of an internal fixed target. Three STAR sub-detectors upgrades will be prepared in anticipation of BES-II.

- (1) The Inner TPC (iTPC) upgrade[27] improves the spatial resolution of the TPC anodes which leads to better dE/dx(~25% improvement), and better momentum resolution (~15% improvement at larger momenta).
- (2) The Event Plane Detector (EPD)[28] is an entirely new detector, which is proposed for the forward rapidity region $1.5<|\eta|<5$. The EPD will provide the precise measurements of both the collision centrality and event plane.
- (3) The eTOF upgrade will provide particle identification (PID) in the extended pseudorapidity range provided by the iTPC upgrade[27] to the main tracking chamber.

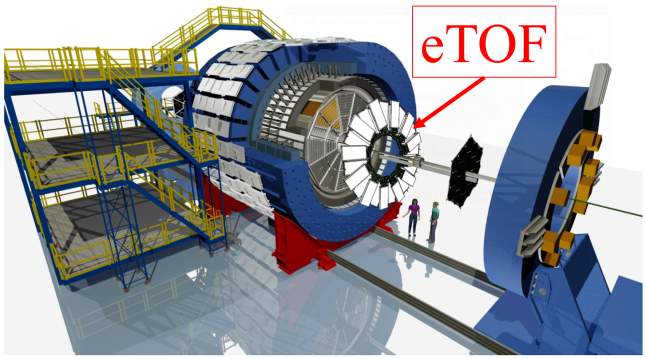

Fig. 1.8 Perspective view of the STAR detector, with a cutaway for viewing inner detector systems and STAR/CBM eTOF Upgrade.

3. CEE project

CEE will be the first large-scale nuclear physics experiment device at the Cooling Storage Ring (CSR) of the Heavy-Ion Research Facility in Lanzhou (HIRFL), China. The layout of HIRFL is shown in Fig-1.10[29].

（1） Physics Purpose

The main function of CEE is to detect the final-state particles produced in heavy-ion collisions with large acceptance, and provide important measurements to understand fundamental questions in the nuclear physics field, e.g. the nuclear equation of state in high baryon number density and the nuclear phase diagram.

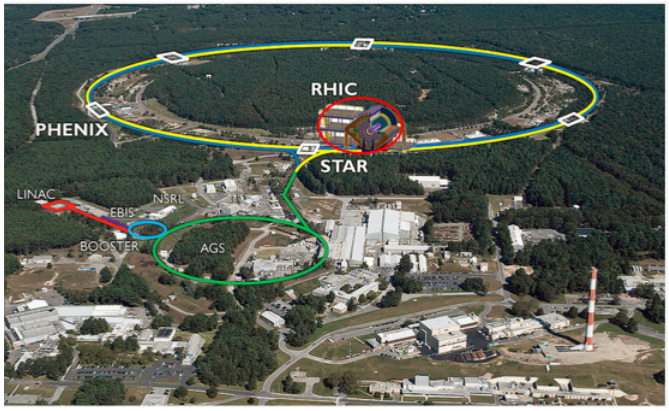

Fig. 1.9 The layout of Relativistic Heavy Ion Collider and the STAR experiment positon at RHIC.

The CEE project proposed to study the density dependence of nuclear symmetry energy by measuring the π^-/π^+ ratio (and other relevant observables) from various heavy-ion collision systems and study the nuclear equation of state (EOS) at supra-saturation density and the rich QCD phase at high-density/low-temperature. The C-SR[29] can deliver a wide range of heavy-ion beams from deuteron (up to 1 AGeV) to Uranium nuclei (to 520 AMeV), thus will provide a significant opportunity to carry out such a study of $E_{sym}(\rho)$, and studies on the properties of cold nuclear matter and quarkoyonic matter phase at very high baryon number density[30].

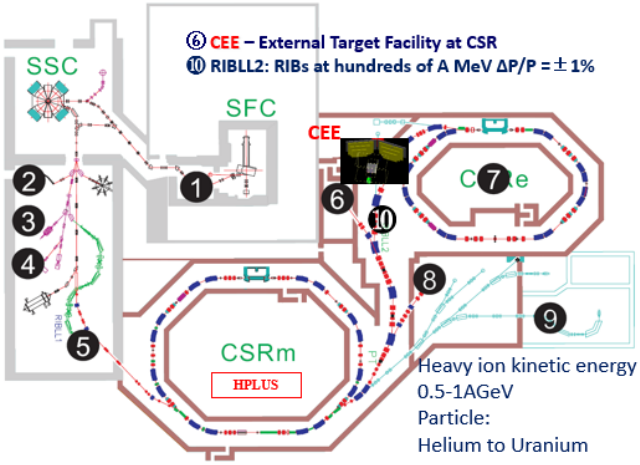

Fig. 1.10 The facility layout of HIRFL. In the centre of HIRFL is the CEE.

（2） The conceptual design of CEE Detector

The CEE system includes a large angle dipole magnet, tracking detectors(a TPC and an array of multi-wire drift chamber (MWDC)), TOF system and a zero-degree calorimeter (ZDC), as depicted in Fig. 1.11[19]. The TOF system contains a T0 detector, an inner TOF (iTOF) and an external TOF (eTOF), mainly employed to identify the charged

final state particles. As the start detector of the TOF system, the T0 detector not only determines the collision time with high precision, but also serves as a trigger detector for the experimental system, providing information on the event multiplicity and reaction plane. It is located ∼10 cm around the target. Both the target and the T0 detector sit in the strong magnetic field, just in front of the TPC.

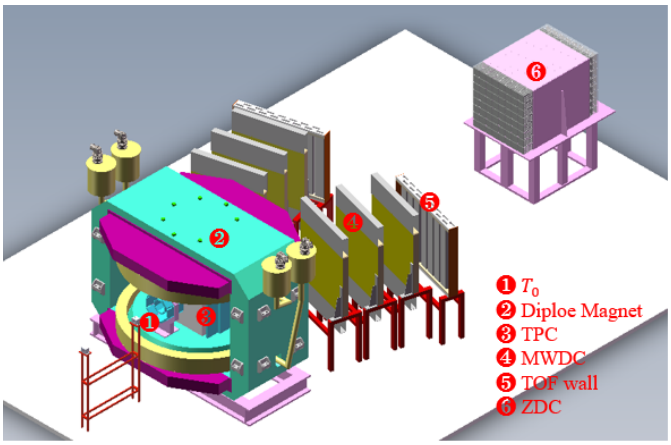

Fig. 1.11 The conceptual design of CSR external-target experiment. It is composed of a T0 detector, a dipole magnet, a TPC, several MWDCs, iTOF and eTOF walls, and a ZDC.

1.2 Time of Flight for Heavy ions Experiment

1.2.1 Time of Flight system

1. Final state particles after collision

To study the QCD and quark (de)confinement under extreme conditions in heavy-ion interactions, Particle Identification (PID) is a crucial aspect of the heavy ion experiment. Just after the heavy ion collision, the fireball quickly thermalizes and forms QGP, while the energetic partons traverse this plasma and end in a shower of particles called jets (Fig.1.12). Thousands of final state particles are emitted from the collision area. Analyzing these final particles in a variety of different ways allows us to study the properties of QGP and the complex dynamics of multi-scale processes in QCD which govern its formation and evolution. For example, pairs of muons are used to observe the full spectrum of heavy-quark vector-meson resonances (J/Ψ, ⋯). The physics programme at heavy-ion experiment relies on the ability to identify all of final state particles –i.e. to determine if they are electrons, photons, pions, etc –and to determine their charge. Besides, charged hadrons are unambiguously identified if their mass and charge are de-

termined. The mass can be deduced from measurements of the momentum and of the velocity.

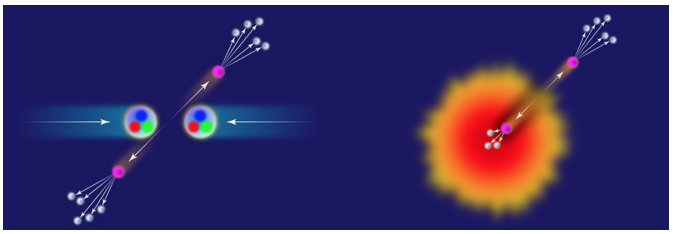

Fig. 1.12 The collision and final state particles of two jets.

To obtain the particle velocity, there are four methods based on measurements of TOF and ionization, detection of transition radiation and Cherenkov radiation. Each method works well in different momentum ranges or for specific types of particle. Among them, the time of flight (TOF) detector are popularly used in measuring particles in GeV range. is a particle detector which can discriminate between a lighter and a heavier elementary particle of same momentum using their time of flight between two Detectors.

2. Time of Flight system

（1） Time of Flight Technique

For a specific experiment, the momentum of provided particles is usually known by TPC or other tracking detector, the mass of the particle can then be derived from the TOF measurements. The simple schematic Fig.1.13[31] briefly summarizes the basic principle, which can be deduced from the theory of relativity that a particle with mass m_0 and momentum P has a velocity β (relative to the speed of light in vacuum),

$$\beta = \frac{P}{\sqrt{P^2 + {m_0}^2 c^2}} \tag{1.1}$$

According to the fundamental formula of relativity

$$m_0 = \frac{P}{\beta\gamma c}, \gamma = \frac{1}{\sqrt{1-\beta^2}}, \beta = \frac{v}{c} \tag{1.2}$$

, we can get the particle mass

$$m = \frac{P}{c}\sqrt{\frac{1}{\beta_2} - 1} = \frac{P}{c}\sqrt{\frac{c^2 t^2}{L^2} - 1} \tag{1.3}$$

where L is the path length of flight. Two particles, with different masses but the same momentum, will have a time difference after traveling a distance L. This time difference,

for highly relativistic particles, is given by:

$$\Delta T = T_1 - T_2 = \frac{L}{c}(\frac{1}{\beta_1} - \frac{1}{\beta_2}) = \frac{L}{c}\frac{({m_2}^2 - {m_1}^2)}{P^2}c^2(\frac{\beta_1\beta_2}{\beta_1 + \beta_2}) \approx ({m_2}^2 - {m_1}^2)\frac{Lc}{2P^2} \tag{1.4}$$

,which is usually used to estimate the timing precision needed to identify particles at a given momentum.

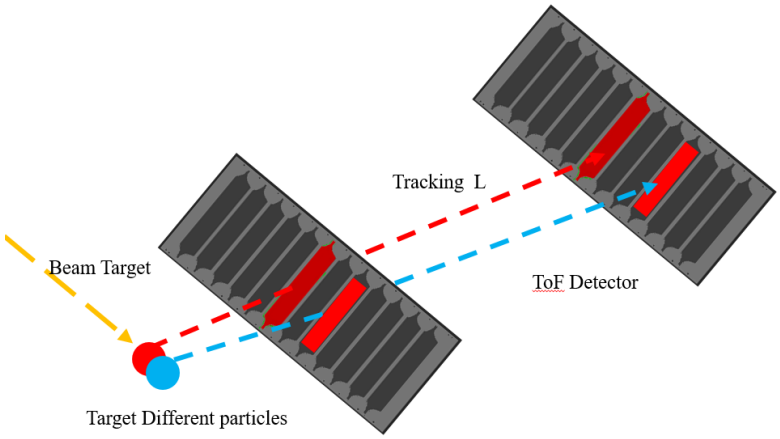

Fig. 1.13 A simple schematic figure of Time of Flight Technique

（2） Particle identification Requirements for Time of Flight

Time of Flight Technique also has its own limitations for particle identification. Fig.1.14 shows the time difference between K and P and also between π and K for a distance of 2 m. One can easily see that for the detector's time resolution of 100 ps, the 3σ difference (300 ps) gives an upper momentum of 2.2 GeV/c for K/p separation. These limits increase if one can reduce the time resolution to 50 ps as shown in the figure. However this is not a fully complete argument. We stated above that the mass is calculated by measuring the momentum and the velocity, however errors on the other variables will also play a role. In this case there are errors on the momentum and track length. Starting from the expression for mass, it is simple to show that:

$$\frac{\partial m}{m} = \frac{\partial p}{p} \tag{1.5}$$

$$\frac{\partial m}{m} = (\frac{E}{m})^2\frac{\partial T}{T} \tag{1.6}$$

$$\frac{\partial m}{m} = (\frac{E}{m})^2\frac{\partial L}{L} \tag{1.7}$$

One can calculate how long the flight distance needs to be provided before we can identify particles with $\frac{\partial m}{m}$=0.4 and momentum of 1GeV/c due to the time resolution

(100 ps). This value is approximately 3.7 m. This contribution obviously gets very large at higher momentum due the $(E/m)^2$ term. The contribution due to the error in the momentum is small since $\frac{\partial p}{p}$ has a value between 1 % and 5 % for these momenta. It should be noted that the curvature of a particle in a magnetic field depends not only on its momentum, but also on its electric charge[32].

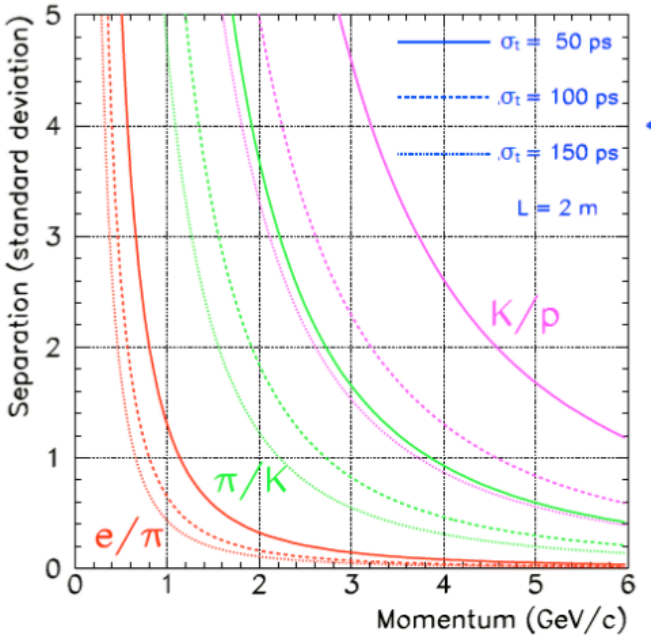

Fig. 1.14 The time difference versus momentum for K/p.

Chapter 2 Multi-gap Resistive Plate Chamber (MRPC) Technology

2.1 MRPC in Heavy ion Physics

2.1.1 Traditional Time of Flight Detector

The heavy ion experiment are designed to study heavy ion, where high multiplicities are expected. The requirement of TOF is to identify as many of these final state charged particles as possible. Thus the TOF array has to be (a) large area, highly segmented, (b) able to operate in a magnetic field, (c) of reasonable cost and (d) consisted of the lowest amount of material. For many years scintillators read out with photo-multipliers have been the standard detector for TOF. However using this technique to build a large detector arrays for the heavy ion experiment with huge multiplicity is impractical. It is difficult for photo-multiplier tube (PMT) to work in a strong magnetic field and also the scintillators should be segmented into small tiles (each fitted with a photo-multiplier) to deal with the high multiplicity of tracks. Besides, high quality photo-multipliers tubes are needed to provide good time resolution and typically expensive. The cost of such a system with large area is prohibitive.

2.1.2 The application of MRPC

Thus, before the year 1999[33-35], although the ALICE experiment had a big need for a TOF array, the traditional candidate technologies all had fundamental problems. However, the MRPC technology offered a solution and was quickly adopted by the heavy ion experiment. MRPC was invented in 1996 which was inspired with the R&D performed by the LAA project for the ALICE experiment[36]. It was designed to give improved time resolution compared to the device known as the wide-gap RPC. The technology has proved to be very inexpensive, easy to build, easily segmented, and has an excellent time resolution (below 100 ps), and an efficiency that is essentially 100 % (a wide voltage plateau leading to >95%), all of which are well suited for the heavy ion experiment. So nowadays most of the heavy ion experiments have adopted MRPC as their TOF detector.

For the ALICE experiment, charged particles in the intermediate momentum range are identified by the TOF detector. For the STAR experiment, a tray of the TOF detec-

tor based on the MRPC technology (TOFr) was constructed and then operated in STAR during the RHIC 2003 spring physics run after beam-tested at AGS of BNL. This denoted the first time large-scale application of MRPC technology as TOF detector in the heavy ion experiment. For the CBM experiment, the TOF wall consisting of an array of MRPCs provides particle identification for all charged hadrons emitted in beam-target interactions in the forward region. For the CEE experiment, its T0/trigger detector, internal and external TOF detectors are all based on the MRPC technology. Besides, MRPC finds many other applications outside the field of heavy-ion physics[37-38]. Tomography with cosmic ray muons is a novel technology for high-Z material detection. Large area of MRPC arrays have been successfully used in such application. Another new direction is medical imaging. The use of MRPCs for in-beam Positron Emission Tomography (PET) in proton and carbon ion therapy need a large number of modules to practically implement a high-sensitivity scanner. The low cost and high resolution MRPC opens up a new possibility as an efficient alternative detector for the TOF based PET, where the sensitivity of the system depends largely on the time resolution of the detector.

2.2 Operation principle of the MRPC

MRPC is one kind of gaseous detector, consisting of a stack of parallel resistive glass plates. The structure is shown in Fig.2.1. A high voltage is applied to the external surfaces of the stack. The internal resistive plates are attributed to electrostatics, they are electrically floating. Further out there are pickup electrodes. A charged particle ionizes the gas and the high electric field amplifies this ionization by an electron avalanche. The resistive plates stop the avalanche development in each gap when a certain amount of electron charge has been accumulated. At the same time they are transparent to the fast signal induced on the pickup electrodes by the movement of the electrons. So the total signal is the sum of the signals from all gaps (the reason for many gaps is to achieve high efficiency), whereas the time jitter of the signal depends on the individual gap width (the reason for narrow gaps is to achieve good time resolution).

When operated in avalanche mode, MRPCs deliver very fast signals ideally suited for time measurements. Typical signals from an anode strip exhibit the following shape parameters at 50 Ω impedance[39-40]:

Rise time: t_R∼1 ns[39]

FWHM: ∼1-2 ns

Fall Time: t_F~0.3 ns

Amplitude: <30 mV

A typical charge spectrum of minimum ionizing particles measured with an MRPC has a shape with a mean value around 30-60 fC. The ionization dE/dx exhibits very large fluctuation (Landau) in a MRPC, so it's impractical to use this information for PID.

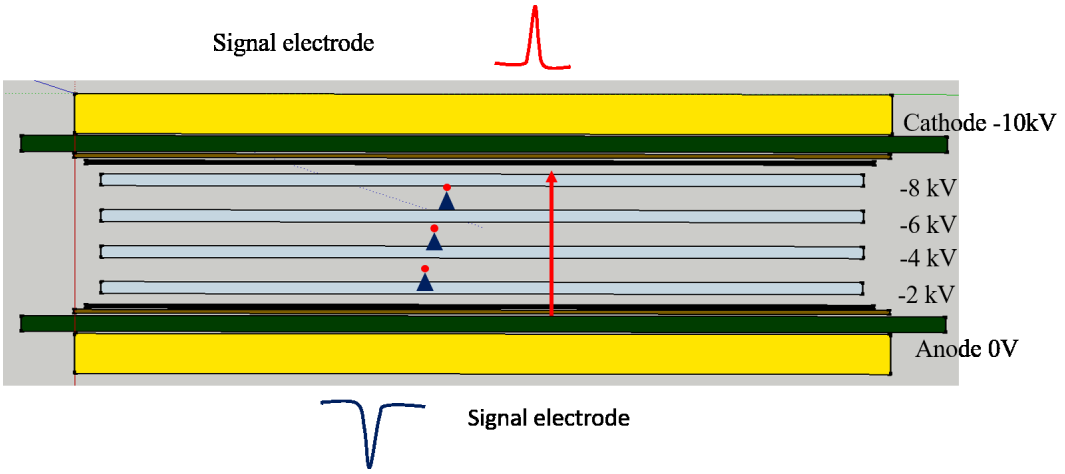

Fig. 2.1 Working principle of MRPC. The voltage of the internal plates are electrically floating.

2.2.1 Detector Physics

1. Energy Loss of Charged Particles in Matter

A charged particle passing through the electron clouds of atoms would continuously take away some of their electrons, a phenomenon called "ionization". Strictly defined, ionization is the complete loss of an electron from an atomic or molecular species. The remaining species is called ion.

（1） Bethe-Bloch function

The relativistic charged particles other than electrons lose energy in matter primarily by ionization. The mean rate of energy loss (stopping power) is given by the Bethe-Bloch equation,

$$\frac{\mathrm{d}E}{\mathrm{d}x} = Kz^2\frac{Z}{A}\frac{1}{\beta^2}[\frac{1}{2}ln\frac{2m_ec^2\beta^2\gamma^2T_{max}}{I^2} - \beta^2 - \frac{\delta}{2}] \tag{2.1}$$

Here T_{max} is the maximum kinetic energy which can be imparted to a free electron in a single collision, and the other variables are defined in table2.1. The units are chosen so that $\frac{\mathrm{d}E}{\mathrm{d}x}$ is measured in mass per unit area, e.g., in g· cm^{-2}. The stopping power in several other material is shown in Fig.2.2. Except in hydrogen particles with the same

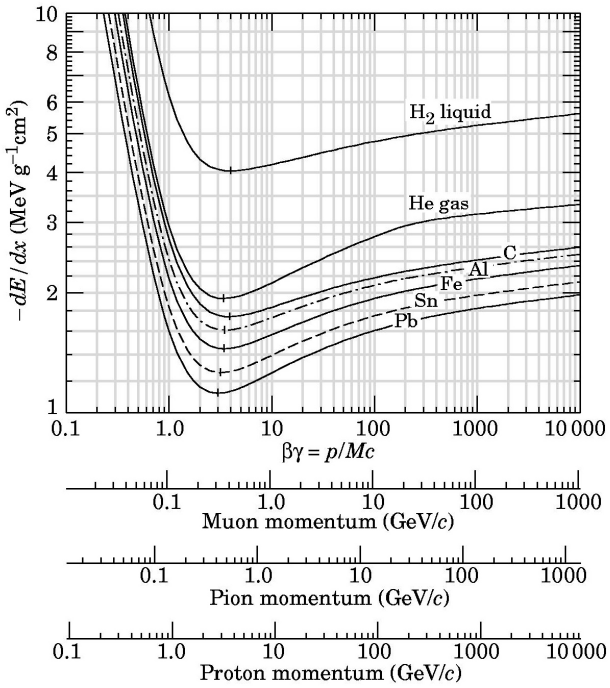

Fig. 2.2 Mean energy loss rate in liquid hydrogen, gaseous helium, carbon, aluminum, iron, tin, and lead. Radiative effects, relevant for muons and pions, are not included. These become significant for muons in iron for $\beta\gamma \geqslant$1000, and at lower momenta for muons in higher-Z absorbers.

Table 2.1 Variables used in this thesis, The kinematic variables β and γ have their usual meanings.

N_A	Avogadro's number
Z	Charge number of medium
z	Charge of incident particle
K	$=4\pi N_A r_e^2 m_e c^2$
δ	Density effect correction to ionization energy loss
I	Mean excitation energy of medium
A	Atomic mass of medium
r_e	Classical electron radius

velocity have similar rates of energy loss in different materials, although there is a slow decrease in the rate of energy loss with increasing Z.

（2） The Landau distribution

When a particle pass through the MRPC, the energy loss for a given fixed momentum is not constant but fluctuates around the mean value. For a thin layer of the stopping material (e.g. the sensitive gas layer of a MRPC) and high-energy charged particles, the most probable energy loss is also not equal to the mean energy loss. The energy loss distribution is skewed, with large energy transfers. Landau theoretically worked out this problem for a thin layer of material. The slowing down of particles in thin layers of material is described by the Bethe-Bloch equation. Although it does not directly lead to energy deposition distribution needed for particle identification, it nicely describes the mean energy loss for different momenta of the particle. Because of the small number of interactions between particles, the statistical fluctuation of the energy loss is very large, the energy distribution is very asymmetric, closer to the distribution of Landau rather than Gaussian distribution.

2. Detector Working Mode and Charge Collection

If we apply static electric field in the detector, original ionized electron, e^-, will drift to the positive electrode, anode, and positive ions, A+, will move to the negative electrode (cathode). With enough high electric field, electron avalanche happens and generate a large number of secondary electron-ion pairs. Two charged clouds move in opposite direction. Electrons are moving with much larger drift velocity than ions due to lower. The value of drift velocity depends by complicated way on the strength of electric field, E, the properties of gas molecules, density or pressure, P , and temperature. For particular gas mixture it is common to plot drift velocity versus E/P, where E is in kV/cm.

The number of ions collected depends on the field intensity. This is illustrated in Fig.2.3 which plots the total charge collected as a function of V. At zero voltage the charge is not collected as the ion-electron pairs recombine under their own electrical attraction. As the voltage rises, the recombination forces are overcome and the current begins to increase as more and more of the electron-ion pairs will be collected. But further to increase the voltage shows no effect. This corresponds to the first flat region(II). A detector working in this II region is called an ionization chamber since it collects all the ionization charge produced directly by the passing particle. However, the signal current is very small and usually be measured with an electrometer. Ionization chambers are generally used for measuring gamma ray exposure and as monitoring instruments for large fluxes of radiation. If we continue increase the voltage, we will find that the current increases again with the voltage. At this point, the electric field

is strong enough to accelerate freed electrons to an certain energy where they are also capable of cause the gas to occur secondary ionization then accelerate to produce more ionization and so on. This phenomenon is called avalanche multiplication. This results in an ionization avalanche or cascade. The number of electron-ion pairs in the avalanche is directly proportional to the number of primary electrons. What results then is a proportional amplification of the current, with a multiplication factor depending on the working voltage V. This factor can be as high as 10^6 so that the output signal is much larger than that from an ionization chamber, but still in proportion to the original ionization produced in the detector. This region of proportional multiplication extends up to region(III) and a detector operating in this domain is known as a proportional chamber. If we now increases the voltage beyond region(III), the total amount of ionization created through multiplication becomes sufficiently large meanwhile the space charge created distorts the electric field. Proportionality thus begins to be lost. This is called the region of limited proportionality. The MRPC we're talking about are working at this region. If the voltage is further increased, the energy becomes so large that a discharge occurs in the gas. The secondary avalanches are caused by photons emitted by deexcitation molecules which travel to other parts of the chamber to cause further ionizing events. The output current thus becomes completely saturated, always giving the same amplitude regardless of the energy of the initial event. The quenching gas must be present in the medium to absorb the photons and to stop the discharge. Detectors working in this voltage region(V) are called Geiger-Muller counter. In fact, the Geiger voltage region(V) is characterized by a plateau over which the count rate varies little. Finally, now, if the voltage is increased still further a streamer or breakdown occurs without radiation. This region(VI) , of course, is to be avoided to prevent damage to the counter. In this illustration, we thus see how phenomena such as gas multiplication and discharge, in addition to gas ionization, can be used for detection.

2.2.2 Avalanche Dynamics

When a particle enters into the MRPC volume, it interacts with the gas and ionizes the atoms of the gas. If the electric field is intense enough, the electrons are highly accelerated and they further ionize the gas. Under these conditions, the number of electrons grows rapidly forming what is known as avalanche. The created electrons and ions drift towards the anode and cathode respectively. The motion of electrons and ions in the gas gives rise to an electric current on the electrodes which can be gathered by an external circuit.

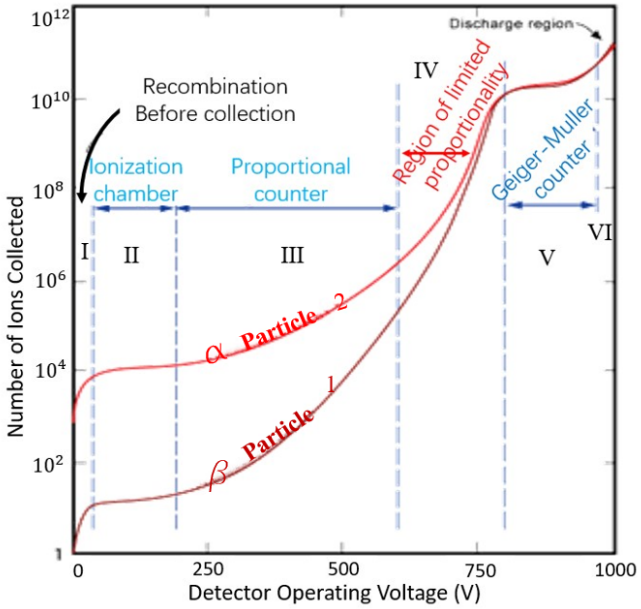

Fig. 2.3 Gain-voltage characteristics for gaseous detectors, showing the different operating mode.

The high voltage is applied to the outer surfaces of the MRPC's electrode plates, so that an electrical field is generated in the gas gaps. When the electric field is high enough, electrons will be accelerated to the point where they have enough kinetic energy to liberate electrons in collisions with other atoms/molecules i.e., $e^- + A \rightarrow e^- + e^- + A^+$. The entire ionization and avalanche process of electrons is described the image in Fig.2.4. As an electron drifts towards the anode it travels in an increasing cluster. According to the avalanche image, the number of ions generated by collision of an electron through a unit length at particular field strength E is $\alpha = \frac{1}{\lambda}$, where α is called Townsend coefficient, it describes gas multiplication factor; the λ is the linear charge density. The Townsend coefficient significantly depends on gas mixture composition. Besides, the gas gain via electric field strongly depends on field configuration or detector geometry. For MRPC, we want the gas gain of the order of 10^{6-7}.

Electron avalanche grows according to the Townsend law:

$$N = N_0 e^{\alpha \cdot x} \tag{2.2}$$

where N_0 is the initial number of electrons, α is the Townsend coefficient and x is the distance of avalanche that progress from its initial position.

Most of the electrons are produced very close to the anode. The movement of these electrons is rapid (compared to the positive ions) and generates the fast signal. Since positive ions are produced at the same place as the electrons, these ions are mostly produced close to the anode, but will drift slowly in the opposite direction towards the

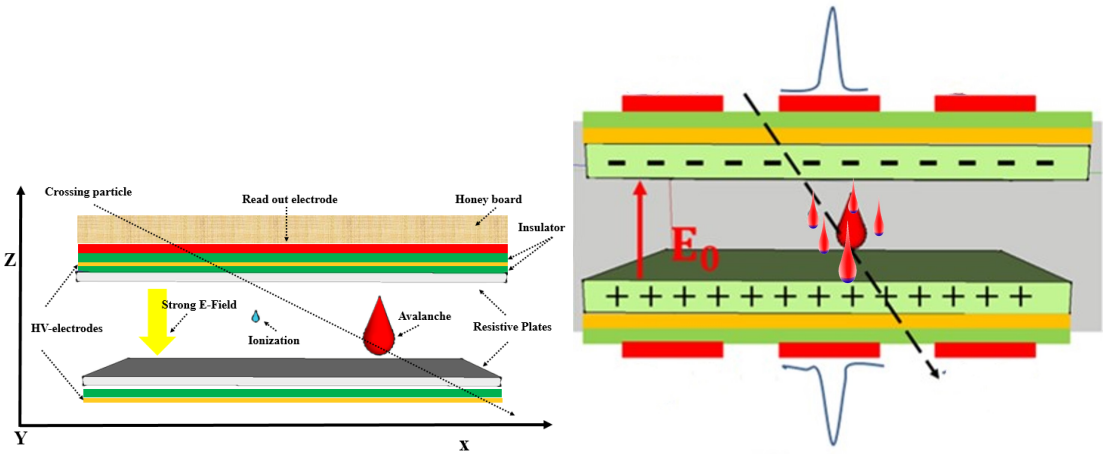

(a) (b)

Fig. 2.4 (a) Working principle of MRPC. (b) The avalanches originated by the primary clusters grow at the same time and the signal is the sum of their simultaneous contributions

cathode and will transverse the whole gas gap before being absorbed by the cathode electrode. Thus the slow signal, produced by movement of the positive ions, is much larger than the fast signal. The total signal charge is equal to the sum of the fast and the slow signal and is equal to the total ion charge (or electron charge in its absolute value) generated in the gas gap. It is easy to show that the ratio of the fast signal to the total is given by:

$$\frac{q_{fast}}{q_{total}} \sim \frac{1}{\eta} \cdot d. \tag{2.3}$$

If we focus on the electron avalanche in more detail, i.e. to see the number of electrons changing in a small step,[41], the equation is listed below.

$$\frac{d\overline{n}}{dx} = (\alpha - \beta) = \eta \tag{2.4}$$

where $\overline{n}$ is the average number of electrons at position x, β is the attachment coefficient and η is the effective Townsend coefficient. The electron avalanche process can be described in a statistical language, which is briefly summarized below.

An electron starts at x = 0, and the probability P(n,x) that an avalanche has n electrons at x (x >0) (first order) can be written as[42]

$$\begin{aligned} P(n, x+dx) = {} & P(n-1, x)(n-1)\alpha dx[1-(n-1)\beta dx] \\ & + P(n, x)(1-n\alpha dx)(1-n\beta dx) + P(n, x)n\alpha dx n\beta dx \\ & + P(n+1, x)[1-(n+1)\alpha dx](n+1)\beta dx. \end{aligned} \tag{2.5}$$

The meaning of the formula is that the probability of having n electrons at x+dx can be derived from the sum of four probabilities: (1) the probability, at x position, n-1 electrons neither duplicates nor is attached as shown in the first line; (2) the probability, at x position, n electrons neither attached nor duplicates and (3) one of them is attached and one of them is duplicates as shown at the second line; (4) the probability, at x position, n+1 electrons one of them is attached but none of them duplicates as shown in the last line. Evaluating the expression and omitting the higher order terms of $\mathrm{d}x$ we find the solution of this equation-2.5. The general solution to the equation is in the Ref.[42] and is shown in the below

$$P(n,x) = \begin{cases} k\dfrac{\overline{n}(x)-1}{\overline{n}(x)-k} & for\ n=0 \\ \overline{n}(x)(\dfrac{1-k}{\overline{n}(x)-k})^2(\dfrac{\overline{n}(x)-1}{\overline{n}(x)-k})^{n-1} & for\ n>0 \end{cases} \tag{2.6}$$

where $\overline{n}(x) = e^{\eta dx}$, $k = \frac{\beta}{\alpha}$. Since MRPC only works in high electric fields, we ignore the solution in specific conditions of $\alpha = \beta$ or $\alpha = 0$. The variance $\sigma^2(x)$ of the distribution is given by

$$\sigma^2(x) = (\frac{1+k}{1-k})\overline{n}(x)(\overline{n}(x)-1) \tag{2.7}$$

To calculate the induced signal, we have to simulate the avalanche development for the final avalanche charge. We can think the avalanche development for a single initial electron starting at one edge of the gas gap. We divide the gap into N steps of Δx (dx). The average multiplicaiton $\overline{n}(\Delta x)$ ($\overline{n}(dx)$) for a single electron over this distance is given by $\overline{n}(x) = e^{\eta x}$. If the number of electrons n_i at a given distance of iΔx is sufficiently large, due to the looping over n electrons in Monte Carlo simulation is very time consuming, we can use the central limit theorem and calculate the n(x+dx) electrons at x+dx which start from the number of electrons n(x) at a distance x. It can be directly obtained by drawing a random number from a Gaussian distribution with mean $\mu = n(x)\overline{n}(\mathrm{d}x)$ and sigma $\sigma_\mu = \sqrt{n(x)}\sigma(\mathrm{d}x)$.

2.2.3 Intrinsic Time Resolution and Efficiency

（1） Intrinsic Time Resolution

For MRPC time resolution, we first assume the MRPC signal takes the from

$$i(t) = Ae^{(\alpha-\beta)vt} \tag{2.8}$$

where v is the drift velocity, α is the Townsend coefficient , β is the attachment. coefficient. Applying a threshold A_{thr} to this signal gives a threshold crossing time of

$$t(A) = \frac{1}{(\alpha - \beta)v} \ln \frac{A_{thr}}{A} \tag{2.9}$$

The amplitude A is exponentially distributed around some average amplitude A_{av}: Therefore, the time distribution P(t) for a given threshold is given by[]:

$$P(t) = \int_0^\infty \frac{1}{A_{av}} e^{\frac{-A}{A_{av}}} \delta(t - \frac{1}{(\alpha - \beta)v} \ln \frac{A_{thr}}{A}) dA = (\alpha - \eta) v \frac{A_{thr}}{A_{av}} exp(-(\alpha - \beta)v - \frac{A_{thr}}{A_{av}} e^{-(\alpha-\beta)vt}) \tag{2.10}$$

with δ(x) the Dirac delta function. A different threshold amplitude leads only to a time shift. Therefore, the shape of the distribution is independent of the threshold and the average amplitude[43]. Time shifting the maximum of the distribution to zero leads to:

$$P(t) = (\alpha - \beta)v \cdot F((\alpha - \beta)vt) \tag{2.11}$$

$$F(a) = e^{(-a - e^{-a})} \tag{2.12}$$

F(x) is the so called Landau function. The variance $\delta(F)$ of the Landau function is

$$\delta(F) = 1.28255 \tag{2.13}$$

The intrinsic time resolution of a one gap RPC is given by[44]:

$$\delta_{RPC} = \frac{1.28255}{(\alpha - \beta)v} \tag{2.14}$$

From the equation, we can get some basic ideas that the intrinsic time resolution of an MRPC depends basically only on the effective Townsend coefficient $\eta = \alpha - \beta$ and the drift velocity v and not on the preamplifier threshold. This fact is confirmed both in simulations[43] and in the experiment. Whereas, in the derivation of equation-2.14 no space charge effects are considered[45] and the oversimplified scaling with $\frac{1}{\sqrt{n}}$ for N-gap MRPCs does not work because the timing in the MRPC is dominated by the gap with the largest signal. The largest signal gives the earliest threshold crossing time. The measurement of the earliest time has a larger rms than the average of n time measurements[43]. Besides, most results reported in paper including electronics jitter so that a statement about the pure counter time resolution is difficult.

（2） Efficiency

Taking the same derivation method as the time resolution, in this section let's briefly estimate the efficiencies that we expect with the detector physics model. In a simplified view, if the first ionization creates an avalanche exceeding the threshold or the first ioniization is attached and the second ionization exceeds the threshold or the first and

second ionizations are attached and the third exceeds the threshold, the time crossing threshold is recorded respectively and so on. In addition, the ionization clusters are assumed to contain only one electron and avalanche fluctuations are neglected[46], thus an inductive charge generated by the primary electron at position x in the gas gap is

$$Q_{ind}(x) = \frac{E_w}{V}\frac{e_0}{\alpha-\beta}e^{(\alpha-\beta)(d-x)} - 1 \tag{2.15}$$

E_w is the weight field, V is the potential between the electrodes, d is the gap width and e_0 is the charge of an electron. Setting a threshold of Q_t, the event that satisfies this condition is $Q_{ind}(x) > Q_t$ meaning x <x_0 with[42]

$$x_o = d - \frac{1}{\alpha-\beta}\ln[1 + \frac{V}{E_w}\frac{\alpha-\beta}{e_0}Q_t] \tag{2.16}$$

The efficiency can be calculated by the probability which the charge larger than the threshold.

$$\varepsilon = 1 - e^{-(1-\frac{\eta}{\alpha})\frac{d}{\lambda}}(1 + \frac{V}{E_w}\frac{\alpha-\eta}{e_0}Q_t hr)^{\frac{1}{\alpha\lambda}} \tag{2.17}$$

However, this formula is calculated assuming a readout of the charge only in one gas gap. The scaling of the efficiency for n gaps is given by $1-(1-\varepsilon)^n$ with the deficiency $1-\varepsilon$ of one gap. In reality, the efficiency is even higher because the induced charge of every gap contributes to the total induced charge and therefore the sum of all gaps counts. Efficiencies around 99 % and better are found in the literature .

2.2.4 Gas Mixture

The choice of the gas is essential to ensure the good operation of gas detectors. Virtually, any type of gas can be used to produce the amplification of the charges in gas detector. However, the ideal working gas mixture is chosen according to specific requests, such as:

- low operating HV, possibility to work with high gain;
- good proportionality, ability to sustain high rates;
- long mean life, fast recovery time.

In particular, for MRPC working at avalanche mode the streamer can cause instantaneous voltage drop on the resistive plate electrode to terminate avalanche occurrence. So for gas detector the quenching gas is necessary. Besides, an advantage to using gas quenchers is the significant increase in the drift velocity of the electrons that can be

good at improving the time resolution, and is crucial to have detectors operating at high rates. However, the use of a large amount of quenchers has negative consequences on the mean life of the detectors because of the dissociation suffered by these molecules. These dissociated molecules can recombine into solid or liquid polymers that can be deposited on the electrodes.

In our experiment, the gas mixture used is 90% R134a, 5% iso-butane, and 5% SF_6. R134a is the main working gas of MRPC, providing a source for electronic avalanche amplification. It's also a kind of electronegative gas that can absorb part of the electrons produced in the avalanche and prevent the discharge from being too large[47]. The iso-butane is employed in many resistive plate chamber (RPC) types as it acts as the quenching gas which reduces the probability of streamer formation[48] by absorbing photons to avoid secondary avalanches[49]. SF_6 is a strong electronegative gas that mainly absorbs electrons[50-51].

2.3 Rate Capability

MRPC designed and built with conventional float glass (bulk resistivity $\rho \sim 10^{12}$ - 10^{13} Ω·cm) have been already running with successful results at rates under 1 kHz/cm^2. Nowadays, there is a strong desire to improve the MRPC's rate capabilities so that it adapts to the new devices or experiments such as the CBM TOF wall.

2.3.1 Rate Capability of MRPC

To fully understand the rate effects of MRPC and improve its rate capability, several models have been proposed. The DC model[52] is considered to be the most successful. The Fig.2.5 shows why MRPC's rate capability decreases during running. When a charged particle passes through the MRPC, it ionizes the gas of MRPC, an avalanche is formed by multiplication in the gas gap if the electric field is sufficiently high. Charges deposit onto the surface of the resistive plates will create a voltage drop across the gas gap. Although the space-charge effects will limit the growth of the avalanche charge to a saturation value in the avalanche mode, the gain level is still at G$\sim 10^6$-10^7. When the particle flux is higher the electric field drop become larger. The flux of particles will be the most important factor affecting the detector rate capability. According to the DC model, the average current $\overline{I}$ drawn by a detector exposed to a particle flux of ϕ is:

$$\overline{I} = \overline{q}\phi \tag{2.18}$$

,where, $\overline{q}$ is the average charge from avalanche. If we consider a small area, A, of the glass sheet, there is a capacitance C = A$\varepsilon_0\varepsilon_r/d$ and resistance R =ρd/A between the surfaces. Thus any charge deposited on the surface will decay with a relaxation time τ = $\rho\varepsilon_0\varepsilon_r$. Fig.2.5 shows the process by which particles pass through the detector to the charge deposition on the surface. Image (a4) is the beginning of charge decay. A basic inference can be obtained from a simple calculation that for float glass $\rho \sim 5 \times 10^{12}$ $\Omega \cdot cm$ and its relative dielectric constant ε_r ~8, so the dead time is τ ~3 s. During this dead time area A of the MRPC will not work.

The avalanche charge q is associated with its actual ionization charge q_i through gain: q=Gq_i. The gain, G, is strongly dependent on the electric field, showing a threshold behavior. The outside surfaces of the MRPC mounted on electrodes apply the voltage. The potential decreases with the increase of resistive plate and internal plates are electrically floating as described in Fig.2.1. In the DC model, the schematic diagram is drawing in Fig.2.6 where the structure of the MRPC can be considered as a DC circuit diagram. When the potential V_{gap} across the gas gap electrodes is below a certain voltage $V_{Threshold}$, the gain, G , tends rapidly to unity. This situation is equivalent to the switch turn-on in the circuit at Fig.2.6. The average gap potential is given by Ohm's law:

$$\overline{V_{gap}} = V_0 - \overline{I}R \tag{2.19}$$

when the detector is in the process of testing and the particle flux is uniform. If the flux increases, V_{gap} decreases towards the $V_{Threshold}$. When the potential is close to the threshold, the MRPC "turn off". We can derive form the Eq-2.19, the value of this current:

$$\begin{aligned} I_{max} &= \frac{V_0 - V_{Threshold}}{R} \\ &= \overline{q}\phi \end{aligned} \tag{2.20}$$

In the opposite direction when $V_{gap} > V_{Threshold}$, it increases rapidly with voltage as the Fig.2.6 switch turn-off. The value of $V_{Threshold}$ depends on the gap width, the gas composition, and the gas temperature and pressure.

Formula-2.20 demonstrates that to keep V_o above $V_{Threshold}$ of the MRPC depends mainly on the plate's resistivity and the detector capacitance does not play any role. Thus for a 6 gas gaps detector assemble with glass sheets of 280 μm thickness, a particle rate of 1 kHz/cm^2 causes a voltage drop of approximately 2000 V, if we assume that 2 pC charge is generated by each through-going particle. Given this we should not expect the MRPC to work at fluxes well above 1 kHz/cm^2.

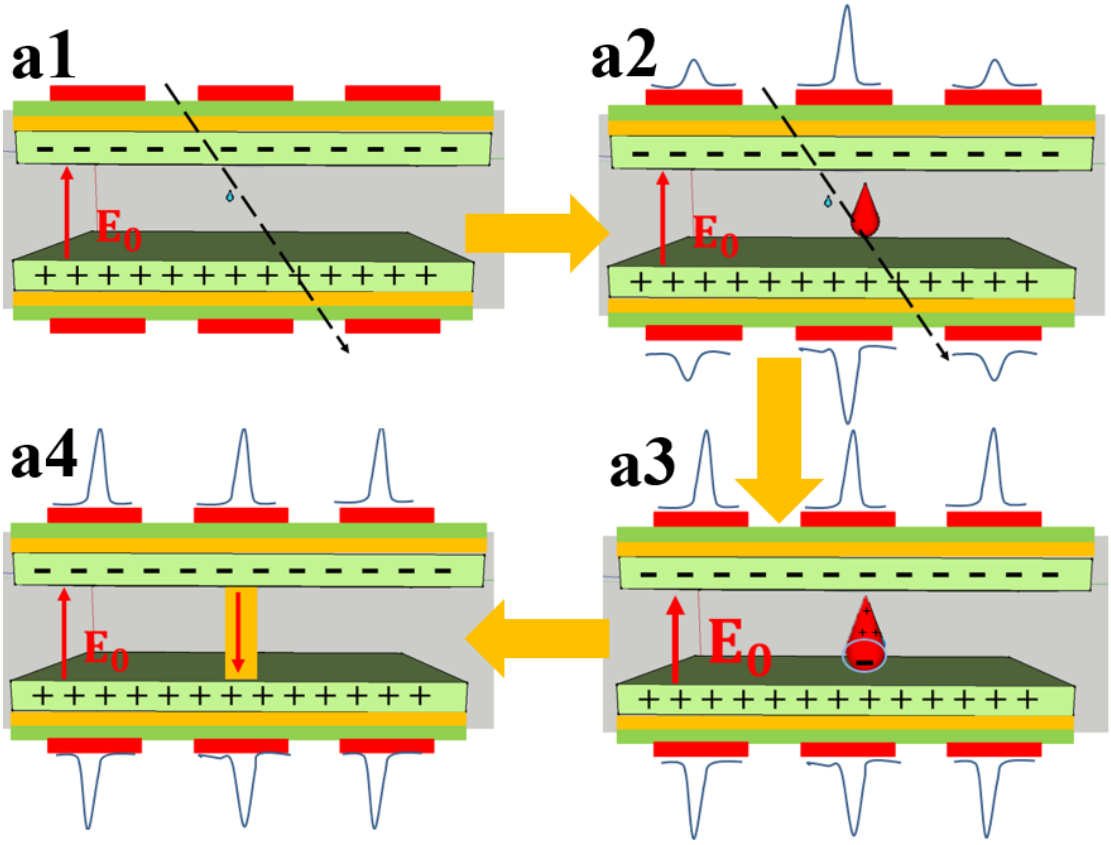

Fig. 2.5 A process diagram of MRPC from avalanche to the final state resulting in rate capability decrease.

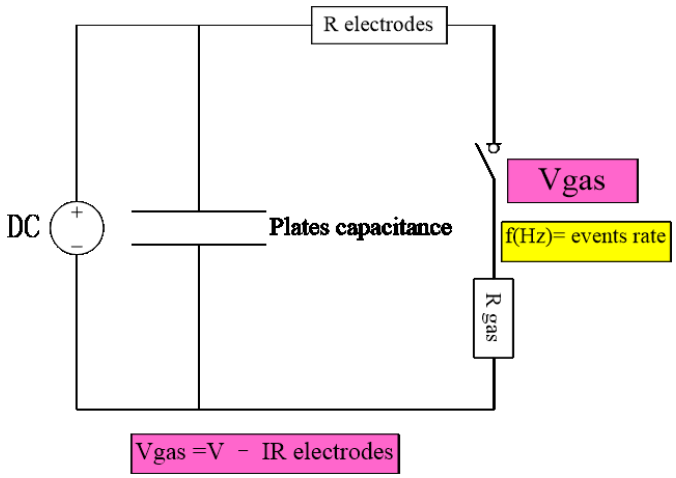

Fig. 2.6 DC model for the MRPC.

2.3.2 Factors of Rate Capability

According to the formula-2.20, we know that the rate capabilities of MRPC is mainly determined by R, and consequently by the bulk resistivity and thickness of the glass plates $R = \frac{\rho \cdot d}{A}$. Therefore thinner and lower resistivity materials are needed to increase the rate capability. New materials with resistivity in the order of 10^{10} Ω·cm are being investigated[53-54]. An alternative way to enhance the rate capabilities of MRPCs is to increase the temperature of the glass plates through which their resistivity decrease. However, it is necessary to evaluate many factors (e.g. dark currents, rate capability) before applying this technique to large detector arrays.

Chapter 3 CBM MRPC TOF

3.1 The requirements of CBM-TOF wall

As one of the core detectors of the CBM experiment, the TOF system provides particle identification for all charged hadrons emitted in beam-target interactions into the acceptance of the setup. The TOF detector will be operated in all experiments of the CBM physics program at SIS100. This includes proton beams with laboratory energies up to 29 GeV, and heavy ions with lab energies from 2 AGeV up to 14 AGeV, even in later SIS300 campaigns with protons up to 90 GeV and ions up to 45 AGeV.

The CBM-TOF wall identifies hadrons i.e. pions, kaons and protons in the angular range covered by the STS detector (2.5^o-25^o). Placed at a distance of 10 m from the primary interaction point it covers an active area of about 120 m^2, approximately rectangular in shape (9 m high, 13.5 m wide). In order to distinguish kaons reasonably well from pions and protons for the major part of the cross section in the geometrical acceptance, a full-system time resolution of at least 80 ps is needed. The intrinsic time resolution of a single channel should not exceed 60 ps. At the same time the individual detection efficiency should reach at least 95%. At present a system of MRPC is considered the only solution that can meet these requirements at affordable costs. Besides that, in order to accumulate enough statistics of rare probes detectors of the CBM have to run at ion beam intensities up to 10^9 /s. This beam rate is needed - with a standard 1% target - to achieve a target interaction rate of about 10 MHz; together with the high particle multiplicity per event this yields considerable rates in the TOF wall[55].

3.1.1 Rate at CBM-TOF wall

Fig.3.2 shows the simulated average track-density rates in kHz/cm^2 for minimum-bias events in Au+Au reactions calculated with the UrQMD generator at beam energies of 25 AGeV with the TOF wall placed at a distance of 10 m from the interaction target representing typical operating conditions at SIS300. Also shown (blue histogram) are the fluxes calculated for Au + Au reactions at an incident energy of 10 AGeV and a distance of 6 m with the reduced setup where only the RICH detector is placed in between the STS and the TOF wall. It can be seen that the distance of the TOF wall to the target can be shortened for the lower incident energies (SIS100) substantially without exceeding the rate requirements imposed from the SIS300 operation. As demonstrated by the Fig-3.1, the flux load on the CBM-TOF wall varies by almost two orders of mag-

nitude over the active surface. The particle flux includes the contribution of secondary particles produced in the upstream material of CBM. Counters placed in the innermost part of the wall positioned typically at a distance of about 50 cm from the beam pipe have to stand particle fluxes as high as 100 kHz/cm^2 without deterioration of their key properties. Note that the extremely high rates at small positive x-position in Fig.3.2 up to 1 MHz/cm^2 are an artifact of the event generator that does not describe fragment production in the spectators properly, but rather disintegrates spectator nuclei into free protons and neutrons[56].

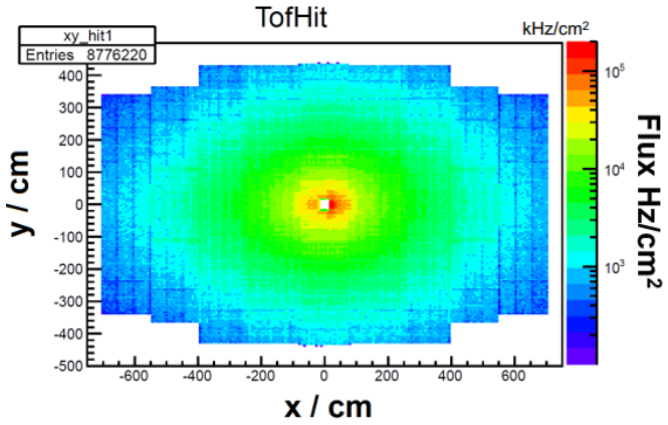

Fig. 3.1 Particle flux distribution in the CBM TOF wall. Picture from the Ref[2]

It can be seen that rate requirements are no longer achievable with MRPCs built in the standard technique with float glass resistive plates; the plates have to be made of low-resistivity material such as semi-conductive glass or ceramics. Over the larger part of the wall surface, however, standard detectors can do the job with minimum modifications, such as reducing the thickness, which will reduce the overall detector costs.

Fig.3.3 shows the layout of the TOF wall (baseline option) in the xz - plane. Each modules are equipped with the same type of MRPC detector. The detector system concept tries to accommodate the different requirements caused by the large range of incident beam energies that need to be covered. The TOF wall has to be operational at beam energies ranging from E_{beam}=2 AGeV to E_{beam}=45 AGeV. For a forward spectrometer like CBM a planar geometry is advantageous, offering the possibility to adjust to the different beam energies by placing it at different distances to the target. The number of different module types should be kept as low as possible in order to allow for easy exchange and minimal number of spares. In addition keeping the number of different counter sizes small reduces the overall production costs. The solution presented above is a modular TOF wall consisting of 6 different modules that are located at fixed position in x - direction (the deflection plane of the dipole magnet) and that can be adjusted

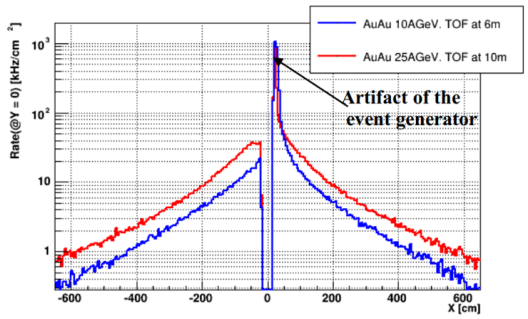

(a)

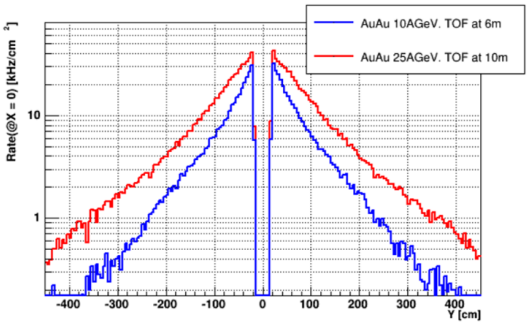

(b)

Fig. 3.2 **Calculated particle flux in the CBM TOF wall placed 10 m (red) and 6 m (blue) behind the primary interaction point using as event generator UrQMD and a target interaction rate of 10 MHz minimum bias Au+Au reactions at two different incident energies, depicting the running conditions at SIS300 (red) and SIS100 (blue). The particle flux includes the contribution of secondary particles produced in the upstream material of CBM. Upper part: Flux as function of X at Y=0 (i.e. left/right of the beam axis), the X-axis also defines the deflection plane of the particles' trajectories in the magnetic field. Lower part: Flux as function of Yat X=0. Picture from the Ref[2]**

in vertical (y) direction according to the actual distance of the wall in order to minimize dead areas. In the proposed scenario the full wall consists of only 4 different types of MRPC counters shown in Fig.3.4 that are arranged into 6 different types of modules.

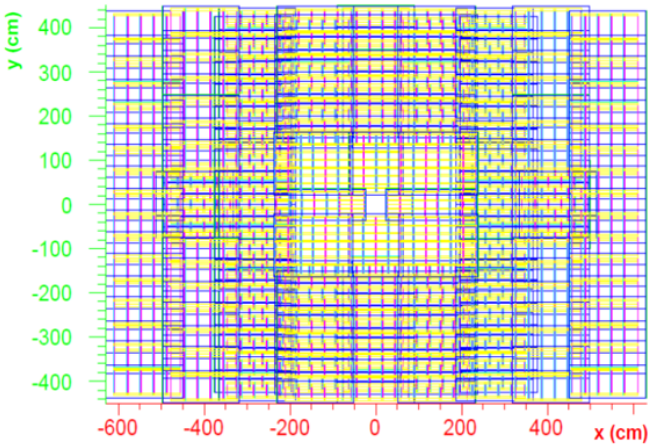

Fig. 3.3 The conceptual design of CBM-TOFwall.Planar projection of the TOF wall in the xy - plane. Picture from the Ref[2]

3.1.2 Requirements for MRPC3b

The existing conceptual design foresees a 120 m^2 TOF-wall composed of MRPC which is subdivided into a high rate region, a middle rate region and a low rate region. The TOF system's overall time resolution has to be better than 80 ps including electronics/digitization jitter and the detection efficiency has to be better than 95%. These requirements have to be met at the anticipated charged-particle flux that drops from a few tens of kHz/cm^2 close to the beam pipe —depending on the incident beam energy —to below 1kHz/cm^2 in the wall's periphery. Actually, for the outer region of about 50% of the total TOF-wall active area, rate capabilities up to 1 kHz/cm^2 are sufficient for the anticipated high rate running scenario with an Au + Au interaction rate of 10^7 s^{-1} at 11 AGeV. MRPC3b Counters with this moderate rate capability will be positioned in the dark green marked region of the current conceptual design as shown in Fig-3.4. To be cost effective the peripheral MRPC modules will be equipped with float glass MRPCs (MRPC3b and MRPC4) instead of using the more expensive low-resistive electrode material[57].

The MRPC3b multi-strip-MRPCs, foreseen to be integrated in the low rate region, have to cope with charged particle fluxes up to 1 kHz/cm^2 and therefore will be constructed with thin float glass (0.28 mm thickness) as resistive electrode material.

The design of the MRPC3b is based on the following requirements, in cases where

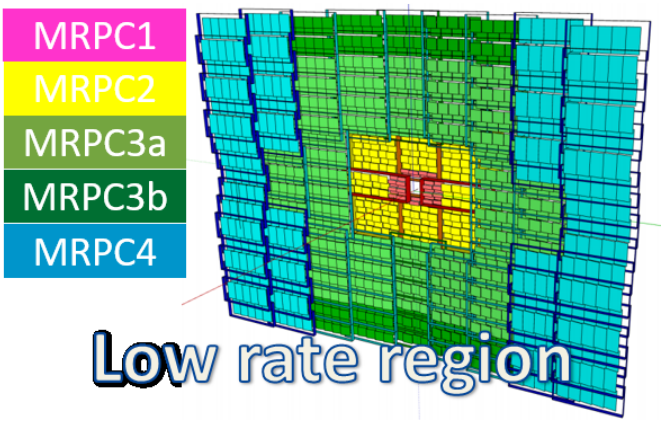

Fig. 3.4 The conceptual design of CBM-TOF wall. The low rate region (marked blue and dark green) will use the MRPC3b counter (granularity 27 cm^2) and MRPC4 counter (granularity 50 cm^2).

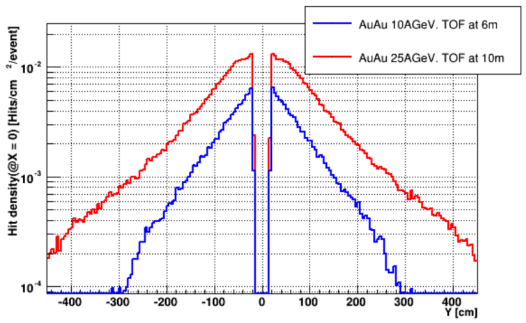

(a)

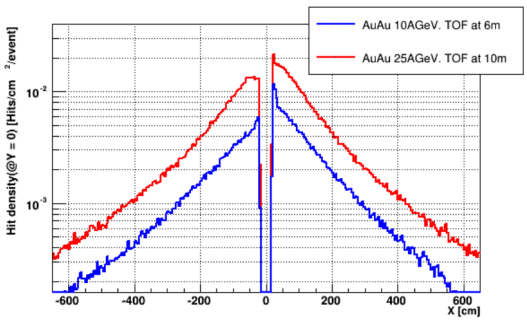

(b)

Fig. 3.5 Hit density (hits/cm2/event) of primary and secondary charged particles in central Au+Au collisions at an incident energy of 25 AGeV with the TOF wall at a distance of 10 m from the interaction target (red) in comparison to the situation at 10 AGeV, 6 m. (top panel: as function of X, bottom panel: as function of Y, cf. Fig. 2.5). Picture from the Ref[2]

the double-hits case is guaranteed to be less than 5% (occupancy). In the central area, a single unit of effective area cannot be greater than 5cm^2. As the distance from the beam axis increases, the track density decreases very rapidly. In the case of large polar angles, the effective cell size can be as high as 100 cm^2. According to the MC simulation. the area where MRPC3b is located, the granularity requirement is 27 cm^2 [2]. The Fig.3.5 shows the track density along with the distance change in X and Y to the beam axis. In the MRPC3b area, the track density is about 7 $\times 10^{-3}$ particles/cm^2/event. The active area here of 27 cm^2 results in an occupancy of 0.007$\times$ 27 $\sim$ 2%. Therefore, the requirement for a single strip of our detector is that its area is less than 27 cm$\times$1cm.

In order to store as much information as possible to provide more possibilities for offline selection, the entire system will use free-stream mode to transfer data, so the MRPC3b must undergo impedance matching to ensure clean output information. Compared to the system in the trigger matching mode, each trigger system records its corresponding valid event. However for a system without trigger (i.e. free-stream) mode, any noise disturbance will be recorded as a valid event. The multiple reflections caused by the impedance mismatch of the MRPC readout strip with the FEE will put a lot of pressure on the data transmission and seriously affect the subsequent data analysis. Impedance matching is performed on each MRPC, which can effectively reduce unwanted reflected signals, ensure the correct track reconstruction, and reduce the pressure of data transmission. Prototypes of MRPC3b have been build and were used in a proof-of-principle study[58] in two test beam campaigns at the SPS accelerator at CERN.

3.2 Prototype Design

3.2.1 A Simulation of MRPC operation

A detailed simulation of the operation of MRPC not only helps us to understand the principle of MRPC, but also provides valuable guidance to design and optimize its structure. In the following we'll introduce the way we simulate the output signal of MRPC at first, then focus on the signal transmission to the electronics. Our main aim is to understand and suppress the signal reflection phenomenon by tuning the characteristic impedance of the MRPC readout strip to match that of the front-end electronics (FEE). In this section, we present a simple Monte Carlo study to investigate the relationship between the number of gas gap, the width of the gas gap and MRPC performance. The simula-

tion results provide a qualitative explanation for the subsequent experimental data. The simulation is based on Garfeild++. Garfield++ is a toolkit for the detailed simulation of particle detectors that use gas and semi-conductors as sensitive medium and shares functionality with Garfield, Heed and Magboltz .

1. Gas parameters

When a charged particle cross the gas gap of a MRPC, the ionization-induced charge deposition is characterized by the average number of clusters per unit length and the probability distribution for the number of electrons per cluster[59]. The numbers can be calculated using Garfield++-Heed[60]. We used the Heed function in Garfeild++ to determine the primary ionization characteristics of the working gas mixture, which includes 90% R134a +5% iso-butane +5% sulfur hexafluoride (SF_6) commonly used in MRPC modules. In the simulation, a μ particle with the energy of 5×10^9 eV is shot into the MRPC volume. The result is shown in Fig.3.6. The pressure and temperature of the gas are set to 1 atm and 25 C^o. Under this working condition, the primary cluster density is $\sim$ 10 mm^{-1} and the average cluster size is $\sim$ 2.

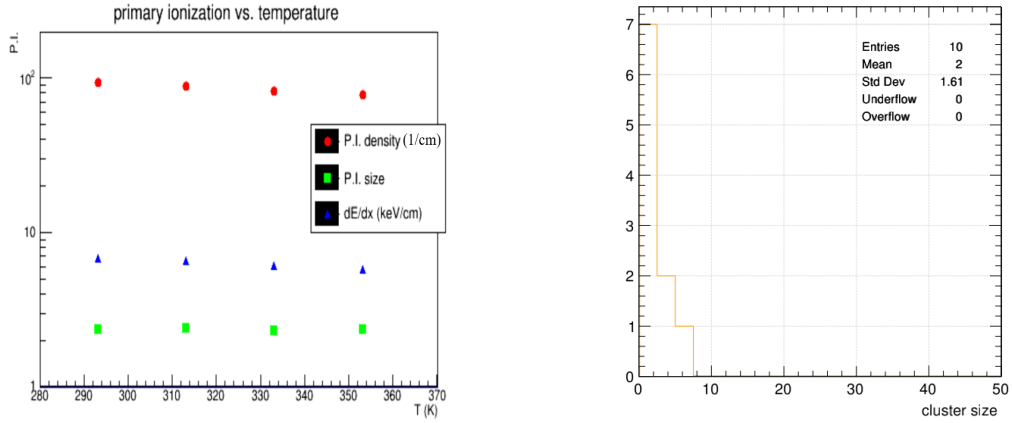

Fig. 3.6 The number and size distribution of primary clusters by ionization of charged μ.

2. Avalanche process

The generated primary electrons will avalanche under high electric field. The characteristics of the avalanche process are determined by several parameters, the Townsend coefficient α, the attachment coefficient β, and the drift velocity. These parameters are calculated by the Magboltz function in Garfeid++. For a typical working electric field of MRPC, the effective Townsend coefficient $\eta = \alpha - \beta$ is 1400 cm^{-1}.

In the simulation process using Garfeild++, the electron multiplication process is

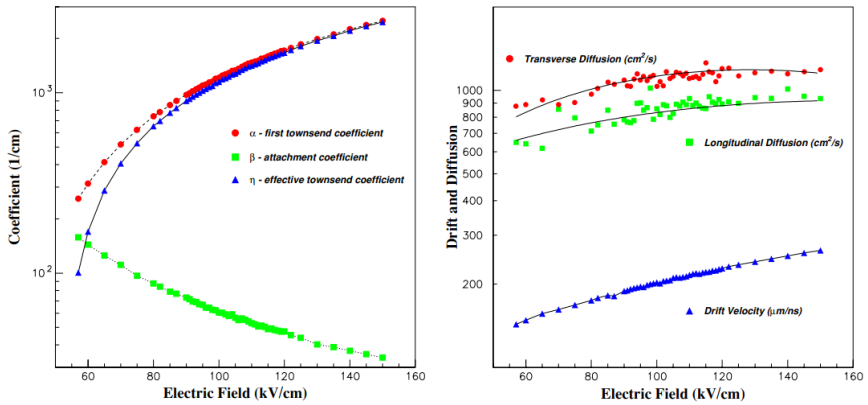

Fig. 3.7 The first Townsend coefficient, attachment coefficient and electron drift velocity calculated by MAGBOLTZ, as a function of the electric field magnitude. The gas mixture is 90% $C_2F_4H_2$ + 5% iso-butane + 5% SF_6. The transverse and longitudinal diffusion coefficients are also shown. Image from reference[3]

calculated by using the gas parameters calculated above (Fig.3.7). Based on Garfield++, we have established a single gas gap MRPC model (Fig.3.8 (a)). There are two readout strips on the readout board. The sensitive area is $2\times 2\ cm^2$. The gas gap interval is 230 μm. The MRPC operates at electric field of 110 kV/cm in the gas gap.

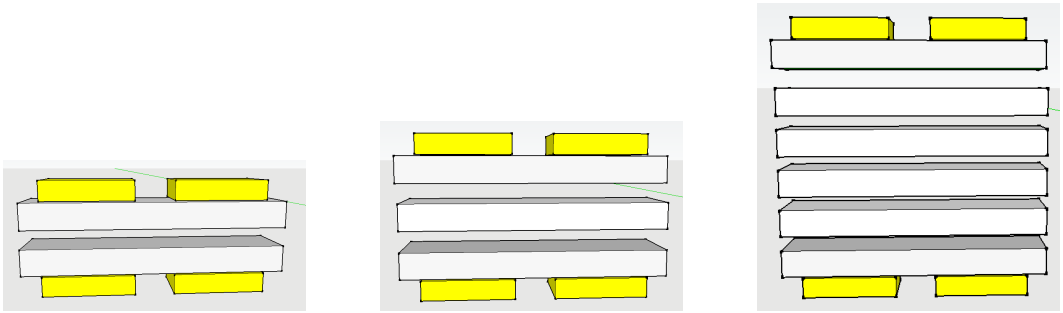

(a) (b) (c)

Fig. 3.8 Image (a) is the geometry of a MRPC in the simulation with one gas gap. Image (b) is the geometry of two gas gaps MRPC in the simulation. Image (c) is the geometry of five gas gaps MRPC in the simulation.

In the simulation, the energy deposited by the primary interactions in the gas gap ionizes electron-ion pairs with an average energy of 20 eV per pair[61]. The electrons, once created, drift to the anode and start the avalanche multiplication under the applied electric field. We assume that the electric field in the gap is uniform and the electrons multiply independently of the position and multiplication. Fig.3.9 (a) shows a typical result from the Garfield++ simulation, demonstrating the process of the avalanche. The left Fig.3.9 (a) is the complete trajectory of the incident particle (blue line) and the main cluster position (asterisk mark) and the avalanche (X-Y cross section) of the electrons

generated in the gas volume. The primary ionization is characterized by a given number of clusters/mm, which is Poisson distributed.

3. Signal induction

The induced current is according to Ramo theory[62].

$$i_{induced} = -q \cdot \vec{v}_{drift} \cdot E_w(\vec{r}) \tag{3.1}$$

Where $E_w(\vec{r})$ is the weighting field at position $\vec{r}$ int the gap. If we place the electrodes at a unit potential and ground all other electrodes, the electric field in the gas gap is the weight field. For the MRPC, the weighting field can be expressed by the following formula

$$E_{weight} = \frac{1}{n_{gap} d_{gap}} + \frac{(n_{gap}+1) d_{glass}}{\varepsilon_{glass}} + \frac{2 d_{Mylar/Kapton}}{\varepsilon_{Mylar/Kapton}} \tag{3.2}$$

,where n_{gap} and d_{gap} are the number and width of gas gaps; d_{glass}, and $d_{Mylar/Kapton}$ are the thickness of resistive plates (usually glass) and Mylar/Kapton tape; while ε_{glass} and $\varepsilon_{Mylar/Kapton}$ are the permittivities of the resistive plate and Mylar/Kapton, respectively. By using the ANSYS software, we calculated the weighting field of the single-gap MRPC. Fig.3.9 ((a) right image) is a simulation of the MRPC weighting field with two readout strips. Fig.3.9 (b) shows a typical signal waveform from the MRPC simulation and is seen to be in agreement with the expected range. The rise time is basically the same as the actual observation.

4. MC results and discussion

In addition, we also performed a simulation of MRPC with two gas gaps and five gas gaps. The simulation process is the same as the MRPC process with a single gas gap. Figure.3.8 (b) and (c) are the MRPC structure with two gas gaps and five gas gaps respectively. The thickness of the glass set in the simulation is the same as the ultra-thin glass we used for the MRPC3b counter, which is 0.28 mm. The gas gap interval is also 230 μm. Fig.3.9 (c)-(f) are simulation results of MRPCs with two gas gaps and five gas gaps. Fig.3.9 (c) and (e) are simulated avalanche processes and weighting fields. As the number of gas gap increases, the total amount of avalanche charge increases. The tendency of the readout strip to correspond to the decrease in the strength of the weight field in the gas gap is more pronounced.. Meanwhile it can be seen that as the number of glass layers increases, the strength of the weighting field decreases, which is consistent with the theoretical prediction. As a result shown in Fig.3.9 (d) and (f), when the number of gas gap layers increases, the avalanche charge increases correspondingly,

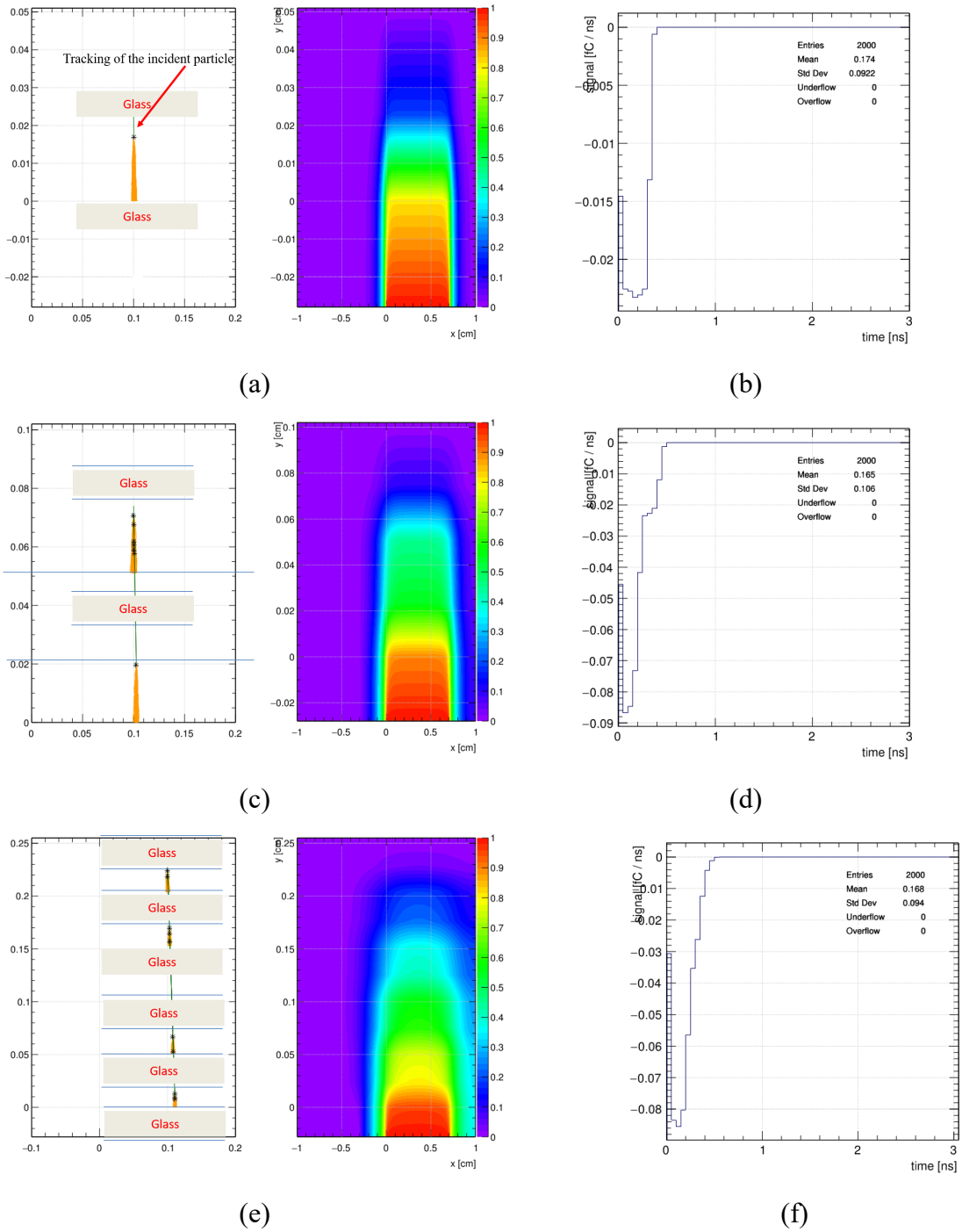

Fig. 3.9 The image shows the simulation results of an one-gap, a two-gap and a five-gap MRPC structure. The gas gap of each MRPC is 230 μm. The first column is the simulation of electron avalanche in the gas gap, the second column is the weighting field with the 2 strip chosen as the readout unit, and the third column is the current signal induced by the avalanches.

and the generated signal becomes larger(but not as fast as the total avalanche charge does).

In addition, we also reduced the gas gap interval to 140 μm to check the performance of MRPC. The other parameters are set as before. We focus on the change in rise time, which is shown in Fig.3.10 (b). By comparing with Fig.3.10 (b), it seems that as the gas gap narrows the MRPC output signal gets narrower and the rise time becomes shorter. However at the same field strength, the avalanche amplification of the MRPC with 140 μm gas gap is less than the MRPC with 230μm gas gap, which means that the working voltage of the MRPC with 140 μm gas gap may be higher than 230 μm gas gap. These simulation results need verification by experimental tests, which will be discussed in the following sections.

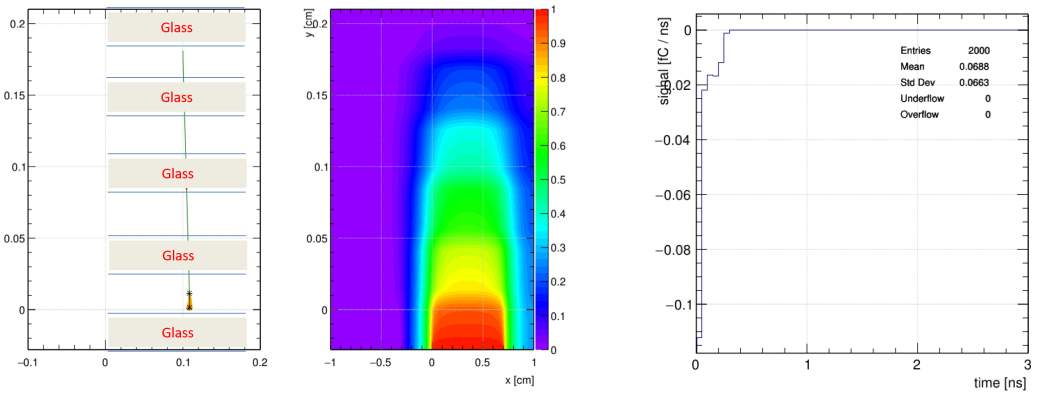

(a) (b)

Fig. 3.10 The figure shows the simulation results of the MRPC with 5 gas gaps, each of 140 μm wide.

5. Signal Propagation

Signals generated by gaseous avalanches are induced on the external pickup strips. The electrode and the induced signal acts as a current source. The pulse propagates in both directions of the strip towards the ends. In this case the readout strips have to be treated as a multi-conductor transmission line[63]. Normally, the strip width is homogeneous and much smaller than its length. Sketch of a two dimensional multi-conductor transmission line is similar to that of the MRPC strips. It can be described by the Transversal ElectroMagnetic (TEM) approximation telegraph equations. This will be discussed in the following.

6. Theory of the Transmission line

The set of electrical conductors used for connecting a signal between its source and its destination is called a transmission line (and not just an interconnection). At least two conductors are required: one for the signal and the other one for the return path, which is usually a ground plane. It is not possible to ignore the impedance of transmission line, if the time it takes for the signal to travel from the source to the destination is comparable to the time period of one-fourth of the wavelength l_c in transmission line. A circuit that satisfies this condition is called a high frequency circuit. Two very important properties of a transmission line are its characteristic impedance and its propagation delay per unit length. If the impedance of the transmission line is not controlled along its entire length, or the line is not terminated by the right value of impedance, signal reflections, crosstalk, electromagnetic noise, etc, will occur. This could degrade the signal quality and maybe create errors in information being transmitted and received.

（1） Impedance

Impedance, usually denoted by Z, is defined as the combined effect of capacitance, inductance, and resistance that a circuit offers a signal at a given frequency. Impedance is the ratio of voltage to the flow of current allowed and is the sum of the resistance and reactance of an electrical circuit. And just like resistance, the unit to measure impedance is Ohms(Ω). Reactance is composed of Capacitor impedance and inductor impedance. For different circuits, impedance calculation are different.

（2） Signal Reflection in PCB Transmission Lines

Signal reflection is conceptually similar to the behavior of waves as they pass between mediums of different densities. As a wave travels through a medium, it will often reach the end of the medium and encounter an obstacle or perhaps another medium through which it could travel. For example, consider a pulse traveling on a string that is rigidly attached to a support at one end. When the pulse reaches the support, a severe change in the medium occurs-the string end. The result of this change is that the wave undergoes reflection-the pulse moves back along the string in the opposite direction[64].

In electronics, a signal trace on a printed circuit board (PCB) is the equivalent to a wire for conducting signals. Each trace consists of a flat, narrow part of the copper foil that remains after etching. In PCB, the electromagnetic field transmits energy mainly by electrical signals. An alternating current that runs on a transmission line usually has a high enough frequency to manifest its wave propagation nature. In this case, the signal is the variation of the voltage with respect to time on the trace. The key aspect of

the propagation of the electrical signals over a transmission line is that the line has an impedance at every point along its length. For longer traces, electromagnetic radiation from other sources may be received, which may cause interference and noise. If the line geometry is the same along the length, the line impedance is uniform, known as a controlled impedance line. For a different situation, non-uniform impedance causes signal reflections and distortions. Signal reflection occurs as a transmitted signal is reflected back toward its origin due to differences in impedance along the transmission line. The MRPC readout strips are narrow traces on the PCB board. The width is the same along the strip, so that the impedance is uniform. But, if this impedance is different from that of the Front End Electronics, reflection will occur at the strip ends. For the FEE, the impedance is normally designed as 50 Ω (single end) or 110 Ω (differential). In order to match to such values, the impedance of the strips are optimized by choosing the proper geometry of the MRPC (strip width, gap between strips, number of gas gaps, gap size, glass size, et al.).

① Signal reflection

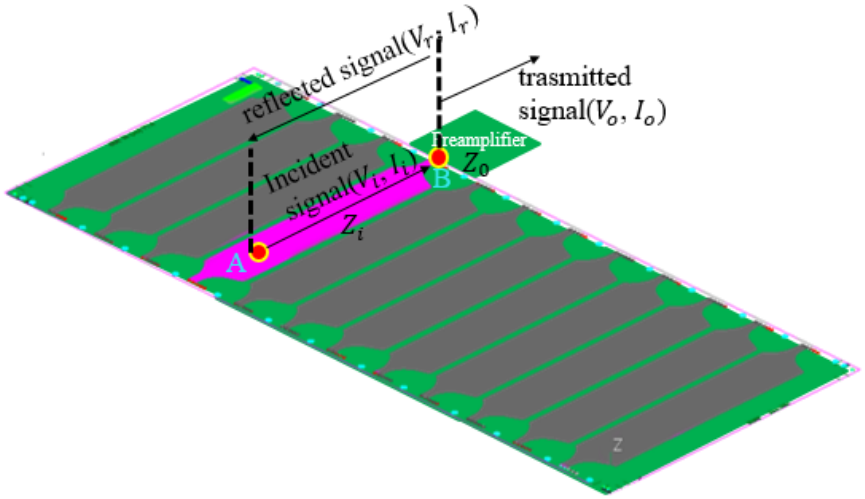

Fig. 3.11 Impedance Discontinuity and Signal Reflection in PCB Transmission Lines.

To understand the reflection, let's say that from point A to point B, the line is uniform with impedance Z_i, but at B point, there is an discontinuous impedance and the line's impedance changes to Z_0 as shown in Fig.3.11. When a signal is sent from A to B, set the incident signal voltage and current be V_i and I_i at B point. It follows that:

$$V_i = Z_i I_i \tag{3.3}$$

Now, if we look at B from the right side where the line impedance is Z_0, then the trans-

mitted voltage V_0 and the transmitted current I_0 at this point B must be related by:

$$V_0 = Z_0 I_0 \tag{3.4}$$

It needs to be emphasized that the relations following the concept of impedance must always be obeyed.

Case (1): Z_0=Z_i. In this case, the both above equations will be simultaneously satisfied by: $V_0 = V_i$ and $I_0 = I_i$. This is to be expected, as in this case, point B is basically any point on a uniform transmission line, so that at every point B on this line, the transmitted signal will equal the incident signal.

Case (2): $Z_0 \neq Z_i$. Following both equations-3.3 and 3.4, since $Z_0 \neq Z_i$, it is easy to conclude that two equations $V_i = V_o$ and $I_i = I_o$ cannot be satisfied at the same. Thus at an impedance discontinuity, the incident signal is not fully and completely transmitted on-wards.

The equations (3.3 and 3.4) can be solved by assuming that a part of the incident signal is reflected back at the point B, and this reflected signal is superimposed on the incident signal at point B. At point B, the result of the incident signal and the superimposed reflected signal will equal the transmitted signal at point B. Therefore a part of (V_i,I_i) is reflected back onto the 'Z_i' transmission line at point B. The reflected signal's voltage and current at point B is recorded by (V_r,I_r). The resulting signal voltage due to incident voltage V_i and the reflected voltage V_r would be ($V_i + V_r$), and as Kirchhoff Law applied at point B, this must equal 'V_o':

$$V_0 = V_i + V_r \tag{3.5}$$

And the resulting current due to the superposition of the incident current 'I_i' and the reflected current 'I_r' (which is in a direction opposite to that of the incident current) would be (I_i ^-I_r), and as Kirchhoff Law applied at point B, this must equal 'I_o':

$$I_0 = I_i - I_r \tag{3.6}$$

And the reflected (V_r,I_r) signal is traveling on the line with impedance 'Z_i', we must have:

$$V_r = Z_i I_r \tag{3.7}$$

Using equations 3.3, 3.4, and 3.7 in equation-3.5, we have:

$$Z_0 I_0 = Z_i I_i + Z_i I_r = Z_i (I_i + I_r) \tag{3.8}$$

And since, as equation-3.6, $I_0 = (I_i - I_r)$, we have:

$$Z_0(I_i - I_r) = Z_i(I_i + I_r) \tag{3.9}$$

$$I_i(Z_0 - Z_i) = I_r(Z_0 + Z_i) \tag{3.10}$$

$$\frac{V_r}{V_i} = \frac{I_r}{I_i} = \frac{Z_0 - Z_i}{Z_0 + Z_i} \tag{3.11}$$

$\frac{V_r}{V_i}$ or $\frac{I_r}{I_i}$ indicates the fraction of the incident signal that is reflected back at point B of impedance discontinuity and is called the reflection coefficient 'R_c':

$$R_c = \frac{V_r}{V_i} = \frac{I_r}{I_i} = \frac{Z_0 - Z_i}{Z_0 + Z_i} \tag{3.12}$$

In terms of 'R_c', the transmitted signal voltage and current at point B are given by:

$$V_0 = V_i + V_r = (1 + R_c) \times V_i \tag{3.13}$$

And

$$I_0 = I_i - I_r = (1 - R_c) \times I_i \tag{3.14}$$

From the above it is clear that the value of reflection coefficient R_c depends on the relative values of 'Z_i' and 'Z_0'; greater the difference between them, more is the amount of reflection. It can be safely concluded that, in case of impedances being purely resistive, the range of values of 'R_c' can be given by:

$$-1 < R_c < 1 \tag{3.15}$$

And if $Z_0 > Z_i$, a partial positive signal is reflected back leading to a voltage overshoot at B in a pulse signal. And if $Z_0 < Z_i$, a partial negative signal is reflected back leading to a voltage undershoot at B in a pulse signal. If 'Z_o' differs from 'Z_i' by ∼20%, the reflection coefficient 'R_c' will be ∼ 10%. This indicates that about 10% of the incident signal will be reflected. In most circuit designs, a 10% distortion in signal due to impedance mismatch is acceptable due to the available noise margins.

We can now discuss some special cases of relative magnitudes of the 'Z_i' and 'Z_0'.

- Case (1):Transmission line open at far end.
  Here $Z_0 = \infty$ (since the transmission line is open at its far end B), leading to $R_c = 1$. This means that the incident signal will be fully reflected so that $V_0 = 2V_i$ and $I_0 = 0$. This means that the superimposed signal voltage will be twice the incident voltage, and the superimposed signal current will be zero, as should be expected at the open end.

- Case (2):Shorted transmission line.
  Here Z_0 = 0 (since the line is shorted at the far end B), leading to R_c = -1 so that V_0 = 0 and $I_0 = 2I_i$. This means that a negative of the full incident signal is reflected back to make voltage zero at the shorted end as expected.

Since the impedance of a transmission line depends on the geometry of the conductors and the PCB material properties, any change in those will cause a change in impedance. Some instances are listed here:

- At the source or the destination/end of the line. Source or receiver impedance is most often not the same as that of the line.
- Through-hole most often do not have the same impedance as the signal traces – very few designers try to find out what the via impedance is[65].

② Multiple Reflections:

Consider a transmission line whose length is such that the total propagation time over it is 't_{pt}' and let its impedance be 65 Ohms. At the destination, it is connected to a load of 50 Ohms. The reflection percentage (R_c) at the load will, therefore, be -13%. Suppose there's a 1 V signal launched on the trace at time 0. At time 't_{pt}', this 1 V signal will reach the destination and will be reduced to 1 V $\times \frac{50}{(65+50)} \times 2$= 0.839 V. Hence a 0. 131 V signal will be reflected back. Suppose this signal is a single-ended transmission, which means the other end of the line is terminated with an impedance of Z_0 = 0. Now, 0.131 V reflected signal will reach the other side at time '$2t_{pt}$', then the full 0.131 V signal will be reflected towards the load. This will reach the load at time '$3t_{pt}$', where -13% of this = 0.027 V will be reflected, thus making the load voltage now = 0.104 V. Meanwhile, the reflected signal of 0.027 V will reach the other side at time '$4t_{pt}$', and then it will be reflected towards the load; it will reach the load at '$5t_{pt}$', where -13% of it = 0.004 V will be reflected back, thus making load voltage now = 0.023 V. Meanwhile, a reflected signal of strength 0.004 V will reach other side at time '$6t_{pt}$'. At '$7t_{pt}$', a -0.004 V$\times$13% = 0.003 V to the load making the load voltage now 0.003 V. and so on. So the signal at the destination will look like:

- From 0 to t_{pt}: 1 V
- t_{pt} to $3t_{pt}$: 0.104 V
- $3t_{pt}$ to $5t_{pt}$: 0.023 V
- $5t_{pt}$ to $7t_{pt}$: 0.003 V And so on.

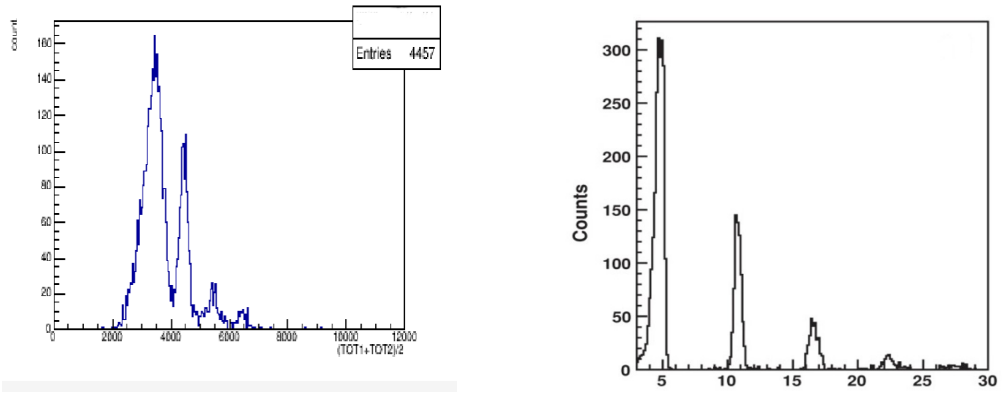

(a) (b)

Fig. 3.12 These two figures are the signal reflection spectra of the TOT obtained by the MRPC during the test through the TDC. The signal is reflected multiple times on the MRPC readout strip PCB to form a reflection ringing.

Thus we will see ringing in the signal at the destination. Fig.3.12 shows a results of this process. Ringing with overshoot and undershoot will occur: if the impedance(of the transmission line) is less than the destination impedance a negative reflection will occur, and if the impedance is higher a positive reflection at the destination is foreseen. So we can estimate the impedance of the PCB by the formula below:

$$Z_i = \frac{Z_0 \cdot (2V_i - V_0)}{V_0} \tag{3.16}$$

（3） Signal speed

At high frequencies, transmission lines need to have a controlled impedance to predict the behavior of the signals and avoid signal reflections and other problem. So it's important to know the speed and time at which the signal propagate on transmission lines.

Electromagnetic signals travel in vacuum and air at the same speed as of light, which is :

$$V_c = 3 \times 10^8\ m/sec = 30\ cm/nanosecond \tag{3.17}$$

A signal travels on a PCB transmission line at a slower speed, affected by the dielectric constant (ε_r) of the PCB material. The signal speed in a homogeneous dielectric material is given below:

$$Signal\ speed\ on\ microstrips : V_p \approx \frac{V_c}{\sqrt{\varepsilon_r}} \approx \frac{30\ cm/ns}{\sqrt{\varepsilon_r}} \tag{3.18}$$

,where ε_r is the dielectric constant of the material. In fact, for microstrips the effective dielectric constant ε_{reff} is used to calculate the speed on a PCB; its value lies between

1 and ε_r and is approximately given by:

$$\varepsilon_{reff} \approx (0.64\varepsilon_r + 0.36)^{[66\text{-}67]} \tag{3.19}$$

Thus, the speeds of signals on a PCB is less than that in air. If $\varepsilon_r \approx 4$ (like FR4 material), the speed of signals on a stripline is about half that in the air.i.e, it is about 15cm/ns. Henceforth, we use V_P to denote the speed of signals on a PCB.

（4） Propagation delay

The propagation delay is the time taken by a signal to propagate over a unit length of the transmission line:

$$t_{pd} = \frac{1}{V_p} \tag{3.20}$$

,where V_p is the signal speed in the transmission line. On PCB transmission lines, the propagation delay is given by:

$$t_{pd} \approx 33\sqrt{\varepsilon_{reff}}\ ps/cm \tag{3.21}$$

（5） Critical length L_c

We are now going to consider the key parameters of the transmission line effects, (1) the critical length, (2) the rise/fall time and, (3) when the length of an interconnection is to be considered as a controlled impedance transmission line. PCB is a type of interconnection used for moving signals from their transmitters to their receivers. When the signal frequencies (in case of analog signals) or the data transfer rates (in case of digital signals) are low (less than 50 MHz or 20 Mbps), the time it will take for a signal to travel from its source to its destination on a PCB would be very small ($< 10\%$) compared to the time period of one-fourth of a wavelength or the fastest rise time of a digital pulse signal. In this case, it is possible to approximate the interconnect by assuming that the signal at the destination follows the signal at its source at the same time. In such a low-speed scenario, the PCB signal can be analyzed by conventional network analysis techniques and we can ignore any signal propagation time or transmission line reflections, etc.

However, when dealing with signals at higher frequencies or higher data transfer rates, the signal propagation time on PCB conductors between the source and the destination cannot be ignored in comparison to the time period of one-fourth of a wavelength or the fastest pulse rise time. Therefore, it is not possible to analyze the behavior of such high-speed signals on PCB interconnects using ordinary network analysis techniques. The interconnects need to be considered as transmission lines and analyzed accordingly.

For high-speed or high-frequency signals, a few rules apply. In case of high-frequency analog signals, let the maximum frequency content in the signal = f_m Hz.

$$\begin{aligned} Time\ period\ of\ 1\ wavelength: t_\lambda &= \frac{1}{f_m} \\ Wavelength: \lambda_m &= \frac{V_p}{f_m} \\ Critical\ length: l_c &= \frac{\lambda}{4} = \frac{1}{4 t_{pd} f_m} \end{aligned} \tag{3.22}$$

3.2.2 Design of MRPC3b

1. Impedance Matching

When high-frequency signals are carried on any significant length of transmission lines, it is important to note that the transmission medium is matched to its terminations. The transmission line of impedance discontinuities or mismatches will degrade the amplitude, phase accuracy and the temporal fidelity. For the impedance matching, the source and load impedances should be equal to the characteristic impedance of the transmission line, as this minimizes signal reflections. MRPC's readout PCB is one of type

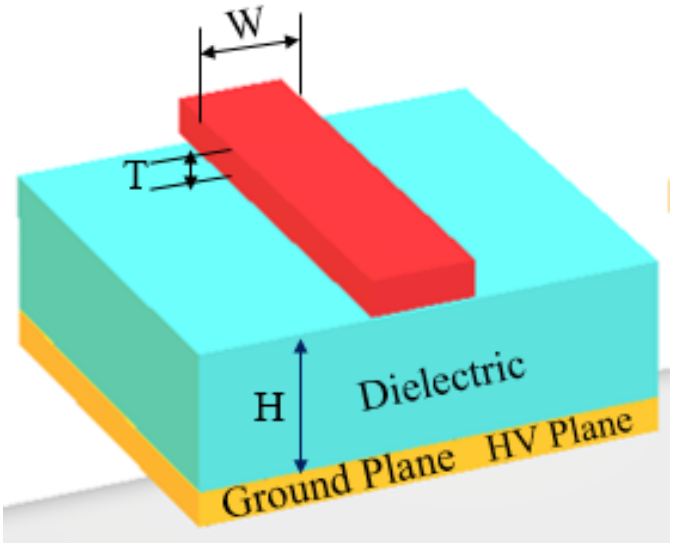

Fig. 3.13 A microstrip transmission line.

of microstrip PCB that is a basic type of signal transmission line. Fig-3.13 shows the microstrip schematic diagram. Microstrip transmission line is composed of a uniform trace for the signal located on the outer layer of a PCB, and a parallel conducting ground plane, which provides the return path for the signal. The trace and the ground plane are separated by a certain height of PCB dielectric. How to match impedance to eliminate reflection and other effects is very important for high speed circuits. Here are the commonly used impedance matching methods.

(1) Series Terminal Matching

The series terminal matching is that when the impedance of signal source is lower than the characteristic impedance of transmission line, a resistor R is concatenated between the source and transmission lines of the signal, so that the output impedance of the source end is matched with the characteristic impedance of the transmission line. And the signal reflected back from the load end is suppressed.

(2) Parallel terminal Matching

When the impedance of the signal source is small, the input impedance of the load end is matched with the characteristic impedance of the transmission line by adding a parallel resistance, and the purpose of eliminating the reflection of the load end is achieved.

(3) Adjust the characteristic impedance of PCB trace

A PCB trace is described by its characteristic impedance. This is the impedance encountered when the incident wave enters the transmission line model. The characteristic impedance of PCB trace is determined by its geometry. Different types of PCBs have different characteristic impedance calculation methods, and their impedance values are calculated depending on their respective models. Impedance matching is typically achieved by adjusting the physical and geometrical dimensions of the PCB trace width, thickness, thickness of the PCB dielectric, and the like. In addition, for a professionally designed PCB, most of the copper traces bend at 45 angles. One reason for this is that 45 angles shorten the electrical path between components compared to 90 angles. Another reason is that high speed logic signals can get reflected off the back of the angle, causing interference. A basic principle is that for high speed communication protocols above 200 MHz or digital logic, one should probably avoid 90 angles and vias in our traces.

2. Design

The layer thickness and the width of traces will affect how much current can flow through our circuit. So the thickness and width of traces should be considered when designing the MRPC readout board.

（1） Adjusting impedance

The basic idea of design is to keep the components in each section grouped together in the same area of the PCB, to keep the conductive traces short and avoid long traces as much as possible, because it can pick up electromagnetic radiation from other sources, which can cause interference and noise.

Fig-3.14 is a simplified MRPC readout board diagram and Fig.3.15 is a normal

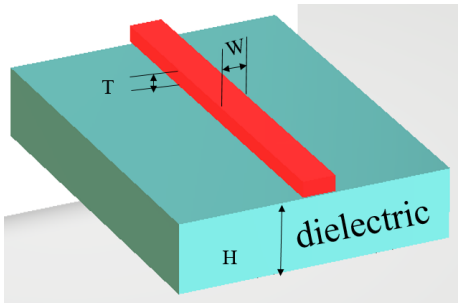

Fig. 3.14 Schematic MRPC readout PCB.

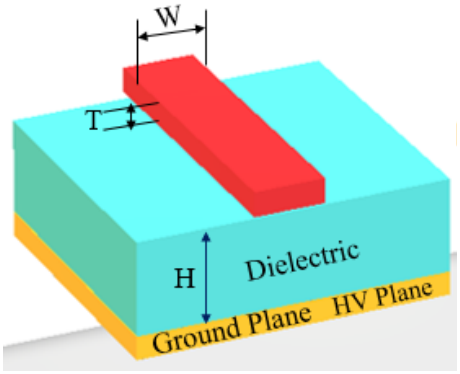

Fig. 3.15 Schematic micro-strip PCB.

microstrip PCB diagram. By comparing Fig.3.14 and Fig.3.15 we can clearly see the difference between the two diagrams. MRPC readout has no ground plane. Although MRPC readout board can be classified as a microstrip type, the missing of ground layer poses great difficulties for the impedance design. Most PCB design software is based on the normal microstrip types to calculate the impedance. In such case, we can only get an estimation of the primary parameters based on these software firstly. As mentioned above, the key parameters of the impedance are the width and thickness of the traces and the dielectric's thickness.

The material's dielectric constant ε_r is around 4 for the readout board PCB. For the MRPC3b, we prefer to set the strip's width to 7 mm and the interval between two strips to 3 mm. As discussed in the section above, such setting gives an impedance of around 50 Ohms. The width of the strip and the spacing value between the strips are mainly derived from the experiment, since they are hard to be calculated from PCB designing softwares. Besides, we have designed a MRPC detector with a series of readout strips with different widths, and its test results showed that a good time resolution was achieved with strips of 7 mm wide and intervals of 3 mm. Furthermore, according to the unified efforts on CBM-TOF design and experimental test, an empirical design equation is proposed for the MRPCs[68].

$$gap = 1.5 \cdot h + \frac{h}{W} + \frac{20}{\varepsilon_r} \tag{3.23}$$

where gap is the interval between two neighboring strips, W is the width of strip, and h is the thickness of the PCB. The CBM-TOF experimental system needs to have a consistent impedance. Therefore, the differential transmission line defined by the corresponding strips of the readout electrodes should have a 50 Ω impedance. For a double stack MRPC detector, it takes 25 Ω impedance for a single readout. The differential out-

put to the FEE requires an impedance matching with the 50 Ω input impedance of the fast amplifiers. These parameters are input to the common Microstrip model (3.16), and the other parameters are tuned to find a desired impedance. Setting the target impedance to ∼25 Ω, we can get the values of all other parameters. Here we have assumed that the graphite electrode is at ground potential.

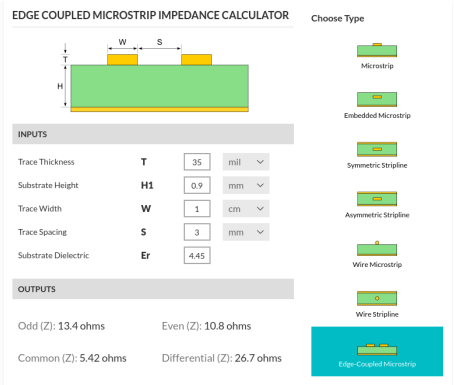

Fig. 3.16 edge-coupled microstrip model

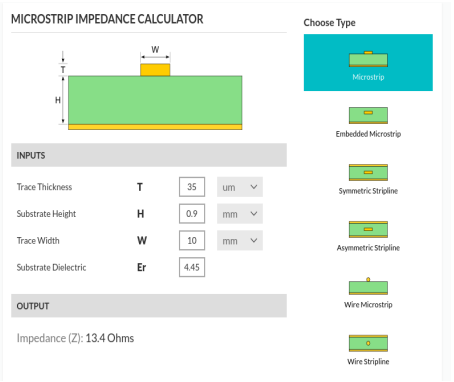

Fig. 3.17 Normal microstrip model.

In order to eliminate the parameters differences caused by the microstrip model as much as possible, we used two models to calculate the impedance. Shown in Fig.3.16 and Fig.3.17 are the results from the edge-coupled microstrip model and the normal microstrip model respectively. The calculation result from the edge-coupled model indicates that if the impedance is to be maintained at around 50 Ω for the differential transmission or 25 Ω for the single end readout, the thickness of the strip is 35 μm and the thickness of the dielectric is 0.9 mm. However, the result calculated by the normal microstrip model is inconsistent with that from the edge-coupled model. The normal microstrip model is based on the calculation of only one strip on the entire PCB, which may be over-simplified since the actual MRPC containing a series of multiple strips. The characteristic impedance is strongly dependent on the geometry, so this simple model may not be suitable for calculating the impedance of the MRPC readout board.

（2） Prototype of MRPC3b

Based on these primary parameters from model calculation, a prototype MRPC3b readout board is designed. Fig.3.18 shows the strip layout of the MRPC3b detector. The strip width is 7 mm with a spacing of 3 mm and a length of 27.6 mm. This design meets the granularity requirements of the CBM TOF for MRPC3b and satisfies the gap size requirements of PCB readout boards under normal conditions (equation-3.23). Fig.3.19 shows a closer view of the end of the readout strips. In order to avoid impedance mismatches from the electronic design, we follow the principles mentioned above, with all

corners less the 45^o to reduce the signal reflecting off the back of the angle. In the case where the pitch of the readout strip we set is unchanged, the thickness of the readout strip and the thickness of the PCB are adjusted so that the impedance of the readout strip is set at around $\sim$25 Ω.

Considering that the MRPC3b detector is used for CBM-TOF, in the region with a rate of around 1 kHz/cm^2. Ultra-thin float glass (280 μm) is used to construct the MRPC3b module, for the reason we have discussed in the chapter2.

The MRPC3b counter is a multi-gap RPC with 32 read out strips which are read out on both sides. From the simulation results, the number and width of gas gaps are related to the avalanche of charge in MRPC. In the design of the prototype, we have chosen two kinds of gas gap widths. One of the design has a gas gap width of 140 μm with a total of 12 gas gaps, and the other has a gas gap width of 230 μm with a total of 10 gas gaps. The gas gap widths are defined by nylon fishing lines of proper diameters. Both counters are arranged in a double-stack configuration mirrored with respect to the central electrode as shown in Fig.3.21, placed between 6 (for 230 μm gas gap) or 7 (for 140 μm gas gap) float glasses plates each 0.28 mm thick. The glass plates have the dimension of 33 $\times$ 27.6 $\times$ 0.028 cm^3, while the active area is 32 $\times$ 27.6 cm^2. In addition, we have designed a 12-gap prototype with a single stack structure. The readout board and other parameters are identical to the prototype with 230 μm gas gap as shown in Fig-3.21 (left). We tested the readout board of the single-stack prototype using a Time

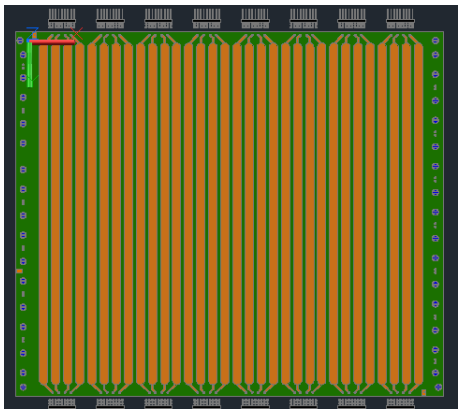

Fig. 3.18 MRPC3b readout electrode and the active area is 32 $\times$ 27.6 cm^2

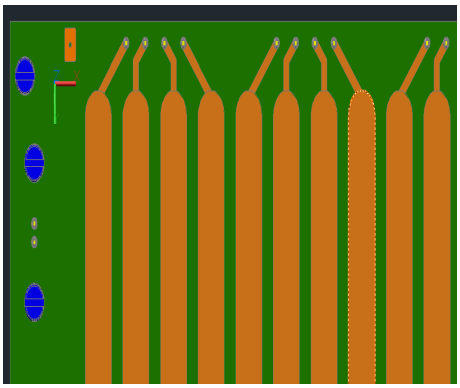

Fig. 3.19 design of the end of readout strip.

Domain Refractometer (TDR), and the results are shown in Fig.3.21. From the figure we can see that the MRPC with impedance matching has a characteristic impedance of the 92 Ω, which is close to our expectation.

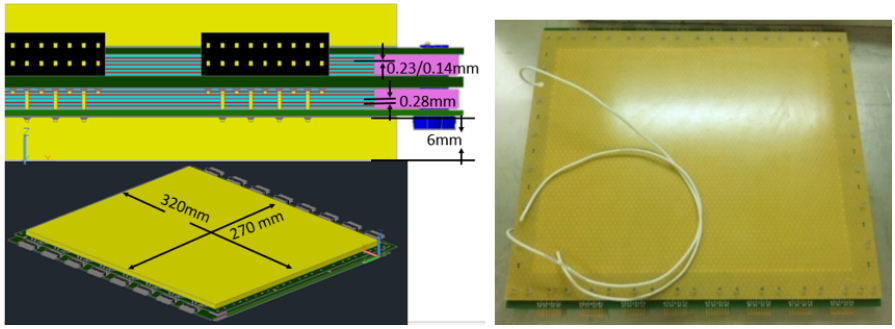

Fig. 3.20 On the left is a double-stacked prototype structure diagram. The photo on the right is finished prototype.

Fig. 3.21 The test results show that the characteristic impedance of the single-stack MRPC is 92 Ω.

3. Optimization

We want to find a way to continue optimizing the impedance of the detector. Based on the reference[69], we performed a similar simulation using the APLAC software. The following sections describe our exploration of impedance simulation methods and the plans that follow. To further optimize our MRPC3b design and obtain an even better impedance matching, the APLAC circuit simulation technology is employed.

（1） APLAC Circuit Simulation Technology

The APLAC harmonic balance / transient circuit simulation engine is a key technology found within the NI AWR Design Environment™. Acquired by AWR back in 2005, the APLAC simulation engine had been used in Nokia product development for many years as its foundry-approved harmonic balance method. Today the APLAC harmonic balance simulation engine is further enhanced by the release of AWR's patented Multi-Rate Harmonic Balance™ (MRHB) technology. MRHB enables users to simulate designs that were previously beyond the reach of the harmonic balance technique, and provides a 5x speed increase when simulating large, complex multi-tone designs[70]. It was used also by us in estimating the transmission line impedance for the MRPC3b prototypes and the predictions were confirmed by the measurements.

（2） Optimization of MRPC3b design by APLAC

For MRPC, each readout unit basically consists of a pair of transmission-line-like parallel conductors exhibiting certain characteristics due to distributed capacitance and inductance along its length. The characteristic impedance of a transmission line is equal to the square root of the ratio of the line inductance per unit length L divided by the line capacitance per unit length C,

$$\begin{aligned} Z_0 &= \sqrt{\frac{L}{C}}; \\ where\ C &= \frac{\varepsilon_0 \varepsilon_r w L}{h}; \end{aligned} \tag{3.24}$$

Through the capacitance per unit length the characteristic impedance depends on the distance between the two conductors (h), the width of metallic layer (w) and the relative dielectric constant of the insulator between them (ε_r). One can derive from Eq-3.24 that the characteristic impedance (Z_0) of this transmission line increases as the conductor spacing h increases and the width w of metallic layer decreases.

The strip width of the readout electrode is determined based on the MRPC architecture signal propagation simulation results described in the previous section. The entire structure of the MRPC, in the transmission line simulation for the signal propagation,

was defined as a multilayer structure consisting of the cathode and anode readout strips separated by the PCB layers, kapton foils, resistive glass electrodes and gas layers for one single stack of the counter (see Fig.3.22). The individual dielectric layers positioned between the anode and cathode readout strips were considered as capacitors coupled in series. In the simulation, the relative dielectric constant of glass, kapton, FR4, gas and other layers is considered as an equivalent dielectric constant, ε_r, and the thickness is h, as shown in the Fig.3.22. The equivalent dielectric constant can be found in Ref-[71]

$$\varepsilon_r = \frac{\varepsilon}{1 + \varepsilon \frac{d_{gas}}{D_{glass}}} \tag{3.25}$$

where ε is the dielectric constant, D_{glass} is the nominal thickness of a single sheet of dielectric material, d_{gas} the average air layer thickness between two dielectric sheets.

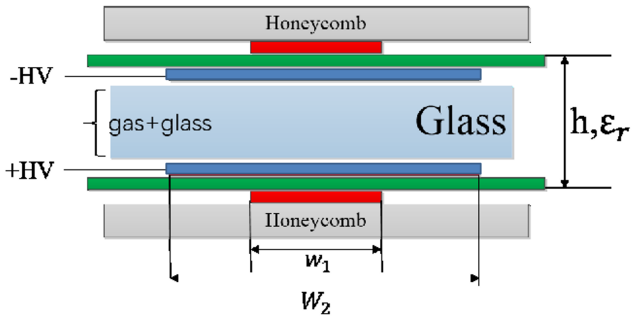

Fig. 3.22 Equivalent detector structure in the simulation.

A differential signal with timing characteristics of 50 ps rise time, 300 ps width and 50 ps fall time was injected at the input of the transmission line. The opposite end of the transmission line was differentially connected to an load resistor with an impedance of Z_L. The input and output signals were recorded for different values of the readout strip width w and height h. Under this model, the circuit of equivalent detector structure in the simulation is shown in Fig.3.22.

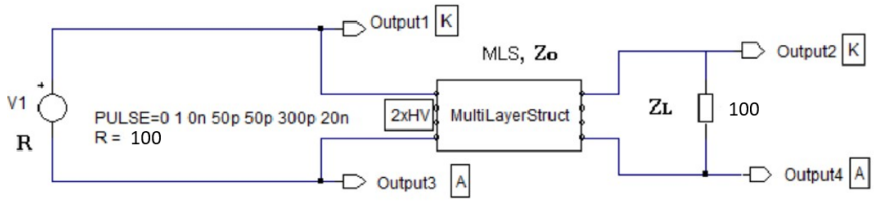

Fig. 3.23 Equivalent schematic diagram of MRPC in the APLAC simulation..

If the impedance of the input and output ends of the transmission line match, i.e.

$$R = Z_0 = Z_L \tag{3.26}$$

there should be no reflection in transmission lines. R is a standard resistors which we can modify the value according to detector's impedance requirements. If we know how much impedance the detector needs to set, this value can be fixed. By modifying other parameters, Z_0 and Z_L, to this resistance value, R, the impedance matching of strips is achieved.

The simulated signal waveforms are picked up from the anode (input - magenta, output - green) and cathode (input - blue,output - red) electrodes, as shown in Fig.3.24. The simulation signals are injected by a pulse generator with an 100 Ω internal resistor on the strip and readout on a 100 Ω load resistor on the other side. The output signals reproduce very well the input ones, without any visible distortions of their shapes and magnitudes, showing that the transmission line is matched to the input/output impedances. The delay of the output signals relative to the input ones is of Δt = 0.65 ns for l = 9.6 cm strip length. This implies a signal propagation velocity along the transmission line of:

$$v_s = \frac{l}{\Delta t} = 14.8\ cm/ns \tag{3.27}$$

Therefore, for a MRPC with 7 mm strip width, 0.280 mm glass thickness, 230 μm gas

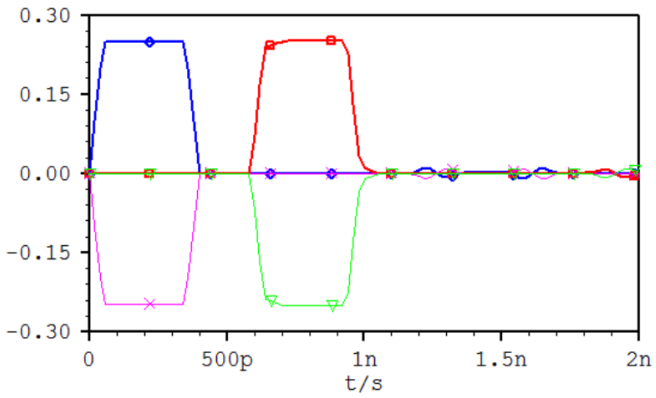

Fig. 3.24 Simulated signals picked up on the anode (input-magenta, output-green) and cathode (input-blue, output-red) electrodes with a matched impedance of 100 Ohms.

gap with five gaps, equivalent thickness h of 2.83 mm, and equivalent glass relative dielectric constant ε_r = 9.1, APLAC simulations predicted a transmission line impedance of Z_0 = 100 Ω . As it was specified above, this value was estimated for a single stack, representing one half of the structure. As the corresponding transmission lines of the two stacks are connected in parallel, the equivalent impedance of a MRPC3b transmission line is $Z_0/2$ = 50 Ω. This value matches the input impedance of the front-end electronics (FEE) used for MRPC3b signal processing, which is based on the PADI chip developed within the CBM-TOF collaboration[39]. The next plan is to build the simula-

tion framework according to the actual MRPC3b detector structure to further optimize the impedance.

3.3 Test on Prototype of MRPC3b

In order to ensure that the MRPC3b modules meet the requirements of particle identification at high rate, the prototypes are tested by cosmic ray in our laboratory at USTC and hadron beam at the BEPC-E3-line. This section presents the results of these prototype MRPC3b.

3.3.1 Analysis Framework

The USTC high energy group has been developing MRPC detector for 20 years. However, the calibration procedure ha not beacome an universal, scalable and modular set of code. Based on the existing USTC calibration program, a new set of data analysis software packages has been developed. It is schematically shown in Fig.3.25. Fig.3.25 (a) shows the process of this data analysis. When we get the data from the DAQ system, the raw data are unpacked by the dedicate ROOT code and transform to a ROOT file containing relevant information accordingly, which is then taken as the input of the calibration code. The entire calibration procedure has three steps, including the T0 reference time calibration, the MRPC calibration and the tracking calibration. The T0 reference time calibration means that first we calibrate the reference time of the whole system. MRPC calibration means that in this step we need to calibrate the clustersize, time slewing, efficiency and time resolution of the detector. The tracking calibration is that the performance of the detector is calibrated by the tracking information established by either an additional tracker system or the MRPC test system itself. However, the code of this 3rd step is still being optimized.

Fig.3.25 (b) shows the software framework. We split the whole analysis program into small software packages. These packages can be called or commented depending on the analysis requirements. This new calibration software has been proven very convenient for data calibration.

3.3.2 NINO System

NINO is an ultra-fast and low-power front-end amplifier/discriminator application-specific integrated circuit (ASIC) designed for the MRPC by the ALICE TOF group[40]. The

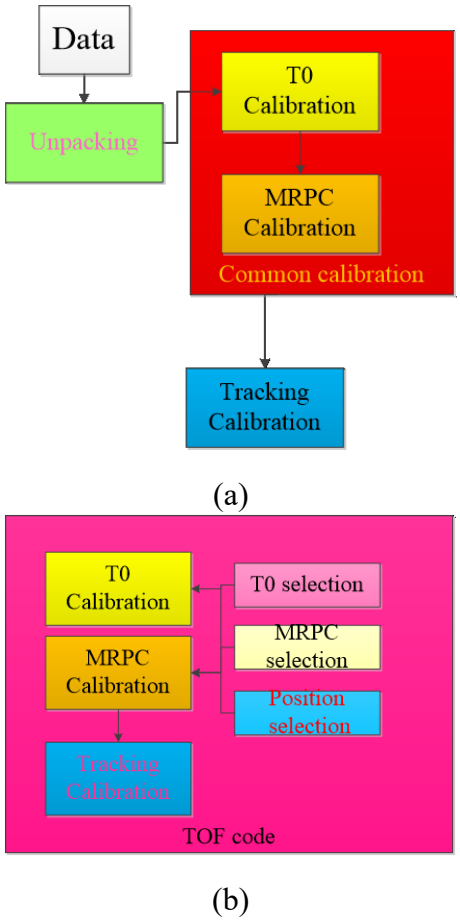

Fig. 3.25 (a) The developed process of data analysis in the calibration, and (b) the details of software package in the program.

chip has 8 channels. Each channel is designed with an amplifier with less than 1 ns peaking time, a discriminator with a minimum detection threshold of 10 fC. The leading edge time jitter of output pulse is less than 25 ps, and the pulse width is dependent on the input signal charge. Each channel consumes 27 mW, and the 8 channels fit in a 2x4 mm^2 ASIC processed by IBM 0.25 μm CMOS technology.

1. NINO used for CBM/STAR eTOF pre-production

（1） Readout Electronics

The NINO front-end electronics (FEE) boards were designed and produced by the Institute of High Energy Physics (IHEP) of the Chinese Academy of Sciences (CAS). The 3D circuit design diagram of the FEE is shown in Fig.3.26 (a)[72]. The FEE comprises of two NINO chips for 16 readout channels. Each FEE module outputs correspondent LVDS signals with the signal charge encoded in their widths (Time Of Threshold (TOT)). The FEE performance test showed that the time accuracy (RMS) of all channels were less than 20 ps[73-75]. Fig.3.26 (b) shows the real image of the FEE PCB, which

was used to build the system during the cosmic ray test and beam test for the counter. The signals from FEE were recorded by a CAEN V1290A TDC[76]. The V1290A TDC

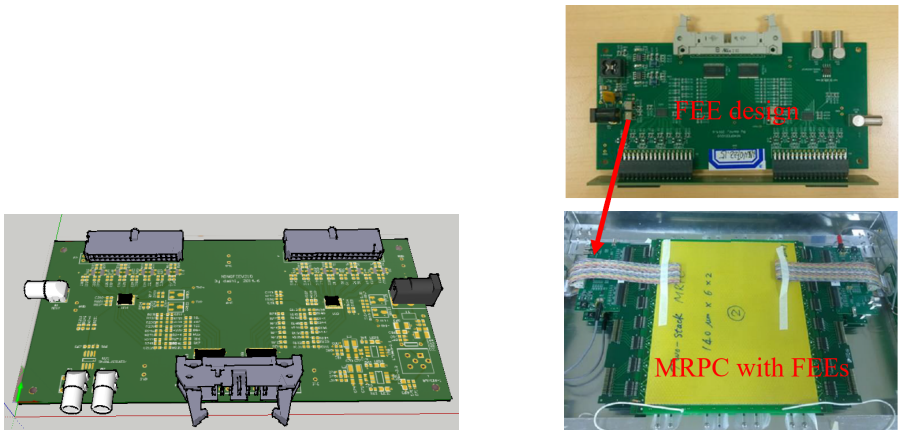

(a) (b)

Fig. 3.26 The conceptual design of the FEE(a). Fig (b) is FEE board and under test detector are equipped with FEE-boards.

can record both leading and trailing edge time of LVDS signal.

（2） Data acquisition (DAQ)

A piece of DAQ code for the NINO system was developed and implemented in the USTC DAQ software framework. It is based on the Labview Software[77] to develop the entire slow control system. Labview (Laboratory Virtual Instrumentation Engineering Workbench) is an engineering software package for applications that require test, measurement, and control with rapid access to hardware and data insights. The DAQ system can control more than 144 channels at the same time. For the NINO system, depending on the test experiment, we increase or decrease the number of TDC according to the number of channels in the system. A Graphical User Interface (GUI) was also implemented to simplify the operation of the test system as shown in Fig-3.27.

（3） Cosmic Ray test stand system

For the prototype MRPC3b, the reference time detector is composed of two plastic scintillator detectors readout from double ends by photomultiplier tubes (PMT). The detector under test is positioned in the middle of the reference time detector as shown in Fig.3.28. The two BC408 plastic scintillators each has a size of 5×20 cm^2 (1 cm thick) are coupled with fast PMT H2431. Fig.3.29 (a) shows the flow chart of the cosmic ray test system. In order to ensure the timing accuracy of the measurement, we first tested the time resolution of the whole system by a fast pulse generator. Fig.3.29 (b) shows the time jitter of this cosmic test stand, which is measured to be 17.8 ps.

Fig. 3.27 GUI of the slow control.

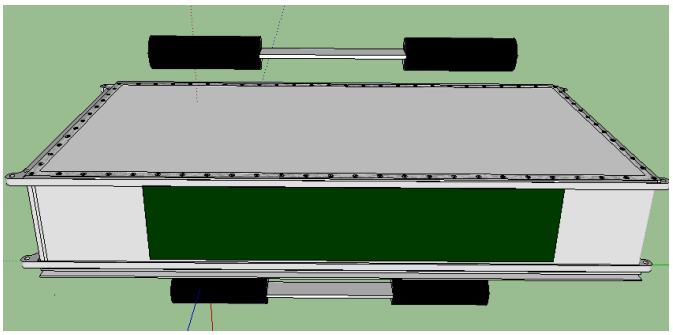

Fig. 3.28 The test stand setup

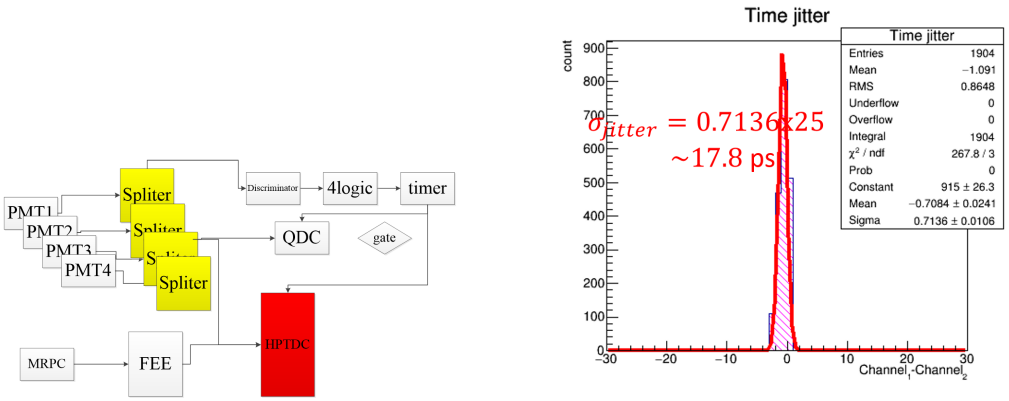

(a) (b)

Fig. 3.29 The electronic system block diagram(a). (b) is the time resolution of NINO test stand system. The LSB is 25 ps.

3.3.3 Basic performance of MRPC3b

In the cosmic ray testing, the impedance of the readout strips for prototype MRPC3b was designed and optimized to 50 Ω, which matches the impedance of FEE. We want to know if the adjustment of the impedance of the prototype is effective. Fig.3.30 (a) shows a typical TOT spectrum from the cosmic test, we can see there is no obviously reflection manifested by multiple peaks. This indicates that the improved design is successful. The impedance of the prototype basically matches that of the FEE. Besides, Fig.3.30 (b) shows the time vs TOT correlation. The time information is represented by the measured TDC (X-axis), with a LSB of 25 ps/bin. The distribution is fitted by a empirical formula with 5 parameters for the further time slewing (T-A) correction. The T-A corrected time is obtained by subtracting the fit value (for a measured TOT) from the measured time. The time distribution ($T_{mrpc} - T_{\mu}$) after the time slewing correction is shown in Fig.3.31 (b). The distribution is fitted with a Gaussian function, which shows a variance, σ_r, of 81.2 ps. The time resolution contains the jitter from the reference time $\sigma(\frac{T1+T2+T3+4}{4} - T_{\mu})$ which should be quadratically subtracted $\sigma_{MRPC} = \sqrt{\sigma_r^2 - \sigma_{T0r}}$, where σ_{MRPC} is the intrinsic time resolution of the MRPC3b prototype, σ_{T0r} is the jitter of reference time, which for this cosmic-ray system is 59 ps, as shown in Fig. 3.30 (a). Then the intrinsic time resolution of the MRPC3b module is measured to be σ_{MRPC} = 55.8 ps, derived from Fig.3.31 (b).

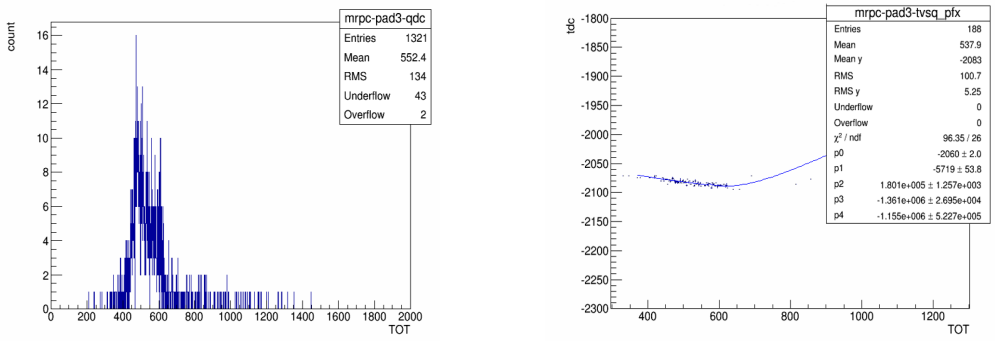

(a) (b)

Fig. 3.30 The TOT spectrum of the prototype MRPC3b (a), and the time vs TOT distribution (b).

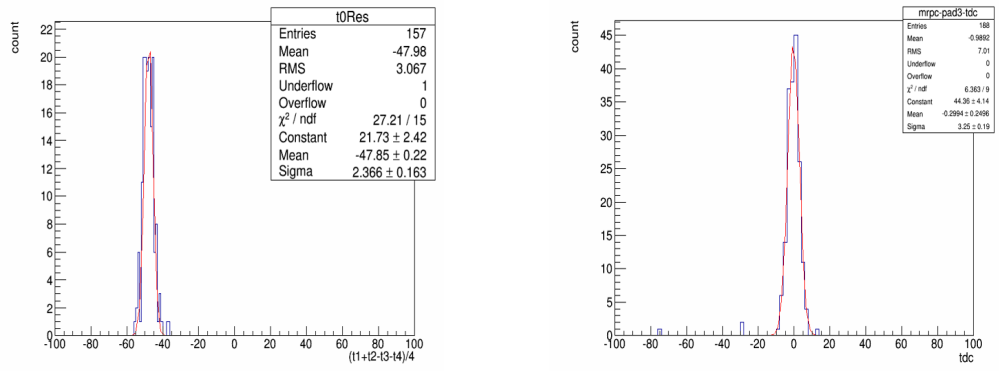

(a) (b)

Fig. 3.31 (a) The reference time distribution with a Gaussian sigma of 59 ps. Each TDC bin (X coordinates) corresponds to 25 ps. (b) The corrected MRPC timing relative to T0.

3.3.4 The Hadron beam test system

1. The IHEP-E3 beam line

The IHEP-E3 beam line at the Beijing Electron-Positron Collider II (BEPCII), IHEP, Beijing, China has been used to study the performance of the CBM TOF MRPC3b STAR eTOF MRPC, CEE-T0 MRPCs and the functionality of new electronics. Secondary particles (mainly protons, $\pi^{-/+}$ and $e^{-/+}$) from an incident electron beam hitting a carbon target[78] were filtered and delivered to the IHEP-E3 line. Among these secondary particles, protons and pions were dominant. The particle momenta were tuned to 700 MeV/c. A Cherenkov detector (C0) and two scintillators (SC1 and SC2, overlapping area of 5 cm $\times$ 5 cm) assembled by the PMTs XP2020 were used for trigger. A coincidence of the two scintillators and anti-coincidence with the Cherenkov detector allowed the selection of protons and pions[79]. Three multi-wire chambers (MWPC) are installed for the measurement of the beam trajectory. However, in this work the Cherenkov detector and MWPC detectors were not included in the beam test system.

2. The test setup

A sketch of the in-beam test setup is shown at the Fig.3.32 (b). The SC1 and SC2 scintillators provide the coincidence trigger, and the four BC420 thin (5 mm thickness) plastic single-end readout scintillators (size: 2 $\times$ 5 cm^2, divided into 2 groups: T1/T2 and T3/T4) coupled with fast PMT H6533 provide the accurate event reference time (Tr0). The inner and outer MRPC modules for CSR-T0 detector are placed with several CBM/STAR-eTOF prototypes, at the downstream position of the test beam. T1 and T2

(a)

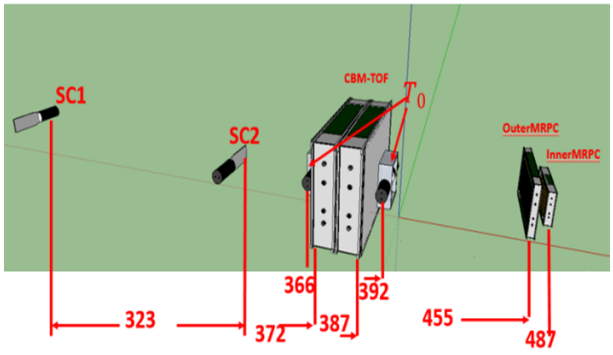

(b)

Fig. 3.32 The photo and schematic plot of the E3 beam line and the test setup. Only the relevant parts, including the trigger detector (SC1 and SC2) and the T0 detector are shown along with the MRPC modules. .

were placed at the upstream position, and T3 and T4 were at the downstream position relative to the CBM/STAR-eTOF prototypes.

3.3.5 Beam Test study on prototype MRPC3b

1. Beam test setup for MRPC3b

Signals from the four PMTs (T0r) are fed to the splitters. The signals of one copy are sent to QDC, while another copy are sent to the discriminator and then recorded by V1290A TDC. The signals of (SC1 and SC2) PMTs are sent to the spliters and discriminator, one copy output is sent to the logic unit C04020, while another copy output signals from the spliters are recorded by V1290A TDC. The MRPC signals are amplified and discriminated by the FEE, then recorded by the V1290A TDC. The difference between leading and trailing-edge timing gives the signal width (TOT) information. The MRPCs were placed in a gas-tight aluminum box, and were fixed on movable platform as shown in Fig.3.32 (a). Four CBM-TOF MRPC detectors were placed in two boxes as in the Fig.3.33. Along the direction of the beam, the gas gap of the first single-stack MRPC

module is 230 μm with 12 gaps, the second one is 230 μm a double-stack detector with 10 gaps each of 140 μm wide, the third and fourth detectors are both double-stack MRPC modules with 12 gas gaps each of 140 μm wide as depicted in Fig.3.33. Unfortunately, during the test, the single-stack 230 μm prototype did not work properly due to frequent discharge. The reason may be that in the strong electric field, ultra-thin glass sheets do not provide a good mechanical support for the MRPC prototype containing 12 gas gaps in a single-stack configuration. The glass sheets deform under the electric force, causing direct contact of the neighboring sheets which in turn generates discharge.

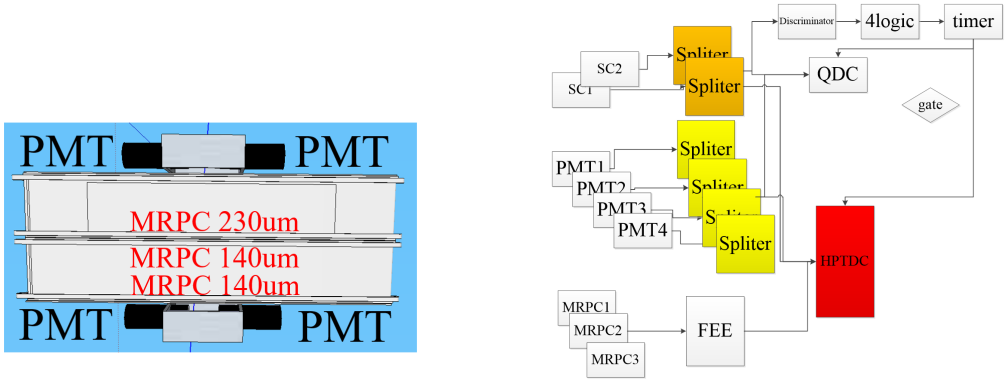

(a) (b)

Fig. 3.33 The image is the top view of setup of the prototype MRPC3b in the beam test. The direction of the beam from the top to the bottom.

2. Particle Selection

Fig.3.34 (a) shows the detail structure of the trigger detectors in the hadron beam test system, which are also used for particle selection. The time of flight between SC1-2 and PMT1-4, as well as the PMT1-4 QDC information (charge spectrum of the T0 detectors) can be used to distinguish particles in this beam test. Fig.3.35 (a) shows the time difference between the two groups of the T0 detector (i.e. (T1+T2) - (T3+T4)). Two peaks are clear seen, denoting the pion (left peak) and proton (right peak) particle respectively. The distributions of the time difference from SC1-SC2 and T0 are fitted with Gaussians, and the mean and variance are obtained. We select the mean$\pm\sigma$ as the confidence interval for the selected particles, which means that 68% of the particles are in this range. The charge spectra of the T0 detectors are fitted with Landau function, and are used to select the needed particles (in Fig.3.36). After these three cuts (see the table-3.1), a typical time difference measurement by the T0 detector is shown in Fig.3.35 (b), for the pion candidates. Thus we find clean hadron samples after the selection cuts.

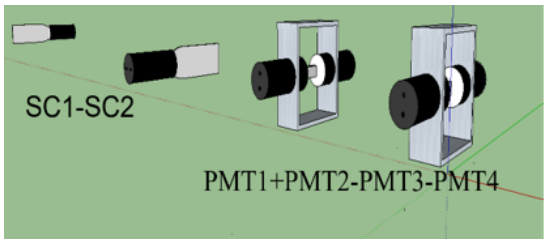

Fig. 3.34 Image (a) is the coincidence trigger reference T0. Four PMTs (1-4) are used as reference time for system.

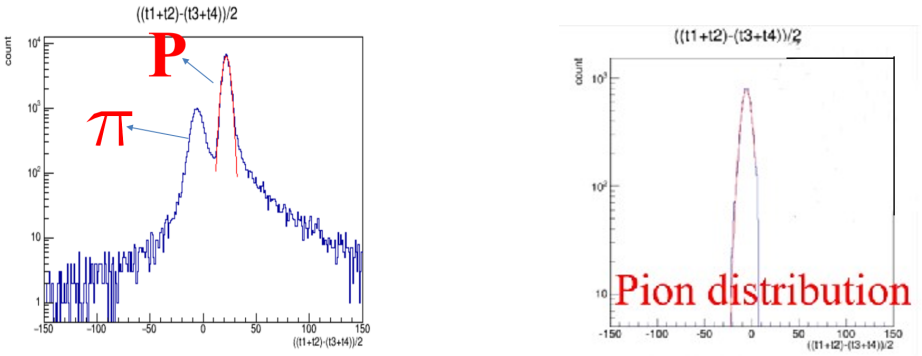

(a) (b)

Fig. 3.35 (a) The leading edge timing distribution of the four PMTs of T0=$\frac{(PMT1+PMT2)-(PMT3+PMT4)}{2}$. (b) The same timing distribution as (a), but with a pion selection cut.

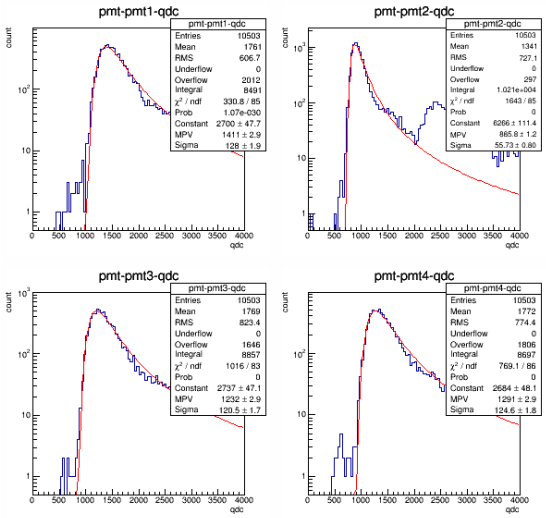

Fig. 3.36 The charge spectra of the T0 detectors are fitted with Landau function, and are used to select the needed particles.

Table 3.1 Selection cuts.

$SC1 - SC2$	time difference from SC1-SC2(mean$\pm\sigma$)
T0	time difference from T0 (mean$\pm\sigma$)
T0	the QDC cut windows of the T0

3. Slewing correction strategy

Leading-edge discrimination is used for time measurement in this beam test system. According to previous experiences and tuning in the lab, the threshold is set to around 200 mV in the beam test. With a fixed-threshold leading-edge discrimination, the time slewing (T-A) effect should be corrected by using the TOT information, which is a good substitute for the signal charge (Q) measurement. Fig.3.37 schematically shows the Time-TOT correlation without correction. The implication is that the time measured varies with the MRPC signal width reaching the TDC. The basic strategy is to use a function to fit this correlation then subtract them from the measured time. An empirical formula-3.28 is used to do the T-A correction. Due to a size limitation of the beam test data, we developed a new procedure to better correct the time. The time-TOT correlation distribution can be separated into several subsets. As shown in Fig.3.37 the empirical function-3.28 is used to fit the data except those in the red circles, where the statistics is poor. The data in the red circles are dealt with a bin-by-bin method, in which the mean time of each TOT bin, rather than the function fitted value, is used in the correction.

$$y = par[0] + \frac{par[1]}{\sqrt{x}} + \frac{par[2]}{x} + \frac{par[3]}{x\sqrt{x}} + \frac{par[4]}{x^2} \tag{3.28}$$

The function-3.28 with 5 parameters are used to fit the most parts of distribution. The slewing correction was done by subtracting this function (outside the red circles) and the mean of each bin (inside the red circles) from the measured time. Fig.5.16 shows the distribution of time difference ($T_{leading} - T_{0r}$) vs TOT after the slewing correction. It can be noticed that corrected time vs. TOT is obviously flatter.

4. Test result of 230 μm-gap MRPC

The movable platform was adjusted so that the beam was set in the center part of the MRPC module. In this beam test we focus on the middle strips of the MRPC to test their operation parameters. The slewing correction is done by using the function fit and bin-by-bin method as mentioned in the previous section. Since the size of pion data sample

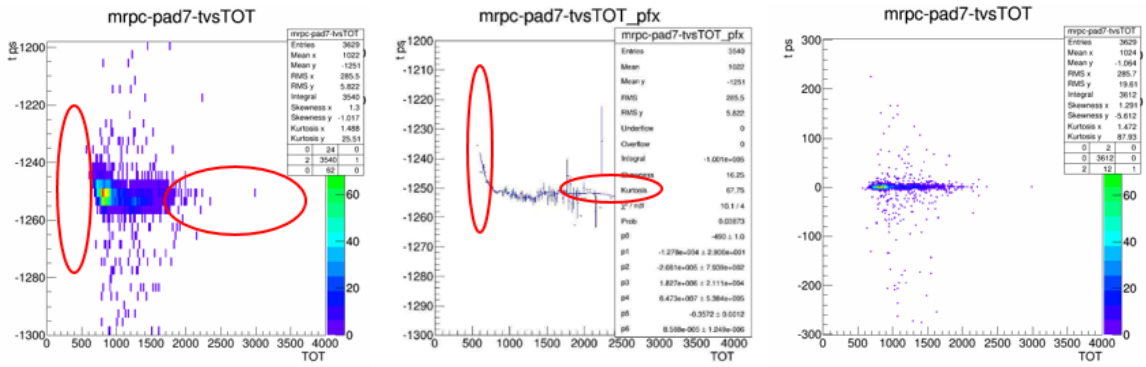

(a) (b) (c)

Fig. 3.37 The process of time slewing. (a) The original time-TOT correlation. (b) The slewing correction strategy. (c) The time-TOT distribution after the slewing correction.

is relatively small, the calibration of MRPC mainly depends on the proton data recorded. It should be noted that the protons are not minimum ionization particles (MIP) with a test beam momentum of 700 MeV/c. After corrected the T-A effect, the time distribution relative to T0 is shown in Fig.3.38 (a). The distribution is fitted with a Gaussian function, and we find a resolution (σ) of 2.827×25∼70.7 ps. Fig.3.38 (b) shows the reference time (T0r) distribution, whose resolution is 44 ps. Thus the intrinsic time resolution $\sigma_{MRPC} = \sqrt{70.7^2 - 44^2}$=55 ps is obtained for protons, including the electronic time jitter and all other systematic uncertainties (e.g. beam position, momentum, and so on).

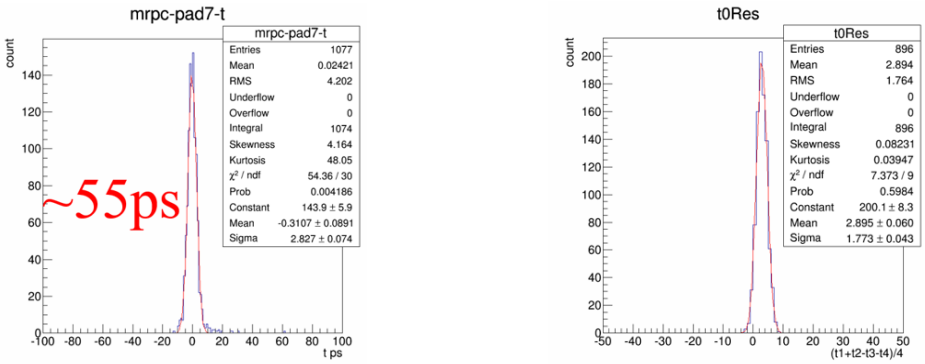

(a) (b)

Fig. 3.38 The measured time distribution of the MRPC prototype of 230μm gas gap. (a) The typical time distribution relative to T0, and (b) the timing jitter of T0.

5. Test Results of 140 μm-gap MRPC

A typical TOT distribution of the 140 μm-gap MRPC is similar to the 230 μm-gap one as shown in Fig-3.39 (a). It can be seen from the figure that although there is a

pronounced tail, the TOT distribution is featured by a main peak, indicating that the impedance matching is still OK and the reflection is suppressed to a certain extent. A similar correction process, by combining function fit and bin-by-bin counting, is applied as that been done for the 230 μm-gap MRPCs. The time resolution of MRPC relative to T0 after the slewing correction is 86.7 ps, as shown in Fig.3.39 (b). Subtracting the reference time jitter, the MRPC's intrinsic time resolution is around 75 ps ($\sigma_{MRPC} = \sqrt{86.7^2 - 44^2}$=75 ps). Illustrated in Fig-3.39 (c) is the reference time distribution whose resolution (Gaussian sigma) is 44 ps.

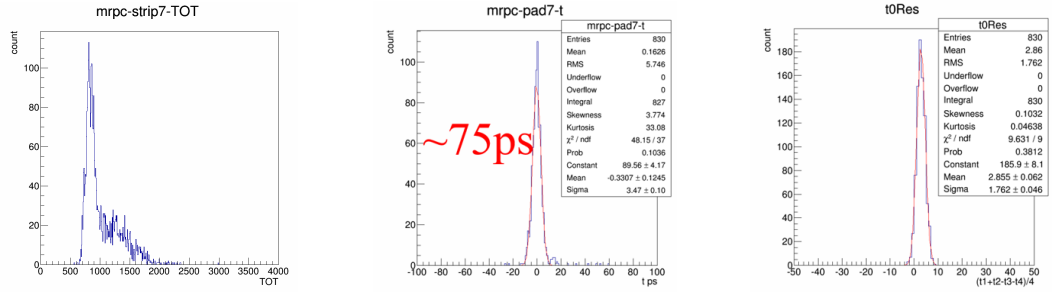

(a) (b) (c)

Fig. 3.39 The measurements of the 140 μm-gap MRPC, including (a) the TOT spectrum, (b) the corrected time relative to T0 and (c) the T0 time resolution.

6. The efficiency plateau & HV scan

To find out the proper working condition for the MRPCs, a wide-range HV scan was done and the efficiency plateau is shown in Fig.3.40 (a) for 140 μm-gap MRPC and (b) for 230 μm-gap MRPC respectively. The detection is defined by the ratio between the number of valid hits on the MRPC and the number of trigger hits provided by the T0 detector. From the plateau, we select 6500 V and 6300 V as the working HVs for the 140 μm-gap and 230 μm-gap MRPCs. These experimental results are consistent with that from the simulation. The efficiency of either type of MRPC reached 95%, fulfilled the requirements of CBM-TOF. Nevertheless the time resolution of the 230 μm-gap MRPC with 10 gaps may be better than the 140 μm-gap with 12 gaps, as also shown in Fig.3.40. Consequently we have chosen the MRPC module with 10 gaps of 230 μm as the baseline design for the CBM TOF.

7. Protection of the HV contact

Occasionally the MRPC module did not work normally due to frequent sparks. For such a situation, we have conducted the following research. Fig.3.41 (a) shows the photo of

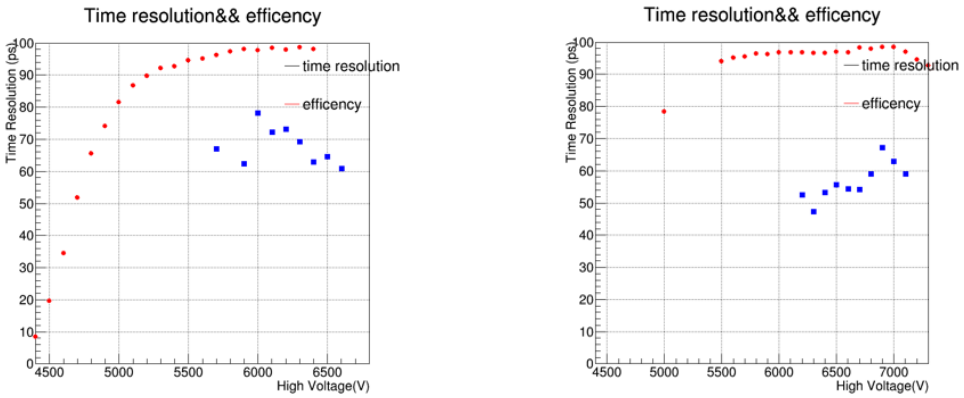

(a) (b)

Fig. 3.40 The measured detection efficiency and time resolution vs. HV, (a) for 140 μm-gap MRPC and (b) for 230 μm-gap MRPC respectively.

the detector that is not working, and the ellipse indicates where the problem occurred. It can be seen that the reason why the prototype does not work is that the discharge occurs near the contact point of the high voltage electrode, so that the two readout plates of the detector are shortened. The possible reason is that the protection insulator around the high voltage electrode is not wide enough, as depicted in Fig.3.41 (b). Therefore, we have proposed two ways to solve this problem. One is to apply silica gel to the edge of the high-voltage electrode to enhance the insulation ability. Another is that we can increase the length of the outermost glass to fully cover the high voltage electrode, through which to play a protective role. Accordingly we have redesigned the blocker as shown in Fig.3.41 (c), where a 0.5 mm deep groove on the surface is added. This groove is used to fix the larger outermost glass so to avoid the discharge of the HV strip , 30 mm long and 4 mm wide, as shown in the center part of the Fig.3.41 (b). In the test following, it was found that increasing the length of the outer glass effectively removes the discharge at the HV strip. The results confirmed our understandings and later on such a design has been used for all CBM TOF MRPC3b detectors.

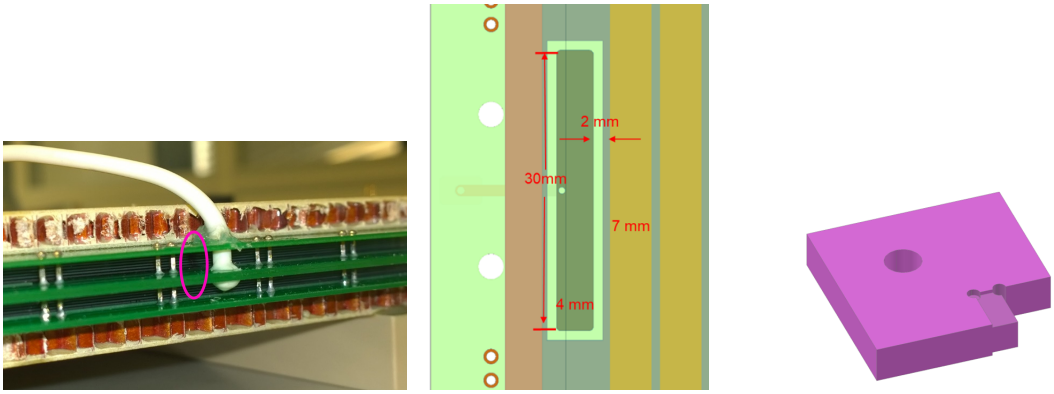

(a) (b) (c)

Fig. 3.41 Image (a) shows the counter damaged by the discharge close to the HV contact. (b) depicts the design of the HV strip. Figure (c) is our newly designed glass blocker with 3D printing technology and a precision of 100 μm.

Chapter 4 CBM/STAR-eTOF Mass production

4.1 The CBM/STAR-eTOF Program

4.1.1 The Motivation

Understanding the QCD phase diagram is one of the important scientific goals for STAR physics experiment. RHIC completed the first phase of the Beam Energy Scan (BES-I) program, using GeV Au+Au collisions to find critical and first-order phase transition boundaries under $\sqrt{s_{NN}}$=200, 62, 39, 27, 19.6, 14.5, 11.5, and 7.7 GeV. The results of the study narrowed the area of interest to the collision energy between 7.7 and 20 GeV. However, to get a clear conclusion, better measurement accuracy and theoretical explanation are also needed. The former can be achieved in the second phase of the BES program (BES-II) in 2019-2020, with the STAR detector upgrades. The installation of an eTOF is accompanied by two more upgrades of the STAR detector targeted towards BES-II physics runs: the inner part of the TPC is upgraded with additional readout channels (iTPC upgrade)[27,80] and the Event Plane Detector (EPD) is added to the experiment[81]. Combined with the iTPC upgrade, the eTOF upgrade will provide additional particle identification capability in the forward direction at STAR, which will especially enhance the Fixed Target program at BES-II. This endcap TOF (eTOF) detector is extending STAR's particle identification (PID) in the intermediate momentum range up to at least a pseudorapidity η of -1.5 in Ref.[81].

The preliminary development of the CBM TOF MRPC has been achieved, but the completion of FAIR will be completed by 2025. During this time, it is urgent to test the performance of the entire TOF system under actual operating conditions. Therefore, FAIR has introduced phase-0 program, including HADES, STAR-BES II, BM@N and mCBM. As one of them, the CBM MRPC will be used in the STAR experiment in 2019 and 2020 as part of the so called FAIR phase-0 program. The CBM collaboration institutions: Heidelberg, Darmstadt, Tsinghua, CCNU, USTC and the STAR collaboration are cooperating in installing, commissioning, and operating a "wheel" of CBM TOF detectors mounted on the inside face of the STAR east side pole tip. As initially designed for a TOF system, the main performances of the CBM MRPCs are sufficient for the STAR eTOF. The simulation result of rate distribution on the STAR eTOF plane is shown in Fig.4.1. It's noted that MRPC3b's rate ability is completely suitable for STAR eTOF due to the particle flux is below 45 Hz/cm^2. Within the STAR eTOF program,

10% of the full CBM TOF system including read-out chain has been installed as eTOF subsystem at STAR/RHIC.

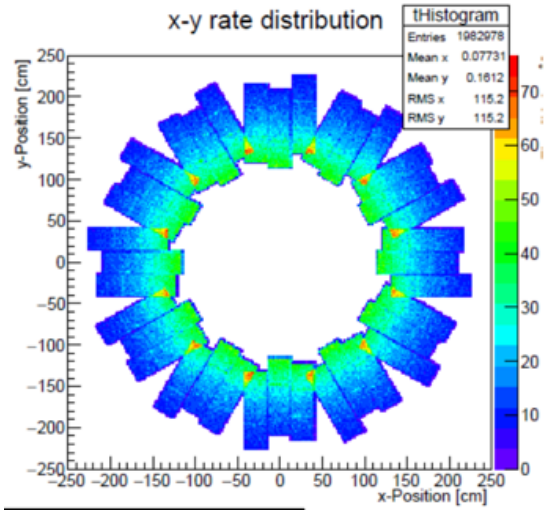

Fig. 4.1 Simulation of eTOF hits and rate distribution[4]

4.2 Mass Production

From 2017, we have started the preparations for the mass production of CBM/STAR eTOF counters at the high energy laboratory of USTC. Since the STAR eTOF upgrade work is to be completed by the end of 2018, we must complete the mass production of 80 MRCP3b counters that USTC is responsible for before this time. After the 29th CBM collaboration meeting, we draw up a detail production schedule as shown in Fig.4.2. Besides, in order to guarantee the quality in the mass production, we have developed a strict Quality Control (QC) in the production process. After the counter production, the preliminary performance test followed by the Quality Assurance (QA) test was carried out. After that, the qualified counters were shipped to the Heidelberg University for module installation. The eTOF module was tested again for QA performance.

I participated in the entire eTOF upgrade process, from the counter prototype development to the final eTOF Module assembly and QA test. In order to improve the test efficiency, two cosmic test stands with different readout systems were built for QA in the laboratory at USTC. One system is developed by USTC electronic group, while the other system uses the third version of the TDC Readout Board (TRB3) system[82] which was developed by GSI, Germany. These two systems are calibrated using different analytical methods. In this section, we will detail discuss the QC and QA processes for the counter mass production, QA results for batch testing, calibration methods for

two cosmic test stand systems, performance of the counters, and the future plan for the counter's improvement.

2018	J	F	M	A	M	J	J	A	S	O	N	D	J
R&D													
Counter component production													
Counter assembly		5	15	20	20	20	10						
Quality assurance		5	16	16	16	16	16	9					
MRPC shipment			20	15	15	15	15						

Fig. 4.2 Mass production schedule of the MRPC3b.

4.2.1 MRPC3b: design and geometry

After years of R&D work, the design of MRPC3b type for CBM TOF is almost finalized. In general, the MRPC3b is a two-stack, 10 gas gap, strip readout MRPC. Fig.4.3 (a) shows its appearance in a real size 3D model. The active area is 32 cm × 27.6 cm, read out by 32 two-end strips. The pitch of the strips is 1 cm. Fig.4.3 (b) shows the readout pattern and the dimensions.

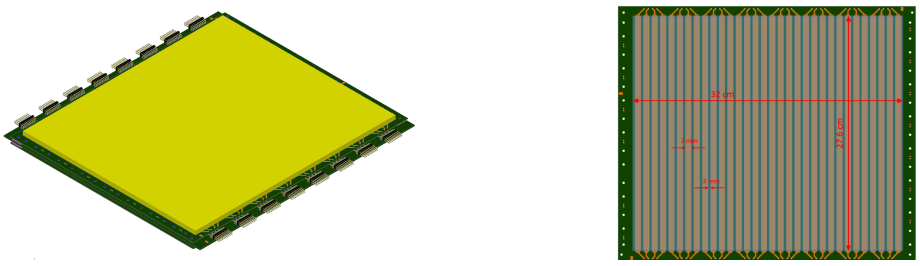

(a) (b)

Fig. 4.3 (a) The appearance of MRPC3b in a real size 3D model and (b) The readout pattern.

(a) (b)

Fig. 4.4 (a) The signal transmission to the middle PCB and the connector to FEE. (b) The HV connection on the bottom PCB.

The resistive plates – thin float glass – are 0.28 mm thick. Six sheets of glass, separated by fishing line of 0.23 mm diameter, generate 5 gas gaps in one stack. The High Voltages are applied on the graphite layers sprayed on the outer surfaces of each stack. The induced signals from the avalanches are collected by the readout strips located on the multilayer printed circuit boards (PCB). The middle PCB collects negative signals from both stacks. The positive signals are collected by the strips on the top and bottom PCBs and transmitted to the middle PCB by pins, as shown in Fig.4.4 (a). The signals are then collected by the Front End Electronics (FEE) boards plugged on the middle PCB directly.

The size of the MRPC is defined by the profile of the middle PCB, which is 354 mm $\times$ 324 mm. The total thickness, including the honeycomb board, is 22 mm.

The HV connection is made by a piece of carbon tape between the graphite layer and a copper pad located on the PCB. The size of the copper pad is 30 mm $\times$ 4 mm. A hole of 32 mm $\times$ 6 mm is made on the Kapton foil which is used for the insulation between the HV layer and the PCB. The HV wire is soldered on the other side of the PCB for better HV protection. The connection between the solder point and the copper pad is inside the PCB. The details can be found in Fig.4.4 (b). The solder point will be protected by CAF4 silicone.

The characteristic impendence was carefully calculated and designed to be 50 Ω differential. The impendence of the transmission line between the strip ends and the readout connector is designed to be 25 Ω to GND, which is also 50 Ω differential. (The GND layer is not indicated in Fig.4.4 (a).)

4.2.2 Quality Control of the MRPC3b counter Mass Production

In addition to the performance check after assembly, the QC procedure during production is equally important. A diagram of the QC procedure for each production stage is shown in Fig.4.5. The quality of all components and manufacturing steps are constantly monitored and recorded in the MRPC3b production data base. This includes step-by-step MRPC production manual, flow diagram of MRPC quality control, manufacture cards, check cards, manufacture log sheets and record tables (shown in Fig.4.6) for test results.

1. Material check

As a gaseous detector, the cleanness, smoothness and planarity are the key characteristics for the material. These qualities, including the mechanical dimensions, are carefully inspected during the mass production.

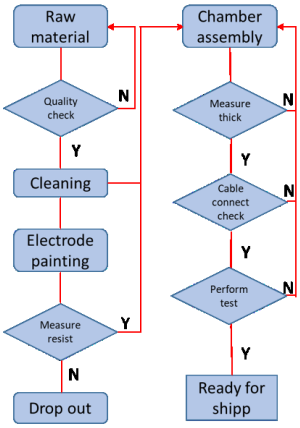

Fig. 4.5 The flow diagram of QC&QA at various production stages.

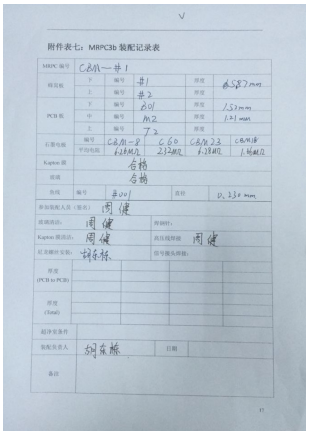

Fig. 4.6 MRPC assembly record for the mass production.

（1） Honeycomb board

- Flatness check. Put the honeycomb board on the clean glass platform. Check if all the corners and edges touch the platform tightly. Both sides of the honeycomb must be checked.
- Label. Give the flat honeycomb a unique ID No. Write the ID directly on the board with a marker.
- Clean. Clean the honeycomb board with alcohol.
- Measure. Measure the thickness of board with a vernier caliper at 8 points. The number of the positions is indicated in Fig.4.7. Fill the measured results into the Table “Honeycomb board check record”.

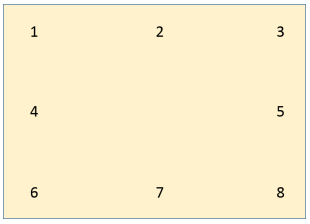

Fig. 4.7 The definition of the position ID.

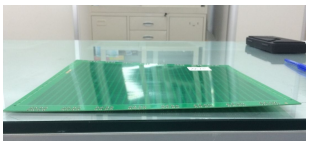

Fig. 4.8 Unqualified PCB found in the mass production.

（2） PCB

- Quality check. Check the surface of the copper for scratches, defects and stains. Check the size of the screw holes, the solder holes. Fig.4.8 shows an unqualified PCB readout board which is bent.
- Clean. Clean the PCBs with alcohol.
- Label. Give the PCB a unique ID No. starting with B-, M-, T-, respectively. Write the ID directly on the board with a marker.
- Measure. Measure the thickness of board with a vernier caliper at 8 points. Fill the measured results into the Table “PCB check record”.

（3） Glass

- Label. Glass is labeled on each package (20 pieces in one package).
- Measure. Glass is measured by 5 samples over one package. The size is checked with a “glass size check TOOL”. The thickness is measured by a micrometer at 8 positions. Fill the results into the Table “Glass check record”.
- Quality check. Check the surface quality of each piece of the glass for scratches and defects.
- Clean. Clean the glass with hot steam and alcohol.

（4） Fishing line

Measure the diameter of fishing line with micrometer. Measure on 10 sample points for each roll of fishing line. Fill the results into the Table “Fishing line diameter record”.

（5） Graphite layer

Measure the surface resistivity of the graphite spray on the glass. Measure on 9 sample points and fill the results into the Table “Electrode surface resistivity record”.

2. Check during assembly

In order to guarantee the quality of the detectors, the clean room has been upgraded. Currently we have a clean room (Fig.4.9) of 100 m^2 with a cleanness level of 100 k. The mounting table has additional air drains which improves the cleanness level by an order of magnitude. The temperature and humidity of the room is kept stable at 22 $\pm 2\ ^{o}$C and $\leqslant$40%, respectively. The material is cleaned and moved to the clean room for the counter assembling. The Check steps for the assembly are listed below and the

results are filled in the “MRPC assembly record” Table(as shown in the Fig.4.6) for each MRPC.

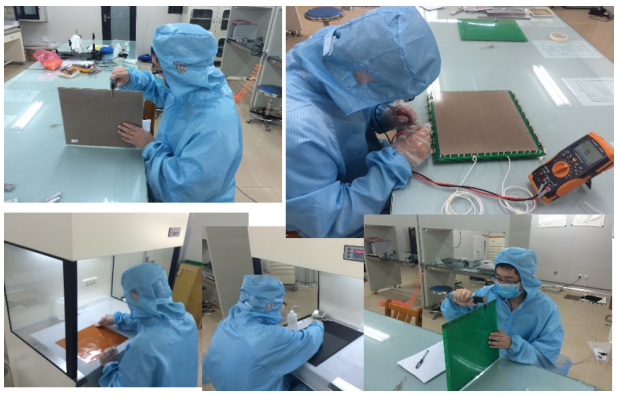

Fig. 4.9 Manufacturing MRPCs in the clean room and assembling MRPC on the clean desk.

- Thickness check before soldering pins. Measure the thickness between the Top and Bottom PCBs with a vernier caliper along four edges. Check the possible reasons if the value is different than 9.66±0.3 mm.
- Electrical connection check. After finished soldering the pins and connectors, check the electrical connections with a multimeter.

3. Performance check

After the detector assembly, the MRPCs must pass a performance check with cosmic ray.

（1） Gas conditioning

Install the MRPC in the gas tight box for cosmic ray test. Connect the FEE cards, low voltage (LV) and HV connections. Supply the box with the gas mixture contains Freon 95% + iso-C_4H_{10} 5%. Make sure that the system is gas tight.

（2） HV training

After 24 hours of gas conditioning, the MRPC can be trained with HV. Tune the voltage up slowly and monitor the current. Set the voltage to ±6.4 kV with current lower than 100 nA.

（3） Noise rate

After 24 hours of HV training, check the noise rate on each FEE channel. Record the dark current of the MRPC and measure the noise rate channel by channel.

At this point, the QC process of MRPC3b is completed. For the MRPC3b QC procedure, we design a QRcode which records the information about the assembly process

as shown in Fig.4.10. The QR-code was glued on the detector surface containing a link with the content of the MRPC3b data base .

Fig. 4.10 Qrcode for the mass production.

4.2.3 Quality Control of Module in Mass Production

When the detector of MRPC3a and MRPC3b are shipped to Heidelberg University, we unpacked these boxes and take these detector into the clean room. Then we will follow the flow diagram (Fig.4.11) to assemble the counters into Modules. Each step is performed in strict accordance with the process table. The differences between MRPC3a

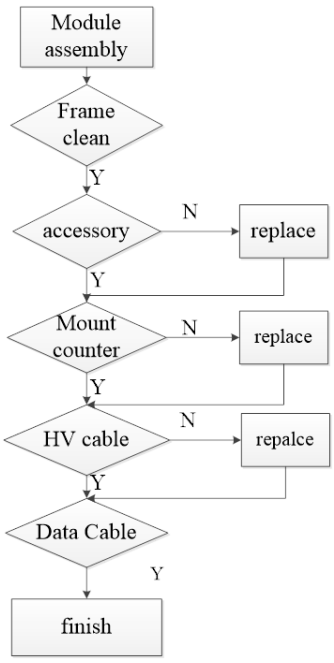

Fig. 4.11 The assembly flowchart for eTOF module.

and MRPC3b are shown in the Fig.4.12. The biggest difference of this two kinds of counter is the glass, MRPC3a uses the low resistance glass, but MRPC3b uses the ultra-

thin float glass, due to their operation at different rate region. Second is that the number of the gas gap. MRPC3a has eight gas gaps, but MRPC3b has ten gas gaps.

Parameter		MRPC3a	MRPC3b
		Double-stack	Double-stack
Glass	Type	Low resistance glass	ultra-thin float
	Size	330 x 276	330 x 276 x 0.28 mm
Gaps	Size	0.25mm	0.230 mm
	Number	4 x2	5 x 2
Readout strips		(0.7 cm + 0.3 cm) x 32 ,double-end strip readout	(0.7 cm + 0.3 cm) x 32 ,double-end strip readout
Impedance		~50 Ω	50 Ω differential signal to PADI
Active area		32 cm x 27.6 cm	32 cm x 27.6 cm
Detector size		360 x 338 x 26 mm	354 x 324 x 22 mm

Difference:
Glass:
Material
(low resistance glass (mrpc3a)
ultra-thin float glass (mrpc3b));
Size;
Gaps number:

MRPC3a :
36 counters for eTOF.

MRPC3b:
72 counters for eTOF.

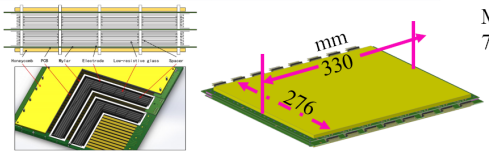

Fig. 4.12 The parameters of both counters

（1） Checking counter

Every counter taken from the box is inspected to check if the detector is damaged during transportation. Among the 108 counters, we found a counter similar to the one shown in Fig.4.13, the high-voltage line damaged counter, this counter will not be used for module assembly.

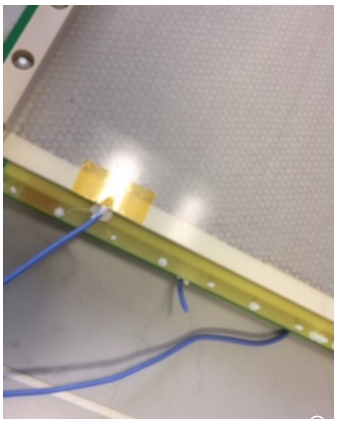

Fig. 4.13 In the course of transportation, the high voltage line breaks.

（2） Checking PADI FEE

Each PADI FEE has a corresponding number, and we record the number of each PADI FEE. The number of PADI inserted on the left and right sides of the counter is also recorded, and the PADI number information corresponding to the counter is entered into the database.

（3） Fix the plastic bar

These counters are fixed with the plastic bar which is used to fix the detector into the Module. The two kinds of MRPC use different ways to fix the plastic bar see Fig.4.14. MRPC3b counter glues the plastic bar to the detector's honeycomb board. MRPC3a screws the plastic bar on the surface of the honeycomb board. The plastic bar needs to be cleaned with alcohol before it is fixed.

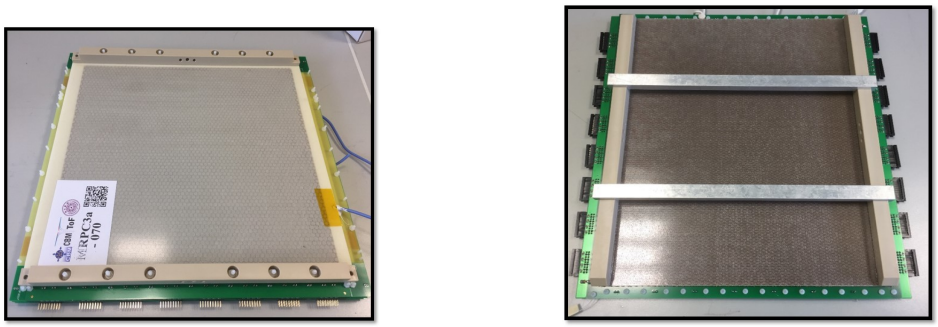

(a) (b)

Fig. 4.14 The photo shows two kinds of MRPC. (a) is MRPC3a. (b) is MRPC3b.

（4） Frame clean

The counter of eTOF will be installed in the aluminum case as shown in Fig.4.15. Every part of the aluminum box is cleaned with alcohol. The cover of the aluminum box is cleaned with an ultrasonic cleaner and then cleaned with alcohol.

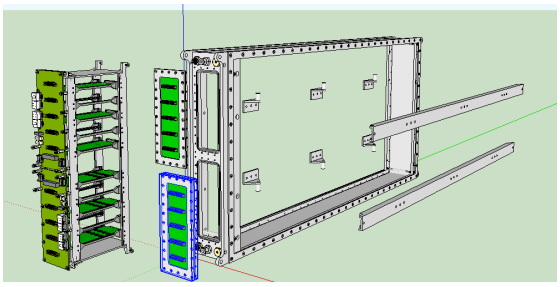

Fig. 4.15 Exploded view of the eTOF module box.

（5） HV cable

Three counters of the same type will be placed in each aluminum box, and the positive high voltages cable of the three counters are inserted into the same high voltage connector on the aluminum box as shown in Fig.4.16. The negative high voltage is inserted in the box of another high voltage connector.

（6） Data cable

The data line is the top priority of our inspection. There will be two data cable interfaces on each FEE, one of which is the interface labeled SPI and the other is unmarked. The

Fig. 4.16 high voltage connector.

aluminum box also has two connectors on the adapter board, one of which is also labeled SPI. The Feed through board mounted on the aluminum box also has two interfaces, one of which is also labeled SPI. The correct connection of the data cable is that the interface marked with SPI on the FEE is connected to the SPI interface marked on the Feed through board through the data cable. We check each module three times to make sure the connection is correct.

At this point, we have completed the QC part of the mass production of the eTOF Module. The entire eTOF wheel will use 36 MRPC3a detectors and 72 MRPC3b detectors. Fig.4.17 (a) and (b) show the module diagram after the installation. It took us about one year to complete the installation of this eTOF wheel. Fig.4.18 shows us the photos of all the assembled eTOF module.

(a) (b)

Fig. 4.17 eTOF module assembled by MRPC3a (a) and MRPC3b (b).

Fig. 4.18 Actual picture of 36 modules after assembly in the clean room.

4.2.4 STAR/CBM-eTOF Componet Database

Scientific experiments in fields such as High energy physics experiment typically requires accumulating, storing, and processing very large amounts of information. Handling informations related to the status of the detectors at the time of the acquired event is crucial in an experiment. Database applications that use multi-terabyte datasets are becoming increasingly important for scientific fields such as Heavy ion physics, astronomy and biology. Scientific databases are particularly suited for the application of automated design techniques, because of their data volume and the complexity of the scientific workloads.

In large-scale scientific databases, Motivating a physicist to use a sophisticated database system in his/her data analysis program could be a rather challenging task. Even if changing to a database will make their job easier, most people would rather fall back on old , familiar ways. Indeed. why should a complicated database system be used. In this section, I will describe the database design and application for CBM/STAR eTOF mass production. The CBM/STAR eTOF component database is based on software packages i.e.Sqlite3, Fairroot, FairDB, nodejs, html and jsroot[83-84]. It will be used to store the basic information accumulated during mass production.

1. Previous research

For the FAIR phase 0 program, CBM/STAR eTOF consists of several parts including module, detector, electrons. Each part has its own information. Accessing info of particular electronics among hundreds would be a difficult task. An individual has to manually search through all the records of counter or other parts information till they

find the relevant counter, and accessing electronic info on eTOF wheel would be more complicated.

Before Denis Bertini re-design the FairRoot Virtual Database(FairDB), the FairROOT framework uses the Hades Runtime Database Library[85] as third-party code to initialize parameter from ascii or ROOT[86] input files. The FairROOT framework is an object oriented simulation, reconstruction and data analysis framework based on ROOT[87] and it is the standard simulation, reconstruction and data analysis framework for the FAIR experiments at GSI Darmstadt. The FairROOT framework for simulation and analysis[85] should be able to handle a large amount of different parameters and their variation in time.

2. FairDB

The FairROOT Virtual Database[88-89], FairDB, provides the end-user a way of centralized data storage for the FAIR experiments. It is based on the FairROOT framework and extends the built-in database support of an underlying ROOT framework by creating a layer of abstraction to store and access data using different database technologies. Fig.4.19 depicts the architecture of the FairDB and the integration of the FairDB into the FairROOT scientific framework. Presently the FairDB (being based on the ROOT frame-work's TSQLServer) supports following relational database backends, and it provides the user with a well-defined and uniform API for database manipulation. Using internally the ROOT TSQLServer class[87], the same user code can be executed independently on SQL database engine such as Oracle, MySQL, PostGresSQL and even SQLite. The FairROOT virtual parameter database is able to access FairDB to read and display the stored data for given detector systems, ROOT binary files, detector configurations etc. The rollback functionality allows to discard the latest state of the database and revert it to the previous consistent state based on the database state journaling.

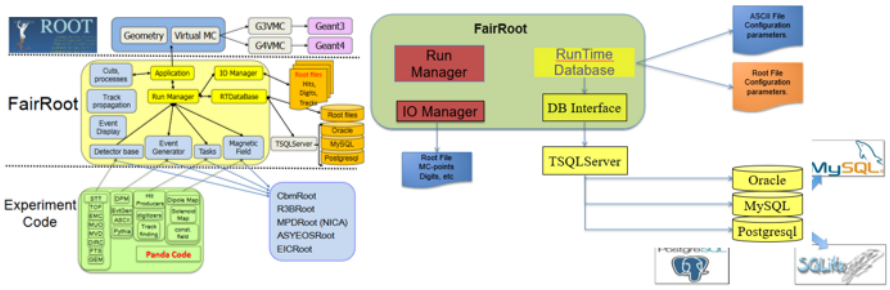

Fig. 4.19 FairDB design framework

3. Conceptual design

（1） Database Management System (DBMS)

Database is a structured system to put your data in that imposes rules upon that data, and the rules are yours, because the importance of these problems changes based on your needs. Maybe your problem is the size, while someone else has a smaller amount of data where the sensitivity is a high concern. It's the things you can't see that are going on in the background; the security, the enforced integrity of the data, the ability to get to it fast and get to it reliably, the robustness; serving lots of people at the same time and even correctly survive crashes and hardware issues without corrupting the data. And that's what we need to do here; understand how to describe our structure and define those rules, so all these invisible things will actually happen.

We often mistakenly say our database is Oracle, MySQL, SQL Server, MongoDB. But, they aren't databases, they are database management systems (DBMS). The DBMS is the software that would be installed on your personal computer or on a server, then you would use it to manage one or more database. The database has your actual data and the rules about that data, while the DBMS is the program that surrounds and manages your actual data, and it enforces the rules you specified on your data. The rules could be the type of the data, like integer or string, or the relationship between them. In many organizations, you don't just have multiple databases but multiple DBMS. Sometimes it's because one DBMS is better at something than the other. For the design of our database, we are going to focus on the relational database management systems (RDBMS).

（2） Conceptual design

Our database is designed to match the experimental requirements, so it needs to contain some important features. The following points were considered important for the design of the database. The component database should have a GUI to enter data, should be easy to operate, should be conveniently modifiable, should be able to store images and histograms, should display histograms in the browser, and should be based on CBMROOT[90] or FairROOT.

Based on these ideas, we put forward a conceptual design of the CBM-TOF component database. Fig.4.20 illustrates the above ideal process in a simplified sequence flow diagram. The CBM/STAR eTOF component database separates the connectivity to the specific DBMS into a front-end and a back-end. The front-end allows the stored data visualization in the user-defined format. For example the users are accessing the Web Application to view (all users) and manage (users with appropriate access permis-

sions) data. The back-end implements the platform and database specific interaction with the underlying DBMS. The front-end part exposes the application programming interfaces to implement the user defined relational data model. It provides the means of the platform independent database connectivity, permission management and the object relational mapping, e.g. allows to execute the queries to the database tables and returns the C++ objects which can be accessed within the ROOT framework. Data are stored in the relational tables of a Sqlite3 engine. The front-end connect back-end by Nodejs software. The entire back-end driven by consists of two parts, one is FairDB and the other is SQlite3. For the back-end, FairDB connect with the SQlite by two ways. One is use the CERN ROOT internally TSQLServer class to connect FairDB, the other is use the Nodejs that be use to connect with the front-end.

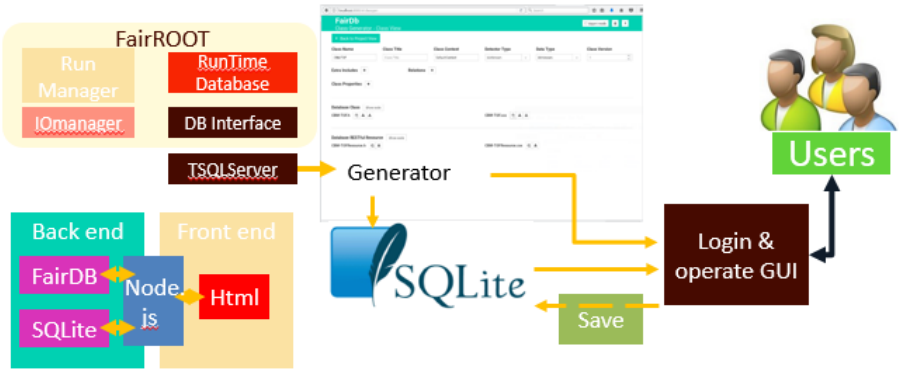

Fig. 4.20 Conceptual design of the CBM/STAR eTOF database

（3） CBM/STAR eTOF database

The CBM-TOF need a web server to store, process and deliver web pages to clients. The communication between client and server takes place using the Node.js. It has a built-in module called HTTP, which allows Node.js to transfer data over the Hyper Text Transfer Protocol (HTTP). Pages delivered are most frequently HTML documents, which may include images, submitting web forms, uploading of files, style sheets and scripts in addition to the text content. So the basic function of the server should be include the features mentioned above. While the primary function is to serve content, a full implementation of HTTP also includes ways of receiving content from clients. A user agent, commonly a web browser or web crawler, initiates communication by making a request for a specific resource using HTTP and the server responds with the content of that resource or an error message if unable to do so.

The structure of the CBM/STAR eTOF database is developed based on the FairDB kernel. A graphical user interface for accessing and editing data has been built using html scripting language and nodejs technology. The GUI is accessible through a vari-

ety of browsers and regardless of operating system, though it has been most intensively tested using Mozilla Firefox and Google Chrome. Maintaining Database overcomes this problems. Users can just type in and get all the information regarding the relevant module quickly without any effort. Databases organize data items and maintain relationships between them in order to facilitate effective information sharing across an organization.

For this database operation interface, it is composed of the main interface and the functional interface see in Fig.4.21. The main GUI of the component database consist of 6 parts including login webpage, main webpage, generator webpage, enter data webpage, query webpage and Qrcode webpage as shown in Fig.4.22 and Fig.4.23. In addition, we have designed a webpage that can show the generator, enter data webpage, query webpage at the same time and have designed a webpage that introduce the CBM-TOF group.

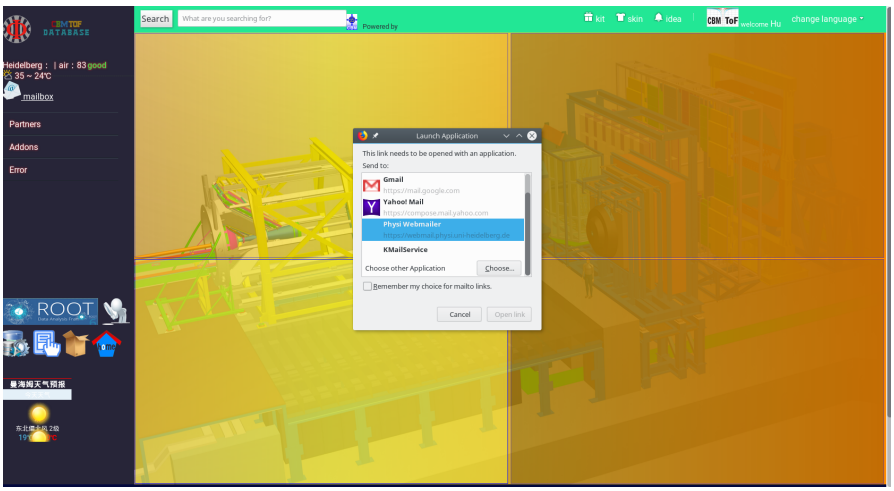

Fig. 4.21 main webpage of the database website.

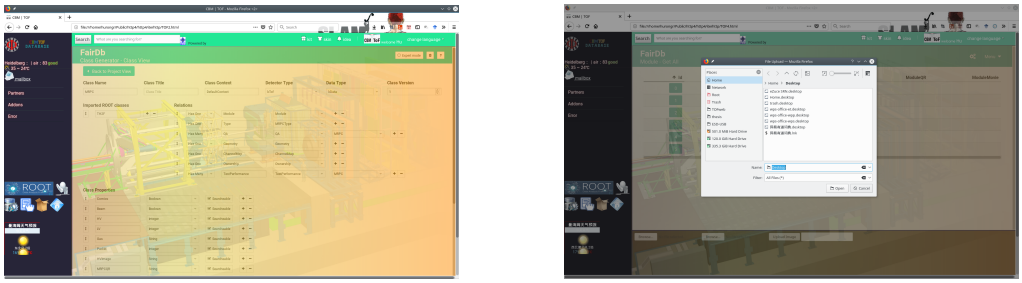

(a) (b)

Fig. 4.22 The generator webpage (a) and enter data webpage (b).

It provides the feature that the database code can be directly generated through the webpage that generator webpage based on the FairDB kernel and when install this code,

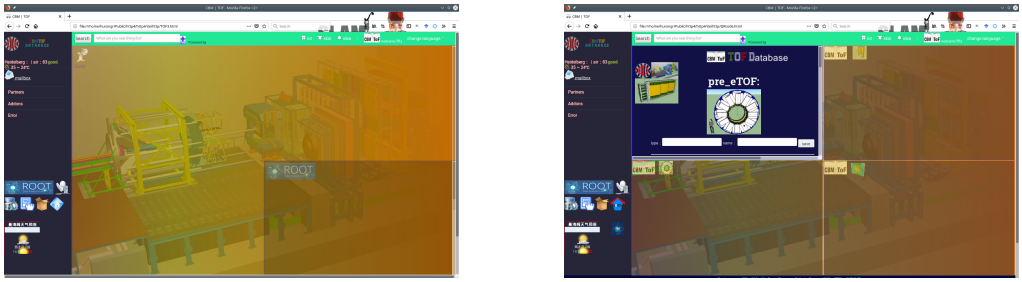

(a) (b)

Fig. 4.23 (a) is qurey webpage and (b) is the data display page.

it will make a link with the Fairoot ,SQlite and the front-end. Users can implemented though login the webpage enter the data into the database.

4.3 Quality Assurance for CBM/STAR-eTOF

The QA result of each counter determines whether it can be used for the assembly of CBM/STAR eTOF. To ensure a good quality for each counter, we strictly control the QA process through three cosmic-ray test systems,with the readout electronics and DAQ (1) developed by the USTC group, or based on (2) the TRB3 system and (3) the GET4 digitalization system (at Heidelberg University) respectively. All of them use PADI based FEE. The USTC readout electronics system and the TRB3 readout electronic system use FPGA TDC (FTDC) as the readout unit, while the GET4 readout electronic system uses a TDC based on an application specific integrated circuit (ASIC). In addition, the DAQ and calibration methods of the three systems are different. The calibration method of USTC electronics is to perform data analysis by mutual calibration between counters. And the TRB3 system and the GET4 system are calibrated by the method of track reconstruction. The track reconstruction method improves the efficiency of data usage and allows the counter to be calibrated as a whole. The QA processes for the three systems are discussed in detail in this section.

4.3.1 PADI

PADI is a general purpose PreAmplifier-Discriminator (PADI) ASIC to be used as the FEE for the readout of timing RPC detectors, designed by the CBM-TOF group[39]. Since an intrinsic time resolution of $\sigma_{tD} < 50$ ps is required for the MRPC, for the preamplifier-discriminator stage the contribution to time jitter should not exceed $\sigma_{tE} < 15$ ps.

The time-of-flight wall of the CBM detector will comprise about 100000 channels in a 120 m^2 area. In order to reduce the total cost and the power consumption, the design and use of customized ASIC becomes mandatory. The design of PADI is derived from the NINO architecture which is an ASIC realization of a low power FEE used for the ALICE TOF. For a simple comparison between TOT and Q measurement for time slewing correction, it added a supplementary buffer block to obtain both information's time and charge. The whole design was matched for CMOS 0.18 μm IMEC technology, and the layout of the chips is shown in Fig.4.24.

For the ALICE TOF, HPTDC ASIC was used for the time digitizer. The HPTDC chip developed by CERN can only measure the leading and trailing edges of an input pulses with a widths greater than 6 ns. The NINO chip has a stretcher before the driver that outputs the LVDS signal. The pulse stretcher increases the pulse width by 10 ns. However, the requirement of the CBM experiment is that the resolution of the FPGA TDC double pulse is better than 5 ns, so the output signal of the PADI chip is not extended.

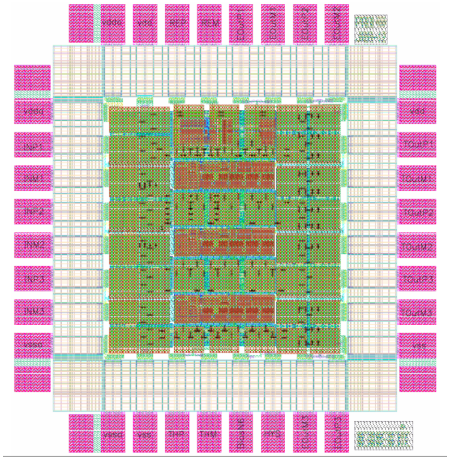

Fig. 4.24 PADI layout

1 PADI FEE

The FEE board is based on the 10th generation PADI (PADIx) chip for MRPC signal processing. Fig.4.25 (a) shows the design layout of the FEE, while Fig.4.25 (b) is the real photo. Each FEE board has 4 PADI chips that can deal with 32 channels. The threshold can be set by the internal SPI DAC (Digital to analog converter) interface. The SPI interface (Serial peripheral interface) is very simple and robust, which is currently used in many types of micro controllers. It simplify the implementation of PADI test/control equipment. SPI DAC allows differential signal transmitting, to SE (single-ended) converter on board. The SPI master provides a simple CPU inter-

face which includes a TXD (Transmit(tx) Data) register for sending data and an RXD (Receive(rx) Data) register for receiving data.

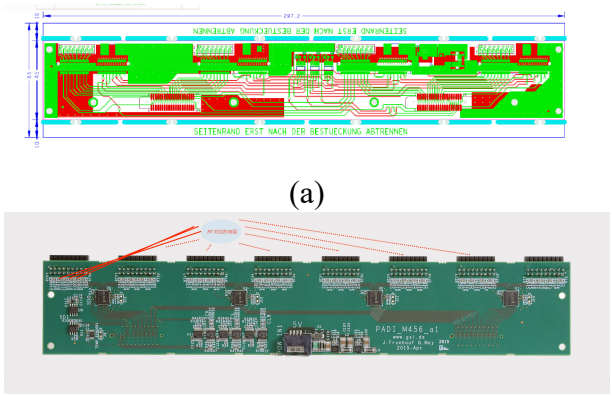

(a)

(b)

Fig. 4.25 Design layout of the PADI FEE (a), and the real FEE board (b).

4.3.2 USTC Readout Electronics System

1. Readout electronics at USTC

（1） Electronics

For the QA in the mass production, the USTC electronics group developed an electronic and DAQ system as seen in Fig.4.26. This quality evaluation electronics is based on the peripheral component interconnect extensions for instrumentation (PXI) platform. The fast timing information is recorded by the high precision FPGA based TDC. The prevailing implementation principle of most high resolution FPGA TDCs is combing coarse time stamp with fine time measurement. A counter provides coarse time resolution for easily adjusting dynamic range, and a tapped delay line (TDL) is used to perform time interpolation within a coarse clock period to acquire better resolution. FPGA underlying resources (e.g., carry logic and Lookup Table (LUT) in a slice of Xilinx's FPGA) are widely utilized to perform the interpolation[91]. The time jitter of this DAQ system without the FEE is better than 20 ps, see Fig.4.27 (a). Fig.4.27 (b) shows the uniformity of 32 channels in the electronics system. As can be seen from the plot, the uniformity of the whole electronics is satisfactory. The reason why the time jitter of several channels in Fig.4.27 (b) is large (25 ps) is that there is a bug with the format transcoding during data decompression. In the actual batch test, this bug has been resolved.

（2） Test stand

This DAQ system is used for the batch test of CBM-TOF MRPC3b counters at USTC. The cosmic ray test stand is shown in the Fig.4.26 (b). The discriminated MRPC signals

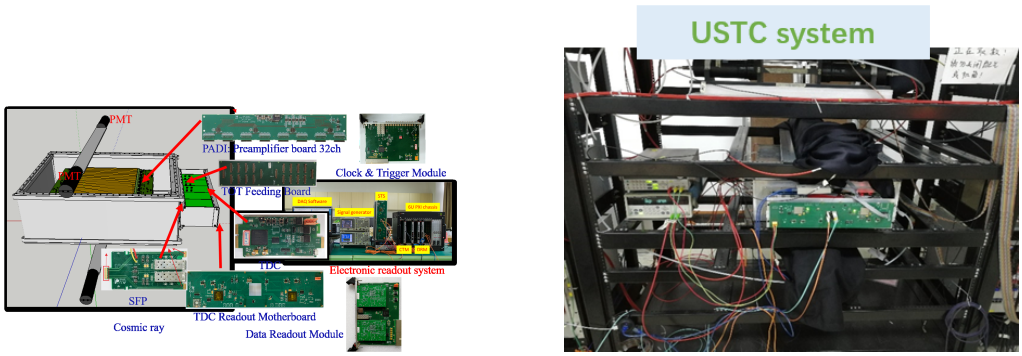

(a) (b)

Fig. 4.26 (a) The electronics module for the cosmic-ray test stand at USTC, and (b) the real setup of the batch test system.

are digitized by the FPGA TDC. Then the digitized time data are aggregated at the TDC readout motherboard (TRM) and are transmitted to the data readout modules (DRMs) via optical links. Finally, the DRMs relay the digitized data to the DAQ system through the Gigabit Ethernet ports in parallel. The flow chart for electronics is shown in Fig.4.28. A telescope based on plastic scintillators coupled with PMTs is used to provide a trigger for the system. For each cosmic ray test, four counters are placed in the module and tested simultaneously. The entire test system consists of three parts, a trigger telescope, a module with four counters to be tested, and the electronics part mentioned above.

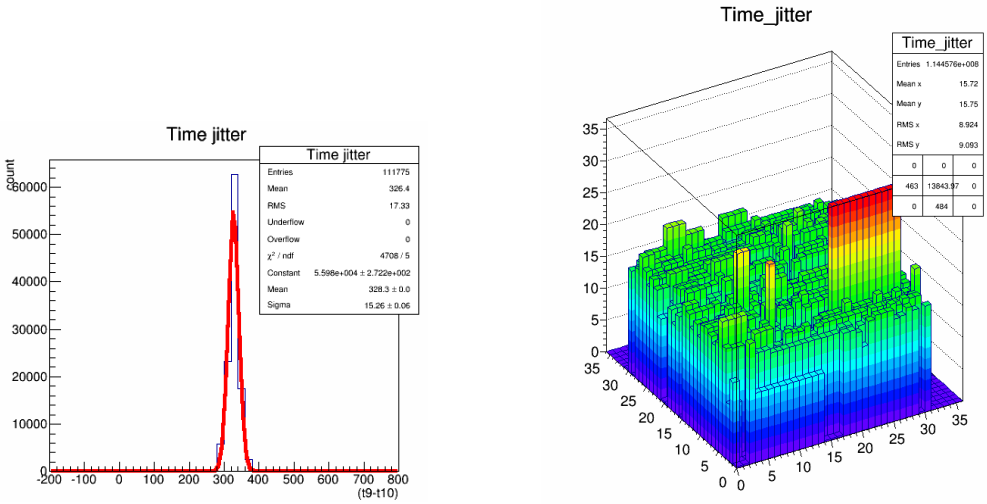

(a) (b)

Fig. 4.27 The measured (a) time jitter and (b) uniformity (32 channels) of the electronics system (without the FEE).

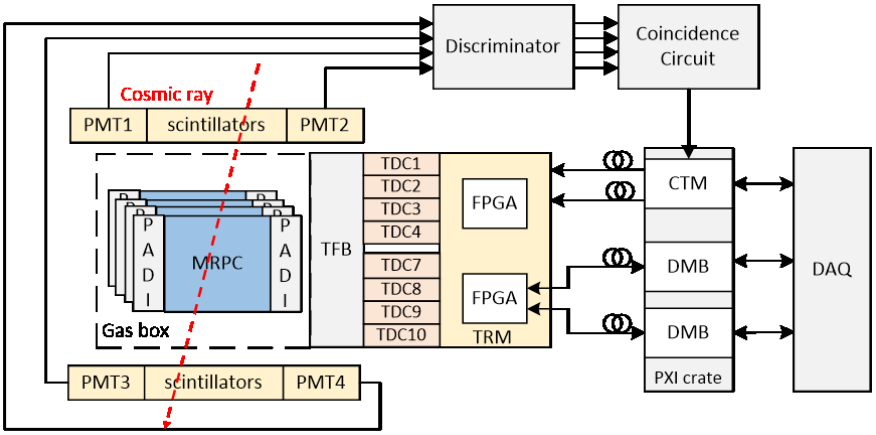

Fig. 4.28 The flow diagram of the electronics for the batch test system at USTC.

2. Time walk

Inherently, differential signals are obtained from the anode and cathode strips of MRPC. The so-called differential transmission means that on two signal lines the electrical signals with the equal amplitude and opposite polarity are transmitted, then at the receiving end the received two line signals are subtracted, thus obtaining a signal that the amplitude doubles. The output charge of the signal from the MRPC is sent to the FEE and encoded into the width of the LVDS pulse, which is then recorded by the FPGA TDC. The TDC measured the time of both leading and trailing edge of the LVDS pulse.

In the leading edge discriminators appears a phenomenon as shown in Fig.4.29, the so called time slewing (or time walk) effect. The time slewing effect can be corrected in the off-line analysis, as described in Chapter 3. We have used function fit (with an empirical function 3.28) combined with bin-by-bin counting method to perform the correction.

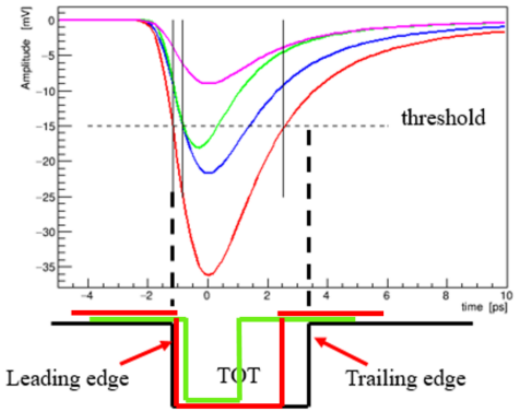

Fig. 4.29 Illustration of the time slewing effect emerging in a leading edge discriminator.

3. Data analysis

In the batch test process, the system contains no precise reference time T0r. We have established a set of algorithm to deduce the time resolution of MRPCs in such an environment. Base on the USTC electronic system, we get the preliminary time resolution results, $\sigma^{'}$. Define $\sigma_i(i = 1, 2, 3, 4)$ as the time resolution of each MRPC, and $\sigma_i^{'}$ as the measured overall time resolution of $T_i - TR_i$, where T_i represents the mean measured time from the dual readout ends of a selected strip of the i-th MRPC, and $TR_i = \frac{1}{n-1}\sum_{j\neq i}^{N} T_j$ (For our test stand TR_i=$\frac{(T_j+T_k+T_l)}{3}$) represents the reference time independent of T_i. Since the time resolution of each counter is independent of each other, we have

$$\begin{aligned}
\sigma_i^{'2} &= \sigma^2(T_i - TR_i) \\
&= \sigma^2(T_i - \frac{\sum_{j\neq i}^{N} T_j}{n-1}) \\
&= \sigma^2(T_i) + \frac{1}{(n-1)^2}\sigma^2(\sum_{j\neq i}^{N} T_j) \\
&= \sigma^2(T_i) + \frac{1}{(n-1)^2}\sum_{j\neq i}^{N}\sigma^2(T_j)
\end{aligned} \tag{4.1}$$

$$\sigma_i^{'2} = \sigma_i^2 + \frac{1}{(n-1)^2}\sum_{j\neq i}^{n}\sigma_j^2 \tag{4.2}$$

Considering the time walk effect, the four preliminary resolutions obtained from the $(T_i - TR_i)$ distributions have to be corrected in an iterative way. After several iterations, the slewing correction parameters for all the four $T_i - TR_i$ distributions would reach convergence. Fig.4.30 shows the four $(T_i - TR_i)$ distributions after slewing correction. The time resolution $\sigma_i^{'}$ of four MRPCs are 62.76, 61,36, 56.97, and 61.61 ps respectively. In fact, the time resolution of each MRPC differs a little. From the equation-4.2 we can get an n-array equation-4.3 with σ_i as the unknowns.

$$\begin{cases}
\sigma_1^2 + \frac{1}{(n-1)^2}\sigma_2^2 + \frac{1}{(n-1)^2}\sigma_3^2 + \frac{1}{(n-1)^2}\sigma_4^2 = \sigma_1^{'2} \\
\frac{1}{(n-1)^2}\sigma_1^2 + \sigma_2^2 + \frac{1}{(n-1)^2}\sigma_3^2 + \frac{1}{(n-1)^2}\sigma_4^2 = \sigma_2^{'2} \\
\frac{1}{(n-1)^2}\sigma_1^2 + \frac{1}{(n-1)^2}\sigma_2^2 + \sigma_3^2 + \frac{1}{(n-1)^2}\sigma_4^2 = \sigma_3^{'2} \\
\frac{1}{(n-1)^2}\sigma_1^2 + \frac{1}{(n-1)^2}\sigma_2^2 + \frac{1}{(n-1)^2}\sigma_3^2 + \sigma_4^2 = \sigma_4^{'2}
\end{cases} \tag{4.3}$$

Eventually the intrinsic time resolutions of four MRPCs can be obtained by solving the equation-4.3, and we arrive at.

$$\begin{pmatrix} \sigma_1^2 \\ \sigma_2^2 \\ \sigma_3^2 \\ \sigma_4^2 \end{pmatrix} = \begin{pmatrix} 33/32 & -3/32 & -3/32 & -3/32 \\ -3/32 & 33/32 & -3/32 & -3/32 \\ -3/32 & -3/32 & 33/32 & -3/32 \\ -3/32 & -3/32 & -3/32 & 33/32 \end{pmatrix} \begin{pmatrix} \sigma_1'^2 \\ \sigma_2'^2 \\ \sigma_3'^2 \\ \sigma_4'^2 \end{pmatrix} \tag{4.4}$$

The derived time resolutions for a batch of MRPC3b modules are shown in Fig.4.31. During the mass production, around 30 MRPC3b counters had been tested with this USTC electronics system. The average resolution is ∼56 ps including the contribution from the electronics. After subtracting the electronic time jitter, the MRPC3b's intrinsic time resolution is around 52 ps, which fully satisfies the requirement of <60 ps for the CBM-TOF MRPC3b modules.

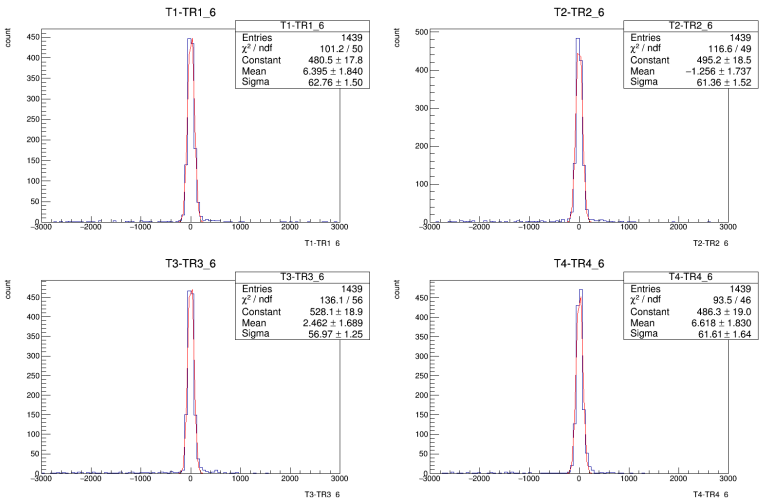

Fig. 4.30 $T_i - TR_i$ **distribution after slewing correction.**

4.3.3 TRB3 Readout System@USTC

Another cosmic-ray test system based on the third version of the TDC Readout Board (TRB3) hardware platform has also been setup at USTC. The TRB3, developed at GSI, has been chosen as a triggered DAQ system for the STAR-eTOF counter mass production[82]. This system includes a 264 channel high precision TDC platform that offers a multi-hit timing capability to measure the leading and trailing edges with 10 ps RMS time precision for the input LVDS signals with a minimum pulse width of 500 ps. The actual maximum hit rate capability is 50 MHz per channel while the maximum readout trigger rate is 700 kHz[82].

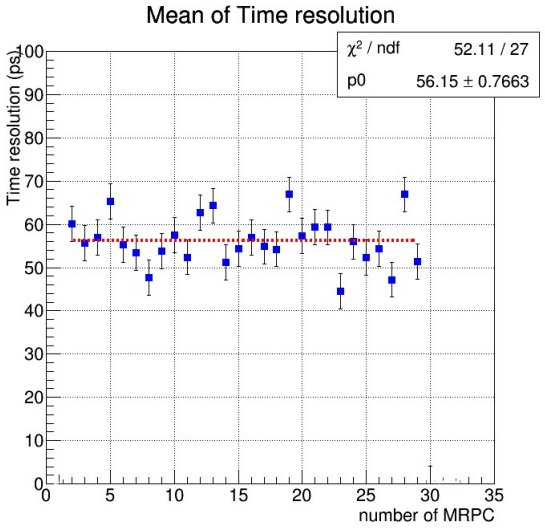

Fig. 4.31 The mean time resolution of MRPC3b with USTC electronics system.

1. FPGA TDC Board@ TRB3

The FPGA TDC communicates via the SPI master communication with the PADI FEE, which then connects to the MRPC module via a feed-through board. A high-resolution 32-channel differential I/O lines TDC is implemented in a general purpose FPGA. The FPGA TDC is also based on the XILINX Lattice ECP3, with the circuit diagram shown in Fig.4.32 (a). The Fig.4.32 (b) is the real image of the FPGA TDC board.

The experimental result[92] suggests calculating the time jitter between the two channels in one clock cycle (5 ns). A 10 ps time jitter on a single channel shown in Fig.4.33. The integral non-linearity (INL) and differential non-linearity (DNL) are 11.6 ps and 5.5 ps, which indicate that the proposed TDC offers high performance among the available channels[92].

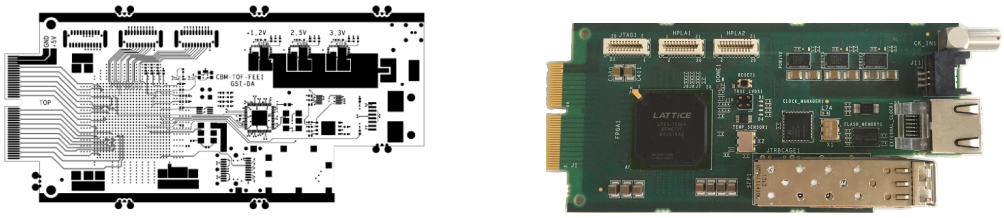

(a) (b)

Fig. 4.32 The (a) design and (b) finished board of the TRB3 FPGA-TDC board.

2. TRB3 platform

The TRB3 is actually designed as an extensible general purpose read-out platform. The main parts are shown in Fig.4.34. The board comprises 5 commercial Lattice

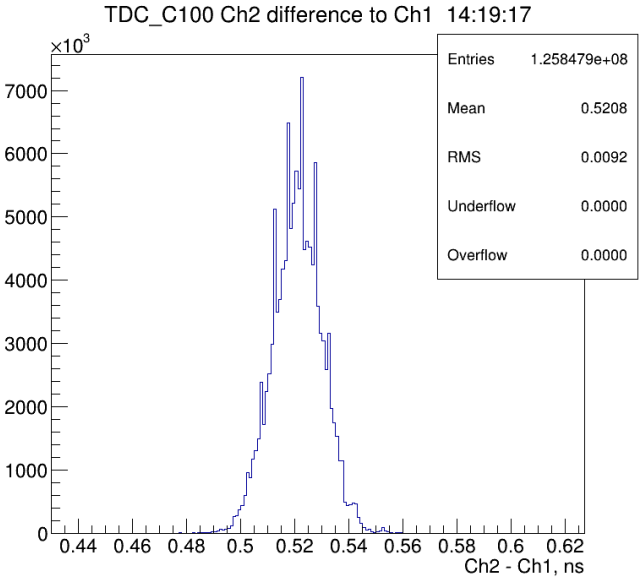

Fig. 4.33 FPGA TDC time jitter ∼ 10 ps.

ECP3/150EA FPGAs: the central FPGA that can work as readout controller provides a Gigabit Ethernet link as well as central trigger system with 4 TDC channels; 4 peripheral FPGAs are programmed to provide 64 TDC channels each and a synchronization time. The synchronization of two different FPGAs in the same board is well defined with a timing precision of ≈ 13 ps RMS as shown in Fig.4.35. The TRB3 firmwares use the Trigger and Readout Board Network (TrbNet)[93] for asynchronous readout and busy-release scheme trigger distribution. Its configuration can be transparently controlled via command line tools including bindings to Perl.

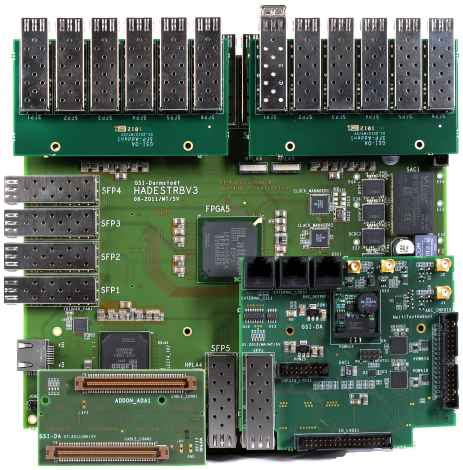

Fig. 4.34 TRB3 platform.

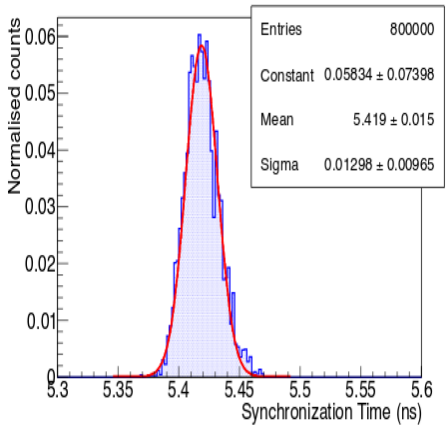

Fig. 4.35 Synchronisation time precision between two FPGAs on a TRB3 board.

3. Slow control

In order to control the TRB3 system, a slow control system is developed, which includes a user-friendly interface with web2.0 interactivity. Both the trigger and the readout process are controlled by a central instance, the Central Trigger System (CTS) as shown in Fig.4.36. The CTS is supplied with fast input signals from different detector subsystems. Based on these signals, a trigger decision is made. For each accepted trigger, first a reference time signal is sent to all front-ends via a dedicated differential link. The synchronization between all subsystems is provided with an accuracy better than 30 ps. Second, a LVL1 trigger packet is sent over the optical network to all front-ends. It contains all necessary information to process the trigger, e.g. the trigger type or event number. Here, also special trigger types for calibration and status information are implemented which are not preceded by a reference time signal. Upon a received trigger, the front-ends perform the read-out of the detector electronics and stores all data inside buffers. Typically, these buffers are able to store several hundred events before read-out has to take place. Besides, it has a webpage that shown the statue of the FPGA TDC, which can be seen from Fig.4.37.

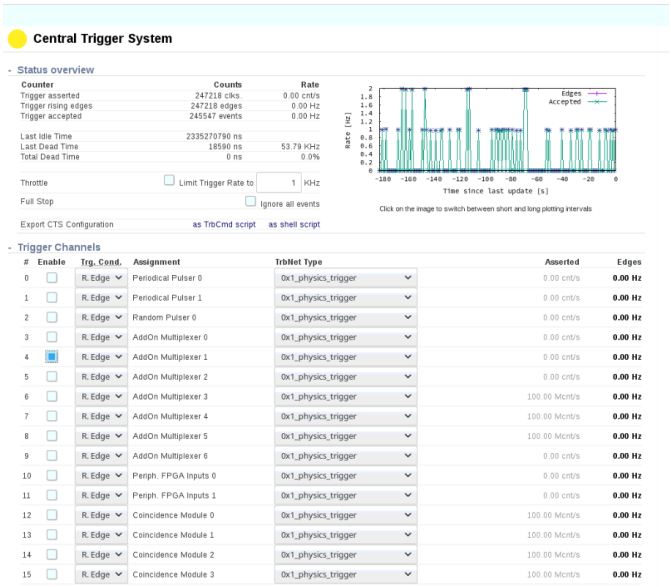

Fig. 4.36 Central Trigger System

4. Online analysis

In the TRB3 system, the module's readout will generate data continuously. The data pre-processing is necessary to allow the reduction of the wrong data storing into the PC. If we find an error in the plots on the GUI of the online analysis system, we can

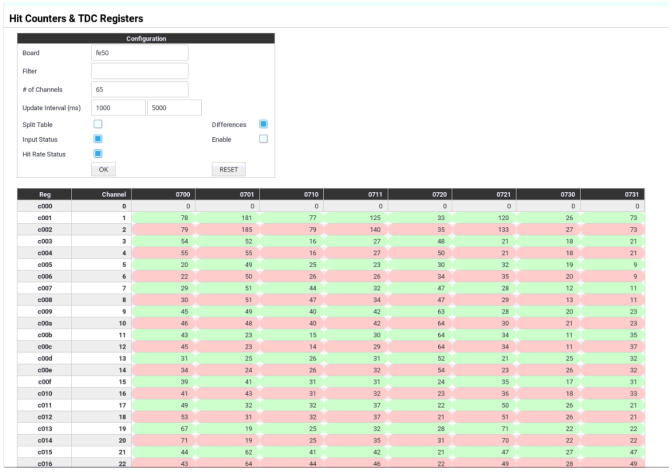

Reg	Channel	0700	0701	0710	0711	0720	0721	0730	0731
c000	0	0	0	0	0	0	0	0	0
c001	1	78	181	77	125	33	120	26	73
c002	2	79	185	79	140	35	133	27	73
c003	3	54	52	16	27	48	21	18	21
c004	4	55	55	16	27	50	21	18	21
c005	5	20	49	25	23	30	32	19	9
c006	6	22	50	26	26	34	35	20	9
c007	7	29	51	44	32	47	28	12	11
c008	8	30	51	47	34	47	29	13	11
c009	9	45	49	40	42	63	28	20	23
c00a	10	46	48	40	42	64	30	21	23
c00b	11	43	23	15	30	64	34	11	35
c00c	12	45	23	14	29	64	34	11	37
c00d	13	31	25	26	31	52	21	25	32
c00e	14	34	24	26	32	54	23	26	32
c00f	15	39	41	31	31	24	35	17	31
c010	16	41	43	31	32	23	36	18	33
c011	17	49	32	32	37	22	50	26	21
c012	18	53	31	32	37	21	51	26	21
c013	19	67	19	25	32	28	71	22	22
c014	20	71	19	25	35	31	70	22	22
c015	21	44	52	41	42	21	47	27	47
c016	22	43	54	44	46	22	49	28	49

Fig. 4.37 Hit Counters & TDC Registers, a webpage-based status viewer of the FPGA TDC

immediately turn off the DAQ. Such erroneous data will not be recorded in the raw data collected. Fig.4.38 shows the online analysis GUI of the TRB3 system. In this interface, we can check information of the leading-edge and trailing-edge timing, TOT, the time jitter of TDC etc.

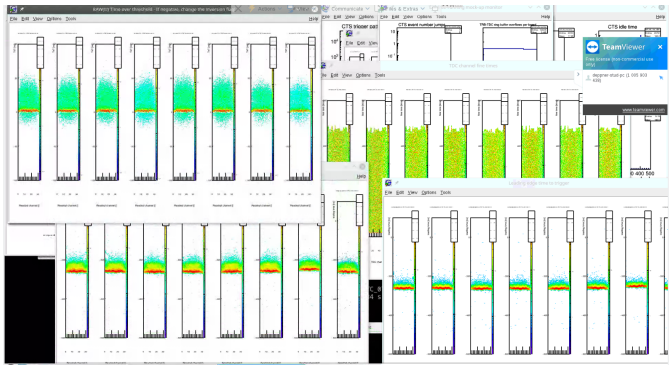

Fig. 4.38 Online analyze system

5. Cosmic-ray system

The cosmic-ray test platform is established based on the electronic systems described above. Four MRPC3b counters, each with an active area of 32 $\times$ 27 cm^2, are housed in the module box, whose size is 70$\times$ 64 $\times$17.8 cm^3. The gas mixture used is 95% Freon R-134a and 5% iso-C_4 H_{10}. The Fig.4.39 shows the layout of the module and the trigger detector, which composes of two scintillators each of 40$\times$20$\times$2.5 cm^3 size. The picture of 4.39 shows that the two scintillators, each coupled to a PMT, are placed above and below the module box respectively.

Signals from the two PMTs are fed to the discriminator and then sent to the logic unit C04020. The coincidence output is sent to the the TRB3 system as the trigger signal.

Signals of MRPC are amplified and discriminated by the PADI FEE, then recorded by the FPGA TDC of TRB3 system. The difference between the leading- and trailing-edge timing gives the signal width (TOT) information. The block diagram of the test system in Fig.4.40 present the logic map of the system. The top detector in this system is set as the earliest output column in the data structure, including time, TOT, mapping information and so on, and the bottom detector is set to the last output column in the data.

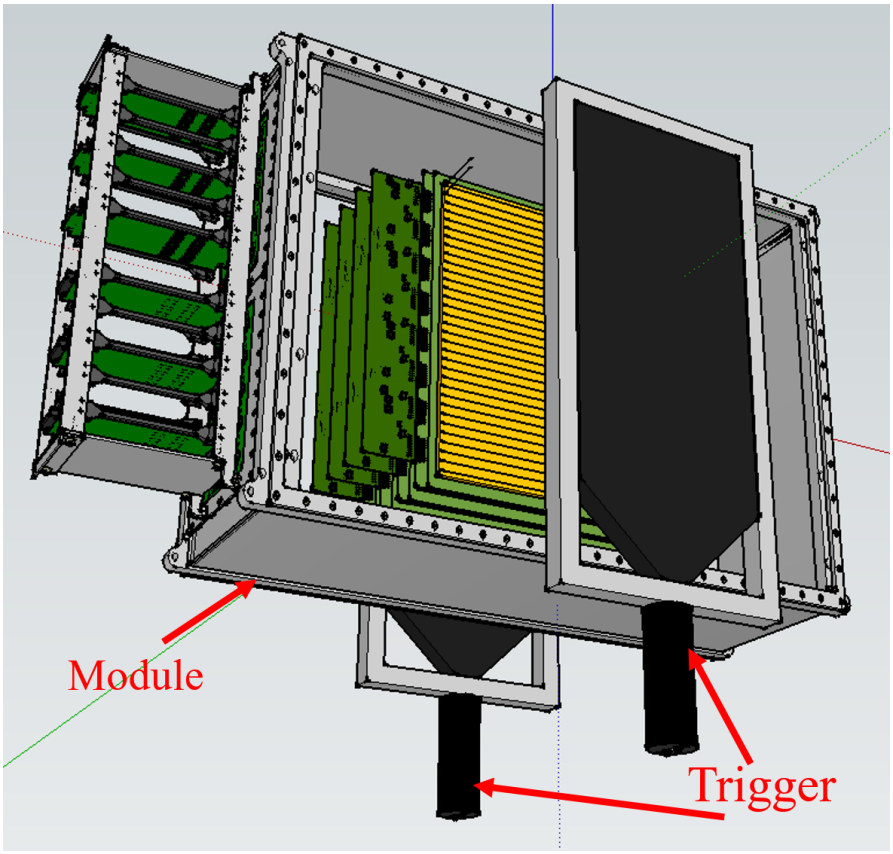

Fig. 4.39 The module (middle part) and trigger detector of the cosmic-ray test stand.

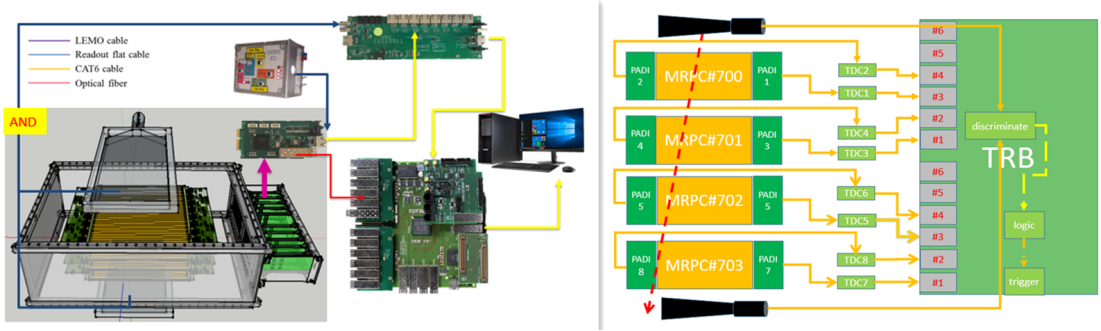

Fig. 4.40 The block diagram

4.3.4 Software Structure of the TRB3 Cosmic-ray test System

1. CBMROOT

The data analysis is performed in the framework of CBMROOT. CBMROOT starts in 2003 serving as the simulation and data analysis package for the CBM. For simulation the Virtual Monte Carlo concept is chosen. This concept allows performing simulation using Geant3, Geant4 or Fluka[94] without changing the user code or geometry description. The same framework is then used for the data analysis in the CBM experiment. The schematic design of the CBM TOF analysis framework is shown in the Fig.4.41. The framework consists of four parts: the analysis source code part, the geometry part, the parameter part and the macro part. The analysis source code part is the core of the framework, and contains the entire code's class. New functions can be added to the framework by properly modifying this part. The geometry describes the simulation geometry according to the real test stand. It has to be built in advance before being used for the calibration. The parameter part records all parameters of the analysis code, while the macro part is in control of the software. The function code can be executed by running the macros.

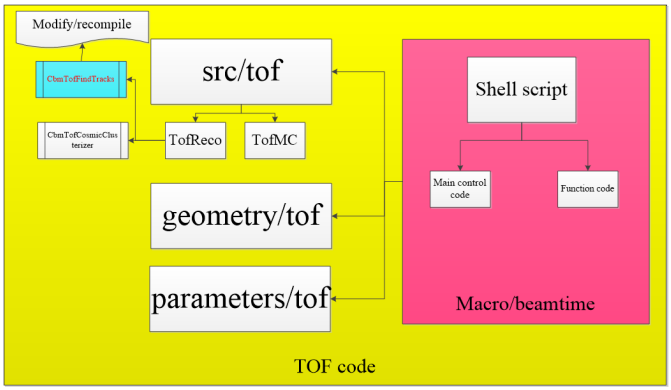

Fig. 4.41 Schematic design of the TOF analysis framework.

2. Software structure

Now we can discuss how the CBM TOF analysis software works. Fig.4.43 depicts the basic structure of the analysis procedure. The raw data from the DAQ system are stored in the time slice archive (.tsa) file format that need to be unpacked before performing calibration. After unpacking the raw data, we get the ROOT file which contains necessary information of the counter, including e.g. the TOT, the signal mapping and the leading-edge time of the signal. Other information such as the address, direction and position of MRPC are also included, through the mapping files. These information as

"digits" are saved in the ROOT file.

The signal on one MRPC strip produces oppositely charged signals on the neighboring strips due to capacitive or inductive coupling, which is called crosstalk. The crosstalk can be measured by how much a signal on one channel can affect another channel. Ideally, acquiring a signal on one channel should not affect another signal being acquired, but this is not always the case due to unwanted conductive, capacitive, or inductive coupling from one part of the transmission line to another. The signal propagation along the long readout strip might bring about undesired side-effects, such as worsening of the time resolution and the counting capability, especially in the environment of high multiplicity. The crosstalk is largest between adjacent cells of adjacent layers.

To eliminate the influence of crosstalk, it is important to find the actual hit points for the data analysis of MRPC. The signal "digits" from each strip of the MRPC contain TOT information, representing its charge information. Therefore, here we use the charge centroid method to determine the real hit point. In addition, a narrow time window is required for the offline charge centroid method (charge collection and centroid calculation) to get clear hit point. This point can be further used for the track reconstruction. Beyond that, an event display tool is developed which allows graphical representation of the experimental data.

The next step is calibration. This procedure includes the time walk correction, the clustersize and position correction. During this step, one searches for associated hits points in each detector. If two or more digits are particularly close to each other in time and space, it is likely that these digits are produced in the same avalanche induced process. Thus if that happens, a signal on two or multiple membership strips, the same digits can be merged into one cluster. This progress is done in cbmTofCosmicClusterizer.

The last step is tracking. By establishing the track, efficiencies, time resolution and space resolution of all counters can be obtained. Fig.4.42 shows the principle of the track reconstruction. Here we use the USTC TRB3 system as an example to describe its principle. There are four counters in the system. We name them counter1, counter2, counter3, and counter4 from the top to the bottom. When a μ crosses four counters from above, it is very likely that a hit point will be generated in each counter. Each hit point, as described above, contains the μ time T_{hit} and position P_{hit} crossing the counter. We choose two counters, the counter1 and the counter4, as the starting point to reconstruct the track. Then another counter is chosen as the reference counter and the final one

is used as the Detector Under Test (DUT). Here the counter3 is used as the reference counter and the counter2 is taken as the DUT. If hits found in both of the counter1 and the counter4, we connect the two points with a straight line to get a candidate track. If this candidate track crosses the reference counter (counter3) at a position close to the hit point, then the track will be considered a valid track as shown in Fig.4.42 (track1). This track will continue to be used by subsequent analysis. If a hit point is not found near the candidate track as shown in Fig.4.42 (track 2), this candidate track will be discarded and the hit points are released. Through the process of track reconstruction we can greatly suppress the impact of noise on the system, thus avoid false information entering the analysis to disturb the extraction of the performance of the counter. The

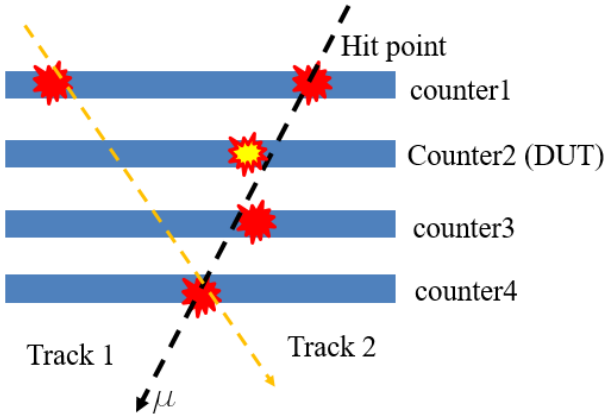

Fig. 4.42 Schematic diagram of track reconstruction.

tracking class is controlled by some parameters that can be accessed and modified in the macros. The most important parameter is the χ^2 value. It tells the algorithm how close a hit point needs to be in space and time so that it can be accepted by a reconstructed track. By increasing the χ^2 value, the corresponding detector's efficiency increase, meanwhile, the time resolution and space resolution get worse, since a larger χ^2 value means allowing to accept more hits as the tracking reference points. In addition, large χ^2 may lead to reconstructing a track with hits that are not from the original same particle, and get a ghost track. So to chose a reasonable χ^2 is very important for the tacking reconstruction. The counter's order is defined in the parameter "tracking_setup". This setup contains the number of counters participating in the tracking reconstruction and the minimum number of participating counter to accept the track.

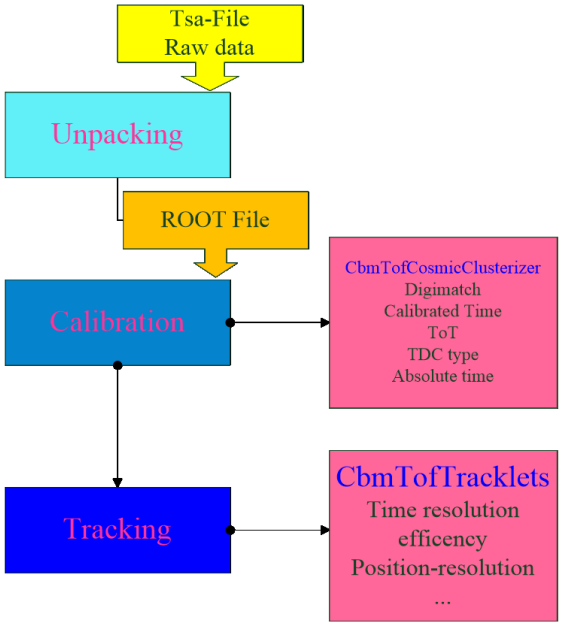

Fig. 4.43 The flow diagram of data analysis using the CBM TOF software.

4.3.5 TRB3 Results

The goal of the QA effort in the mass production for the CBM/STAR-eTOF is to guarantee the same excellent performances obtained so far with all the MRPC3b counters. A set of quality assurance tests has therefore been developed for this purpose; these tests are applied to the MRPC3b counters and as part of the QA, the TRB3 system contributes a lot to the mass production.

These tests are applied both to the MRPC3b counters and to the eTOF modules.

1. Time slewing

The first step is to correct the time walk effect. The time walk effect obtained from the raw data is shown in Fig.4.44 and this effect after corrected once is shown in Fig.4.45. Both plots show the arrival time subtracted by the reference time against the corresponding hit's TOT. The correlation of the time and TOT is clearly seen in histogram (Fig.4.44). Each time value is shifted by the corresponding mean of each TOT bin to the same reference time, here zero, to remove the time walk effect. This method is called the bin-by-bin method, already discussed in previous chapters. This process will be iterated over several times by the shell script (the number of iteration can be set in the script), and the final figure is shown in Fig.4.46 where the red area that includes most of the statistics is essentially made flat. The entire time walk slewing is done.

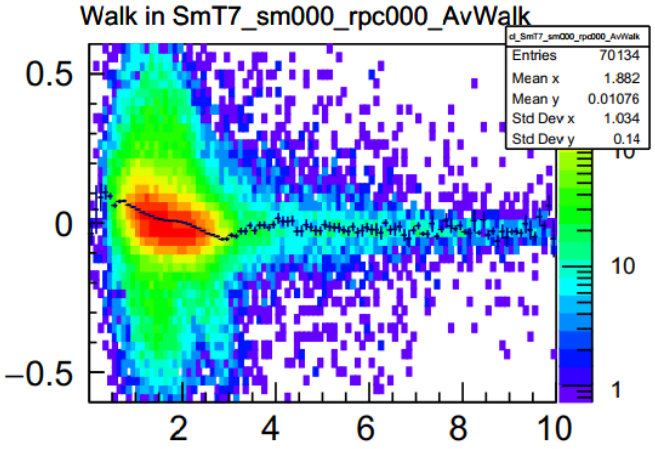

Fig. 4.44 The measured time walk effect from the raw data. The x-axis reads the hit's TOT in a logarithmic scale. The y-axis shows the hit's arrival times relative to the reference time in ns.

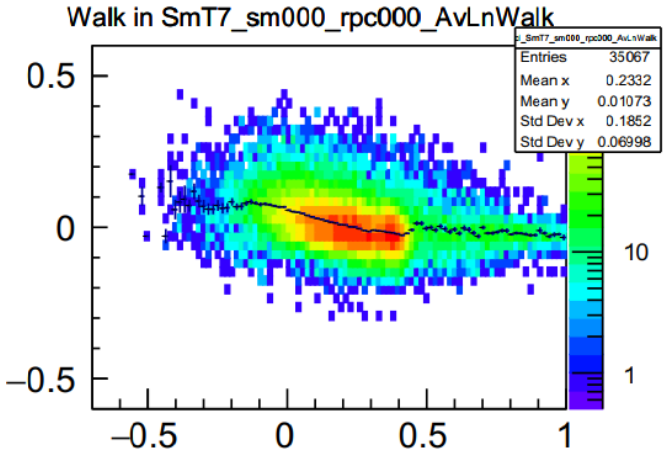

Fig. 4.45 The time-TOT distribution after one iteration of slewing correction.

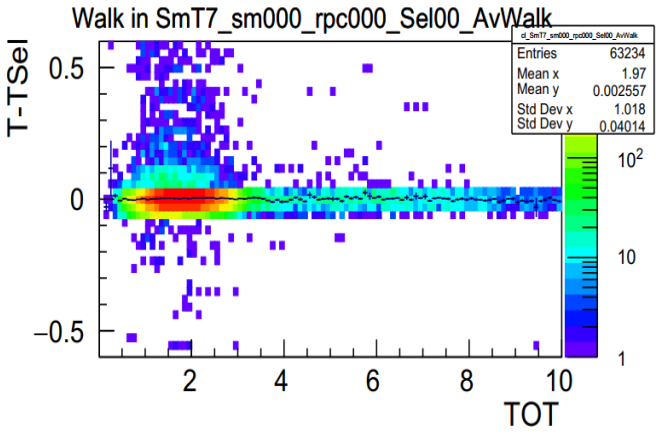

Fig. 4.46 The time-TOT distribution after several iterations (>20) of slewing correction.

2. Clustersize

We tested 8 MRPC3b counters with the TRB3 readout electronic at USTC. Shown in Fig.4.47 (a) and (b) are a typical clustersize distribution and the mean clustersize of these 8 detectors. The average cluster sizes are consistently as 1.21, which means the probability of two strips are fire at the same time is around 21% from the calibration result.

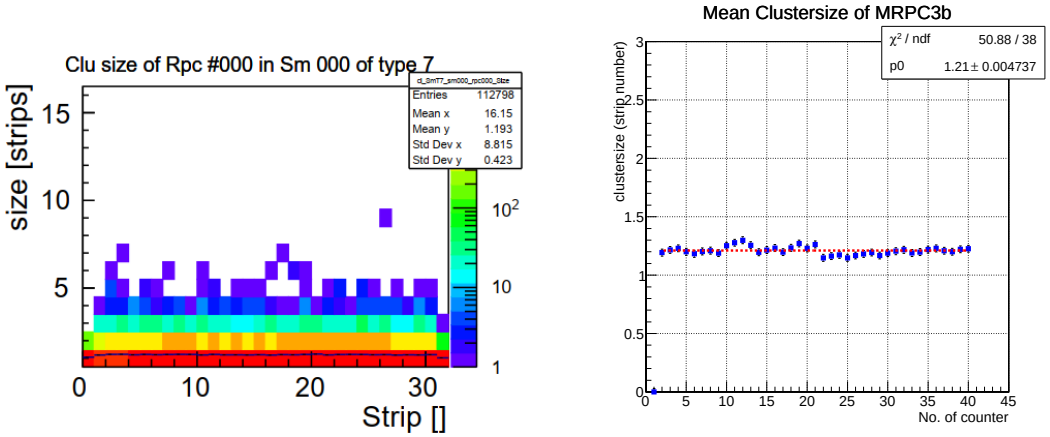

(a) (b)

Fig. 4.47 (a) A typical clustersize distribution of the MRPC3b detector, and (b) the mean clustersize, measured by the TRB3.

3. Efficiency

The calibration of counter's efficiency and time resolution depends on the reconstructed track. For the TRB3 system we set 4 counters participating the track reconstruction, and the minimum number for effective track is 3 counters. In addition, in which order the counters are checked for hit matching is defined by the parameter "tracking_setup". Experience shows that to set the outermost counter (in our case the counter1 and counter4) as the two starting tracking seed and interpolating inwards shows better results than extrapolation to outer counters. For a certain counter, the efficiency is determined by the equation-4.5, which defines the fraction of hit points that are found in the reconstructed tracks. The formula shows how to calculate the efficiency in our case.

$$\varepsilon[i] = \frac{\#4\_counter\_tracks}{\#4\_counter\_tracks + \#3\_counter\_track} = 1 - \frac{3\_counter\_tracks}{4\_counter\_tracks + 3\_counter\_tracks}, \tag{4.5}$$

where $\varepsilon[i]$ means the efficiency of the ith counter, 3_counter_ tracks means a track with hits in three counter, excepts the DUT which we want to calculate the efficiency (this means a track is constructed from the other 3 detectors, but we find no related hit on the

DUT) , and 4_counter_tracks means every counter has been found the hits in the track (this means a track is constructed from the other 3 detectors, and we find a related hit on the DUT) . Fig.4.48 shows a result from the TRB3 system. The histograms on the left show the position of all hits found in the reconstructed tracks, while the histograms in the middle column show that of the missing hits. The plots on the right are the efficiencies of the corresponding counters and all hits found in 4_counter_tracks for the test counter. We tested 8 detectors with the TRB3 system at USTC, and the efficiency of the detector is around 93% with 6000 V as shown in Fig.4.48) (right).

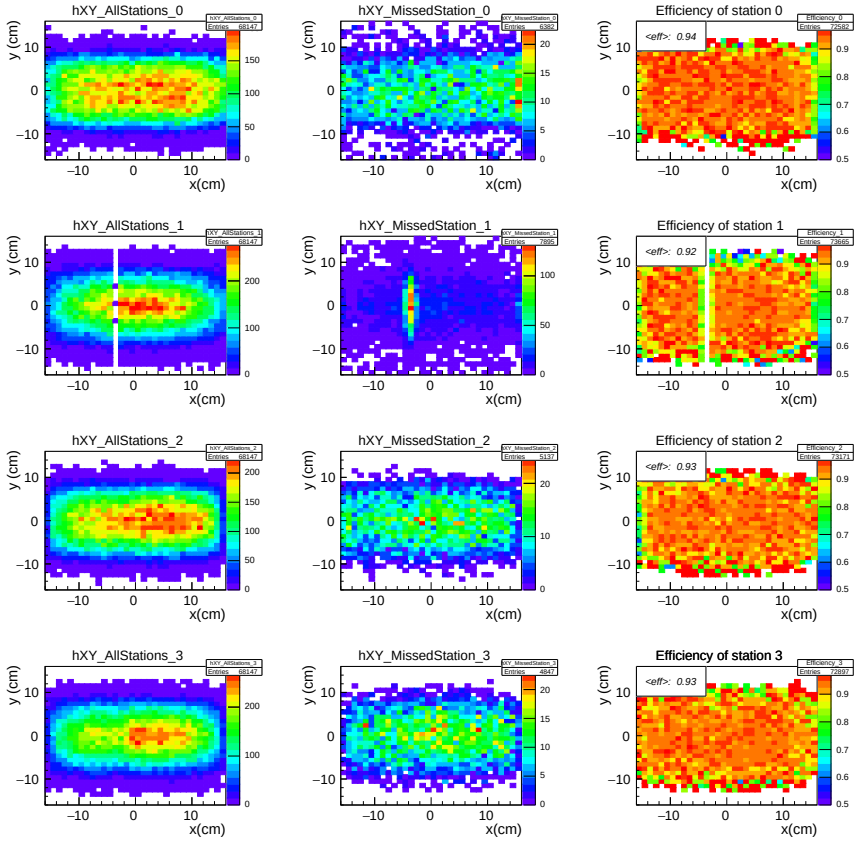

Fig. 4.48 The hit position of (a) 4-detector tracks and (b) 3-detector tracks, as well as (c) the deduced efficiency of each detector.

Fig.4.49 shows the efficiency-HV curve of the MRPC3b counter. The detection efficiency is greater than 90% when the applied HV is higher than ±5.9 kV.

4. Time resolution

The time resolution is shown in Fig.4.49 together with the corresponding detection efficiency. The working HV is chosen as ±6.15 kV, where the detection efficiency is greater than 95% and the time resolution is the best. In order to get the time resolution of a MRPC3b counter, the full track reconstruction must be considered. For a reconstructed

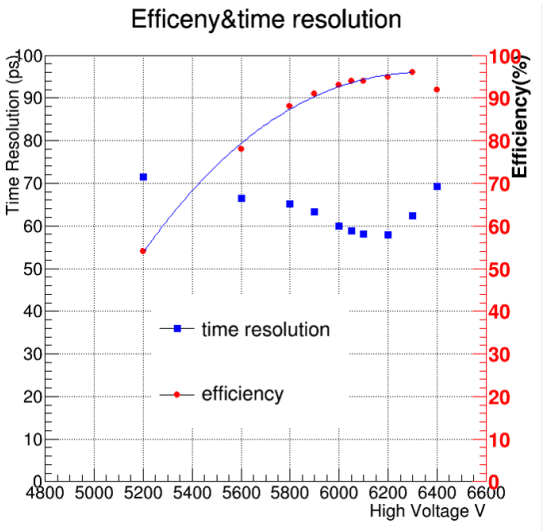

Fig. 4.49 The detection efficiency and time resolution vs. HV for the MRPC3b detectors.

track, when crossing each counter it will give the time $T_{Trk}^{(i)}$ and position $P_{Trk}^{(i)}$ information of the track entry point. The time at which the track passes through the incident point on the DUT is T_{Trk}^{DUT}. The corresponding real hit point on the DUT also contains the measured time T_{hit}^{DUT}. Then the time resolution of the DUT is $\sigma(T_{hit}^{DUT} - T_{Trk}^{DUT})$. For the TRB3 system operating at USTC, the principle of the calibration is as described above. Fig.4.50 is a typical distribution of $(T_{hit}^{DUT} - T_{track}^{DUT})$, with time calibrated by the methods described in previous sections. Fitting this distribution with a Gaussian function yields a variance of 65 ps, which is taken as the time resolution of the selected counter in the cosmic-ray test. Fig.4.51 shows the time resolution of the 8 MRPC3b counters tested by the TRB3 system. The average resolution is around 60 ps.

5. Event display

In order to check if the track reconstruction is correct, we developed an event displayer as shown in the Fig.4.52. Fig.4.52 (a) shows an example of a track reconstructed in error, with two tracks passing through the same fire point. Fig.4.52 (b) shows the track that has been rebuilt after adjusting the parameters. The event display helps us adjust the chi-square and find the appropriate parameter values to reconstruct the track.

6. Simulation of the TRB3 system base on CBMROOT

Besides the real experimental test, we also want to perform a simulation study for the TRB3 system to evaluate the performance of the system and the cosmic-ray test results. The setup in the simulation is constructed according to the real cosmic-ray system, and the same analysis code is used to deal with the simulation data. In this way we can

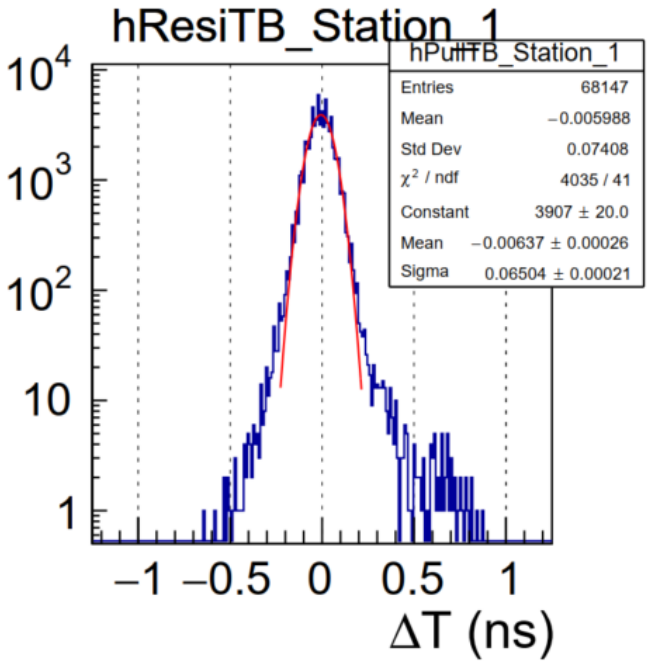

Fig. 4.50 The time distribution of $T_{Hit}^{DUT} - T_{Trk}^{DUT}$ after calibration.

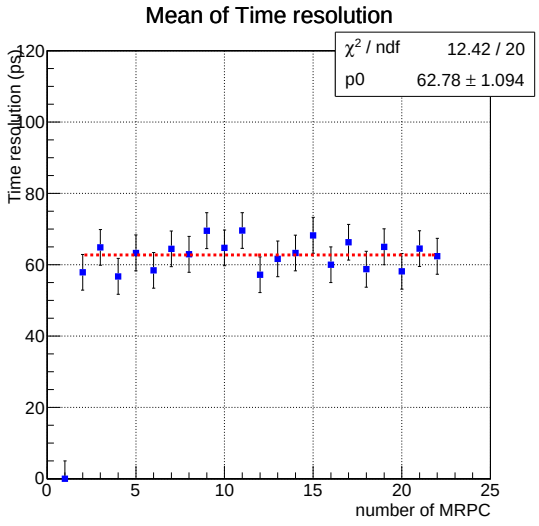

Fig. 4.51 The mean time resolution of the 8 MRPC3b counters. All counters have undergone two times cosmic-ray tests.

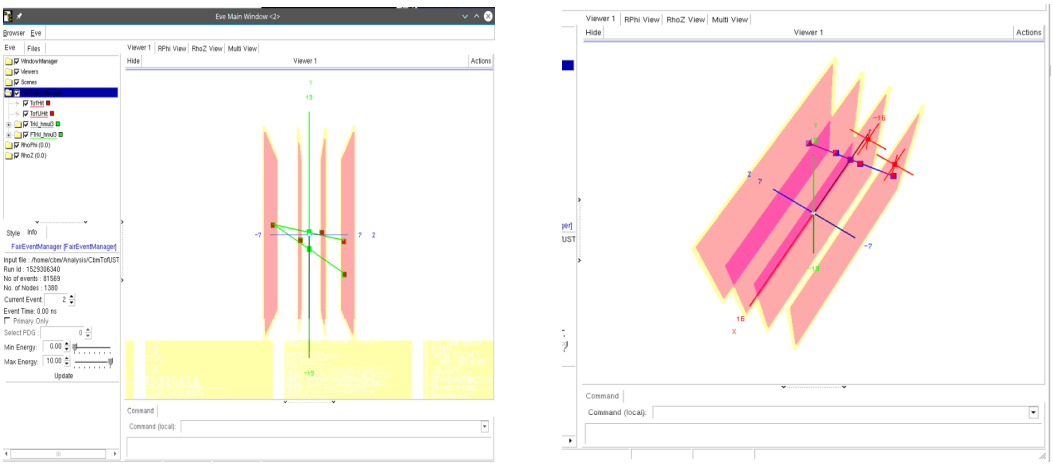

(a) (b)

Fig. 4.52 The event display GUI.

compare the results (efficiency and time resolution) from the simulation data and experimental tests. The simulation study is divided into four steps: (1) building geometry, (2) writing a particle generator, (3) running the simulation and, (4) analyzing the simulation data. Fig.4.53 shows the geometry of the cosmic-ray test system in the simulation. They are built based on the real experimental setup. Two scintillator detectors are set as the trigger detector for the system. 4 MRPCs are used to check the performance. The simulation study is currently ongoing.

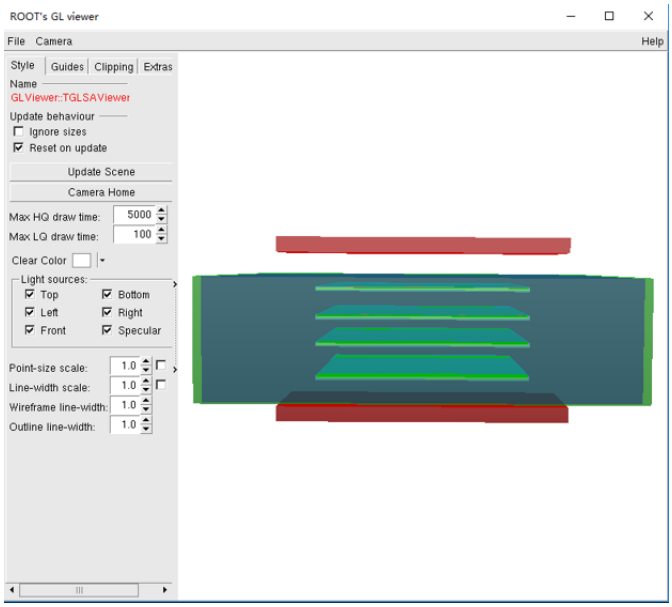

Fig. 4.53 geometry of the test system in the simulation.

4.3.6 Cosmic-Ray Test Stand at Heidelberg (GET4-PADI system)

When the counters were produced, qualified and shipped to the University of Heidelberg, we assembled the counters into the modules and commissioned them in conjunction with the electronics actually used on the STAR eTOF. After another round of cosmic ray test (with the GET4 system) on the counter level, the qualified modules and corresponding electronics are numbered and shipped to BNL. Unfortunately, in the joint debugging process, electronics has found a bug, so the cosmic ray test in Heidelberg is not perfect. But I still did my best to analyze this part of the data and this section will discuss the results of the test.

1. Readout electronics

The signals of the FEE PADI boards located in the modules are fed into the GET4 that is attached to the module. The FEE is still based on the PADI ASIC. However, the GET4 (GSI Event Driven TDC with four channels) are used as the digitizer[95-96]. The GET4 ASIC is developed by the GSI ASIC electronic group for the CBM TOF experiment (see Fig.4.54). The main aim of this ASIC is to get a high resolution TDC with a time resolution better than 25 ps that can operate in a triggerless data acquisition environment. The required data rate is about 100 kHz / channel. The double hit resolution should be better than 5 ns and the power consumption less than 30 mW/channel.

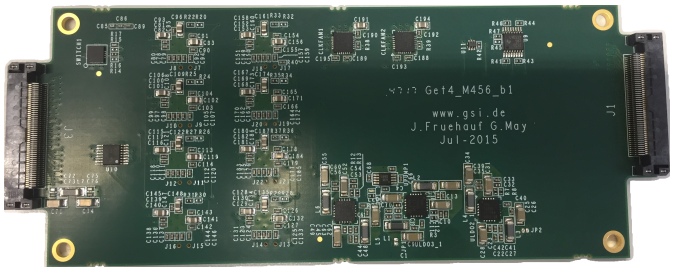

Fig. 4.54 GET4 TDC board for the eTOF module.

In such a high data transfer rate, the basic idea is to use the GBTx (Gigabit Transceiver) ASIC for data transmission, trigger distribution, and clock forwarding toward the FEE. GBTx[97-98] is a radiation-hard fiber-optic transmission chipset, developed by the GBT collaboration for the LHC experiment upgrades. It can receive and transmit serial data at 4.8 Gb/s, encode and decode the data into the GBT protocol and provide the interface to the FEE.

2. Test stand system

As one of the FAIR phase 0 programs, 10% of the full CBM TOF system, including read-out chain, will be install as an eTOF subsystem at STAR/RHIC. In order to fit the STAR experiment requirement, the readout board module is currently being redesigned by the CBM-TOF group. The test system using this modified readout system can be operated either in the free stream mode or in the trigger mode. Three counters are placed inside each STAR eTOF module. Fig.4.55 shows the eTOF module and the electronics. The eTOF module houses FEE boards that implement the PADIx amplifier and discriminator for MRPC signal processing. The signals of the PADI FEE boards are fed into the GET4-TDC that is attached to the module.

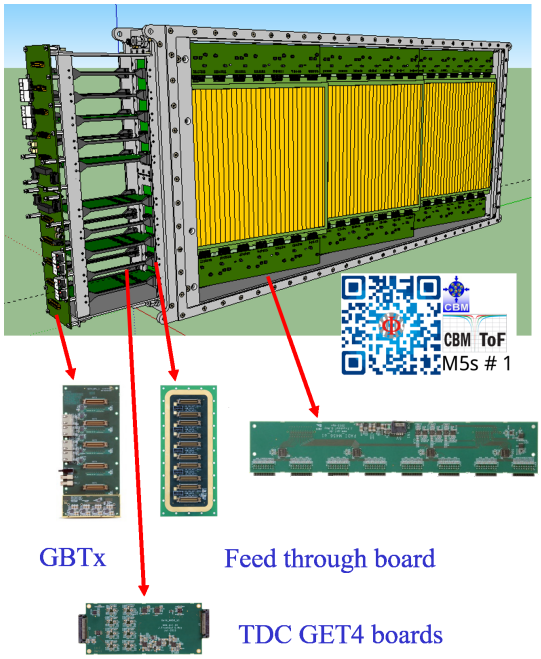

Fig. 4.55 eTOF module

All the eTOF modules were tested with cosmic-ray in a stack of 6 stations(modules) at Heidelberg as shown in Fig.4.56. About 100000 tracks which traverse all 6 stations could be accumulated per day. The gas mixture was 95% R134a and 5% iso-butane. No SF_6 was added due to the limitation in gas usage of the STAR experiment. The system is self triggered and the data flow is free streaming as foreseen in the CBM experiment.

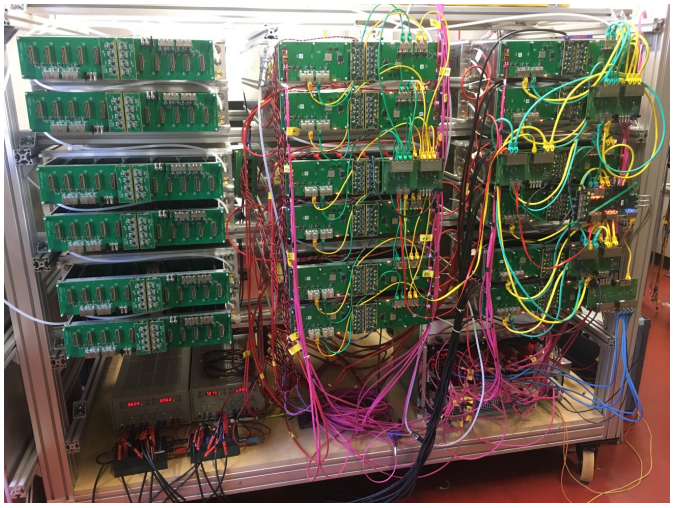

Fig. 4.56 The cosmic-ray test stand at Heidelberg University.

4.3.7 QA of STAR eTOF modules at Heidelberg

1. Date unpacking and event filtering

The GET4 system is running in free stream mode and all candidate events are recorded. How to select the events is very important for further analysis and calibration work. In the framework of CBMROOT, the TOF software uses a tracking method to pick candidate events. Its principle is shown in Fig.4.57. The 6 eTOF modules in the test stand are placed in the order as in the figure (4.57). Like in the Section 4.3.4, we first take the outermost 2 modules, which are module1 and module6 in Fig.4.57, as the reference candidate counters for the track reconstruction. If a cosmic-ray μ passes through the test stand, then along its trajectory a series of hit points may be generated in each layer of the MRPC counters. Provided the module1 and module6 are fired, each with a valid hit, we will connect the two hit points to form a candidate track 1 (if we have more hits on module1 and module6, each pair of hits will be looped and checked). Assume that the DUT is module2 and the reference counter is module3, then the candidate track 1 may have a hit point on the reference counter. We set a range for the position where the track 1 passes through the reference module, which contains the position and time information of the predicted hit point, represented by a parameter Chi-square in the analysis framework. If there is a hit on module3 within this range, this trajectory is considered a real track. If the hit point within the limited range is not found on module3, the candidate track will be discarded, e.g. the track 2 in Fig. 4.57. Hit points on both module4 and module5 can also be searched to further confirm that a true charged particle passes through the detectors. How many modules are needed to confirm a reconstructed track, which is determined by the parameters set in the code of data unpacking and later

analysis.

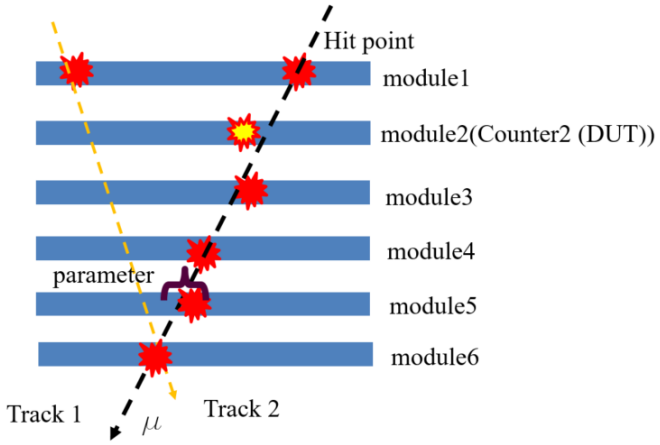

Fig. 4.57 Algorithm schematic diagram of event filtering.

In the off-line data analysis, the data unpacker builds events when at least 3 hit signals from different detectors were found. Although there are six modules in our test system at the same time, due to the imperfection in the electronics, in most cases only 3 modules contain valid data in the actual raw data.

The data are calibrated regarding the time and position offsets and the time walk. After calibration the track finding algorithm is applied and the resulting tracks are used to determine the efficiency, the time and position resolution. The algorithm is consistent with that in the TRB3 system.

The efficiency of each detector is determined by comparing the number of tracks with 2 hits to those with 3 hits. In other words, 2 hits on 2 counters define a track (acting as a reference) which is inter/extrapolated to the DUT. When a hit on the DUT is found close in the space and time to the reference track, the detector is considered to be efficient. Further more, residuals between the hit measured on the DUT and the track formed by the other 2 hits, can be determined. The width of the Gaussian shaped residuals deliver the time and space resolution of each counter. This method has the advantage that a multiple differential analysis can be performed and by track reconstruction the incident angle and the velocity spread of the cosmic rays are taken into account. Such as, there are 9 counters in the three eTOF modules. The counter in the first module can be calibrated with any of the counter in the second and third modules.

2. Time slewing

One thing we pay particular attention to throughout the testing process is the TOT distribution. In addition to its usage in the time slewing correction, we would like to know if

the TOT distribution contains only a single peak in the system operating in the cosmic-ray test, which indicates whether the impedance matching of our counter is still effective. Before the data of a counter is put into the analysis, we artificially choose two numbers 0 and 1 to represent the left and right end of the counter respectively. Fig.4.58 shows a typical TOT distribution of one eTOF MRPC3b counter, where the measured TOT is plotted vs. the strip number. (0 to 31, represents the left side of the counter, and 32 to 63 the right side). A clear single-peak structure of TOT is consistently distributed among all channels, shown in the figure as the red band. The lacking of multiple peaks indicates that the impedance adjustment of MRPC3b is effective, and the signal reflection is suppressed.

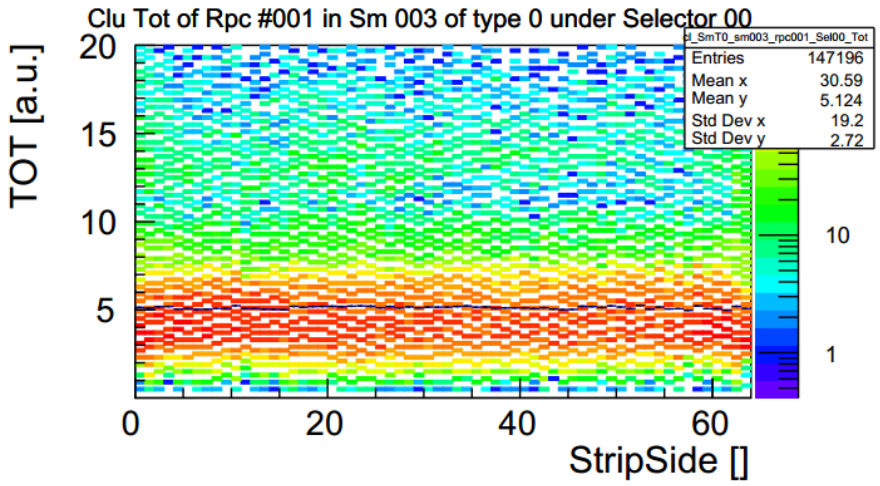

Fig. 4.58 A typical TOT distribution of one eTOF module.

A similar time slewing correction, as that for the TRB3 system, is done following the procedure in Section 4.3.5. Fig.4.59 shows a typical time slewing correlation in this QA test. We correct the time walk effect by using the bin-by-bin method in the CBMROOT. Fig.4.59 (a) is the distribution of time-TOT before correction, while Fig.4.59 (b) shows the same distribution after the 1st-round slewing correction. After about 20-50 iterations the corrected results come to converge.

3. Cluster size

Cluster size is another parameter we want to care about, which may affect the occupancy of the TOF modules operation. Fig.4.60 shows the results of the cluster size in this testing. Fig.4.60 (a) is the measured cluster size of one eTOF counter. The mean cluster size of this counter is 1.31, while the mean cluster sizes of all eTOF modules in the test are shown in Fig.4.60 (b). The overall average cluster size is 1.26, which is consistent

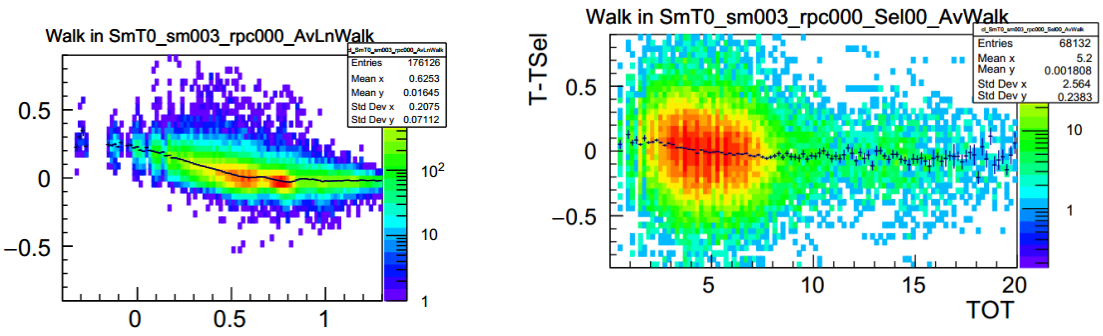

(a) (b)

Fig. 4.59 The distribution of time-TOT (a) before and (b) after the 1st-round slewing correction.

with the results obtained from the TRB3 system (Section 4.3.5).

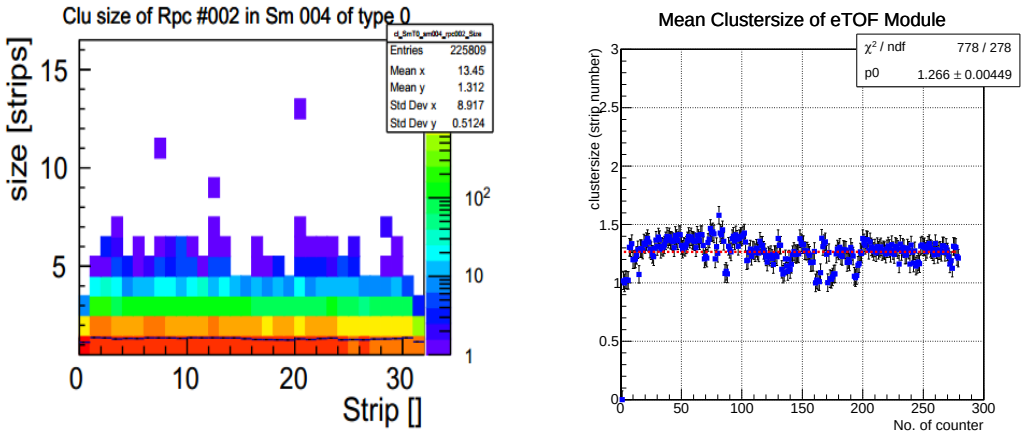

(a) (b)

Fig. 4.60 (a) is a typical clustersize image of one eTOF MRPC. (b) is the mean clustersize of all tests for the eTOF module.

4. Efficiency

In the whole QA procedure of the STAR-eTOF modules, due to the limitation of the STAR detector upgrade schedule, and the problems in the electronic clock synchronization, the module efficiency is reduced. The algorithm for calculating the efficiency is based on the track reconstruction, which is consistent with that in the TRB3 system. From Fig.4.61, we find that the eTOF module's efficiency is less than 95%. The left column of Fig.4.61 is the hit position (on the DUT) of all reconstructed tracks. The middle column shows the lost track, which means the reference track passes by and no fire point is found on the DUT. The right column of Fig. 4.61 gives the deduced detection

efficiency of the tested MRPCs. In Fig.4.61 we can see many "dead" channels with no fire, which is caused by the problem in the electronics mentioned above. Nevertheless we have managed to overcome the difficulties in the analysis of the QA data, although the efficiency obtained is a little lower.

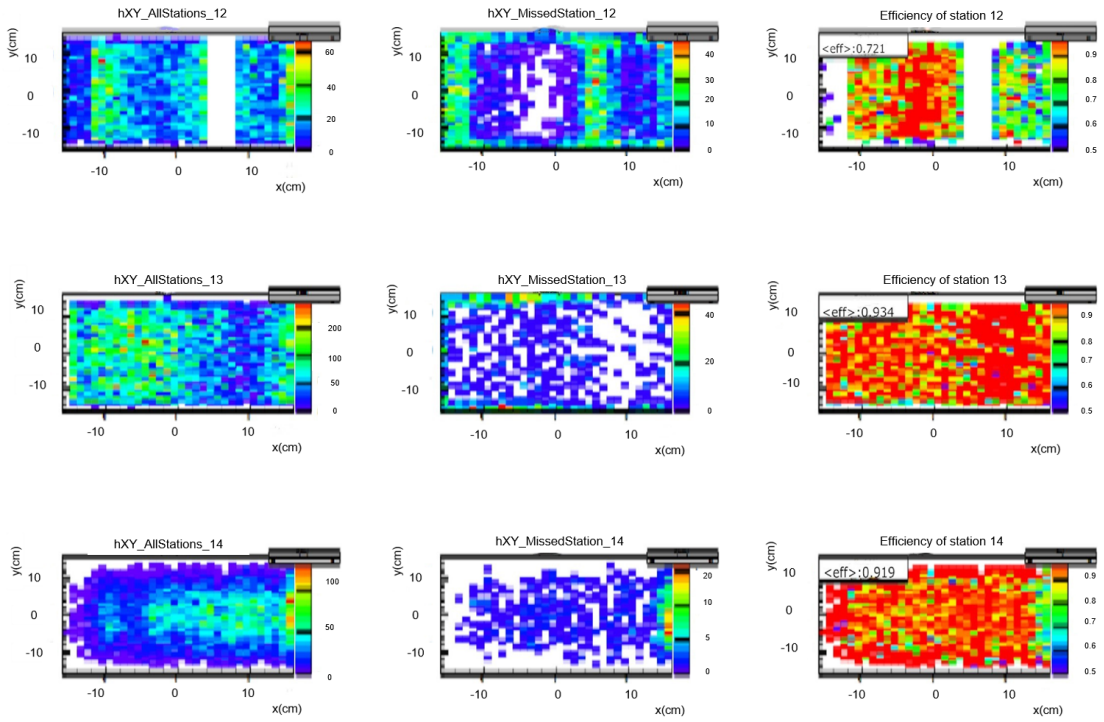

Fig. 4.61 The efficiency of the eTOF module tested at Heidelberg University.

5. Time resolution

In the QA test system at Heidelberg, the way to calculate the time resolution is consistent with the TRB3 system, and the distribution of $\sigma(T_{hit} - T_{track})$ is also measured by the tracking. The $\sigma(T_{hit} - T_{track})$ distribution gives an estimation of the time resolution through a Gaussian fitting. However during the QA test at Heidelberg, due to the instability of electronics, the data quality is relatively poor and the time jitter of electronics is worsened. Thus the time resolution obtained from the test is not so good. A typical time resolution histogram is shown in Fig.4.62, where 18 detectors are tested at the same time. Because the clock is not well aligned, two or more peaks appear in the distributions. The last plot in Fig.4.62 shows the time resolution of all 18 detectors in one test, which is around 100 ps with the exception of detector 0 and 3 whose time distribution are significantly distorted (so their resolution are not reliable). The time resolution results of all the MRPC modules tested are summarized in Fig.4.63. The

mean time resolution of the eTOF modules is 104.1 ps with the GET4-GBTX-PADI system.

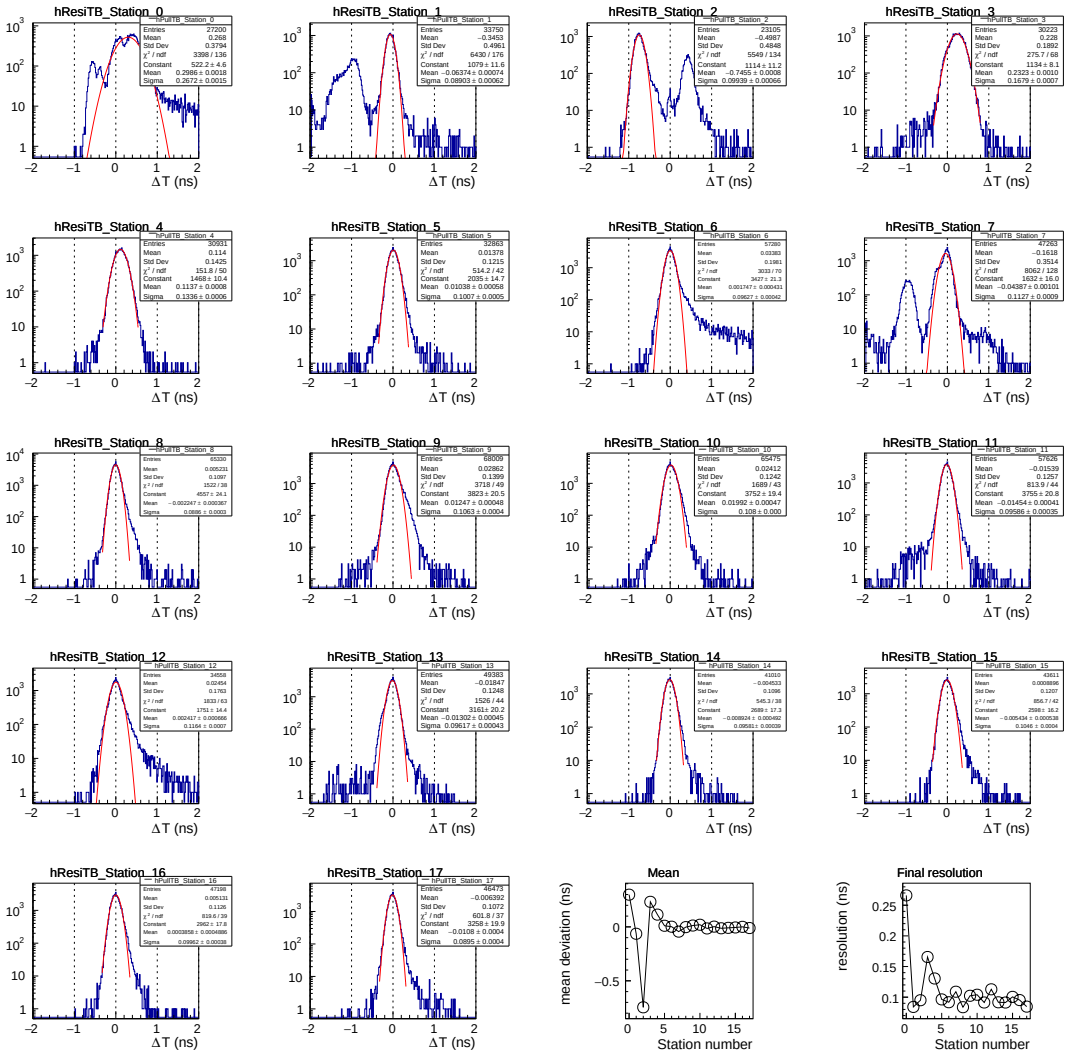

Fig. 4.62 A typical time resolution distribution of eTOF module in one time testing.

4.3.8 Summary of the mass production

All MRPC3b counters used in the CBM/STAR-eTOF are mass-produced at USTC. Batch testing of the MRPC3b counters was also done simultaneously at the USTC High Energy Physics Laboratory. In total, 100 MRPC3bs have been produced and tested. 99 counters passed the QA procedures with excellent performances. This amount counts for around 10% of the counters to be constructed for CBM TOF by USTC. By this pro-production, the manufacture procedures and the QA & QC methods have been demonstrated working properly. Fig.4.64 shows the preliminary PID results with the installed STAR-eTOF which validates the functionality of the system.

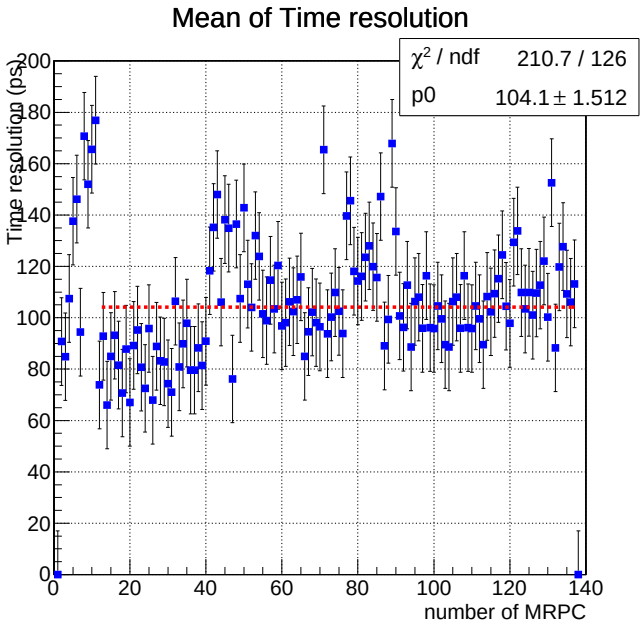

Fig. 4.63 The time resolution of all the eTOF modules tested at Heidelberg. Some of these counters have undergone two times cosmic-ray tests.

During the mass production, all the MRPC3b counters tested were completed by the same high-voltage modules (the iseg high-voltage suppliers plug-in on the Wiener HV crate) during the HV training. These high-voltage modules are shown in the Fig.4.65 (a). The leak current of the counter is monitored and recorded in real time by the Control and Monitor interface GUI base on the LabView. A typical leak current value is shown in Fig.4.65 (b). The leak current of the MRPC3b counter is usually measured to be around 25 nA (Fig.4.66), which is well qualified for this type of MRPC.

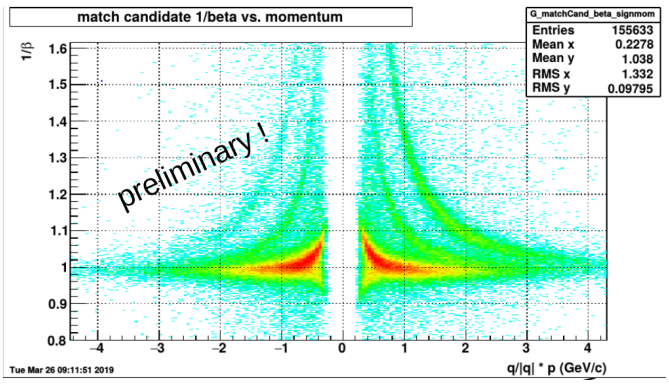

Fig. 4.64 The preliminary PID results with the installed STAR-eTOF.The picture taken form Philipp Weidenkaff .

The noise rate, as an important parameter related to the counter performance, was measured during the QC steps. Fig.4.67 shows the mean noise rate of all the tested counters. It's clear that the measured values are well below the upper limit of the QC

(a) (b)

Fig. 4.65 (a) The HV module used in the QA and HV training of the mass-produced MRPC3b counters, and (b) the leak current monitor GUI.

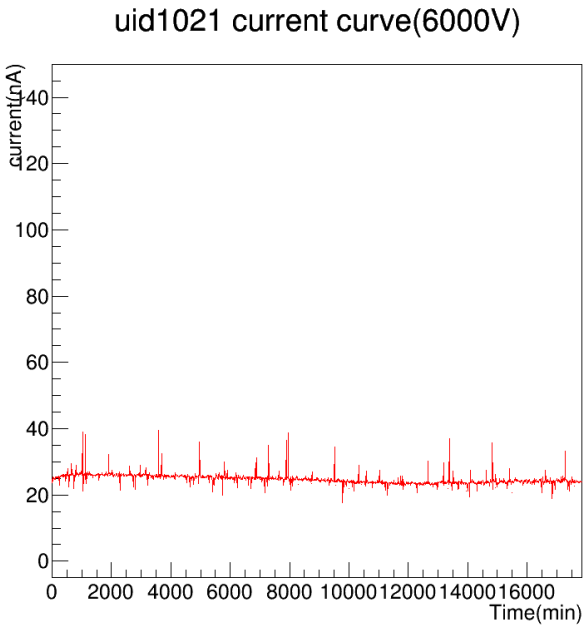

Fig. 4.66 The mean leak current of MRPC3b counter.

standard, as indicated by the red line. But, from the strip-wise distribution, we found some problem with such statistics. We draw a statistical histogram for the mean noise rates on each strip for all the 80 counters. A Gaussian fit gives the mean value of the distribution and the σ. We use the mean value as the noise rate of the certain strip, and the doubled σ as the statistical errors. We draw a noise statistical distribution of all the 32 strips with the mean values and the given statistical errors, as shown in the Fig.4.67. Fitting with a straight line to 31 of the strips (except for the first one), we get a mean value around 31.7 Hz/strip, which consist with the counter-wise result. But, as can be seen from the figure, the first strip has a higher noise rate. The position of this strip is closest to the high voltage strip. Especially, by comparing to the value from the last strip, we suspect that there should be some correlation with the HV injection method. We will continue to study the reason of the high noise rate on this strip.

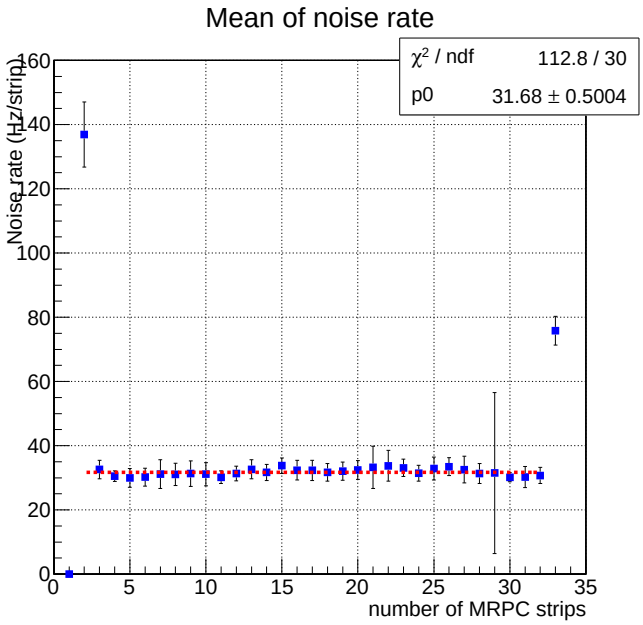

Fig. 4.67 The mean noise of each strip.

For the MRPC3b counter time resolution, we compare the results of the USTC electronics test system shown in Fig.4.31 with the test results given by the TRB3 system (as shown in Fig.4.51), the intrinsic time resolution of the MRPC3b counter is around 52 ps. Since different analysis methods were applied to these two systems, the difference of the obtained results is understandable. For the USTC system, the contributions from the reference counters has been taken into account and eliminated from the final results. But in the case of TRB3 system, the distribution of T-hit - T-track including the contribution from the reconstructed tracking time, which is difficult to estimate. Never the less, these results are lower than the CBM TOF requirement for the QC standard of MRPC3b

counters. So, in terms of time resolution, the mass-produced MRPC3b counters are qualified. In addition, the MRPC3b counters are also qualified from the efficiency of both the USTC electronics system and the TRB3 system test. Fig.4.68 is the efficiency statistics from the two systems. Figure (a) is an efficiency profile obtained by the USTC electronics test. Figure (b) is the efficiency chart obtained by the TRB3 system test. By comparing the two figures, we can get that the efficiency of MRPC3b counter in batch test is around $\sim$ 95%.

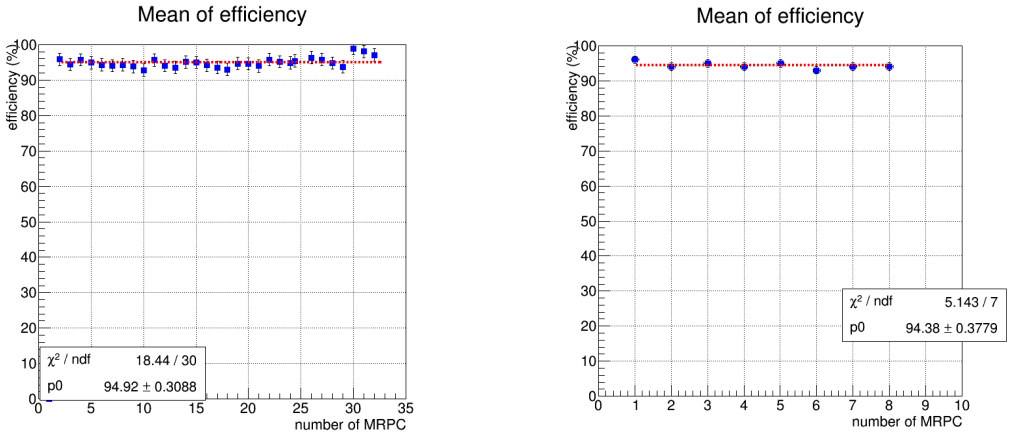

(a) (b)

Fig. 4.68 Image a is an efficiency diagram of the MRPC3b counter tested by the USTC electronics system, and Figure b is an efficiency diagram of the MRPC3b counter tested by the TRB3 electronics system.

From the TOT distribution, as an important evidence of the correct impedance matching, we can conclude that the signal reflection is suppressed to a certain extent, as shown in Fig.4.69 where the results of the beam test on a prototype and the batch test with TRB3 system are shown. The TOF requirements for MRPC3b have been basically met. The optimization will continue along this direction.

So far, the mass production and QA&QC of the eTOF module has come to an end. In total, 36 modules and 108 detectors have been produced and tested. Although there are some bugs in the test system to be fixed and abilities to be improved, the performance of there are various bugs in the electronics system during the testing process, the performances of the detectors meet our requirements from the results given by several test stand systems respectively. By November of 2018, the installation of the full eTOF wheel has been finished at BNL.

Fig.4.70 shows the full wheel installation layout. The entire eTOF system comprises 36 modules, 3 layers, 12 sectors, 6912 channels, and the corresponding readout electronics. In the whole eTOF detector system, 24 modules use MRPC3b built

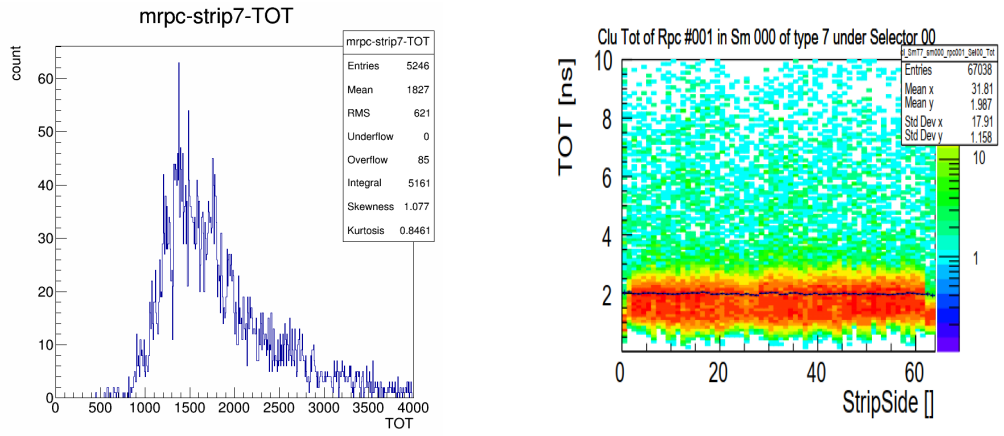

(a) (b)

Fig. 4.69 Figure (a) is a TOT distribution of the results of the prototype beam test, and Figure (b) is a typical TOT distribution from the 64 readout channels in the TRB3 system test.

by USTC and 12 Modules use MRPC3a built by Tsinghua University, respectively. Fig.4.71 shows the eTOF module and the electronic. Each module's active area is 97 × 27 cm^2 subdivided into 96 readout strips. Each module has 192 readout channels and houses 3 detectors.

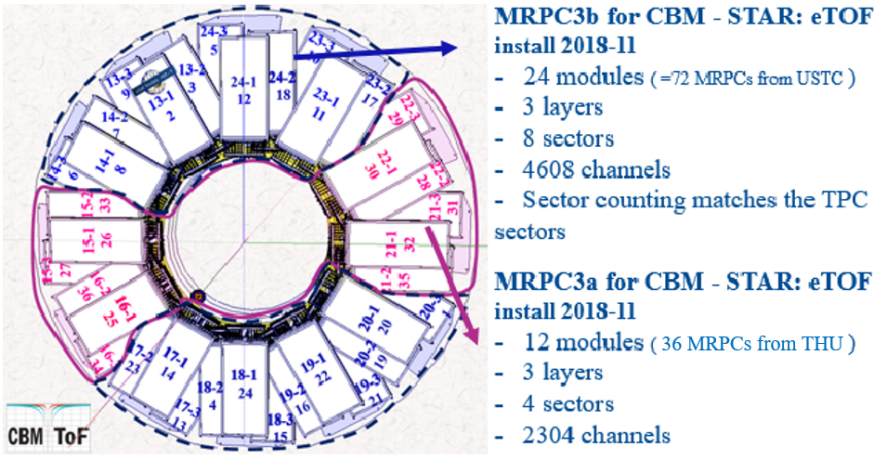

Fig. 4.70 The actual layout of the eTOF wheel, in the east endcap region of the STAR experiment at BNL.

4.3.9 Plan for the future improvement

As demonstrated in Fig.4.67, the first strip of the MRPC3b counter shows a noise rate significantly higher than the rest strips, which to our opinions may be crosstalk caused by the HV strip. To better understand this phenomenon, we have done some simulation work based on the Computer Simulation Technology (CST) software[99], which is a

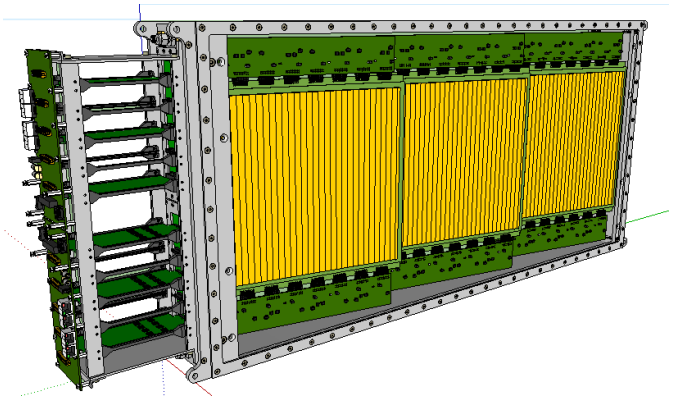

Fig. 4.71 eTOF Module image with electronic.

powerful simulation platform for all kinds of EM problems and related applications. The following simulation attempts have performed focusing on the HV strip and the first readout strip.

- Increase the distance between the HV strip and the first readout strip.
- Add a dummy (GND) strip between the first readout strip and the HV strip.
- Change the shape of the HV strip.
- Change the area of the HV strip.

Fig.4.72 shows the simulation results by changing the distance between the first readout strip and the HV strip. In the simulation we set up three readout strips and one HV strip. The size and position of the HV strip is consistent with one of the actual MRPC3b counter. In the plots, the red line represents the inductive signal of the first strip, the green one the second strip and the blue one the third strip. As can be seen from the figure (a) to (c), as the distance between the readout strip and the HV strip increases, the inductive signal of the first strip decreases. And in all cases the noise rate on the 2nd and 3rd readout strips are small compared to the 1st strip. From the current results, it is true that the position of the HV strip will affect the noise count rate of our first strip. Further simulation study is still on-going, and an improved version of MRPC will be designed and tested.

Another aspect that may need more attention is the impedance matching. Although the structure of MRPC3b have been designed to suppress the signal reflection, as discussed in Chapter 3, there still exist in a small fraction of the produced MRPC counters with mis-matched impedance, which is usually manifested as multiple peaks in the measured TOT distribution. The reason is not clear for the moment. Study on this topic is

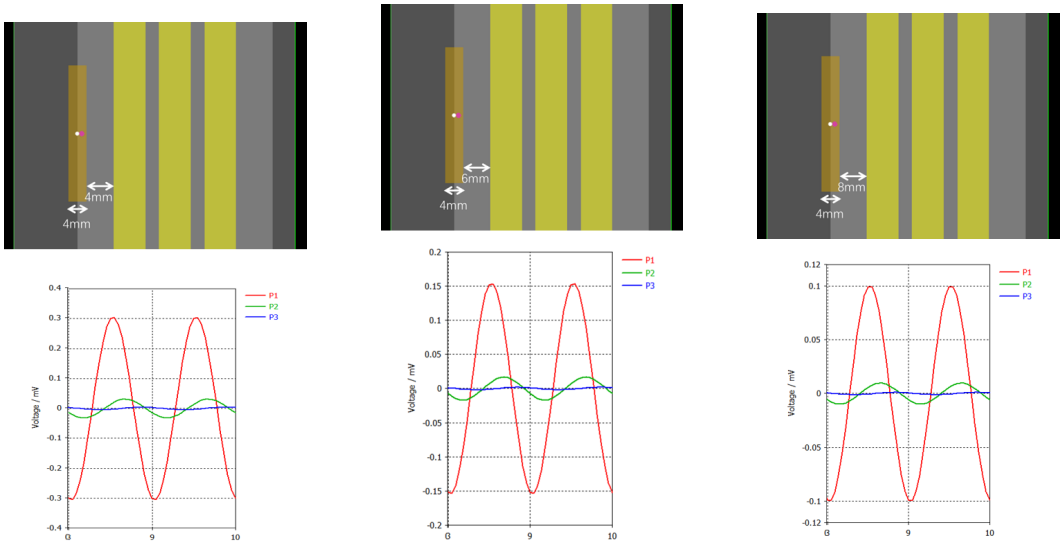

(a) (b) (c)

Fig. 4.72 The CST simulation results: noise rates on the 3 readout strips caused by the HV strip, with different distances (a) 4 mm, (b) 6 mm and (c) 8 mm between the first readout strip and the HV strip.

continuing and further improvements are essential for the future mass production of CBM-TOF, especially the MRPC4 counters with longer strips.

Chapter 5 The study of prototype MRPCs for the T0 detector at the CEE

5.1 Design of CEE-T0

Although CBM/STAR eTOF detector and CEE T0 detector are both make up of MRPC detector, their functional requirements and operation environments are very different. In order to adapt fit the experiment condition at CEE, a Monte Carlo simulation based study is required before we design the detector. For this reason, Fast Simulation of CEE detector has been developed, based on the Geant4 toolkit, with developed components dedicated to heavy ion physics.

5.1.1 Simulation of the TOF

A GEANT4 based Monte Carlo (MC) simulation is used to determine the criteria for the CSR-TOF. The relevant structure of the CEE is built in the simulation, including the magnet, the tracking detectors and the TOF system. The main parameters of the sub-systems are listed in Table 5.1.

Table 5.1 The main parameters of the subsystem.

Sub-system		*Position (m)*	*Size (m)*	*Note*
Target		*0*	*0.01*	*Air target*
Magnet	*Yoke*	*0.7*	*3.2×3.0×4.2*	*Super-conducting dipole*
	Inner field		*2.2×1.0×1.8*	
Tracking	*TPC*	*0.7*	*1.1×0.9×1.0*	
	MWDC	*2.0*	*~ 1.6×1.2×0.1*	*3 layers, 2 modules per layer*
TOF	*T0*	*0*	*0.2/0.4 radius*	*MRPC, inner/outer layers*
	iTOF	*0.7*	*1.0×0.9×0.1*	*MRPC, 2~4 modules*
	eTOF	*2.5*	*3.0×2.0×0.1*	*MRPC, 2 modules*

In the GEANT4 simulation, a kinetic energy 1.0 AGeV Ar-Ar collision is generated by UrQMD3.4.6[100], about 10 k UrQMD generated events have been fed to the MC detector system to test the TOF performance. The time difference between the collision point and the hit on TOF detector is recorded. Several TOF timing uncertainties are studied, from 50 ps to 200 ps at a step of 50 ps. A 5% smearing to the particle momentum has been added to account for the reconstruction uncertainty. The track length

uncertainties of 0.5 cm and 2 cm are also included in the simulation for particles hitting the iTOF and eTOF respectively. The simulation results are shown in Fig.5.1, for both iTOF and eTOF, with the TOF time resolution setting at 100 ps. In the plots the red and blue areas denote bands within 2σ of the m^2 distribution of pions and protons, as a function of momenta. The pink arrow marks the upper momentum under which 99.5% of the pions reside. The black arrow has similar meaning for protons. There were very few kaon in the final state, so they were neglected in the plots. It is clear from the figure that the pion/proton separation is easier for eTOF because of the much longer flight path (>2.5 m) than iTOF (0.5∼1.2 m), and a TOF system with an overall time resolution of 100ps is quite adequate for pion/proton identification at CEE.

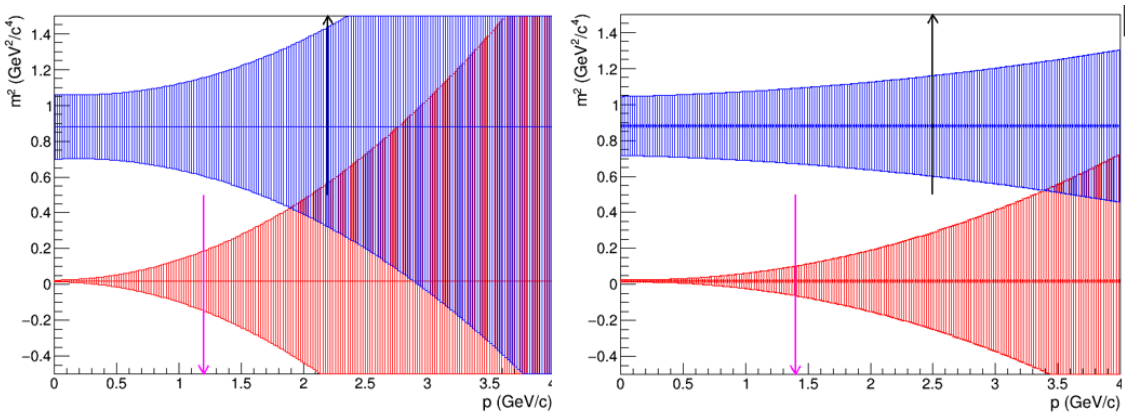

Fig. 5.1 The m^2 distribution vs. particle momentum, measured by CEE iTOF (left) and eTOF (right). In both plots the red and blue areas denote bands within 2σ of the m^2 distribution of pions and protons, as a function of momenta. The pink arrow marks the upper momentum under which 99.5% of the pions reside. The black arrow has similar meaning, but for protons.

5.1.2 Requirements of the T0

In order to achieve good timing and event plane resolution, high granularity is needed to keep the occupancy low. At CSR energy region (<1 AGeV for light nuclei and ∼0.5 AGeV for heavy nuclei) the charged final-state particle yield is close to A+B, where A and B are the atomic numbers of the projectile and target nucleus respectively. Even for the heaviest collision system of Uranium+Uranium, the charged particle multiplicity is around 200. The T0 system covers ∼10% of the final products (by simulation study), corresponding to ∼20 particles. By requiring an occupancy of no more than 20%, the T0 needs at least 100 readout channels. At CEE experiment, the collision rate is estimated to be at most 10 kHz. Assuming 20 charged particles hitting T0 detector for

each collision, and ∼800 collisions per cm^2 sensitive area for inner modules of the T0 (see T0 design later in the thesis), the counting rate is at most 250 Hz/cm^2. This rate is suitable for the multi-gap resistive plate chamber (MRPC) using normal float glass[101].

The T0 detector need to provide a high precision collision time for the experimental system. In addition, low noise, fast signals must be provided by the T0 detector to serve as low-level trigger inputs for the CEE. The multi-gap resistive plate chambers is a gaseous detector with excellent timing accuracy, suitable for precision timing and fast trigger purpose. Considering all the experimental condition and requirements, the MRPC[35,101-103] is chosen to build the detector, which combines the required performance with an affordable cost. This device, developed during a long time research and design, shows very good uniformity, long streamer-free working plateau, good efficiency, excellent time resolution and low cost. It is also irradiation resistant and immune to magnetic field. From the simulation, a CEE-T0 detector system with time resolution better than 80 ps and efficiency above 95% is considered to meet all the requirements.

5.1.3 Design Considerations of T0 Detector

1. Consideration of T0 Detector A

In the GEANT4 simulation we included only the MRPCs, along with the gas boxes and FEEs. The target and other supporting structure were ignored. To improve simulation efficiency, the T0 detector was assumed to have full acceptance, like in Fig.5.3. The heavy-ion collision event was simulated by the UrQMD3.4 generator[100]. The incident beam consisted of argon-40 nucleus and the target was carbon-12. The kinetic energy of the beam was 300 AMeV. We assumed in the simulation that the MRPC intrinsic timing uncertainty was 50 ps, 75 ps and 100 ps. The Fig.5.2 (a) plot shows the deduced T0 time resolution by a single track, while the (b) plot illustrates its dependence on the number of tracks that hit the T0 detector. The collision vertex was fixed, so its position did not contribute to the overall resolution. Fig.5.2 (b) also shows that the T0 time resolution quickly decreased to ∼50 ps for more than five track, and it was saturated at ∼30 ps. We would expect even better performance by fine-tuning and calibration of the experiment. For comparison, the T0 time resolution with a one-layer design for the T0 detector is also shown, it is about 30-50% worse than the double-layer design.

Through the simulation, it is found that due to the low relative energy of CEE, the velocity distribution of the final-state charged particles spreads wide, therefore, the T0 resolution obtained by a one-layer timing measurement design is poor. The double-

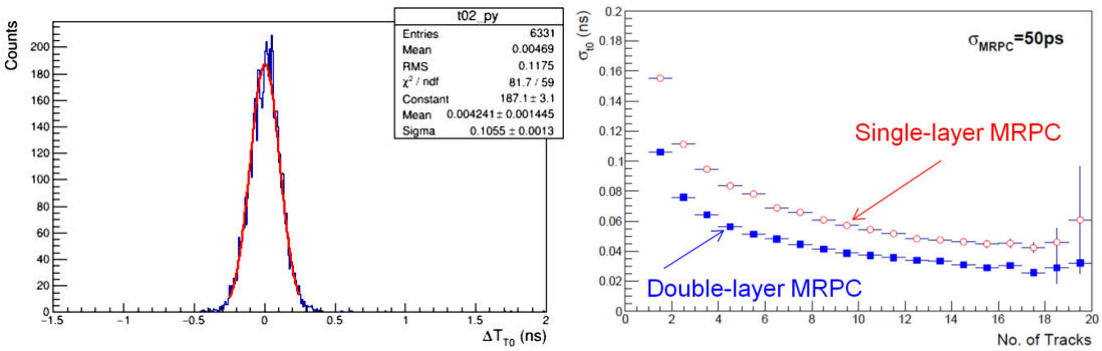

(a) (b)

Fig. 5.2 The T0 time resolution from simulation data.

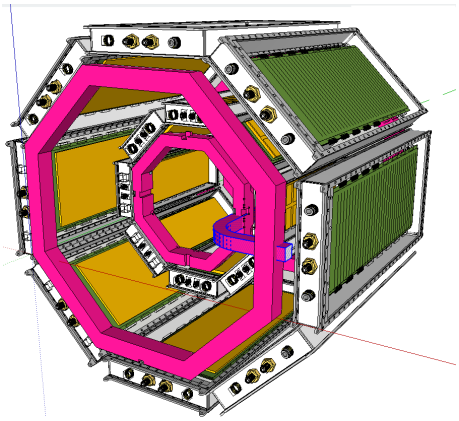

Fig. 5.3 The conceptual design of the CEE-T0 module.

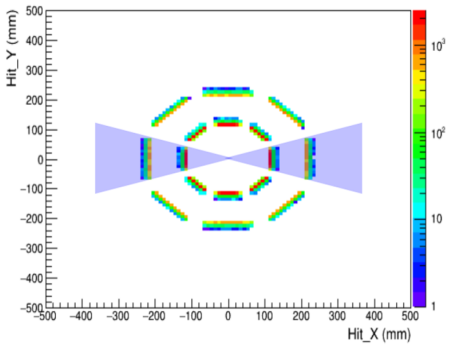

Fig. 5.4 CEE prototype T0 module.

layer design improves the T0 performance significantly, which confirms our expectation when designing the detector.

2. Consideration of T0 Detector B

The CEE-T0 detector is required to provide not only the collision time precisely, but also the reaction event plane determination. In order to achieve good timing and event plane resolution, high granularity is needed to keep occupancy low. In CSR energy region (~1 AGeV for light nuclei and ~0.5 AGeV for heavy nuclei) the charged final-state particle yield is close to A+B, where A and B are the atomic numbers of the projectile and target nucleus respectively. Even for the heaviest collision system uranium+uranium, the charged particle multiplicity is around 200. The T0 system covers ~10% percentage of the final products (by simulation study), corresponding to ~20 particles. By requiring an occupancy of no more 20%, the T0 needs at least 100 readout channels. In the CEE experiment, the collision rate is estimated to be at most 10 kHz. Assuming 20 charged particles hitting T0 detector for each collision and ~800 /cm^2 sensitive area for inner

modules of the T0 (see T0 design later in the paper), the counting rate is at most 250 Hz/cm^2 see Fig.5.4. Such a counting rate is suitable for MRPC detector using normal float glass plates.

3. Consideration of T0 Detector C

Fig.5.5 shows the results of the gold-gold collision system at 500 AMeV incident energy, and it can be seen that the T0 detector has good measurement accuracy for the reaction plane is semi-head-on collisions. Considering the entire T0 system design and its installation acceptance, even if the azimuth coverage is only half (this is, 180 degrees), the reaction plane determination accuracy can also reach about 10 degrees, so it can be used for experimental rapid trigger selection.

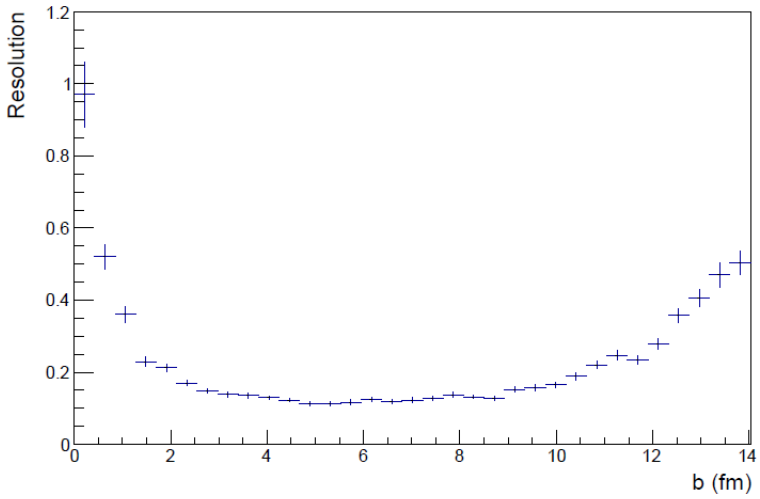

Fig. 5.5 The accuracy of the event plane angle changes with the collision parameters in the gold-gold collision at an incident kinetic energy 500 AMeV.

5.1.4 Design of CEE prototype T0 Detector

1. Design of T0/trigger Module

（1） Conceptual Design of T0/trigger Module

Considering that the final charged particles with low energy may be scattered or absorbed by the T0/trigger detector material medium, the thickness of the aluminum box is set to a conservative 1 cm and the thickness of the cover is set to 1mm. Our first version of the conceptual design is to place the FEE in the upper part of the cover as shown in Fig.5.6. The FEE board is installed closely on the left and right sides of the box, it is connected to the data readout board on the top of cover through flexible plate. Fig.5.7 is a first version of prototype Module.

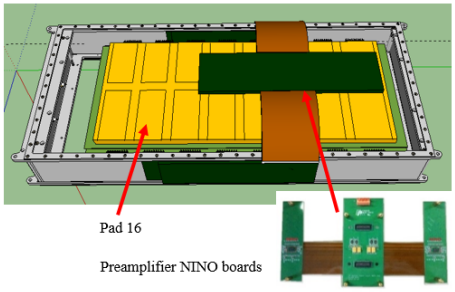

Fig. 5.6 The conceptual design of the CEE-T0 module.

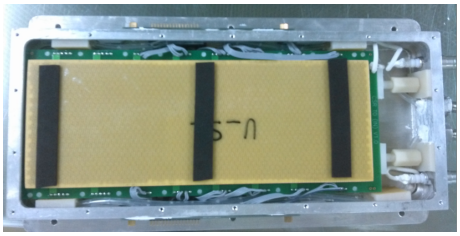

Fig. 5.7 CEE prototype T0 module.

（2） Module optimization

We did a series of experiment with this first version T0/trigger Module, which will be described in detail at the later chapter. After the practical experimental testing, we have optimized the entire module, focusing on the layout of the module, recently.

2. Design of prototype T_0-MRPC

（1） Conceptual of Prototype MRPC

From the design considerations mentioned above, we know that the T0 detector composes of two parts, contains an inner and an outer layer. Each layer is made up of several MRPCs, suitable for high precision timing and fast trigger purpose. Base on the simulation, two kinds of the MRPC is designed for the T0 layers. Due to the higher multiplicity density, for the inner layer MRPC we plan to use pad readout, as shown in Fig.5.8. For the outer layer MRPC, strip readout is chosen see Fig.5.9

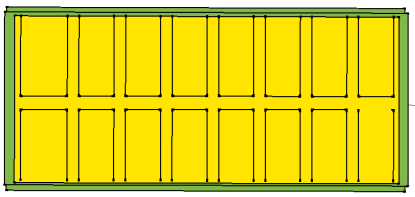

Fig. 5.8 The conceptual design of the inner layer MRPC.

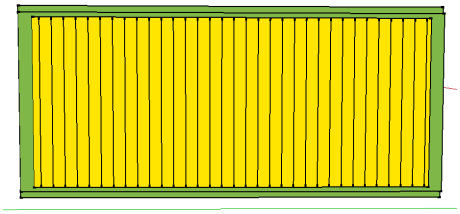

Fig. 5.9 The conceptual design of the outer layer MRPC.

（2） Structure of Prototype MRPC

The inner and an outer layers of the T0 detector are each composed of eight. Fig.5.10 shows the design of the two kinds of MRPCs, one for the inner layer of T0 and another for the outer layer. The smaller inner MRPC shown at the top of Fig.5.10 (a) have 16 single-end differential readout pads, each 2.15 cm wide and 3.05 cm long with a 0.35 cm gap, and the outer MRPC has 12 dual-end differential readout strips, each 2.6 cm

wide and 12.0 cm long with 0.4 cm gap. The active volume is subdivided by 0.5 mm thick float glass plates to form a total of twelve gas gaps arranged in a double-stack configuration that is mirrored with respect to the central electrode (Fig.5.10 bottom (c)). High voltages (HV) are applied to the external electrodes surfaces. Each gap width is 0.22 mm, defined by nylon fishing line. Fig.5.10 (upper right (b)) shows a photo of the finished inner and outer MRPC modules.

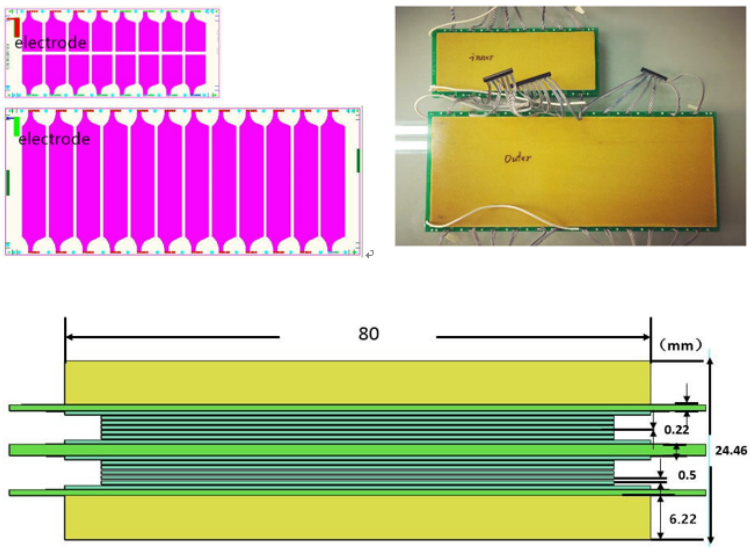

Fig. 5.10 MRPC module design and prototypes. The readout pad design for the inner layer is shown in left image (a) at the top left, and the design for outer layer of the MRPC is shown in the lower image (a) at the top left. The photo of the finished MRPC prototypes are shown at the top right (b). The side view of the MRPC is shown in the bottom image (c).

5.2 Test Stand System for CEE T0/trigger in USTC

5.2.1 Front-end Electronics

The front-end electronics (FEE) are located outside the gas box containing the MRPC module (Fig.5.12 bottom (b)), which makes use of the NINO chip[104]. Fig.5.11 shows that the inner MRPC module's two NINO chips are used for 16 readout channels, and the outer MRPC module's four NINO chips are used to handle 24 channels. The off-chip resistor in the FEE (the "External matching resistor" in Fig.5.12 top (a)) is used for impedance matching[40], and each FEE module outputs corresponds LVDS signals with fast leading edges for timing purposes and the signal charge information contained in its width.

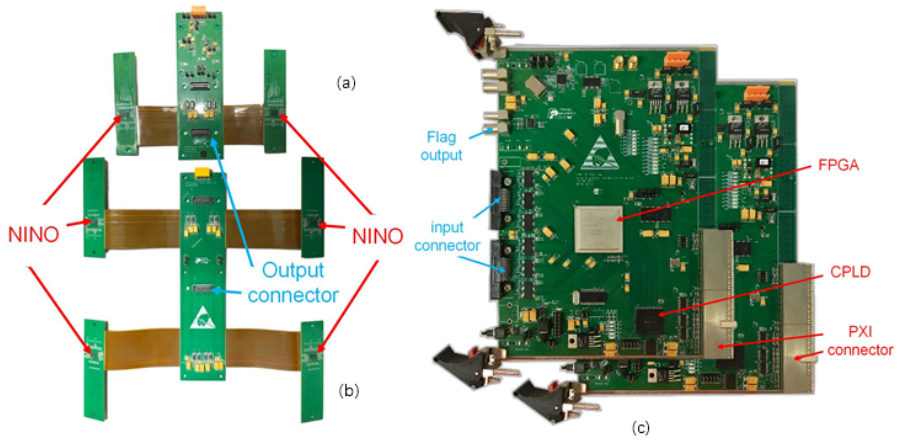

Fig. 5.11 NINO-based FEE modules for the inner (top a) and outer (bottom b) MRPC module. FPGA-based time-to-digital convector (TDC) is shown on the right. This FPGA TDC can achieve both leading and trailing edge time measurement with high precision. The trigger matching and other functions are also integrated.

5.2.2 Readout Electronics

The signal from FEE is then processed by the field programmable gate array array-based time-to-digital convertor (TDC) module[105]. The field programmable gate array (FPGA) TDC can achieve both leading- and trailing edge time measurement in a single channel based on the carry chain structure within the FPGA slice resource with an accuracy of <25 ps. Trigger pre-processing, trigger matching based on CAM and DPRAM, and other functions are also integrated in one single FPGA device. The TDC module is designed based on PCI eXtensions for Instrumentation (PXI)-6U standard. The hardware configuration, data transfer, and online reconfiguration of the FPGA logic can be conducted by using a single board computer (SBC) located in Slot 0 through a PXI bus. A USB interface is also employed for system debugging. The block diagram of the readout electronics is shown at the top of Fig.5.12 (a). Fig.5.11 (c) shows photographs of the FEE and FPGA TDC modules. After the readout electronics were designed and tested[106], preliminary commissioning tests with the four T0-MRPC prototypes, including the two inner and two outer modules, were conducted in the laboratory with cosmic rays. Next, the whole system was fully tested with hadron and heavy-ion beams to study its performance in detail.

5.2.3 Time resolution of the test system

To ensure the stability of the system, we use the signal source and T0r system to check this DAQ system. Fig.5.13 shows the time jitter from this DAQ system. From the image

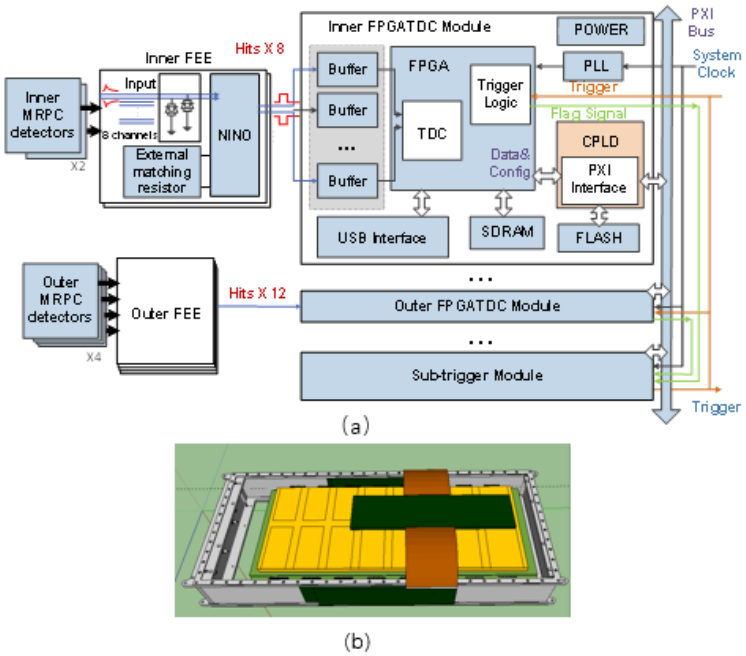

Fig. 5.12 Block diagram of the readout electronics and CSR T0 Module.

(a) we can see. The time jitter of this DAQ system is less than 20ps and has a better uniformity as shown in Fig.5.13 (b).

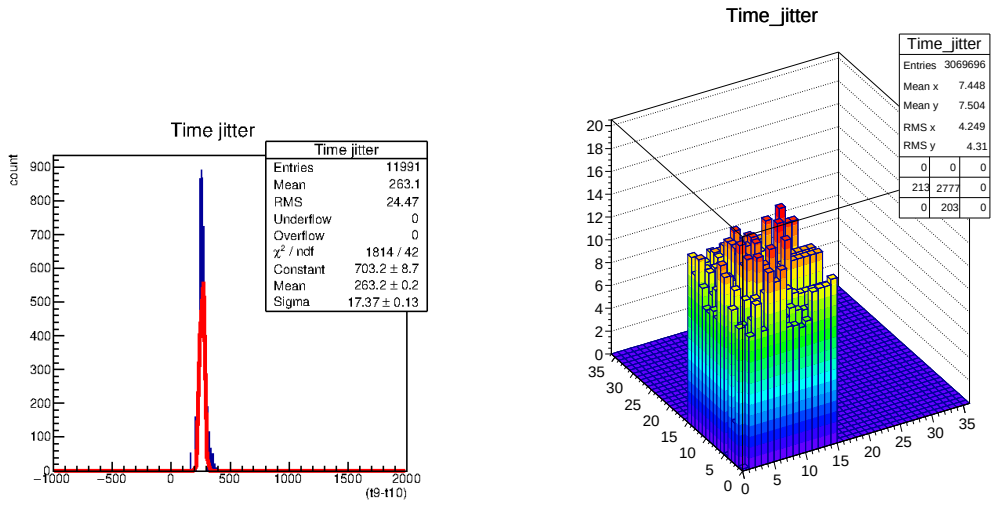

(a) (b)

Fig. 5.13 Figure (a) shows cosmic ray test block diagram. Figure (b) shows cosmic ray test stand at USTC. The trigger detector, MRPC module and the readout system are shown.

5.3 Results of CEE prototype T0 detector

5.3.1 Cosmic test stand

Before we perform detailed study with test beam, the cosmic ray test for prototype T0 detector is need. So a cosmic ray test system was set up to check the MRPC's performance. Four T0-MRPC prototypes, two inner and two outer modules, are constructed and preliminary tested in the lab with cosmic-rays. As shown in Fig. 5.14 (b) is a photo of the test stand and in Fig.5.14 (a) is the schematic structure. When the cosmic ray passes through the scintillators, the coincidence signal of the 4 PMTs gives the trigger to the system. We use the average timing of all 4 PMTs times as the reference time (T0).

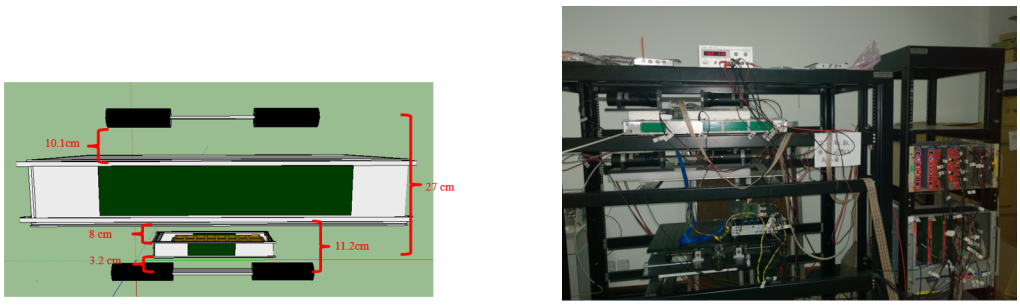

(a) (b)

Fig. 5.14 Figure (a) shows cosmic ray test block diagram. Figure (b) shows cosmic ray test stand at USTC. The trigger detector, MRPC module and the readout system are shown.

5.3.2 Cosmic Ray Test Study of Prototype

We digitize the timing information from MRPC FPGA TDC and HPTDC. The Calibration is done pad by pad. Fig.5.15 shows the position of every pad in the test module, which is determined by the time difference of PMTs (coupled to different sides of the scintillator).

After corrected for the T-TOT correlation effect, the MRPC's time distribution relative to T0 is shown in Fig.5.16. The distribution is fitted with a Gaussians function, and gives a variance (σ) of 109 ps. After subtracting the T0 jitter of $\sim$60 ps, the MRPC's intrinsic time resolution of different MRPC readout pads are shown in Fig.5.17. The time resolution of inner layer MRPC is around 80 ps, consistent with other cosmic-ray results of similar MRPC structure. Fig.5.17 (a) shows the MRPC time resolution of different readout pads measured by HPTDC and Fig.5.17 (b) shows the results measured

by FPGA TDC for the same MRPC module and FEE. Both results are consistent.

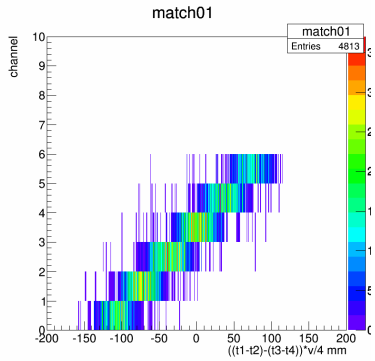

Fig. 5.15 Hit position in the test module measured by the cosmic-ray test stand.

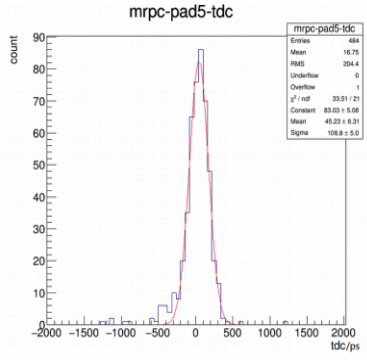

Fig. 5.16 Typical MRPC time distribution relative to T0.

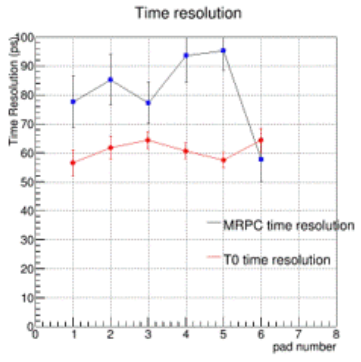

(a)

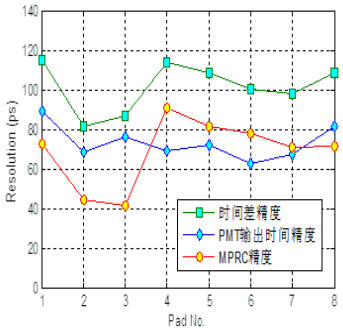

(b)

Fig. 5.17 (a) MRPC time resolution of different readout pads measured by HPTDC. (b) MRPC time resolution measured by FPGA TDC.

5.3.3 Beam test setup for T0

In October 2016, two inner and two outer MRPCs for the CEE-T0 detector were tested at the IHEP-E3 line. The sketch of the in-beam test setup in shown at the chapter 4. The HV was set at 7200 V, and the threshold was set to 220 mV for the test. If a particle though SC1, SC2, T1, T2, T3, T4, its signals are fed to a splitter. One copy is sent to HPTDC for precise timing measurement[104,107], while another output copy is fed to the discriminator. The HPTDC module, which has discrimination and signal transfer ability, was built by the USTC Electronics Group. After discrimination, the coincident signals of the SC1 and SC2 act as the trigger for the system. The digital signal from T1 to T4 act as the reference time start signals of the test system. The MRPC signals are amplified and discriminated by the FEE and then recorded by the FPGA-TDC. The difference between leading- and trailing-edge timing gives the signal

width (TOT) information. The MRPC module were placed in a gas-tight aluminum box and flushed with a working gas mixture of 90% R134a, 5% iso-butane, and 5% sulfur hexafluoride (SF_6). The operational parameters values were set according to the cosmic ray test results[5,108].The results and the analysis of the collected data are described in the following.

5.3.4 The result of hadron beam test

1. Time resolution

The IHEP-E3 beam was generated by bombarding a target with a primary electron beam such as Cu, Be or C. The secondary particles mix with e, π and p, primarily protons and pions, so the first step of the analysis was to distinguish different particles. Fig.5.18 (a) shows the scatter plot of time difference between T1/T2 and T3/T4 and the signal charge of the Tr0 detector. The Q_{T0} plot on the right (b) shows the average signal charge of all four channels of Tr0 detector, which represents the energy deposition, and ΔT=$\frac{(T1+T2+T3+T4)}{4}$, which represents the TOF from T1/T2 to T3/T4 of the incident particles. At a beam momentum of 700 MeV/c, protons deposit more energy in the Tr0 detector (scintillator) because of the larger dE/dx, and they travel more slowly than pions, resulting in smaller ΔT values across a defined path length (the distance between the T1/T2 pair and the T3/T4 pair). These influences are reflected in Fig.5.18. The separation of pions and protons can be clearly seen. Fig.5.18 (b) also shows the ΔT distribution. By a Gaussian fit, we estimated the Tr0 time resolution to be $\sim$ 40 ps for proton beam. For pions, the Tr0 time resolution was a little larger, being close to 60 ps.

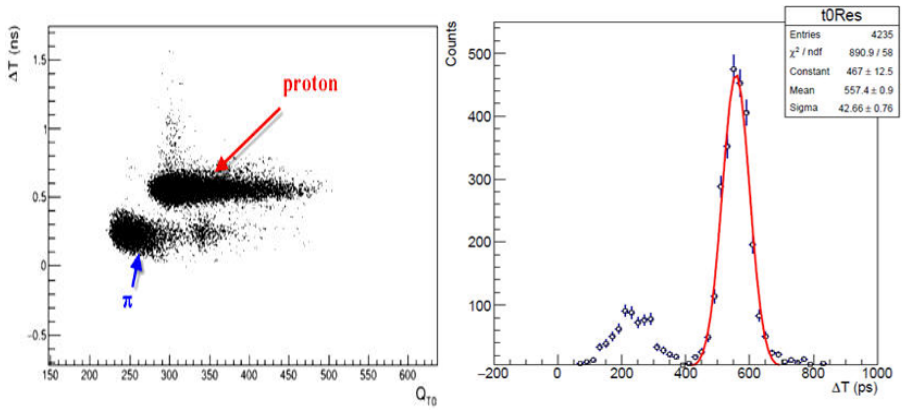

Fig. 5.18 (a) and (b) The Tr0 time vs. signal charge information for pions and protons, and (right) the time difference of ΔT=$\frac{(T1+T2+T3+T4)}{4}$.

The digital timing of the inner and outer MRPCs were filtered by the T1 to T4 scintillators, which required all of them to have signals. The average cluster size of

the MRPC was 1.6, as shown in Fig.5.19. The timing of inner and outer MRPCs was corrected with respect to Tr0, mainly for the time-amplitude slewing effect. The signal amplitude was estimated by its width (TOT). We have developed a new slewing correction method to correct the relationship between time and amplitude that combines fitting and bin counting. The MRPC timing and TOT plot were divided into several parts. To do the slewing correction, function fitting was used for the parts with enough statistics and bin-by-bin counting method was used for the other parts (Fig.5.20). Compared to the method used in Ref.[109], this new method has a better correction effect, especially for the channels with poor statistics. For poor statistics, there is not a suitable function that fits them, so the bin-by-bin method is a good way to do this slewing. The calibration strategy was pad-by-pad or strip-by-strip, so for every single pad or strip, we have very poor statistics. Fig.5.22 and 5.23 show the distribution of a typical MRPC timing relative to Tr0, ΔT= T_{MRPC} - Tr0 =T_{MRPC} - $\frac{(T1+T2+T3+T4)}{4}$ for proton and pion beams. The plots show that time resolution of MRPC were measured to be ~160 ps for protons and ~85 ps for pions. It was also found that the time resolution of inner and outer MRPCs are similar. The Fig.5.21 shows the efficiency plateau at BEPCII.

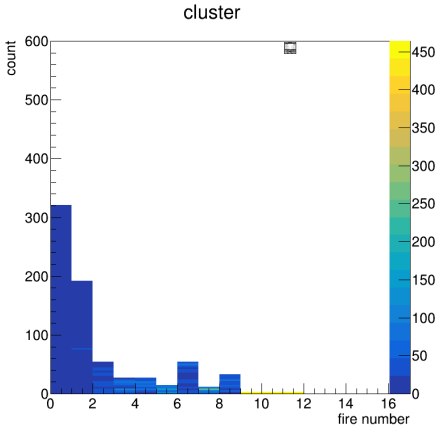

Fig. 5.19 The clustersize of the MRPC in hadron in-beam test.

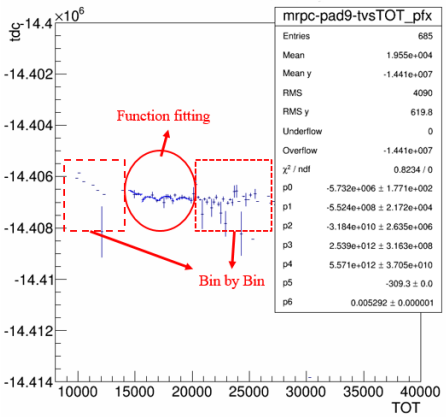

Fig. 5.20 The MRPC timing and TOT plot is divided into several parts.The circled part uses the function fitting and the rectangle parts use a bin-by-bin method to do slewing.

2. Simulation

Compared to the beam test result of the MRPCs with similar structure[5,102-103,108,110], the time resolution obtained for the simulation was significantly worse. The reason for this discrepancy is that, for beam test described in Ref.[109], the MRPCs were located in

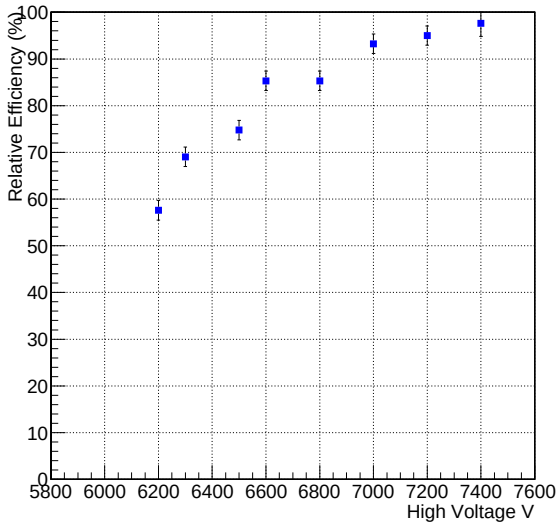

Fig. 5.21 Efficiency plateau at BEPCII.

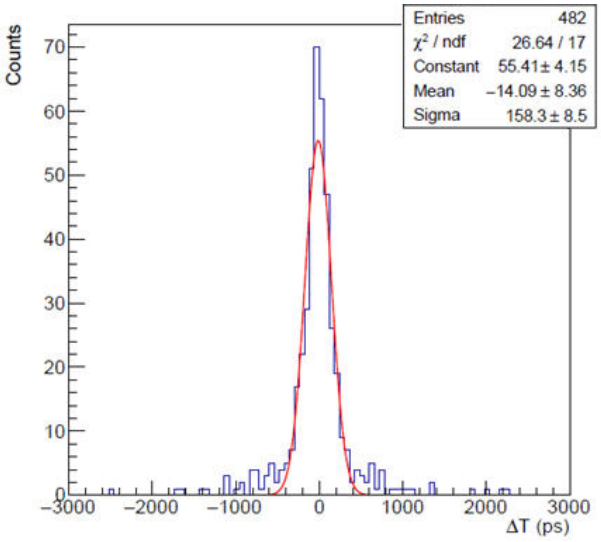

Fig. 5.22 MRPC time distribution relative to T_0 for a proton beam.

the middle position of the Tr0 detector. Thus the formula Tr0=$\frac{(T1+T2+T3+T4)}{4}$ provides a good estimation of the reference time for the MRPCs. However, in this work, the inner and outer MRPCs were placed downstream of the beam line at distances of ∼80 and ∼100 cm, respectively, from the geometric centre of the Tr0 detector. Because of the beam momentum uncertainty and the interaction with the detector materials that led to energy loss, multi-scattering etc., there was additional timing jitter compared to the measurement in Ref.[109]. This means what we measured and reported in Fig.5.22 and 5.23 are actually ΔT=$T_{MRPC} - (T0 + T_F)$, where T_F is the time of flight between the Tr0 and CSR-T0 MRPC modules. T_F varies because of beam momentum variation, so the intrinsic MRPC time resolution with this effect taken into account should be

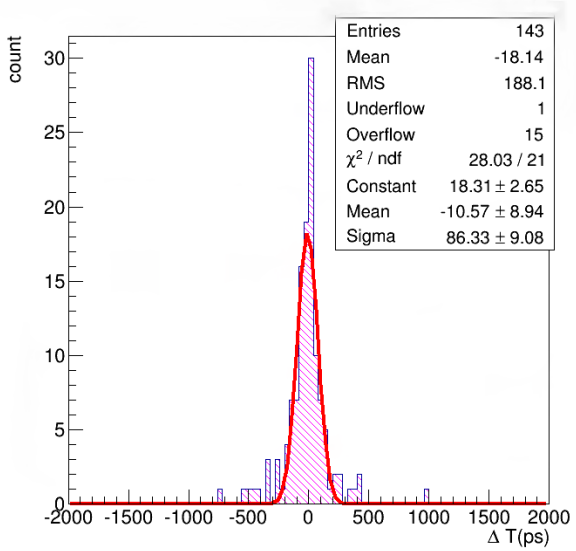

Fig. 5.23 MRPC time distribution relative to T_0 for a pion beam.

σ_{MRPC}=$\sqrt{\sigma^2_{\Delta T} - \sigma^2_{Tr0} - \sigma^2_{T_F}}$.

To quantitatively understand the experiment results, we used the GEANT4 toolkit[111] to simulate the beam test experiment at IHEP-E3. The beam test system was simplified in the simulation by only considering the most relevant detectors, including the two thin slices of plastic scintillator (SC1 and SC2, 5 cm × 5 cm × 0.5 cm) used for beam trigger, two groups of plastic scintillator strips (T1/T2 and T3/T4, 5 cm x 2 cm x 1 cm) used as the Tr0 detector, four CBM-TOF MRPC modules, and two CSR-T0 MRPC modules arranged along the beam direction. As much as possible, we used the materials used in the actual situation in the Geant4 description. Along the beam direction, each MRPC module mainly includes the following materials: an aluminum gas-tight shielding box (2-4 mm thick in total), three pieces of PCB (3-6 mm thick in total), 12 pieces of glass plate (6 mm thick in total), and a gas sensitive region (2.5 mm thick in total).

The beam momentum resolution was measured to be ∼2.5% at IHEP-E3 at an injection hadron beam momentum of 700 MeV/c. These parameters were considered in the GEANT4 simulation. The energy loss and the multiple Coulomb scattering were also taken into account. The reference time Tr0, was the the average of all four channels of the Tr0 detector. An intrinsic MRPC timing uncertainty of 40 ps and a Tr0 timing uncertainty of 20 ps were smeared into the simulation data. Fig.5.24 shows the distribution of T_{MRPC} - Tr0. By comparing Fig.5.24 to Fig.5.22, we see that the simulation and experimental results are consistent with each other, indicating that the MRPC time resolution is 40 ps. Note that the Tr0 time jitter is smaller in the simulation (20 ps) than that shown in experiment (40 ps, Fig.5.18), which includes an additional contribution

from beam momentum uncertainty as well as the intrinsic Tr0 uncertainty.

The above comparison was done for a proton beam. Because the IHEP-E3 beam also contains a small fraction of pions, we also compared the GEANT4 simulation results to the experimental MRPC time response for pions. We found that with an MRPC intrinsic timing uncertainty of 50 ps and a Tr0 intrinsic timing uncertainty of 40 ps smeared into the simulation, the simulated distribution of T_{MRPC} - Tr0 (shown in Fig.5.25) is consistent with the experimental results. The long tail on the time spectra is caused by the Coulomb multiply scattering and dE/dx effects of the beam, which are more significant for protons than for pions.

Through these analyses of simulation and experiment data, we conclude that the time resolution was ∼40 ps for proton and ∼50 ps for pion at 700 MeV/c, for both inner and outer MRPC modules. These values are also consistent with the results from previous test with similar MRPC structure[5,79,102,109].

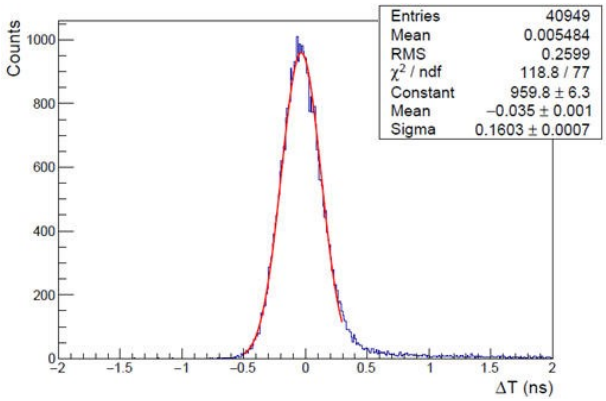

Fig. 5.24 The simulated distribution of T_{MRPC} - Tr0 with proton beam. The beam momentum uncertainty and Tr0 timing jitter are included.

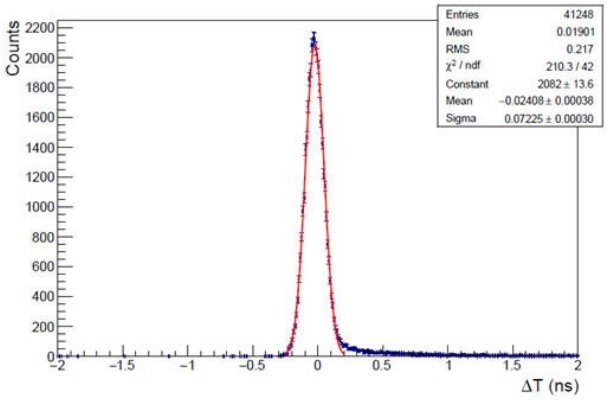

Fig. 5.25 The simulated distribution of T_{MRPC} - Tr0 with pion beam. The beam momentum uncertainty and Tr0 timing jitter are included.

5.3.5 Heavy-ion in-beam test Setup

The T0 detector prototype was tested with the heavy-ion beam at CSR in November 2016. Fig.5.26 shows a sketch of the T0 detector test setup for the CSR external-target experiment. Only 1/4 of the full T0 detector, including two inner and two outer MRPCs, was built and tested. A photograph of the MRPC modules and mechanical structure is also shown in Fig.5.26.

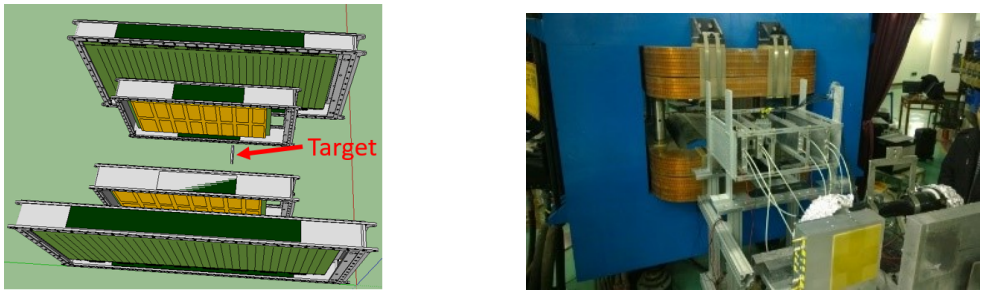

(a) (b)

Fig. 5.26 The design of the T0 detector structure (a) for the beam test at CSR, and the experiment photo (b).

An Ar-40 beam with a kinetic energy of 300 AMeV bombarded a lead and carbon target that was located at the geometrical center of the T0 detector. Operated in a stand-alone mode, the T0 system was self-triggered by requiring all four MRPCs be fired. The MRPC signal, after amplification and discrimination by the FEE, was sent to the digitalization electronics via a long cable (∼10 m). The total number of readout channels was 80, but we did not have enough electronics for this. Therefore, we used two kinds of TDCs with 40 channels recorded by FPGA TDC modules and the other 40 channels were processed by the previously designed time digitization modules based on HPTDCs. Synchronization between these two types of TDC modules was achieved based on two techniques. First, a 40 MHz system clock was fed to all the TDC modules, and thus the coarse time and fine time (after interpolation) were all synchronized with the phase of this clock signal. Second, after the electronics are powered up, a global reset signal is generated, and it was fanned out from the sub-trigger module to all the TDC modules to clear the coarse time counter value and align the “start” point for time measurement.

Fig.5.27 shows that the data from FPGA TDCs were stored in the internal buffer inside the FPGA, and the valid data were read out when a trigger signal was received. Trigger processing was organized in two hierarchies, and the trigger mode in this experiment was as follows. In the first step for the inner MRPC, the hit signals were fed

to a logic OR gate. For the outer MRPC, the hit signals from the two ends of one MPRC strip were input to an logic AND gate and then further processed by the following logic OR gate. The above processing functions were implemented in the TDC modules. Next, the flag signals from both the inner and outer MRPC electronics modules were sent to the sub-trigger module and processed by its logic AND gate. Finally, a trigger signal was generated and transmitted to all TDC modules through the star trigger bus in the PXI crate.

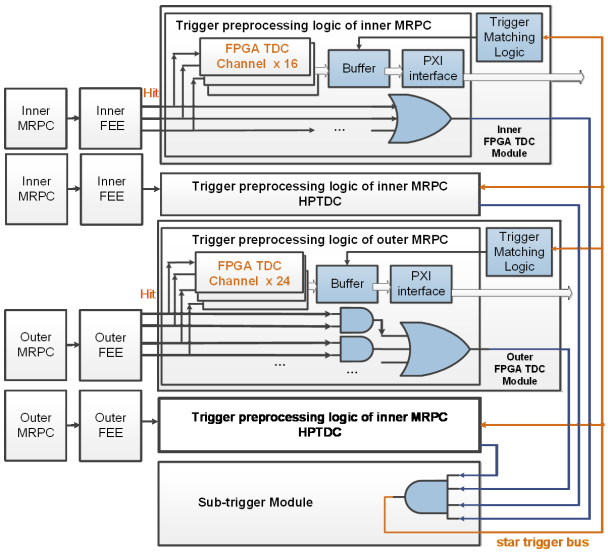

Fig. 5.27 Trigger processing and data readout.

5.3.6 The result of the heavy-ion in-beam test

1. The HV scan

According to the rule V $=V_a \frac{P_0 T}{P T_0}$ [112], where V_a is the applied voltage, T represents the operating temperature and P denotes the gas pressure, the operating voltage V changes with P, and thus with altitude. Therefore, MRPC operation has to adapt to the change in altitude at Lanzhou ($\sim$1500 m a.s.l.). We set up a cosmic-ray test during the beam time at CSR and checked the detection efficiency as a function of the applied HV, See Fig.5.19[5]. The efficiency was a relative efficiency without correction for the acceptance of cosmic-ray, but one can clearly see a plateau. The working HV was chosen to be 6800 V, which is significantly lower than the normal HV ($\sim$7200 V) for tests at the IHEP-E3 line (Fig.5.21) and in the laboratory.

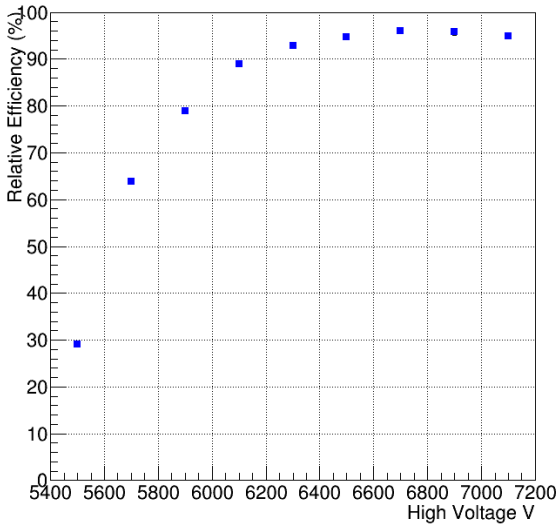

Fig. 5.28 MRPC detection efficiency vs. HV at CSR[5].

2. The calibration procedure

Because the test system was self-triggered, there was neither a reference time nor tracking and momentum information for the T0 detector. The event vertex position and field map that electronically channel match with the pad or strip number were also lacking. Thus, the basic calibration strategy was to correct each channel in a relative way. The time offset, TOT slewing correction, and particle velocity correction all needed to be calibrated.

The first step was to tune the time offset of each channel by comparing signals from neighbouring pads fired by a single particle. Each pair of inner and outer MRPCs of the T0 detector was combined to form one group (two groups in total in our test), and each group was calibrated separately. Fig.5.29 shows the cluster size and hit multiplicity plots. The maximum cluster size of the inner MRPCs (pad readout) was four, while for outer MRPCs (strip readout) was two. To suppress background hits, one fired strip on outer MRPC and two fired pads on inner MRPC within each group were required when calibrating the inner MRPC module. Fig.5.30 shows that the selected particle first hits the inner MRPC and then hits the outer MRPC, firing two neighbouring pads, so the hit point should be near the boundary region between the pads. In this case, when a single particle passes, it causes two fired channels of the inner MRPC, so their hit time should be the same. If channel 0 is considered to be the reference, and if all channels are iterated, the relative time offset can be evaluated and calibrated by a simple time shift for each channel. The calibration procedure for the outer MRPC modules is similar. In

this case, it is necessary for there to be only one fired channel on both inner and outer MRPCs.

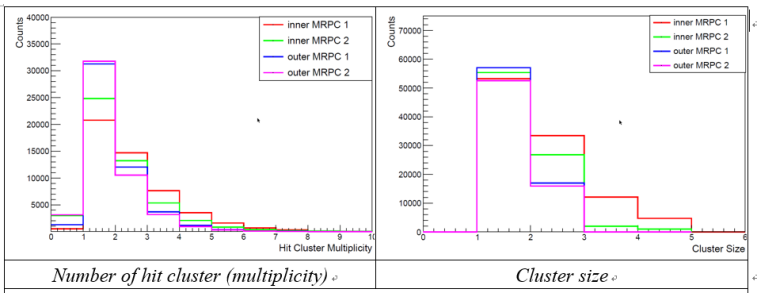

Fig. 5.29 The number of hit cluster and cluster size of the MRPC at beam time.

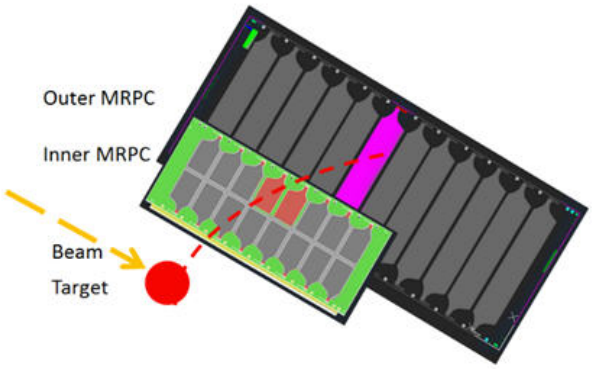

Fig. 5.30 Event selection: two neighbouring pads of inner MRPC and one strip of the outer MRPC were fired by a single particle.

The second step is to correct the time slewing effect for each channel. As in the step 1 calibration, a single charged particle was fired at both inner and outer MRPCs. Next, the time difference between neighbouring channels was plotted as a function of TOT_i , where TOT_i is the measured signal width of the channel to be calibrated. In our analysis the neighbouring pads/strips were those directly sharing one boundary with the selected pad/strip. For the inner MRPCs, one pad had three neighbouring pads (two neighbours for pads at the ends), and for outer MRPCs, one strip had two neighbouring strips (one neighbour for strips at the ends). For the outer MRPCs, TOT_i was the mean TOT measurements from both ends. A typical slewing effect is illustrated in Fig.5.31. A table of bin-by-bin center value, rather than a fit curve, was used to correct the TOT dependence. The procedure was repeated until convergence was observed.

The next step in the calibration concerns the particle momentum spread. In the beam test, the momenta of the final state charged particles varied significantly from ~200 to 600 MeV/c. Particles with momenta <200 MeV/c are likely to be absorbed or scattered by the detector materials. The particle speed can be estimated by the time

difference between the inner and outer MRPCs in the same group and their distance, v = $\frac{L_{Out}-L_{In}}{T_{Out}-T_{In}}$, where L_{Out} ,L_{In} ,T_{Out} and T_{In} are the flight lengths and times from the collision point to the outer and inner MRPC. For this test L_{Out} =22.5 cm and L_{In} = 12.5 cm. The event start time, T0 , can be calculated by $T_0 = \frac{T_{In}L_{Out}-T_{Out}L_{In}}{L_{Out}-L_{In}}$ (Eq. 1). This formula provides accurate collision time if there is no energy loss and if no multiple scattering effects are involved. However, at CSR energy, these factors cannot be ignored. Because relevant timing measurement from both groups of the MRPCs was necessary, to do a velocity calibration, we needed a reference Tr0. This was done by requiring each of the two groups of MRPCs to contain at least one valid track hitting both inner and outer MRPCs. Thus each group of MRPCs can give a measurement of Tr0, which can be used as a (relative) reference for the other group. The T_0 difference between the two groups was plotted vs. particle speed, as shown in Fig.5.32[5]. A clear velocity dependence was seen and used to calibrate the value of T_0.

There are some other factors that should be noted, such as the magnetic field and collision vertex uncertainty. The magnetic field was found to be <0.1 Tesla at the T0 detector location, so the bending radius of a proton was >6.7 m if the momentum was required to be >200 MeV/c. Compared to the flight length L_{Out} and L_{In}, the effect of magnetic field is small and, therefore, the effect was neglected in this analysis. The heavy-ion beam had a round shape and a root mean square (RMS) radius of 3 mm. Because there was no measurement of the collision vertex position, this uncertainty also affected the T0 detector time resolution.

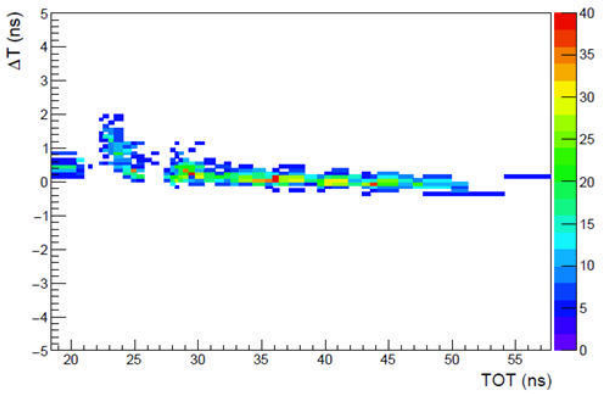

Fig. 5.31 Typical MRPC time vs TOT slewing correlation.

3. Time resolution

According to Eq. 1, the T0 detector's time resolution is mainly determined by the M-RPC timing accuracy, the particle flight length, and momentum spread. The vertex

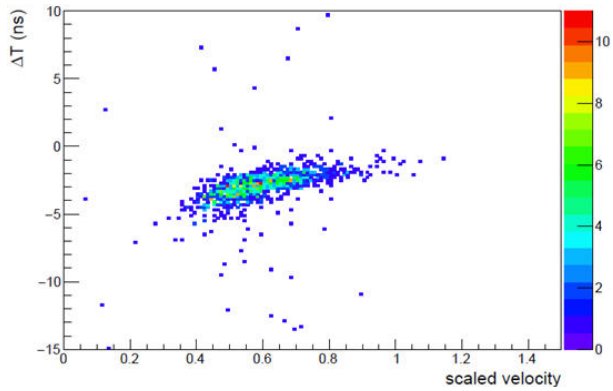

Fig. 5.32 Typical start time difference between two T0 groups vs. effective particle velocity.

uncertainty also affects the resolution by changing the flight length. To estimate the timing performance of the T0 detector, the start time differences between the two T0 groups are calculated using $\Delta T_{T0} = \frac{T_{01}-T_{02}}{2}$. Fig.5.33 (top a) shows their distribution after all corrections were applied. In this plot, each group was required to be hit by only one track, so $\sigma_{\Delta_{T0}}$ represents a good measure of the T0 detector resolution, σ_{T0}, by assuming $T_0 = \frac{T_{01}+T_{02}}{2}$. When there were two tracks recorded by the T0 detector (one track for each group), the T0 time resolution was found by double-Gaussian fitting to be ∼100 ps. See Fig. 5.33 (top a). We further studied the response uniformity of the T0 detector. Each group of the detector was divided into five regions according to the hit position along the beam direction. A total 10 regions were scanned, and the time resolution was measured in a similar way to what was done to generate Fig.5.33. The result is shown in Fig.5.34 (bottom b). It is clear that a uniform performance of the MRPCs was achieved.

Besides MRPC timing uncertainty, the observed T0 time resolution of ∼100 ps (Fig.5.33 (a) and (b)) included contributions mainly from the collision vertex uncertainty, which was measured to be σ_{VTX}= 3 mm in the plane perpendicular to the beam direction. To study this contribution to the uncertainty, events with two or more tracks hitting one of the two groups were selected, and the ΔT_{T0} distribution was drawn for each pair of tracks. Because both tracks were from the same group, the effect of the vertex position variation largely cancelled out. With a double-Gaussian fit, the T0 time resolution of ∼60 ps was determined. It is worthy noted that, in proposed CEE operation, the collision vertex will be precisely measured by other detectors, so it should not contribute to T0 time resolution. Both Ar+C and Ar+Pb collision data are analyzed. The results were found to be very similar and consistent with each other, despite some differences in hit multiplicity.

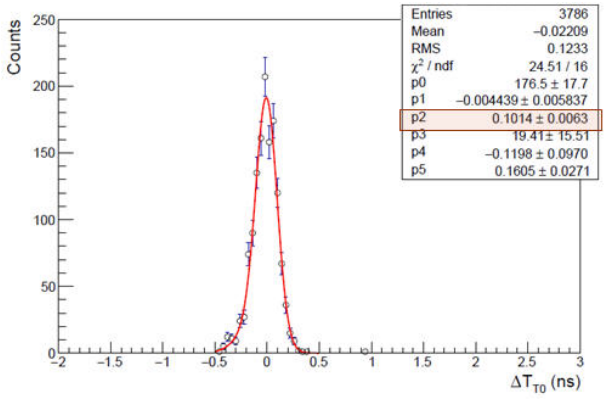

(a)

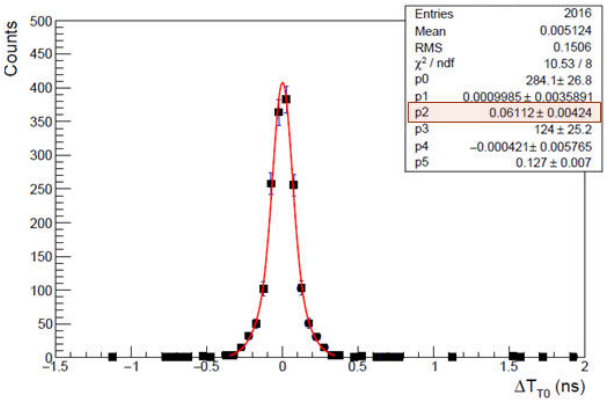

(b)

Fig. 5.33 The start time difference between two T0 groups (top), and within one T0 group (bottom).

4. Simulation study

Due to the lack of reference information of the collision time and other properties of the final state particles, we have used a Monte Carlo (MC) simulation to understand the experimental result and provide a performance expectation for the T0 detector. The GEANT4 toolkit was exploited for description of the detector and its response to particles generated by heavy-ion reaction. The heavy-ion collision event was simulated by the UrQMD3.4 generator[100]. The incident beam consisted of argon-40 nucleus and the target was carbon-12. The kinetic energy of the beam was 300 AMeV. For the simulations, we have given some hypothetical conditions.

- the MRPC intrinsic timing uncertainty was 50 ps, 75 ps and 100 ps
- the T0 detector was assumed to have full acceptance
- the simulation frame contains only MRPCs, gas boxes and FEEs

It was found that the simulation fit the experimental result best with a timing smearing

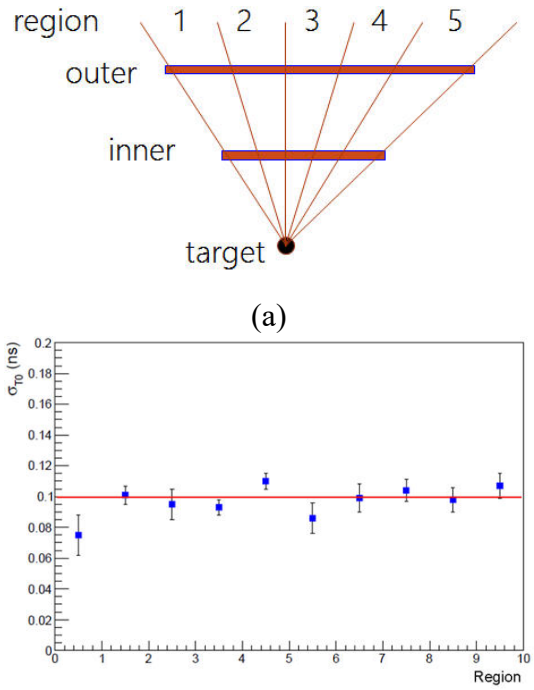

Fig. 5.34 (top) Different hit position regions along the beam direction, and (bottom) the T0 time resolution in each region.

of 50 ps. See Fig.5.35 the plot shows the deduced T_0 time resolution by a single track. The collision vertex was fixed, so its position did not contribute to the overall resolution. By comparing the T_0 time resolution with two tracks in Fig. 5.35 and in Fig.5.33 (bottom b), the MRPC time resolution, including contributions from electronics, particle momentum variation and magnetic field, should be better than 50 ps. This is consistent with the results for IHEP-E3 beam test and validated the excellent performance of the T0 prototype, which fully fulfills the design goal.

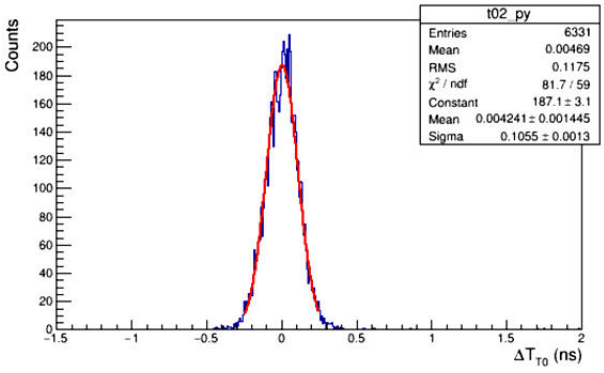

Fig. 5.35 The T0 time resolution from simulation data.

Chapter 6 Conclusion and Outlook

6.1 Conclusions

6.1.1 STAR/CBM eTOF

STAR has proposed several detector upgrades. The STAR Collaboration and the CBM Collaboration propose to install the CBM TOF detectors at the east pole endcap region of the STAR experiment at BNL as an ungrade for the Beam Energy Scan campaign in 2019/2020. MRPC3b detector as a part of CBM TOF wall, in the scope of the FAIR phase 0 program it is planned to install about 36% of the MRPC3b detectors in the STAR experiment.

At USTC the MRPC3b detector using float glass electrodes is developed which is foreseen for the low rate region of the CBM TOF wall. We have adjusted the matching impedance of the readout strips of CBM-TOF, in order to meet the CBM TOF wall-s requirements. The result is satisfactory. The second adjustment is that we used an ultra-thin glass assembly the detector. This device can meet the requirements of the rate ability for CBM TOF wall. In addition, we also study the relationship between the gas gap and the performance of the detector. From the beam test result, it shows that 230μm gap size may be a better choice for CBM-TOF. To clarity the reason, further investigation is needed. Besides that, we have developed a new method to do the slewing correction and a better result is achieved.

In the context of the CBM FAIR phase 0 program modules housing the MRPC3b counter has been installed and operated in the STAR experiment at BNL during the beam energy scan II program. Fig.6.1 shows the entire eTOF wheel after being installed at the STAR experiment. The BESII started in February 2019. During the BESII 2019 run, the readout stability has shown continuous improvements. Fig.6.2 exhibits the eTOF wheel's dark noise. Besides that, we have got the preliminary time resolution of this eTOF module, as shown in Fig.6.3. The BESII run is in progress, and more data samples are coming for further detailed analysis.

6.1.2 CEE-T0 detector

We have designed and produced a prototype CSR-T0 detector (1/4 acceptance) based on MRPC technology. The MRPCs, FEEs and the timing performance of a T0 prototype have been tested with hadron beam and heavy-ion beam. The efficiency of single MRPC

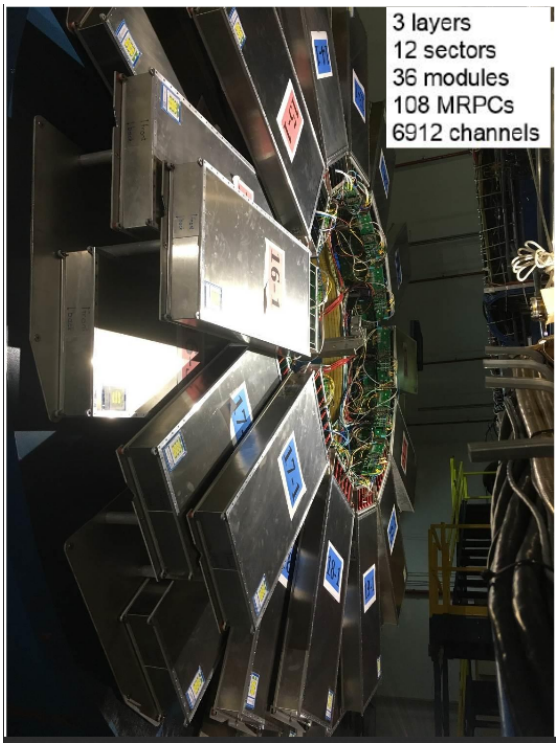

Fig. 6.1 eTOF wheel in the STAR experiment at BNL.

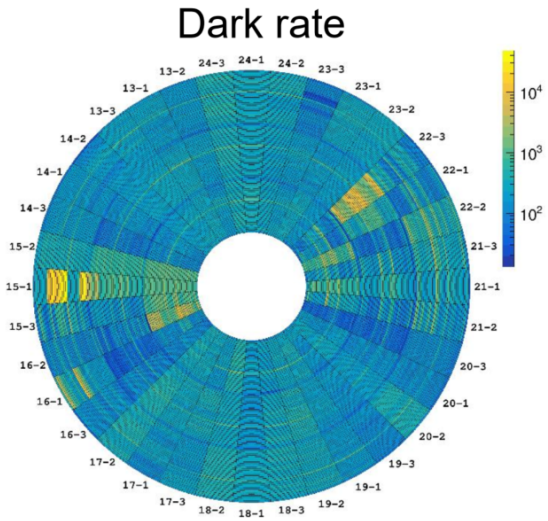

Fig. 6.2 Dark noise of the eTOF wheel.

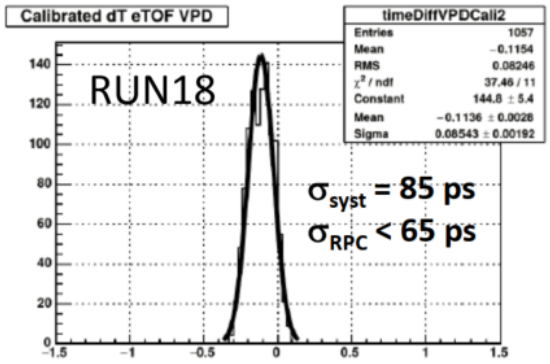

Fig. 6.3 System time resolution and intrinsic time resolution of the eTOF module.

module was also examined, but the overall trigger efficiency for a T0 detector was not able to be quantified due to lack of beam counting rate information. A GEANT4 based simulation was done to evaluate the experimental data analysis results. The intrinsic time resolution of MRPC, including electronics' contribution, was found to be better than 50ps for charged hadrons at a momentum below 1 GeV/c. From the heavy-ion beam test at CSR, the timing performance of the T0 prototype has been evaluated and met our expectation, which suggests that our high expectations for a full-coverage T0 seems promising.

6.2 Outlook

It has been more than 20 years since the invention of MRPC technology. MRPCs have found many applications in the community of high energy nuclear and particle experiments, as well as other fields. Although many progresses have been achieved, the interest and study on MRPC technology still seems vital. A typical MRPC based detector system consists of includes MRPC modules, electronics,DAQ and so on. Along with the studies described in this thesis, there are still many items to be improved. For instance, the impedance of the MRPC is still to be optimized. Although we have studied the impedance matching, a satisfactory model to describe the MRPC impedance is still not established. We will continue the optimization of the impedance of MRPC, based on simulation and experimental test. We are performing simulation studies for the MRPC, including all kinds of contributions from impedance matching, gas gap, gas gain and signal induction. A software package on MRPC performance simulation is being developed. Another aspect is the rate ability for the MRPC detector. The counting ability of MRPC is still a challenge for high rate. A new type of low resistive plate by coating proper resistive materials to the glass is being studied. For a new type of low

resistance material, its stability and uniformity is key point for the rate ability. So there are still many things can be studied. For our test system in laboratory, the modularity and portability of DAQ is also an important aspect, which are being worked on. Besides that, Offline analysis methods and analysis procedures are also to be improved. In brief, for the development of MRPC technology, we still have a lot to be studied.

Bibliography

[1] AARTS G, ATTANASIO F, JÄGER B, et al. Qcd at nonzero chemical potential: recent progress on the lattice[C]//AIP Conference Proceedings: volume 1701. AIP Publishing, 2016: 020001.

[2] HERRMANN N. Technical Design Report for the CBM Time-of-Flight System (TOF) [M/OL]. Darmstadt: GSI, 2014: 182 S. http://repository.gsi.de/record/109024.

[3] SHAO M, ZHAO Y, LI C, et al. Simulation study on the operation of a multi-gap resistive plate chamber[J]. Measurement Science and Technology, 2005, 17(1): 123.

[4] COLLABORATION S, et al. Cbm etof group[J]. Physics Program for the STAR/CBM eTOF Upgrade, 2016.

[5] HU D, SHAO M, SUN Y, et al. A t0/trigger detector for the external target experiment at csr [J]. Journal of Instrumentation, 2017, 12(06): C06010.

[6] RUBIN H, UNGAR P. Motion under a strong constraining force[J]. Communications on pure and applied mathematics, 1957, 10(1): 65-87.

[7] KNUTH D E. Computers and typesetting: A the TEXbook[M]. Reading, MA, USA: Addison-Wesley, 1986.

[8] LEE T D, LEE L. Symmetries, asymmetries, and the world of particles[M]. University of Washington Press, 1988.

[9] BROWN G E, RHO M. On the manifestation of chiral symmetry in nuclei and dense nuclear matter[J]. Physics Reports, 2002, 363(2): 85-171.

[10] HE S, WU S Y, YANG Y, et al. Phase structure in a dynamical soft-wall holographic qcd model[J]. Journal of High Energy Physics, 2013, 2013(4): 93.

[11] GLENDENNING N K. First-order phase transitions with more than one conserved charge: Consequences for neutron stars[J]. Physical Review D, 1992, 46(4): 1274.

[12] STEPHANOV M, RAJAGOPAL K, SHURYAK E. Event-by-event fluctuations in heavy ion collisions and the qcd critical point[J]. Physical Review D, 1999, 60(11): 114028.

[13] FRIESE V. Heavy-ion physics at high baryon densities[C]//EPJ Web of Conferences: volume 95. EDP Sciences, 2015: 03010.

[14] STEPHANOV M A. Qcd phase diagram and the critical point[J]. International Journal of Modern Physics A, 2005, 20(19): 4387-4392.

[15] GAZDZICKI M, COLLABORATION N, et al. Ion program of na61/shine at the cern sps[J]. Journal of Physics G: Nuclear and Particle Physics, 2009, 36(6): 064039.

[16] FRIESE V. The cbm experiment at gsi/fair[J]. Nuclear Physics A, 2006, 774: 377-386.

[17] HENNING W. Fair—an international accelerator facility for research with ions and antiprotons[C]//AIP Conference Proceedings: volume 773. AIP, 2005: 3-5.

[18] TRUBNIKOV G, AGAPOV N, ALEXANDROV V, et al. Project of the nuclotron-based ion collider facility (nica) at jinr[J]. Proceedings of EPAC08, Genoa, Italy, 2008.

[19] LÜ L, YI H, XIAO Z, et al. Conceptual design of the hirfl-csr external-target experiment [J/OL]. Science China Physics, Mechanics & Astronomy, 2016, 60(1): 012021. https://doi.org/10.1007/s11433-016-0342-x.

[20] HÖHNE C, SENGER P, ANDRONIC A, et al. Cbm experiment[M]//The CBM Physics Book. Springer, 2011: 849-972.

[21] SPILLER P, FRANCHETTI G. The fair accelerator project at gsi[J]. Nuclear Instruments and Methods in Physics Research Section A: Accelerators, Spectrometers, Detectors and Associated Equipment, 2006, 561(2): 305-309.

[22] WANG Y, COLLABORATION S, et al. Star upgrade program and future physics[C]//Journal of Physics: Conference Series: volume 535. IOP Publishing, 2014: 012022.

[23] HARRIS J, ADAMS D, ADDED N, et al. The star experiment at the relativistic heavy ion collider[J]. Nuclear Physics A, 1994, 566: 277-285.

[24] ACKERMANN K, ADAMS N, ADLER C, et al. Star detector overview[J]. Nuclear Instruments and Methods in Physics Research Section A: Accelerators, Spectrometers, Detectors and Associated Equipment, 2003, 499(2-3): 624-632.

[25] ACKERMANN K, ADAMS N, ADLER C, et al. The star time projection chamber[J]. Nuclear Physics A, 1999, 661(1-4): 681-685.

[26] ODYNIEC G. Future of the beam energy scan program at rhic[C]//EPJ Web of Conferences: volume 95. EDP Sciences, 2015: 03027.

[27] YANG C, COLLABORATION S, et al. The star beam energy scan phase ii physics and upgrades[J]. Nuclear Physics A, 2017, 967: 800-803.

[28] TLUSTY D. The rhic beam energy scan phase ii: Physics and upgrades[J]. arXiv preprint arXiv:1810.04767, 2018.

[29] XIAO Z, CHEN L W, FU F, et al. Nuclear matter at a hirfl-csr energy regime[J]. Journal of Physics G: Nuclear and Particle Physics, 2009, 36(6): 064040.

[30] XIAO Z G, YONG G C, CHEN L W, et al. Probing nuclear symmetry energy at high densities using pion, kaon, eta and photon productions in heavy-ion collisions[J]. The European Physical Journal A, 2014, 50(2): 37.

[31] KALWEIT A, COLLABORATION A, et al. Particle identification in the alice experiment [J]. Journal of Physics G: Nuclear and Particle Physics, 2011, 38(12): 124073.

[32] LIPPMANN C. Particle identification[J]. Nuclear Instruments and Methods in Physics Re-

search Section A: Accelerators, Spectrometers, Detectors and Associated Equipment, 2012, 666: 148-172.

[33] GROUP T A T, ANTONIOLI P. The alice time of flight system[J]. Nuclear Physics B-Proceedings Supplements, 2003, 125: 193-197.

[34] FONTE P, SMIRNITSKI A, WILLIAMS M. A new high-resolution tof technology[J]. Nuclear Instruments and Methods in Physics Research Section A: Accelerators, Spectrometers, Detectors and Associated Equipment, 2000, 443(1): 201-204.

[35] SPEGEL M, COLLABORATION A, et al. Recent progress on rpcs for the alice tof system [J]. Nuclear Instruments and Methods in Physics Research Section A: Accelerators, Spectrometers, Detectors and Associated Equipment, 2000, 453(1-2): 308-314.

[36] ZICHICHI A. The laa project (cern-ep-87-122)[J]. ICFA Instrum. Bull., 1987, 3(CERN-EP-87-122): 17-23.

[37] WANG X, CHENG J, WANG Y, et al. Design and construction of muon tomography facility based on mrpc detector for high-z materials detection[C]//2012 IEEE Nuclear Science Symposium and Medical Imaging Conference Record (NSS/MIC). IEEE, 2012: 83-85.

[38] WATTS D, BORGHI G, SAULI F, et al. The use of multi-gap resistive plate chambers for in-beam pet in proton and carbon ion therapy[J]. Journal of radiation research, 2013, 54 (suppl_1): i136-i142.

[39] CIOBANU M, HERRMANN N, HILDENBRAND K, et al. Padi, an ultrafast preamplifier-discriminator asic for time-of-flight measurements[J]. IEEE transactions on nuclear science, 2014, 61(2): 1015-1023.

[40] ANGHINOLFI F, JARRON P, MARTEMIYANOV A, et al. Nino: an ultra-fast and low-power front-end amplifier/discriminator asic designed for the multigap resistive plate chamber[J]. Nuclear Instruments and Methods in Physics Research Section A: Accelerators, Spectrometers, Detectors and Associated Equipment, 2004, 533(1-2): 183-187.

[41] TOWNSEND J. The conductivity produced in gases by the motion of negatively-charged ions[J]. Nature, 1900, 62(1606): 340.

[42] RIEGLER W, LIPPMANN C, VEENHOF R. Detector physics and simulation of resistive plate chambers[J]. Nuclear Instruments and Methods in Physics Research Section A: Accelerators, Spectrometers, Detectors and Associated Equipment, 2003, 500(1-3): 144-162.

[43] VAN ASSCHE F. Development of a resistive plate chamber detector simulation framework [Z]. 2016.

[44] MARTIN R, SIMMONS C, OWEN G. Accelerators, beam handling and targets[J]. Nuclear Instruments and Methods in Physics Research A, 2003, 500: 288-358.

[45] RIEGLER W, LIPPMANN C, VEENHOF R. Detector physics and simulation of resistive

plate chambers[J]. Nuclear Instruments and Methods in Physics Research Section A: Accelerators, Spectrometers, Detectors and Associated Equipment, 2003, 500(1-3): 144-162.

[46] DEPPNER I M. Development of a fully differential multi-gap resistive plate chamber for the cbm experiment[D]. 2013.

[47] SANPEI M, ABE K, HOSHI Y, et al. Performance of resistive plate counter with non-ozone depletion freon[J]. IEEE Transactions on Nuclear Science, 1997, 44(3): 752-756.

[48] AKINDINOV A, ALICI A, ANTONIOLI P, et al. Operation of the multigap resistive plate chamber using a gas mixture free of flammable components[J]. Nuclear Instruments and Methods in Physics Research Section A: Accelerators, Spectrometers, Detectors and Associated Equipment, 2004, 531(3): 515-519.

[49] MANDELLI B, CAPEANS M, GUIDA R, et al. Systematic study of rpc performances in polluted or varying gas mixture compositions: An online monitor system for the rpc gas mixture at lhc[C]//2012 IEEE Nuclear Science Symposium and Medical Imaging Conference Record (NSS/MIC). IEEE, 2012: 1135-1140.

[50] AIELLI G, CAMARRI P, CARDARELLI R, et al. Sf6 quenched gas mixtures for streamer mode operation of rpcs at very low voltages[J]. Nuclear Instruments and Methods in Physics Research Section A: Accelerators, Spectrometers, Detectors and Associated Equipment, 2002, 493(3): 137-145.

[51] ZEBALLOS E C, HATZIFOTIADOU D, KIM D, et al. Effect of adding sf6 to the gas mixture in a multigap resistive plate chamber[J]. Nuclear Instruments and Methods in Physics Research Section A: Accelerators, Spectrometers, Detectors and Associated Equipment, 1998, 419(2-3): 475-478.

[52] GONZALEZ-DIAZ D, FONTE P, GARZON J, et al. An analytical description of rate effects in timing rpcs[Z]. 2006.

[53] WEIPING Z, YI W, SHENGQIN F, идр. A thin float glass MRPC for the outer region of CBM-TOF wall[J]. Nuclear Instruments and Methods in Physics Research Section A: Accelerators, Spectrometers, Detectors and Associated Equipment, 2014, 735: 277-282.

[54] WANG Y, HUANG X, LV P, et al. Study on high rate mrpc for high luminosity experiments [J]. Journal of Instrumentation, 2014, 9(08): C08003.

[55] DEPPNER I, HERRMANN N, AKINDINOV A, et al. The cbm time-of-flight wall—a conceptual design[J]. Journal Of Instrumentation, 2014, 9(10): C10014.

[56] GONZÁLEZ-DIAZ D, CIOBANU M, CORDIER E, et al. Progress in the cbm-tof wall, r&d and simulation[J]. CBM Progress Report: 39.

[57] WANG J, WANG Y, ZHU X, et al. Development of multi-gap resistive plate chambers with low-resistive silicate glass electrodes for operation at high particle fluxes and large transported

charges[J]. Nuclear Instruments and Methods in Physics Research Section A: Accelerators, Spectrometers, Detectors and Associated Equipment, 2010, 621(1-3): 151-156.

[58] HU D, SAUTER D, SUN Y, et al. Mrpc3b mass production for cbm-tof and etof at star[J]. arXiv preprint arXiv:1807.02452, 2018.

[59] BICHSEL H, KLEIN S, GROOM D E. Passage of particles through matter[Z]. 2004.

[60] VEENHOF R. Garfield, recent developments[J]. Nuclear Instruments and Methods in Physics Research Section A: Accelerators, Spectrometers, Detectors and Associated Equipment, 1998, 419(2-3): 726-730.

[61] AN F, SUN S, LIU H, et al. Monte-carlo study of the mrpc prototype for the upgrade of besiii [J]. Journal of Instrumentation, 2016, 11(09): C09022.

[62] RAMO S. Currents induced by electron motion[J]. Proceedings of the IRE, 1939, 27(9): 584-585.

[63] GOUBAU G. Surface waves and their application to transmission lines[J]. Journal of Applied Physics, 1950, 21(11): 1119-1128.

[64] SHAHPARNIA S, RAMAHI O M. Electromagnetic interference (emi) reduction from printed circuit boards (pcb) using electromagnetic bandgap structures[J]. IEEE Transactions on Electromagnetic Compatibility, 2004, 46(4): 580-587.

[65] HREISH E B, MILLER C A. High frequency printed circuit board via[Z]. Google Patents, 2003.

[66] BAHL I, GARG R. Simple and accurate formulas for a microstrip with finite strip thickness [J]. Proceedings of the IEEE, 1977, 65(11): 1611-1612.

[67] CASU G, MORARU C, KOVACS A. Design and implementation of microstrip patch antenna array[C]//2014 10th International Conference on Communications (COMM). IEEE, 2014: 1-4.

[68] KOLSRUD A. Pcb’s top ground plane and its effect on a microstrip line’s characteristic impedance[Z].

[69] BARTOŞ D, PETRIŞ M, PETROVICI M, et al. A method to adjust the impedance of the transmission line in a multi-strip multi-gap resistive plate counter[J]. arXiv preprint arXiv:1708.02707, 2017.

[70] NI. Aplac[Z].

[71] GROVE T, MASTERS M, MIERS R. Determining dielectric constants using a parallel plate capacitor[J]. American journal of physics, 2005, 73(1): 52-56.

[72] LIU S, FENG C, AN Q, et al. Bes iii time-of-flight readout system[J]. IEEE Transactions on Nuclear Science, 2010, 57(2): 419-427.

[73] DESPEISSE M, JARRON P, ANGHINOLFI F, et al. Low-power amplifier-discriminators

for high time resolution detection[C]//2008 IEEE Nuclear Science Symposium Conference Record. IEEE, 2008: 1820-1826.

[74] FAN H, FENG C, SUN W, et al. A high-density time-to-digital converter prototype module for bes iii end-cap tof upgrade[J]. IEEE Transactions on Nuclear Science, 2013, 60(5): 3563-3569.

[75] MOTA M, CHRISTIANSEN J, DEBIEUX S, et al. A flexible multi-channel high-resolution time-to-digital converter asic[C]//2000 IEEE Nuclear Science Symposium. Conference Record (Cat. No. 00CH37149): volume 2. IEEE, 2000: 9-155.

[76] MOD C. V1290 n, technical information manual, 00104/03: V1x90[J]. MUTx/11, 2010, 580.

[77] ELLIOTT C, VIJAYAKUMAR V, ZINK W, et al. National instruments labview: a programming environment for laboratory automation and measurement[J]. JALA: Journal of the Association for Laboratory Automation, 2007, 12(1): 17-24.

[78] JIA-CAI L, YUAN-MING W, et al. A test beam upgrade based on the bepc-linac[J]. High Energy Phsics and Nuclear Physics, 2004, 28(12): 1269.

[79] COLLABORATION B, et al. The construction of the besiii experiment[J]. Nuclear Instruments and Methods in Physics Research Section A: Accelerators, Spectrometers, Detectors and Associated Equipment, 2009, 598(1): 7-11.

[80] KAPITÁN J. Star inner tracking upgrade—a performance study[J]. The European Physical Journal C, 2009, 62(1): 217-221.

[81] ETOF GROUP T C C, COLLABORATION S, et al. Physics program for the star/cbm etof upgrade[J]. arXiv preprint arXiv:1609.05102, 2016.

[82] NEISER A, ADAMCZEWSKI-MUSCH J, HOEK M, et al. Trb3: a 264 channel high precision tdc platform and its applications[J]. Journal of Instrumentation, 2013, 8(12): C12043.

[83] BELLENOT B, LINEV S. Javascript root[C]//Journal of Physics: Conference Series: volume 664. IOP Publishing, 2015: 062033.

[84] SATHEESH M, D'MELLO B J, KROL J. Web development with mongodb and nodejs[M]. Packt Publishing Ltd, 2015.

[85] AL-TURANY M, BERTINI D, KARABOWICZ R, et al. The fairroot framework[C]//Journal of Physics: Conference Series: volume 396. IOP Publishing, 2012: 022001.

[86] BRUN R, RADEMAKERS F. Root—an object oriented data analysis framework[J]. Nuclear Instruments and Methods in Physics Research Section A: Accelerators, Spectrometers, Detectors and Associated Equipment, 1997, 389(1-2): 81-86.

[87] BRUN R, RADEMAKERS F, PANACEK S, et al. The root users guide[J]. CERN, http://root.cern. ch, 2003.

[88] AKISHINA E, ALEKSANDROV E, ALEKSANDROV I, et al. Conceptual considerations for cbm databases[R]. Lab. of Information Technologies, 2014.

[89] BERTINI D, BERTINI O, LAVRIK E, et al. The cbm sts quality assurance database[J]. CBM Progress Report 2015: 124.

[90] AL-TURANY M, BERTINI D, KOENIG I. Cbmroot: Simulation and analysis framework for cbm experiment[J]. Computing in High Energy and Nuclear Physics (CHEP-2006), 2006, 1: 170-171.

[91] ZHENG J, CAO P, JIANG D, et al. Low-cost fpga tdc with high resolution and density[J]. IEEE Transactions on Nuclear Science, 2017, 64(6): 1401-1408.

[92] TRAXLER M, BAYER E, KAJETANOWICZ M, et al. A compact system for high precision time measurements (< 14 ps rms) and integrated data acquisition for a large number of channels[J]. Journal of Instrumentation, 2011, 6(12): C12004.

[93] MICHEL J, FRÖHLICH I, BÖHMER M, et al. The hades trigger and readout board network (trbnet)[C]//2010 17th IEEE-NPSS Real Time Conference. IEEE, 2010: 1-5.

[94] BATTISTONI G, CERUTTI F, FASSO A, et al. The fluka code: Description and benchmarking[C]//AIP Conference proceedings: volume 896. AIP, 2007: 31-49.

[95] DEPPE H, FLEMMING H. The gsi event-driven tdc with 4 channels get4[C]//2009 IEEE Nuclear Science Symposium Conference Record (NSS/MIC). IEEE, 2009: 295-298.

[96] FLEMMING H, DEPPE H. The gsi event driven tdc asic get4 v1. 23[J]. GSI Scientific Report, 2013.

[97] MOREIRA P, WYLLIE K, YU B, et al. The gbt project[Z]. CERN, 2009.

[98] WYLLIE K, BARON S, BONACINI S, et al. A gigabit transceiver for data transmission in future high energy physics experiments[J]. Physics Procedia, 2012, 37: 1561-1568.

[99] CST. Cst[Z].

[100] URQMD. Urqmd[Z]. 2005.

[101] GAPIENKO V, GAVRISHCHUK O, GOLOVIN A, et al. Studying the counting rate capability of a glass multigap resistive plate chamber at an increased operating temperature[J]. Instruments and Experimental Techniques, 2013, 56(3): 265-270.

[102] YONG-JIE S, SHUAI Y, CHENG L, et al. A prototype mrpc beam test for the besiii etof upgrade[J]. Chinese Physics C, 2012, 36(5): 429.

[103] ZEBALLOS E C, CROTTY I, HATZIFOTIADOU D, et al. A new type of resistive plate chamber: the multigap rpc[J]. Nuclear Instruments and Methods in Physics Research Section A: Accelerators, Spectrometers, Detectors and Associated Equipment, 1996, 374(1): 132-135.

[104] ANGHINOLFI F, JARRON P, KRUMMENACHER F, et al. Nino, an ultra-fast, low-power,

front-end amplifier discriminator for the time-of-flight detector in alice experiment[C]//2003 IEEE Nuclear Science Symposium. Conference Record (IEEE Cat. No. 03CH37515): volume 1. IEEE, 2003: 375-379.

[105] WANG J, LIU S, ZHAO L, et al. The 10-ps multitime measurements averaging tdc implemented in an fpga[J]. IEEE Transactions on Nuclear Science, 2011, 58(4).

[106] DENG P, ZHAO L, LU J, et al. Readout electronics of t0 detector in the external target experiment of csr in hirfl[J]. IEEE Transactions on Nuclear Science, 2018, 65(6): 1315-1323.

[107] CHRISTIANSEN J. Hptdc high performance time to digital converter[Z]. 2004.

[108] SHAO M, DONG X, TANG Z, et al. Upgrade of the calibration procedure for a star time-of-flight detector with new electronics[J]. Measurement Science and Technology, 2008, 20(2): 025102.

[109] YANG S, SUN Y, LI C, et al. Test of high time resolution mrpc with different readout modes for the besiii upgrade[J]. Nuclear Instruments and Methods in Physics Research Section A: Accelerators, Spectrometers, Detectors and Associated Equipment, 2014, 763: 190-196.

[110] AKINDINOV A, ALICI A, ANSELMO F, et al. Results from a large sample of mrpc-strip prototypes for the alice tof detector[J]. Nuclear Instruments and Methods in Physics Research Section A: Accelerators, Spectrometers, Detectors and Associated Equipment, 2004, 532(3): 611-621.

[111] AGOSTINELLI S, ALLISON J, AMAKO K A, et al. Geant4—a simulation toolkit[J]. Nuclear instruments and methods in physics research section A: Accelerators, Spectrometers, Detectors and Associated Equipment, 2003, 506(3): 250-303.

[112] GONZALEZ-DIAZ D, BELVER D, BLANCO A, et al. The effect of temperature on the rate capability of glass timing rpcs[J]. Nuclear Instruments and Methods in Physics Research Section A: Accelerators, Spectrometers, Detectors and Associated Equipment, 2005, 555(1-2): 72-79.

[113] DE GRUTTOLA D, ABBRESCIA M, AGOCS A, et al. A multigap resistive plate chamber array for the extreme energy events project[J]. Journal of Instrumentation, 2014, 9(10): C10024.

Appendix A Returning particles

A.1 The decay of the muon

In the whole mass production test, we found a very interesting phenomenon that some particles crossing the six eTOF modules from the bottom to top. As shown in the Fig.A.1, X-axis is the particle's velocity and Y-axis is the time to previous particle. Two separate populations of upward-going relativistic particles (with β close to -1) are clearly identified. we are guessing that the relativistic up-going electrons are produced from the decay of downward-going muons stopping in the lowermost part of the test stand, with $\mu^- \rightarrow e^- + \nu_e + \nu_\mu$ [113]. The ratio of the normal particle to the unnormal particles is around 10%. In the future, if possible, a special MRPC telescope system could be set up to detect the decay of munos in cosmic rays and to search for the probability of such extreme events occurring.

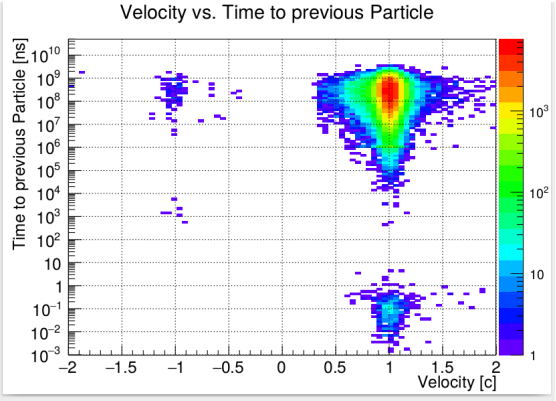

Fig. A.1 Distribution event sample in the time difference to previous event. The signal from the decay of the muon

Acknowledgements

匆匆六年，弹指一挥间，六年间发生了太多的故事，人来人往，在此非常怀念一位逝去的老人。记得刚来到科大的时候，唐老师带着我去您的办公室，您向我问有关我考研的问题，您亲切的拿过一瓶矿泉水，问我渴不渴，当时很紧张，习惯性的说了一声不渴。当我知道您就是我所看的那本原子物理教科书的作者，那时的我无比激动。又无比兴奋，我可以跟这样一位老师继续学习。2017 年，临出国前去看您，您问我工作的问题，我不知如何回答，自己做的完全对不起您对我的期望。每次开完会组会，您把我带到您的办公室，问我这个你应该想，那个应该看。太多的感谢不知如何表达。如今我要毕业了，我想向您说，非常感谢您，我很怀念您。遗憾和希望伴随我成长。

在研究生学习期间，我有幸得到过好多为老师的指导，首先要感谢我的第一位导师邵明教授，从研究生到博士生，他一致耐心的指导我，言传身教，从他身上学习到什么是效率，如何去表达，工作应该如何去完成，如何去分配，总感觉他是能化腐朽为神奇的存在。

另一位我要感谢的导师，孙勇杰副教授。从他身上让我知道我思考的不足，不能去过度的自信，每每的事情都有让我感觉思想达不到的地方，如何去思考问题，虽然已经在他身边呆了六年，依然没有掌握这门绝技，努力还得继续。

在海德堡期间有幸得到 Norbert Herrmman 的细心指导，这位导师年过六旬，依然奋战在科研的第一线，自己亲自写程序，做分析，十分佩服他为科研奉献的精神。每天 5 个小时的睡眠时间，并不是每个人都可以做到，日复一日，年复一年。很期望自己也有这样的能力。

非常感谢唐泽波副教授，他是在科大第一个认识我的导师，对我的生活，工作关心无微不至，非常感谢，唐老师总是让我感到，我做的科研还远远不够，他前沿的思维，让我十分钦佩。感谢李澄教授对我的指导，李老师是我科大的研究生导师，李老师对高能物理的无所不知，高能物理实验的要求，合作组内要求，总是让我大开眼界，原来高能物理是这样要求。

感谢周意副教授，周老师更像是我们这一届的兄长，周老师对实验要求的精益求精，总是让我感觉，原来实验可以玩的这么好看。感谢张一飞副教授，张老师是一位很各方面都很强的老师，很遗憾没有和张老师一起踢球。感谢曾晖老师，每次都是麻烦曾老师帮我订实验仪器。感谢 Ingo Deppner 博士，海德堡的生活如果没有你，我过得将会很艰难。谢谢你对我生活和工作上的帮助。感谢黄贯顺教授，每次遇到问题，您总是那么细心的帮助我解答。感谢我的好友，陈小龙博士，从研究生复试到博士毕业，一路走来，感谢我的舍友，尤文豪博士，他做

事情认真的态度，使我受益良多。感谢我的舍友朱兵博士，海德堡的生活没有你，我的世界将变得很小。

感谢实验室的师兄师姐，师弟师妹，陈天翔博士，帅鹏博士，查王妹博士，杨驰副教授，江琨博士，张生辉博士，杨荣星，杨钱博士，王小壮博士，周龙博士，赵晓坤博士，谢冠男博士，孙艳坤博士，刘圳博士，王鹏飞，吕游，纪媛婧，宋国峰，巨星跃，吴奕涛，张辉，王旭，洪道金，封建新，李贺，李阳，李子阳，李子味，曹泽华，胡天齐，叶世超，梁政，沈凯峰，魏凯。等等，特别感谢，周健和汪新建师弟，他们两个和我一起成长，帮助我修改论文。感谢海德堡的 Christian，Philipp，Dennis, jonathan, 王庆亮，胡隆，lavrik ,nayan, 汪静，裴昱，杨兵博士，张亚鹏副教授。感谢我的好友，李臻，董丽媛，王雷，李强，张文娟，郭云强，汪洪，王勇，张海清，梁旭伟，周思意，祝冲，陈希苑。最后感谢我的家人，父母，姐姐，女友戴张昱对我的支撑和鼓励，使我能在艰难的博士生涯看到光明的。

Publications

已发表论文

1. D Hu, M Shao, Y Sun, et al., A T0/Trigger detector for the External Target Experiment at CSR, Journal of Instrumentation 12 (06) (2017) C06010.

2. W You,Y.Zhou, D Hu, et al.,A new technique for assembling large-size GEM detectors，Journal of Instrumentation 12 (06) (2017) C06036

3. CBM Collaboration: T. Ablyazimov, A. Abuhoza, R.P. Adak, Dongdong Hu, et al.,Challenges in QCD matter physics - The Compressed Baryonic Matter experiment at FAIR, Eur. Phys. J. A (2017)

4. D Hu, X Wang, Y.Sun, et al., The MRPC3b mass production for CBM-TOF and eTOF at STAR, JINT 已接收

5. D Hu, X Wang, Y.Sun, et al., Beam Test of CBM-TOF MRPC Prototype, JINST 已接收

6. D Hu, J Zhou, M Shao, et al., Beam test study of the MRPC-based T0 detector for the CEE, JINST 已接收

7. J.Zhou, Y.Sun, X.Wang, D.Hu, M.Shao, C.Li, Z.Tang, Y.Zhang, Y.Zhou, MRPC3b for CBM-TOF, JINST 已接收

已提交论文

1. D.Hu, J.Lu, J.Zhou, P.Deng, M.Shao, et al., Beam test study of prototype MRPCs for the T0 detector at the CSR external-target experiment NIMA

待发表论文

1. D Hu, N.Herrmann, I.Deppner, M Shao, Y Sun, Quality control of mass production for STAR/CBM-eTOF upgrade

2. D Hu, Y.Sun, C.Christian, J.Zhou, X.Wang, Mass production of MRPC3b for STAR/CBM-eTOF